Applied Computational Electromagnetics Society

Journal

March 2013 Vol. 28 No. 3

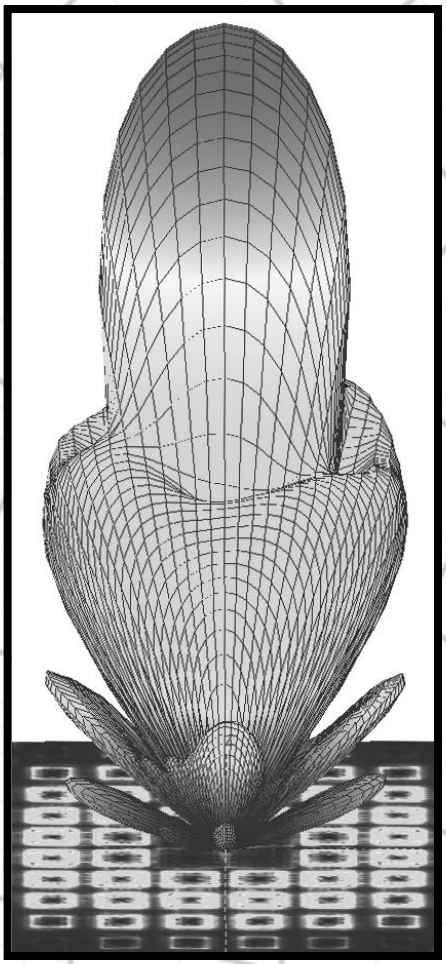

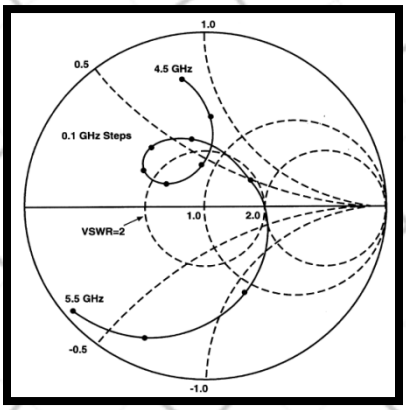

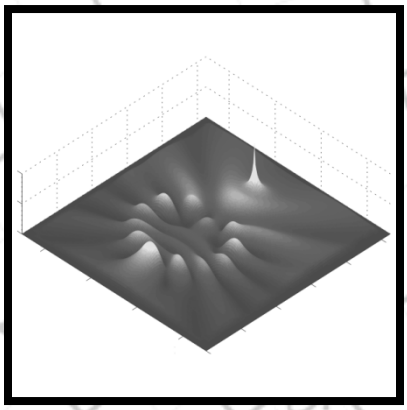

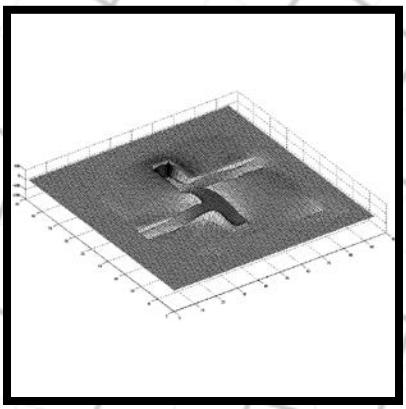

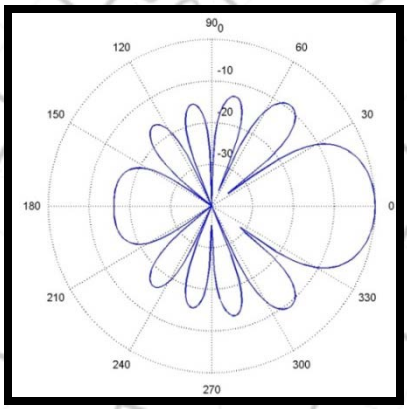

ISSN 1054-4887

GENERAL PURPOSE AND SCOPE: The Applied Computational Electromagnetics Society ***(ACES)*** Journal hereinafter known as the ***ACES Journal*** is devoted to the exchange of information in computational electromagnetics, to the advancement of the state-of-the art, and the promotion of related technical activities. The primary objective of the information exchange is to inform the scientific community on the developments of new computational electromagnetics tools and their use in electrical engineering, physics, or related areas. The technical activities promoted by this publication include code validation, performance analysis, and input/output standardization; code or technique optimization and error minimization; innovations in solution technique or in data input/output; identification of new applications for electromagnetics modeling codes and techniques; integration of computational electromagnetics techniques with new computer architectures; and correlation of computational parameters with physical mechanisms.

SUBMISSIONS: The ***ACES Journal*** welcomes original, previously unpublished papers, relating to applied computational electromagnetics. Typical papers will represent the computational electromagnetics aspects of research in electrical engineering, physics, or related disciplines. However, papers which represent research in applied computational electromagnetics itself are equally acceptable.

Manuscripts are to be submitted through the upload system of ***ACES*** web site http://www.aces-society.org See "Information for Authors" on inside of back cover and at ***ACES*** web site. For additional information contact the Editor-in-Chief:

Dr. Atef Elsherbeni
Department of Electrical Engineering
The University of Mississippi
University, MS 386377 USA
Phone: 662-915-5382
Email: atef@olemiss.edu

SUBSCRIPTIONS: All members of the Applied Computational Electromagnetics Society are entitled to access and download the ***ACES Journal*** any published journal article available at http://www.aces-society.org. Printed issues of the ***ACES Journal*** are delivered to institutional members. Each author of published papers receives a printed issue of the ***ACES Journal*** in which the paper is published.

Back issues, when available, are $50 each. Subscription to ***ACES*** is through the web site. Orders for back issues of the ***ACES Journal*** and change of address requests should be sent directly to ***ACES*** office at:

Department of Electrical Engineering
The University of Mississippi
University, MS 386377 USA
Phone: 662-915-7231
Email: aglisson@olemiss.edu

Allow four weeks advance notice for change of address. Claims for missing issues will not be honored because of insufficient notice, or address change, or loss in the mail unless the ***ACES*** office is notified within 60 days for USA and Canadian subscribers, or 90 days for subscribers in other countries, from the last day of the month of publication. For information regarding reprints of individual papers or other materials, see "Information for Authors".

LIABILITY. Neither ***ACES***, nor the ***ACES Journal*** editors, are responsible for any consequence of misinformation or claims, express or implied, in any published material in an ***ACES Journal*** issue. This also applies to advertising, for which only camera-ready copies are accepted. Authors are responsible for information contained in their papers. If any material submitted for publication includes material which has already been published elsewhere, it is the author's responsibility to obtain written permission to reproduce such material.

APPLIED COMPUTATIONAL ELECTROMAGNETICS SOCIETY JOURNAL

March 2013
Vol. 28 No. 3
ISSN 1054-4887

The ACES Journal is abstracted in INSPEC, in Engineering Index, DTIC, Science Citation Index Expanded, the Research Alert, and to Current Contents/Engineering, Computing & Technology.

The illustrations on the front cover have been obtained from the research groups at the Department of Electrical Engineering, The University of Mississippi.

MARCH 2013 REVIEWERS

Ahmed Abdelrahman
Shuaib Ahmed
Mohamed Bakr
Sami Barmada
Vicente Boria
David Chen
Dajun Cheng
Khaled ElMahgoub
Shan Jiang
Paolo Mezzanotte
Usman Saeed
Apirat Siritaratiwat
Alan Taflove
Fernando Teixeira
Mauro Tucci
Joshua Wilson
Yoshihide Yamada
Guang Yang
Qiang Yu

THE APPLIED COMPUTATIONAL ELECTROMAGNETICS SOCIETY

JOURNAL

Vol. 28 No. 3 March 2013

TABLE OF CONTENTS

RCS2D: A 2D Scattering Simulator for MoM vs. FDTD Comparisons

Gizem Toroğlu [1], Mehmet Alper Uslu [1], and Levent Sevgi [1, 2]

[1] Electronics and Communications Engineering Department
Doğuş University, 34722 Istanbul – Turkey
toroglugizem@yahoo.com, alperuslu@ieee.org

[2] Electrical and Computer Engineering Department
University of Massachusetts, Lowell, MA – USA
lsevgi@dogus.edu.tr, Levent_sevgi@uml.edu

Abstract ─ A Java-based, two dimensional (2D) electromagnetic wave scattering and Radar Cross-Section (RCS) simulation software, RCS2D Virtual Tool, is developed. Both Method of Moments (MoM) and Finite-Difference Time-Domain (FDTD) methods are used to simulate the Transverse Magnetic (TM) and Transverse Electric (TE) polarized scattering waves for arbitrary geometries and materials under the plane wave illumination.

Index Terms - Electromagnetic waves, FDTD, MoM, radar cross section (RCS), scattering, TM, and TE.

I. INTRODUCTION

Electromagnetic (EM) scattering deals with wave and object interaction. Understanding this interaction and scattering is essential in low-visible target design, cancer detection, mine exploration, etc. A Java-based, two dimensional (2D) simulator (i.e., RCS2D) is developed for the investigation of EM scattering from arbitrary objects and different materials. First version of the simulator was presented in [1]. In this paper, the latest version, which can handle arbitrary EM materials, is introduced.

The simulator deals with geometries shown in Fig. 1. Here, an infinitely long, either conducting or dielectric/ferrite cylinder with user-drawn arbitrary cross section located along the z-axis and illuminated by a plane wave from a specified direction is taken into account. The simulations are performed with two powerful numerical models (MoM and FDTD), which make comparisons possible. The TM and TE problems are both investigated.

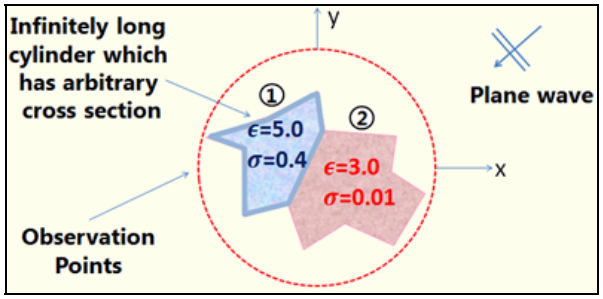

Fig. 1. An object with arbitrary cross section illuminated by a plane wave from a given direction.

II. THE METHOD OF MOMENTS (MOM) MODEL

MoM is a frequency domain model and has been in use since 1960s [2] (see, also [3] for a tutorially review of MoM and some simple applications). It is based on the discretization /reduction of time-harmonic EM field integral equations into a linear matrix system. MoM model for dielectric cylinders of arbitrary cross section was first proposed by Richmond in [4] and then generalized to dielectric / diamagnetic objects with oblique incident case in [5]. Although, both TM_z and TE_z polarizations are implemented only TM_z equations are included here.

Submitted On: July 26, 2012
Accepted On: Dec. 30, 2012

The incident field components for the TM_z case are in the form of,

$$E_z^{(inc)} = E_0 e^{jk_0(x(n)cos(\phi)+y(n)sin(\phi))} \quad (1)$$

$$H_x^{(inc)} = \frac{E_0 k_0 Sin(\phi)}{\mu\omega} E_z^{(inc)}, \quad H_y^{(inc)} = -\frac{E_0 k_0 Cos(\phi)}{\mu\omega} E_z^{(inc)}, \quad (2)$$

where ϕ is the incident angle, k_0 is the free space wave number, E_0 is the amplitude of the incident electric field, and N is the total number of cells (n=1,2,…..,N). After calculating the incident fields, a size of $3N\times1$, Y matrix is constructed as,

$$Y = \left[E_z^{(inc)} \quad \eta_0 H_x^{(inc)} \quad \eta_0 H_y^{(inc)} \right]^T \quad (3)$$

where η_0 is the free space wave impedance.

The incident fields create surface currents on the surface of the object and that currents then produce scattered fields. The total field is the sum of incident and scattered fields,

$$E_z = E_z^{inc} + E_z^s, \quad H_x = H_x^{inc} + H_x^s, \quad H_y = H_y^{inc} + H_y^s. \quad (4)$$

The cross section of the object under investigation is divided into small pieces (compared to wavelength) called segments (or patches). The problem is discretized accordingly and a matrix form is obtained,

$$[Z]\left[E_z \;\; \eta_0 H_x \;\; \eta_0 H_y \right]^T = Y. \quad (5)$$

The $3N \times 3N$, Z matrix shown in equation (5) is expressed as follows,

$$Z = \begin{bmatrix} A & B & C \\ D & E & F \\ G & F & H \end{bmatrix} \quad (6)$$

and the entries of the Z matrix are given in Table 1. Here, $a_{m,n}$ is the area of the rectangular cell at the location of m or n, $\mu_{r(m,n)}$ is the relative magnetic permeability of the m^{th} or n^{th} cell and $\varepsilon_{r(m,n)}$ is the relative electric permittivity of the m^{th} or n^{th} cell. Electric field of each cell can be calculated from equation (5),

$$\left[E_z \;\; \eta_0 H_x \;\; \eta_0 H_y \right]^T = [Z]^{-1} \left[E_z^{(inc)} \;\; \eta_0 H_x^{(inc)} \;\; \eta_0 H_y^{(inc)} \right]^T. \quad (7)$$

The electric field component of the scattered field at any point outside the dielectric body is given by,

$$E_z^s = j\frac{\pi}{2}\sqrt{\frac{2j}{\pi}} \sum_{n=1}^{N} k a_n J_1(k a_n) e^{jk(x_n \cos\phi + y_n \sin\phi)} \frac{e^{-jkr_0}}{\sqrt{k\rho_0}} \times \left[(\mu_{rn} - 1)[\eta_0 H_{yn} \cos\phi - \eta_0 H_{xn} \sin\phi] \right]. \quad (8)$$

Scattered fields of the observation angle ϕ can be represented in terms of RCS (σ) defined as,

$$W(\phi) = \lim_{\rho_0 \to \infty} 2\pi\rho_0 \left| \frac{E_z^s(\rho_0, \phi)}{E_z^i} \right|^2$$

$$W(\phi) = \frac{\pi^2 k}{\left|E^i\right|^2} \left| \sum_{n=1}^{N} (\epsilon_n - 1) E_{zn} a_n J_1(k a_n) e^{jk(x_n cos\phi + y_n \sin\phi)} \right|^2. \quad (9)$$

III. THE FINITE DIFFERENCE TIME DOMAIN (FDTD) MODEL

The FDTD model, first proposed by K. S. Yee in 1966 [6], which is based on the application of second-order center difference approach to time and spatial derivatives in Maxwell's equations. FDTD is a time domain method and frequency domain responses are extracted by using Fourier Transform (FT). Due to its finite nature, original Yee algorithm should be modified at the terminals of the simulation space. In addition, near-to-far field (NTFF) transformation is required to handle RCS problems. The time domain NTFF transforms give broadband frequency response and are useful for mono-static RCS simulations. The frequency domain NTFF transformations give direct (discrete) frequency response but useful for bi-static RCS simulations. Both transformations utilize surface equivalence theorem on a virtual closed surface placed at a particular distance. The far field response is then calculated via these surface currents. In RCS2D, free-space effects are simulated via perfectly matched layer (PML) approach and the frequency domain NTFF transformation is used [7].

VI. THE RCS2D VIRTUAL TOOL AND EXAMPLES

The front panel graphical user interface (GUI) of the java-based RCS2D virtual tool is illustrated in Fig. 2. It has two distinct EM solvers (MoM and FDTD). The virtual tool can run with both models and results may be compared in terms of accuracy and computation time.

Table 1: The entries of the Z matrix.

m ≠ n	**m = n**
$A_{mn} = -(\epsilon_{rn}-1)\frac{\pi k a_n}{2j} J_1(ka_n) H_0^{(2)}(k\rho_{mn})$	$A_{mm} = 1+\frac{j}{2}(\epsilon_{rm}-1)[\pi k a_m H_1^{(2)}(ka_m) - 2j]$
$B_{mn} = \frac{\pi k a_n}{2} J_1(ka_n)(\mu_{rn}-1)(y_m - y_n)\frac{H_1^{(2)}(k\rho_{mn})}{\rho_{mn}}$	$B_{mm} = 0$
$C_{mn} = -\frac{\pi k a_n}{2} J_1(ka_n)(\mu_{rn}-1)(x_m - x_n)\frac{H_1^{(2)}(k\rho_{mn})}{\rho_{mn}}$	$C_{mm} = 0$
$D_{mn} = \frac{\pi k a_n}{2} J_1(ka_n)(\epsilon_{rn}-1)(y_m - y_n)\frac{H_1^{(2)}(k\rho_{mn})}{\rho_{mn}}$	$D_{mm} = 0$
$E_{mn} = \frac{(\mu_{rn}-1)\pi jka_n}{2} J_1(Ka_n)\frac{-1}{(k\rho_{mn})^3}\times$ $\left[\begin{array}{l} -k^3\rho_{mn}(y_m-y_n)^2 H_0^{(2)}(k\rho_{mn}) \\ +[(y_m-y_n)^2-(x_m-x_n)^2]k^2 H_1^{(2)}(k\rho_{mn}) \end{array}\right]$	$E_{mm} = 1+\frac{j(\mu_{rm}-1)}{4}[\pi k a_m H_1^{(2)}(ka_m) - 4j]$
$F_{mn} = -\frac{(\mu_{rn}-1)\pi k a_n J_1(ka_n) k^2}{2j(k\rho_{mn})^3}(x_m-x_n)(y_m-y_n)\times$ $[2H_1^{(2)}(k\rho_{mn}) - k\rho_{mn} H_0^{(2)}(k\rho_{mn})]$	$F_{mm} = 0$
$G_{mn} = \frac{-\pi k a_n}{2} J_1(ka_n)(\epsilon_{rn}-1)(x_m-x_n)\frac{H_1^{(2)}(k\rho_{mn})}{\rho_{mn}}$	$G_{mm} = 0$
$H_{mm} = 1+\frac{j(\mu_{rm}-1)}{4}[\pi k a_m H_1^{(2)}(ka_m) - 4j]$	$H_{mn} = \frac{(\mu_{rn}-1)\pi jka_n}{2} J_1(Ka_n)\frac{1}{(k\rho_{mn})^3}$ $\left[\begin{array}{l} -k^3\rho_{mn}(x_m-x_n)^2 H_0^{(2)}(k\rho_{mn}) \\ +[(x_m-x_n)^2-(y_m-y_n)^2]k^2 H_1^{(2)}(k\rho_{mn}) \end{array}\right]$

Highly effective charts are included; thus, the visualization of the simulation results becomes attractive. The front panel is split into four subsections. The top block contains numerous image buttons to improve accessibility. The left block is divided into two: collapsible workspace and summary subpanels. Workspace demonstrates all features that are supplied by the program. The summary part provides the user to observe all actions as well as computer resources. The right panel has four tabs: simulation area, model, visualization, and simulation results. The user draws any object/geometry he or she desires via the simulation area tab. The model tab shows the segmentation of the objects. The visualization tab is reserved for real-time wave monitoring of FDTD based simulations. Simulation results tab is reserved for the polar plots.

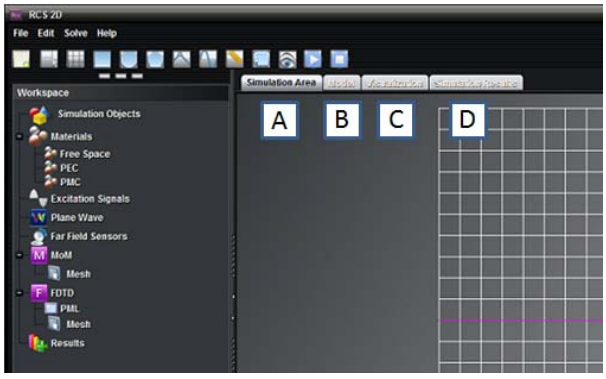

Fig. 2. Front panel of the RCS2D (A: simulation area, B: model, C: visualization, and D: simulation results).

The program provides three basic geometric buttons (square, ellipse, and polygon) to make object creation/drawing easy. Scaling, translating,

rotating, and mirroring the objects is possible. Object dragging is also included. Overlapping objects (after dragging or rotating, etc.) are categorized according to the user decision.

Several tests with different materials and geometries are performed to illustrate the power of the RCS2D tool and comparisons are given below. MoM and FDTD models are also validated through these tests. First, an infinite cylinder with the cross section shown in Fig. 3 (a) is taken into account. The dimensions and the frequency are given in the figure inset. The cylinder is formed of two lossy dielectric parts. This cylinder is illuminated by a plane wave from an angle of 30° and bi-static scattered fields are recorded all around. The observation points are located at 4 m away. Results for the TM_z polarization are given in Fig. 3 (b). As observed, forward scattered field is dominant and MoM and FDTD results agree very well.

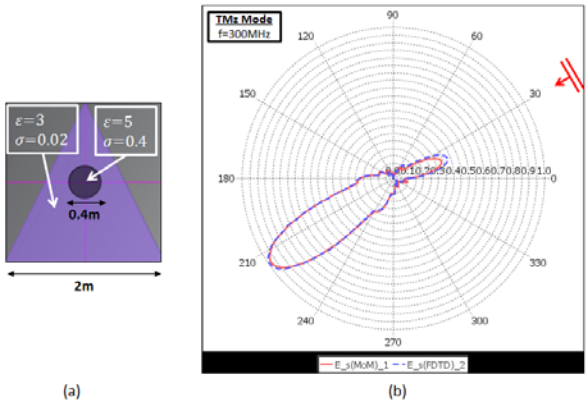

Fig. 3. (a) The first test cylinder and (b) the scattered field of the test cylinder.

The second example belongs to the RCS of another inhomogeneous dielectric object. The cross section of the object used in this example is shown in Fig. 4 (a). The cylinder is composed of two lossy dielectric triangles and the illuminated angle of the incident plane wave is 240°. The results for the same polarization are shown in Fig. 4 (b).

The third example belongs to an F-shaped dielectric infinite cylinder and again the TM_z mode. The object is illuminated by a plane wave having an incident angle of 330°. The results are given in Fig. 5.

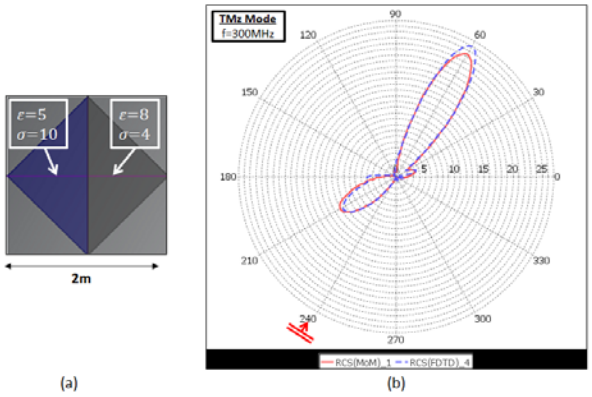

Fig. 4. (a) The second test cylinder and (b) the RCS of the test cylinder.

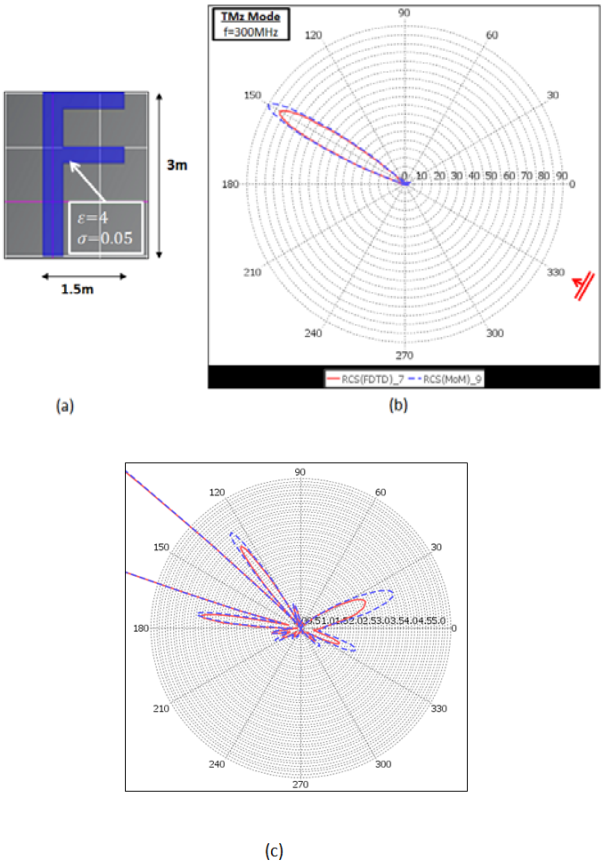

Fig. 5. (a) An F-shaped lossy dielectric cylinder, (b) RCS vs. angle, and (c) magnified view.

The final example investigates an infinite lossy dielectric square cylinder for the TE_z case. The size of a square is 0.4 m. The frequency is 600 MHz. The angle of the incident plane wave is 30° and observation points are located on a circle enclosing the object with 5 m radius. Figure 6 (a)

shows the structure and the scattered fields are given in Fig. 6 (b).

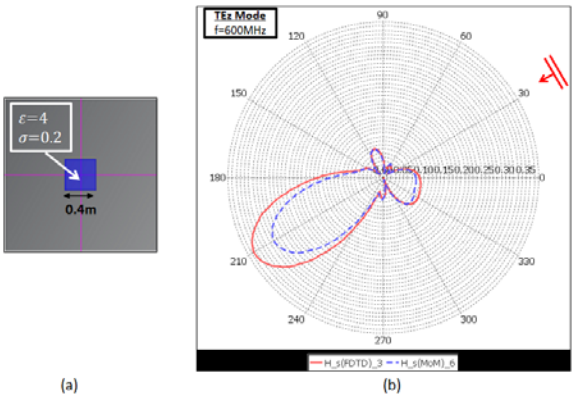

Fig. 6. (a) A square shaped lossy dielectric cylinder and (b) the scattered field of the test cylinder at 5 m away.

Any object can be modeled in RCS2D by specifying conductivity, permittivity, and permeability. PEC objects can also be modeled by giving significantly high conductivities. Note that, rough discretization is used for both MoM and FDTD calculations to speed up the computations. This is one of the reasons of discrepancies between MoM and FDTD results in the plots (another reason is the incapability of diffraction modeling in MoM). Better agreement will be obtained if object discretization is performed with a higher number of cells/segments. FDTD requires much more memory, but is much faster when compared to MoM.

V. CONCLUSION

An attractive EM scattering simulation package (RCS2D) is presented. Method of Moments (MoM) and Finite-Difference Time-Domain (FDTD) method are used to simulate both TM and TE polarized scattered fields. EM scattering of arbitrary geometries and different materials under plane wave illumination can be investigated with RCS2D.

REFERENCES

[1] G. Toroglu, A. Uslu, and L. Sevgi, "RCS2D: A 2D MoM and FDTD based simulator", *MMS 2012, The 12th Mediterranean Microwave Symposium*, Dogus University, Istanbul, Turkey, Sep. 14-16, 2012.

[2] [3] R. F. Harrington, *Field Computation by Moment Method*, New York: IEEE Press, (First Ed. 1968), 1993.

[3] E. Arvas and L. Sevgi, "A tutorial on the method of moments," *IEEE Antennas and Propagation Magazine*, vol. 54, no. 3, pp. 260-275, June 2012.

[4] J. H. Richmond, "TE-wave scattering by a dielectric cylinder of arbitrary cross-section shape," *IEEE Trans. Antennas Propagat.*, vol. 14, no. 4, pp. 460-464, 1966.

[5] R. G. Rojas, "TE-wave scattering by a dielectric cylinder of arbitrary cross-section shape," *IEEE Trans. Antennas Propagat.*, vol. 36, no. 2, pp. 238-246, 1988.

[6] K. S. Yee, "Numerical solution of initial boundary value problems involving Maxwell's equations in isotropic media," *IEEE Trans. Antennas and Propagat.*, vol. 14, pp. 302–307, 1966.

[7] J. P. Berenger, "Three dimensional perfectly matched layer for the absorption of electromagnetic waves," *Journal of Computational Physics*, vol. 127, pp. 363-379, 1996.

MoM Analysis of an Axisymmetric Chiral Radome

Halid Mustacoglu [1], Joseph R. Mautz [2], and Ercument Arvas [2]

[1] Anaren Microwave, Inc.
6635 Kirkville Road, East Syracuse, NY 13057, USA
hmustacoglu@anaren.com

[2] Department of Electrical Engineering and Computer Science
Syracuse University, Syracuse, NY 13244, USA
jrmautz@syr.edu and earvas@syr.edu

Abstract ─ An axisymmetric chiral radome has been analyzed numerically by using the method of moments. The chiral body is illuminated by a plane wave and the surface equivalence principle is used to replace the body by equivalent electric and magnetic surface currents. The effect of adding chirality to a dielectric radome of revolution is investigated throughout numerical results obtained for bodies of different shapes and material parameters. Chiral materials can be used to design anti-reflective structures to control scattering cross section patterns of bodies. A computer program is developed for the chiral radome of revolution and examples of numerical calculations are given for a chiral spherical radome, a chiral cylindrical radome, and a chiral Von Karman radome. Numerical results for the chiral spherical radome are in excellent agreement with the exact ones obtained by the eigenfunction solution. Moreover, the numerical results of the chiral Von Karman radome are in excellent agreement with the published results.

Index Terms - Axisymmetric radome, chiral radome, method of moments, and surface equivalence theorem.

I. INTRODUCTION

An axisymmetric chiral radome has been analyzed numerically by using Method of Moments (MoM) with the surface equivalence principle. Scattering and radiation from radomes and antenna systems with radomes have been studied in the last couple decades by using different methods, such as the ray tracing technique [1-3], the plane wave spectrum-surface integral technique [4], the MoM [5-8], the physical optics (PO) method and dielectric physical optics (DPO) technique [9], the finite element method (FEM) [10], the method of regularization (MoR) [11], the hybrid PO-MoM technique [12], the transmission-line modeling method [13], the adaptive integral method [14], the dyadic Green's function (DGF) technique [15-16], the fast Fourier transform (FFT) [17] and precorrected fast Fourier transform methods (P-FFT) [18], body of revolution (BOR) formulations of MoM [19-26], and the finite difference time domain (FDTD) method [27].

Arbitrary dielectric bodies, 3-D arbitrary lossy dielectric bodies, arbitrary conducting bodies, dielectric bodies of revolution, conducting bodies of revolution with and without apertures, dielectric radomes of revolution, chiral and/or metal coated dielectric bodies, a 2-D chiral radome of arbitrary shape, and dielectric radomes with antenna systems were investigated in [1–35] by using the methods mentioned above.

We have not found any work that uses MoM to analyze an axisymmetric 3-D chiral radome and calculates the internal fields and scattering from it. Here, we consider different shapes of axisymmetric chiral radomes to find out the effects of sizes and shapes on the internal fields and scattered fields outside by using MoM with BOR formulations. This work is a continuation of our previous work [36].

Submitted On: March 18, 2012
Accepted On: Dec. 16, 2012

II. ANALYSIS

A plane wave is incident on the homogeneous chiral shell of permittivity ε_2, permeability μ_2, and chirality ξ_2, shown in Fig. 1, where the η's are intrinsic impedances. A homogeneous region characterized by the medium parameters $\varepsilon_1 = \varepsilon_0$ and $\mu_1 = \mu_0$ surrounds the shell. ($\mathbf{E}^i$, $\mathbf{H}^i$) represents the incident field produced by external sources in the absence of the shell. S_1 and S_2 represent the outer and inner surfaces of the shell, respectively. The field (**E**, **H**) in the region bounded by S_2 and the scattered field external to S_1 are of interest in this paper.

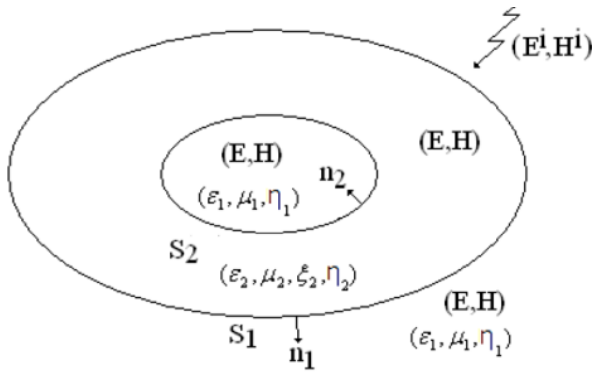

Fig. 1. A chiral radome illuminated by a plane wave.

A. Surface equivalence of the problem

Using the equivalence principle, the problem of Fig. 1 can be reduced to three simpler and equivalent problems shown in Figs. 2, 3, and 4. In the external equivalence, electric surface current $\mathbf{J}_1$ and magnetic surface current $\mathbf{M}_1$ have been placed on S_1. These surface currents are radiating in an unbounded medium of (ε_1, μ_1) with the same incident field of Fig. 1. The total field at any point in the external region bounded by S_1 in Fig. 2 is the same as the total field at the same point of Fig. 1, while the total field at any point in the internal region bounded by S_1 in Fig. 2 is zero.

$$\mathbf{E}_{1\tan}(\mathbf{J}_1, \mathbf{M}_1) = -\mathbf{E}^i_{\tan} \text{ on } S_1^- \quad (1)$$

$$\mathbf{H}_{1\tan}(\mathbf{J}_1, \mathbf{M}_1) = -\mathbf{H}^i_{\tan} \text{ on } S_1^-, \quad (2)$$

$$\mathbf{J}_1 = \mathbf{n}_1 \times \mathbf{H}^+_{out}, \quad (3)$$

$$\mathbf{M}_1 = \mathbf{E}^+_{out} \times \mathbf{n}_1, \quad (4)$$

where the superscript "–" on S_1 indicates the side of S_1 opposite the region into which $\mathbf{n_1}$ points. $\mathbf{E}_1(\mathbf{J}_1, \mathbf{M}_1)$ and $\mathbf{H}_1(\mathbf{J}_1, \mathbf{M}_1)$, respectively, denote the electric and magnetic fields produced by the surface currents $\mathbf{J}_1$ and $\mathbf{M}_1$ when they radiate in the unbounded medium of (ε_1, μ_1). $\mathbf{n_1}$ denotes the unit outward vector on S_1 and $(\mathbf{E}^+_{out}, \mathbf{H}^+_{out})$ are the total fields just outside S_1 in Fig. 1.

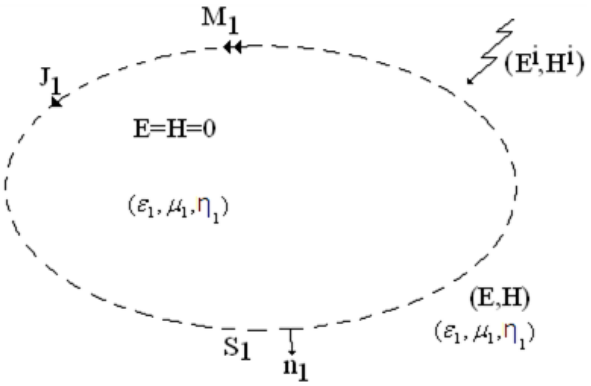

Fig. 2. External equivalence of the problem shown in Fig. 1.

In the internal equivalence for the region bounded by S_1 and S_2, surface currents $-\mathbf{J}_1$, $-\mathbf{J}_2$, $-\mathbf{M}_1$, and $-\mathbf{M}_2$ are placed on S_1 and S_2 where they radiate in the unbounded medium of (ε_2, μ_2, ξ_2). They produce the correct total fields (**E**, **H**) at any point in the region bounded by S_1 and S_2 and produce zero fields at any point outside the region bounded by S_1 and S_2.

$$\mathbf{E}_{2\tan}(\mathbf{J}_1, \mathbf{M}_1, \mathbf{J}_2, \mathbf{M}_2) = 0 \text{ on } S_1^+ \quad (5)$$

$$\mathbf{E}_{2\tan}(\mathbf{J}_1, \mathbf{M}_1, \mathbf{J}_2, \mathbf{M}_2) = 0 \text{ on } S_2^+, \quad (6)$$

$$\mathbf{H}_{2\tan}(\mathbf{J}_1, \mathbf{M}_1, \mathbf{J}_2, \mathbf{M}_2) = 0 \text{ on } S_1^+, \quad (7)$$

$$\mathbf{H}_{2\tan}(\mathbf{J}_1, \mathbf{M}_1, \mathbf{J}_2, \mathbf{M}_2) = 0 \text{ on } S_2^+, \quad (8)$$

$$\mathbf{J}_2 = \mathbf{n}_2 \times \mathbf{H}^-_{in}, \quad (9)$$

$$\mathbf{M}_2 = \mathbf{E}^-_{in} \times \mathbf{n}_2, \quad (10)$$

where S_1^+ and S_2^+ denote the sides of the surfaces S_1 and S_2 facing the regions into which the unit vectors $\mathbf{n_1}$ and $\mathbf{n_2}$ point, and $\mathbf{E}_2(\mathbf{J}_1, \mathbf{M}_1, \mathbf{J}_2, \mathbf{M}_2)$ and $\mathbf{H}_2(\mathbf{J}_1, \mathbf{M}_1, \mathbf{J}_2, \mathbf{M}_2)$, respectively, denote the electric and magnetic fields produced by the equivalent surface currents when they radiate in the unbounded medium of (ε_2, μ_2, ξ_2). $\mathbf{n_1}$ and $\mathbf{n_2}$ denote the unit vectors on S_1 and S_2, respectively and $(\mathbf{E}^-_{in}, \mathbf{H}^-_{in})$ are the total fields on S_2^- as shown in Fig. 1.

In the internal equivalence for the region bounded by S_2, surface currents $\mathbf{J}_2$, and $\mathbf{M}_2$ are placed on S_2 where they radiate in the unbounded medium of (ε_1, μ_1). They produce the correct total fields (**E**, **H**) at any point in the region bounded by

S_2 and produce zero fields at any point outside the region bounded by S_2,

$$\mathbf{E}_{1\tan}(\mathbf{J}_2, \mathbf{M}_2) = 0 \text{ on } S_2^- \quad (11)$$

$$\mathbf{H}_{1\tan}(\mathbf{J}_2, \mathbf{M}_2) = 0 \text{ on } S_2^-. \quad (12)$$

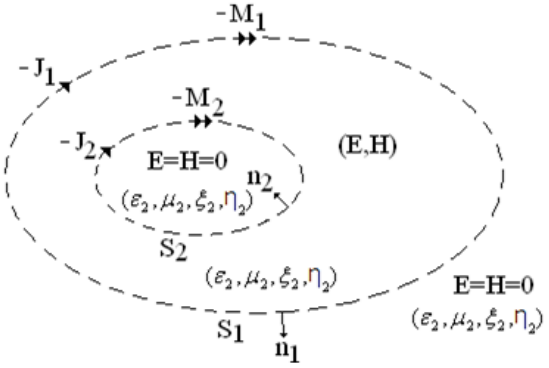

Fig. 3. Internal equivalence for the region bounded by S_1 and S_2 of the problem shown in Fig. 1.

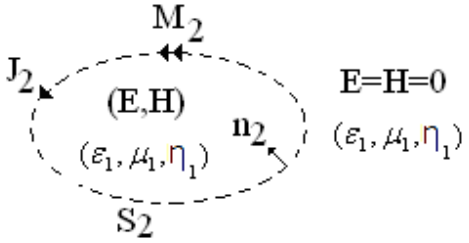

Fig. 4. Internal equivalence for the region bounded by S_2 of the problem shown in Fig. 1.

B. Formulation of the integral equations

Equations (1), (2), (5) - (8), (11), and (12) represent eight coupled integral equations for the four unknown surface currents $\mathbf{J}_1$, $\mathbf{J}_2$, $\mathbf{M}_1$, and $\mathbf{M}_2$. The combined field formulation reduces these eight equations to four by adding equations (1) to (5), (6) to (11), (2) to (7), and (8) to (12). These four coupled integral equations are solved numerically by using the method of moments.

$$-\mathbf{E}_{1\tan}(\mathbf{J}_1, \mathbf{M}_1)\Big|^{S_1^-} - \mathbf{E}_{2\tan}(\mathbf{J}_1, \mathbf{M}_1, \mathbf{J}_2, \mathbf{M}_2)\Big|^{S_1^+} = \mathbf{E}^i_{\tan} \quad (13)$$

$$-\mathbf{E}_{1\tan}(\mathbf{J}_2, \mathbf{M}_2)\Big|^{S_2^-} - \mathbf{E}_{2\tan}(\mathbf{J}_1, \mathbf{M}_1, \mathbf{J}_2, \mathbf{M}_2)\Big|^{S_2^+} = 0, \quad (14)$$

$$-\mathbf{H}_{1\tan}(\mathbf{J}_1, \mathbf{M}_1)\Big|^{S_1^-} - \mathbf{H}_{2\tan}(\mathbf{J}_1, \mathbf{M}_1, \mathbf{J}_2, \mathbf{M}_2)\Big|^{S_1^+} = \mathbf{H}^i_{\tan}, \quad (15)$$

$$-\mathbf{H}_{1\tan}(\mathbf{J}_2, \mathbf{M}_2)\Big|^{S_2^-} - \mathbf{H}_{2\tan}(\mathbf{J}_1, \mathbf{M}_1, \mathbf{J}_2, \mathbf{M}_2)\Big|^{S_2^+} = 0. \quad (16)$$

The electric and magnetic fields produced by $\mathbf{J}$ and $\mathbf{M}$ in an unbounded chiral medium are given by [37, (1.2.4) and (1.2.5)].

C. Expansion functions and testing

Let the electric and magnetic surface currents $\mathbf{J}_1$, $\mathbf{J}_2$, $\mathbf{M}_1$, and $\mathbf{M}_2$ be expanded as,

$$\mathbf{J}_1 = \sum_{n=-\infty}^{\infty} \sum_{j=1}^{N_1} \left(I^t_{1nj} \mathbf{J}^t_{1nj} + I^\phi_{1nj} \mathbf{J}^\phi_{1nj} \right) \quad (17)$$

$$\mathbf{J}_2 = \sum_{n=-\infty}^{\infty} \sum_{j=1}^{N_2} \left(I^t_{2nj} \mathbf{J}^t_{2nj} + I^\phi_{2nj} \mathbf{J}^\phi_{2nj} \right), \quad (18)$$

$$\mathbf{M}_1 = \eta_1 \sum_{n=-\infty}^{\infty} \sum_{j=1}^{N_1} \left(V^t_{1nj} \mathbf{J}^t_{1nj} + V^\phi_{1nj} \mathbf{J}^\phi_{1nj} \right), \quad (19)$$

$$\mathbf{M}_2 = \eta_1 \sum_{n=-\infty}^{\infty} \sum_{j=1}^{N_2} \left(V^t_{2nj} \mathbf{J}^t_{2nj} + V^\phi_{2nj} \mathbf{J}^\phi_{2nj} \right). \quad (20)$$

I^t_{1nj}, I^ϕ_{1nj}, I^t_{2nj}, I^ϕ_{2nj}, V^t_{1nj}, V^ϕ_{1nj}, V^t_{2nj}, and V^ϕ_{2nj} are coefficients to be determined. $\mathbf{J}^t_{1nj}$, $\mathbf{J}^\phi_{1nj}$, $\mathbf{J}^t_{2nj}$, and $\mathbf{J}^\phi_{2nj}$ are given below,

$$\mathbf{J}^t_{1nj} = \mathbf{u}_t f_{1j}(t') e^{jn\phi'} \quad (21)$$

$$\mathbf{J}^\phi_{1nj} = \mathbf{u}_\phi f_{1j}(t') e^{jn\phi'}, \quad (22)$$

$$\mathbf{J}^t_{2nj} = \mathbf{u}_t f_{2j}(t') e^{jn\phi'}, \quad (23)$$

$$\mathbf{J}^\phi_{2nj} = \mathbf{u}_\phi f_{2j}(t') e^{jn\phi'}, \quad (24)$$

$$f_{1j}(t') = \frac{1}{\rho'} T(t' - \bar{t}_{1,2j+1}), \quad (25)$$

$$f_{2j}(t') = \frac{1}{\rho'} T(t' - \bar{t}_{2,2j+1}), \quad (26)$$

$$f_{1i}(t) = \frac{1}{\rho} T(t - \bar{t}_{1,2i+1}), \quad (27)$$

$$f_{2i}(t) = \frac{1}{\rho} T(t - \bar{t}_{2,2i+1}), \quad (28)$$

$$T(t - \bar{t}_{(1,2)2i+1}) = \sum_{p=1}^{4} T_{(1,2)p+4i-4}\ \delta(t - t_{(1,2)p+2i-2}), \quad (29)$$

where $\delta(t)$ is the unit impulse function. The right-hand side of equation (29) is the four impulse approximation to a triangle function shown in Fig. 5. Also, t is the arc length along the generating curve of either S_1 or S_2, ϕ is the angle of the line from the origin to a specified point in the xy-plane with respect to the x-axis, ρ is the distance from the z-axis, and u_t and u_ϕ are the unit vectors in the t- and ϕ- directions, respectively. And dropping the subscripts 1 and 2 in equations (21) - (29),

$$T_{4i-3} = \frac{d^2_{2i-1}}{2(d_{2i-1} + d_{2i})} \quad (30)$$

$$T_{4i-2} = \frac{(d_{2i-1} + \frac{1}{2} d_{2i}) d_{2i}}{d_{2i-1} + d_{2i}}, \tag{31}$$

$$T_{4i-1} = \frac{(d_{2i+2} + \frac{1}{2} d_{2i+1}) d_{2i+1}}{d_{2i+1} + d_{2i+2}}, \tag{32}$$

$$T_{4i} = \frac{d_{2i+2}^2}{2(d_{2i+1} + d_{2i+2})}. \tag{33}$$

An odd number greater than or equal to 5 of consecutive points $\bar{t}_i$ at $(\bar{\rho}_i, \bar{z}_i)$, $i = 1, 2, ..., P$ on the generating curves of the surfaces of revolution are defined. The generating curves are approximated by drawing straight lines between the points $(\bar{\rho}_i, \bar{z}_i)$, $i = 1, 2, ..., P$ and we define

$$d_i = \sqrt{(\bar{\rho}_{i+1} - \bar{\rho}_i)^2 + (\bar{z}_{i+1} - \bar{z}_i)^2}. \tag{34}$$

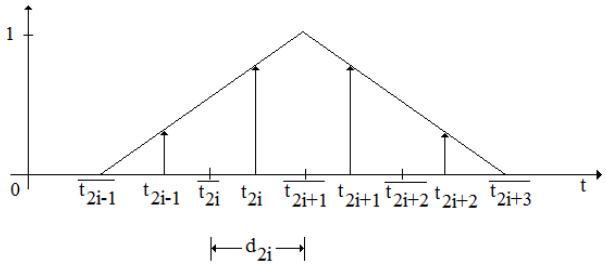

Fig. 5. Triangle function $T(t - \bar{t}_{2i+1})$ and four impulse approximation.

The quantities in equations (30) - (34) need to be specified to either the generating curve of S_1 or the generating curve of S_2. If both **h** and **g** are vector functions on S_1 or if both **h** and **g** are vector functions on S_2, then the symmetric product of **g** with **h** is $\langle \mathbf{h}, \mathbf{g} \rangle$ defined as

$$\langle \mathbf{h}, \mathbf{g} \rangle = \int_S \mathbf{h} \cdot \mathbf{g} \, dS, \tag{35}$$

where S is S_1 if both **g** and **h** are on S_1 and S is S_2 if both **g** and **h** are on S_2.

By taking the symmetric products of equations (13) and (15) with $\mathbf{J}^t_{-1ni}$ and $\mathbf{J}^{\phi}_{-1ni}$, i = 1,2,…, N_1, and taking the symmetric products of equations (14) and (16) with $\mathbf{J}^t_{-2ni}$ and $\mathbf{J}^{\phi}_{-2ni}$, i = 1,2,…, N_2, we obtain a matrix equation for the unknown coefficients. An incident plane wave whose propagation vector is in the *xz*-plane is considered.

D. Scattered field far from the scatterer and scattering cross section

The scattered field far from the scatterer is obtained by using the reciprocity theorem [38, Section 3-8]. For $p = \theta$ or ϕ, the *p*-component of the scattered field at the location $\mathbf{r}^{rec}$ of the receiver is found after some calculations to be [37, 4.6.3]

$$E_{pq}^{scat} = -\frac{j\eta_1 e^{-jk_1 r^{rec}}}{4\pi r^{rec}} \sum_{n=-N}^{N} \left(\tilde{R}_n^p T_n^q \right) e^{jn\phi^{rec}}, \quad p, q = \theta, \phi, \tag{36}$$

where r^{rec} is the distance from the origin in the vicinity of the scatterer to $\mathbf{r}^{rec}$. The extra subscript q in E_{pq}^{scat} is θ for the θ-polarized incident electric field and ϕ for the ϕ-polarized incident electric field. In equation (36), the i^{th} element of T_n^q is the coefficient that multiplies the i^{th} of the $e^{jn\phi}$-dependent expansion functions for the equivalent electric and magnetic currents in the expressions for the equivalent electric and magnetic currents that radiate the far field. The contribution of the i^{th} element of $\tilde{R}_n^p$ to the far field is the right-hand side of equation (36) with the summation with respect to n replaced by the product of the three quantities which are the i^{th} element of $\tilde{R}_n^p$, the i^{th} element of $\tilde{T}_n^q$ and $e^{jn\phi^{rec}}$.

The scattering cross section σ_{pq} is the area by which the power per unit area of the incident plane wave whose electric field is *q*-polarized must be multiplied to obtain, by isotropic radiation, the power per unit area of the *p*-component E_{pq}^{scat} of the scattered electric field. Because the isotropic radiator of power *P* produces the power per unit area $P \Big/ \left(4\pi \left(r^{rec} \right)^2 \right)$ at the distance r^{rec} where a receiver is located, this isotropic radiator will produce the power per unit area $\left| E_{pq}^{scat} \right|^2 \Big/ \eta_1$ of the *p*-component of the scattered electric field at the distance r^{rec} if

$$\frac{P}{4\pi \left(r^{rec} \right)^2} = \frac{\left| E_{pq}^{scat} \right|^2}{\eta_1}, \tag{37}$$

where η_1 is the intrinsic impedance of the medium. Using the definition of σ_{pq} to set *P* equal to the product of σ_{pq} with the incident power per

unit area $\left|\mathbf{E}^q\right|^2 / \eta_1$ of the q-polarized incident electric field $\mathbf{E}^q$, one obtains, after some calculations [37, 4.7.5],

$$\frac{\sigma_{pq}}{\lambda_1^2} = \frac{\left|\sum_{n=-N}^{N} \left(\tilde{R}_n^p T_n^q\right) e^{jn\phi^{rec}}\right|^2}{16\pi^3} \quad \text{where } \lambda_1 = 2\pi / k_1 . \tag{38}$$

E. Electromagnetic field inside the radome

The electromagnetic field inside the region bounded by $\mathbf{S_2}$ is calculated by using the combination of surface currents $\mathbf{J}_2$ and $\mathbf{M}_2$, radiating in all space filled with the homogeneous medium (ε_1, μ_1). The method of moment solutions for $\mathbf{J}_2$ and $\mathbf{M}_2$ are given by equations (18) and (20), respectively.

The electromagnetic field inside the region bounded by $\mathbf{S_2}$ is calculated by,

$$\mathbf{E}_i = \sum_{n=-N}^{N} \sum_{j=1}^{N_2} \Big(I_{2nj}^t \mathbf{E}_i(\mathbf{J}_{2nj}^t, \mathbf{0}) + I_{2nj}^\phi \mathbf{E}_i(\mathbf{J}_{2nj}^\phi, \mathbf{0}) + \eta_1 \left(V_{2nj}^t \mathbf{E}_i(\mathbf{0}, \mathbf{J}_{2nj}^t) + V_{2nj}^\phi \mathbf{E}_i(\mathbf{0}, \mathbf{J}_{2nj}^\phi) \right) \Big) \tag{39}$$

$$\mathbf{H}_i = \sum_{n=-N}^{N} \sum_{j=1}^{N_2} \Big(I_{2nj}^t \mathbf{H}_i(\mathbf{J}_{2nj}^t, \mathbf{0}) + I_{2nj}^\phi \mathbf{H}_i(\mathbf{J}_{2nj}^\phi, \mathbf{0}) + \eta_1 \left(V_{2nj}^t \mathbf{H}_i(\mathbf{0}, \mathbf{J}_{2nj}^t) + V_{2nj}^\phi \mathbf{H}_i(\mathbf{0}, \mathbf{J}_{2nj}^\phi) \right) \Big), \tag{40}$$

where the subscript i in $\mathbf{E}_i$ and $\mathbf{H}_i$ indicates the radiation in all space filled with the medium that is bounded by $\mathbf{S_2}$. The first argument of each of $\mathbf{E}_i$ and $\mathbf{H}_i$ is treated as an electric current and the second argument is treated as a magnetic current.

Using $\mathbf{E}_i(\mathbf{0}, \mathbf{J}) = -\mathbf{H}_i(\mathbf{J}, \mathbf{0})$ and $\mathbf{H}_i(\mathbf{0}, \mathbf{J}) = \frac{1}{\eta_1^2} \mathbf{E}_i(\mathbf{J}, \mathbf{0})$ to reduce all nonzero magnetic current arguments in equations (39) and (40) to zeros and then suppressing all the zero magnetic current arguments, one obtains

$$\mathbf{E}_i = \sum_{n=-N}^{N} \sum_{j=1}^{N_2} \Big(I_{2nj}^t \mathbf{E}_i(\mathbf{J}_{2nj}^t) + I_{2nj}^\phi \mathbf{E}_i(\mathbf{J}_{2nj}^\phi) - \eta_1 \left(V_{2nj}^t \mathbf{H}_i(\mathbf{J}_{2nj}^t) + V_{2nj}^\phi \mathbf{H}_i(\mathbf{J}_{2nj}^\phi) \right) \Big), \tag{41}$$

$$\mathbf{H}_i = \sum_{n=-N}^{N} \sum_{j=1}^{N_2} \Big(I_{2nj}^t \mathbf{H}_i(\mathbf{J}_{2nj}^t) + I_{2nj}^\phi \mathbf{H}_i(\mathbf{J}_{2nj}^\phi) + \frac{1}{\eta_1} \left(V_{2nj}^t \mathbf{E}_i(\mathbf{J}_{2nj}^t) + V_{2nj}^\phi \mathbf{E}_i(\mathbf{J}_{2nj}^\phi) \right) \Big). \tag{42}$$

Define

$$\mathbf{Z}_{nj}^q = -\frac{1}{\eta_1} \mathbf{E}_i(\mathbf{J}_{2nj}^q), \quad q = t, \ \phi, \tag{43}$$

$$\mathbf{Y}_{nj}^q = -\mathbf{H}_i(\mathbf{J}_{2nj}^q), \quad q = t, \ \phi, \tag{44}$$

and use equations (43) and (44) in (41) and (42) to obtain

$$\mathbf{E}_i = -\sum_{n=-N}^{N} \sum_{j=1}^{N_2} \Big(\eta_1 \left(I_{2nj}^t \mathbf{Z}_{nj}^t + I_{2nj}^\phi \mathbf{Z}_{nj}^\phi \right) - \eta_1 \left(V_{2nj}^t \mathbf{Y}_{nj}^t + V_{2nj}^\phi \mathbf{Y}_{nj}^\phi \right) \Big), \tag{45}$$

$$\mathbf{H}_i = -\sum_{n=-N}^{N} \sum_{j=1}^{N_2} \Big(\left(I_{2nj}^t \mathbf{Y}_{nj}^t + I_{2nj}^\phi \mathbf{Y}_{nj}^\phi \right) + \left(V_{2nj}^t \mathbf{Z}_{nj}^t + V_{2nj}^\phi \mathbf{Z}_{nj}^\phi \right) \Big). \tag{46}$$

III. NUMERICAL RESULTS

The bodies analyzed in this paper, shown in Fig. 6, are illuminated by the θ-polarized plane waves. For θ^{inc} = 180º, the θ-polarized plane wave travels in the z-direction and its electric field is in the –x-direction. For θ^{inc} = 0º, the θ-polarized plane wave travels in the –z-direction and its electric field is in the x-direction.

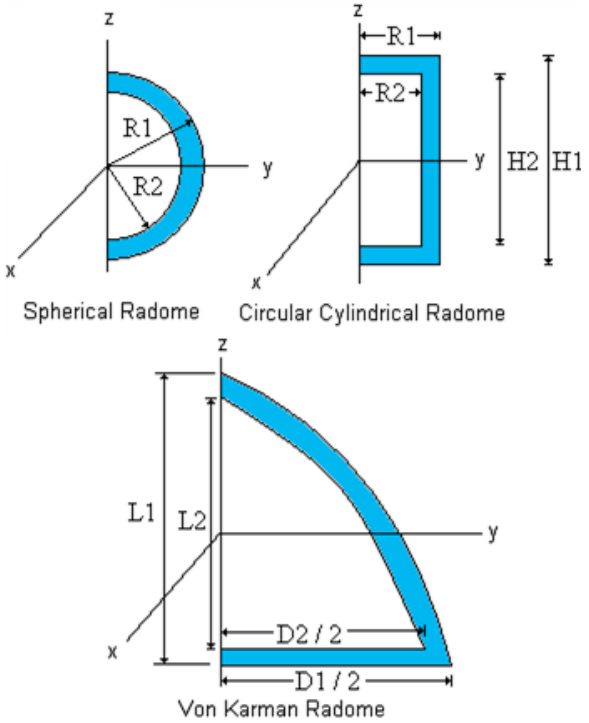

Fig. 6. Structures used to verify the method.

Numerical solution results for inside fields on the z-axis and scattering from a spherical chiral radome are presented in Figs. 7 and 8 for relative permittivity ε_r =2 and 8 and relative chirality ξ_r =0.4. The internal field plots are normalized to the incident field. The computed results are compared with the exact solution results for the spherical chiral radome and they match perfectly with each other. For ε_r =2 problem, 89 triangles on $\mathbf{S_1}$ and 79 triangles on $\mathbf{S_2}$ are used to solve for 672 unknowns, which took 6.6 minutes on a Core2Duo 2.1GHz computer. For ε_r =8 problem, 179 triangles on $\mathbf{S_1}$ and 159 triangles on $\mathbf{S_2}$ are used to solve for 1352 unknowns, which took 21 minutes on the same computer.

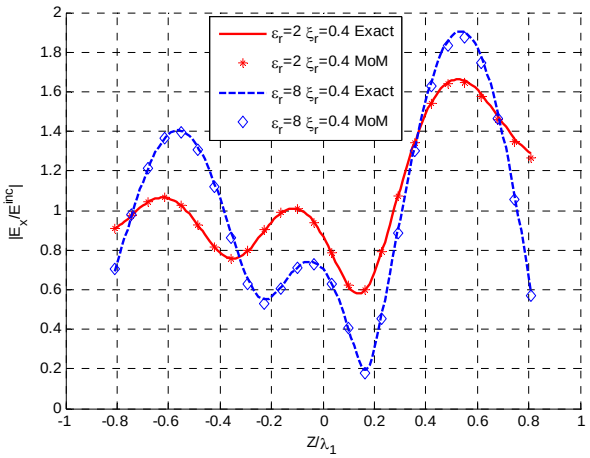

Fig. 7. Fields on the z-axis of a spherical radome for R1 = 1λ_1, R2 = 0.9λ_1, μ_r = 1, and θ^{inc} = 180º.

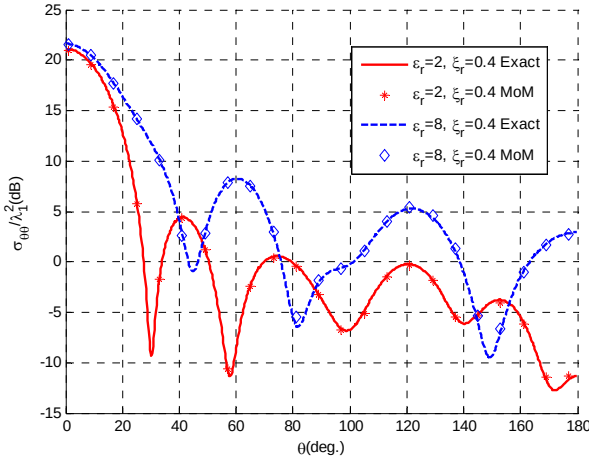

Fig. 8. $\sigma_{\theta\theta}$ of a spherical radome for R1 = 1λ_1, R2 = 0.9λ_1, μ_r = 1, and θ^{inc} = 180º.

Figures 9 and 10 show numerical results for a cylindrical radome of R1 = 1.05λ_1, R2 = 1λ_1, H1 = 10.1λ_1, H2 = 10λ_1, μ_r = 1, and θ^{inc} = 0º. For ε_r =1.55 problem, 277 triangles on $\mathbf{S_1}$ and 273 triangles on $\mathbf{S_2}$ are used to solve for 2212 unknowns. For ε_r =3 problem, 306 triangles on $\mathbf{S_1}$ and 299 triangles on $\mathbf{S_2}$ are used to solve for 2432 unknowns.

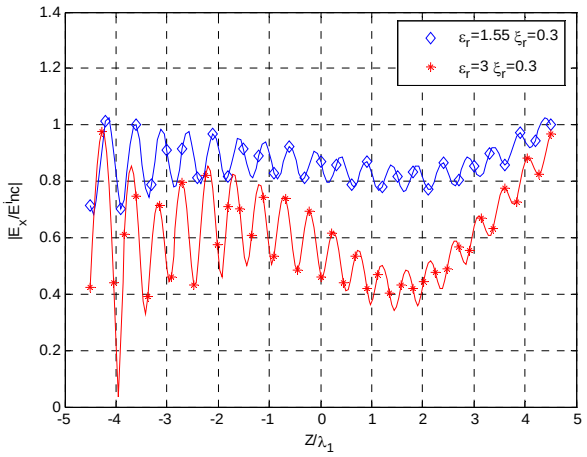

Fig. 9. Fields on the z-axis of a cylindrical radome for θ^{inc} = 0º.

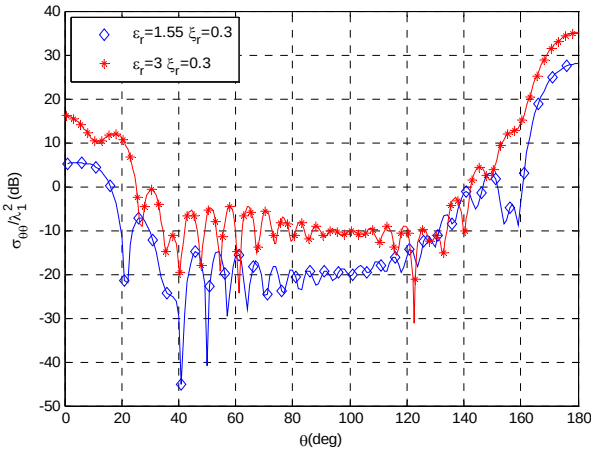

Fig. 10. $\sigma_{\theta\theta}$ of a cylindrical radome for θ^{inc} = 0º.

Results for small Von Karman radomes of different sizes and parameters were computed and validated against [33] - [35]. In Figs. 11 to 13, we show computed numerical results for a Von Karman radome of ε_r =4, L1 = 2λ_1, L2 = 1.8λ_1, D1 = 1λ_1, D2 = 0.9λ_1, ξ_r = 0, μ_r = 1 where 127 triangles are used on $\mathbf{S_1}$ and 115 triangles are used on $\mathbf{S_2}$ to solve for 980 unknowns.

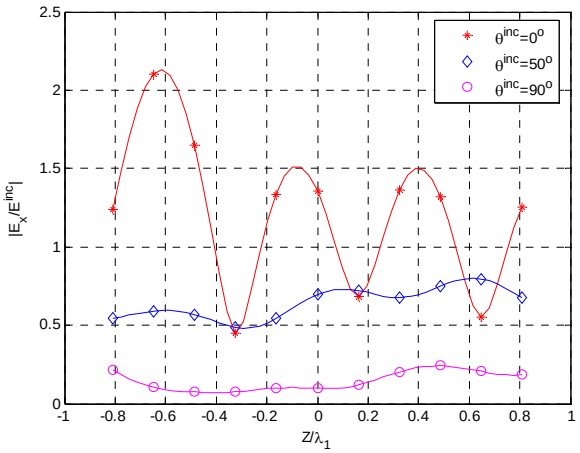

Fig. 11. Fields on the *z*-axis of a Von Karman radome for θ^{inc} = 0º, 50º, and 90º.

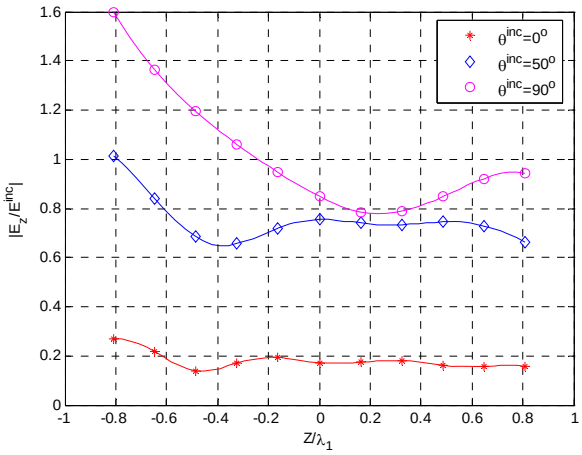

Fig. 12. Fields on the *z*-axis of a Von Karman radome for θ^{inc} = 0º, 50º, and 90º.

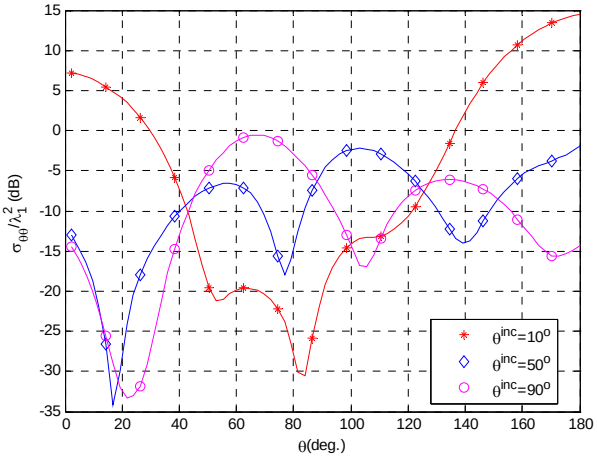

Fig. 13. $\sigma_{\theta\theta}$ of a Von Karman radome for θ^{inc} = 0º, 50º, and 90º.

More results for all these different radome structures and comparisons with previously published results are available in [37].

IV. CONCLUSION

In this paper, MoM analysis of an axisymmetric chiral radome using MoM with the surface equivalence principle is presented. The body is replaced by equivalent electric and magnetic surface currents, which produce the correct fields inside and out. The application of the boundary conditions on the tangential components of the total electric and the total magnetic fields results in a set of eight equations, which then reduces to four coupled equations that needs to be solved. Triangular expansion functions are used for both *t*-directed and ϕ-directed currents. The unknown coefficients of these expansion functions are obtained using the method of moments.

The surface currents, inside fields and the scattering cross section are computed. The results are generated by a computer code, which produces excellent agreement with the exact solution for the spherical radome and agreement with available published results for other radomes. Increasing the number of segments increases the accuracy of the solution. The radar cross section (RCS) of the radome is useful because it tells how visible the radome is from the outside. The field inside the radome due to a plane wave incident on the radome is more useful because it tells how the radome distorts radiation that comes from outside the radome. If a receiver is placed inside the radome, the field inside the radome tells how the radome affects what is received from outside. Therefore, calculations of the RCS of the radome and fields inside the radome are justified. The field radiated outside the radome by a transmitter inside the radome is also of interest. This field was not computed because of its excitation, which is the incident field of the transmitter inside the radome, is more complicated than the incident plane wave excitation used to compute the field inside the radome.

The presence of the radome affects what is transmitted and received by a transceiver placed inside the radome. Adding chirality to the radome material affects the inside fields and the scattered fields significantly for the cases studied in this paper. Although the change from no chirality to a small chirality causes cross polarized field

components to evolve, thereby shifting the directions of the scattered field outside the radome and the field inside the radome away from the direction of the incident field, the effect of the chirality cannot be predicted by a simple theory. Numerical experimentation is needed.

REFERENCES

[1] J. D. Walton Jr., Ed., *Radome Engineering Handbook: Design and Principles*. New York: Marcel Dekker, 1970.

[2] D. T. Paris, "Computer-aided radome analysis," *IEEE Trans. Antennas Propagat.*, vol. 18, pp. 7-15, Jan. 1970.

[3] X. J. Gao and L. B. Felsen, "Complex ray analysis of beam transmission through two-dimensional radomes," *IEEE Trans. Antennas Propagat.*, vol. 33, pp. 963-975, Sept. 1985.

[4] D. C. F. Wu and R. C. Rudduck, "Plane wave spectrum-surface integration technique for radome analysis," *IEEE Trans. Antennas Propagat.*, vol. 22, pp. 497-500, May 1974.

[5] J. P. R. Bayard, "Analysis of infinite arrays of microstrip-fed dipoles printed on protruding dielectric substrates and covered with a dielectric radome," *IEEE Trans. Antennas Propagat.*, vol. 42, pp. 82-89, Jan. 1994.

[6] A. A. Kishk, G. Zhou, and A. W. Glisson, "Analysis of dielectric-resonator antennas with emphasis on hemispherical structures," *IEEE Antennas Propagat. Mag.*, vol. 36, pp. 20-31, April 1994.

[7] S. T. Imeci, F. Altunkilic, J. R. Mautz, and E. Arvas, "Transmission through an arbitrarily shaped aperture in a conducting plane separating air and a chiral medium," *Appl. Comp. Electromagnetics Society (ACES) Journal*, vol. 25, no. 7, pp. 587-599, July 2010.

[8] J. -Y. Li, J. -Li Guo, Y. -L. Zou, and Q. -Z. Liu, "Analysis of a cylindrical dielectric radome covering omnidirectional waveguide slot antennas," *Appl. Comp. Electromagnetics Society (ACES) Journal*, vol. 23, no. 2, pp. 166-173, June 2008.

[9] R. E. Hodges and Y. Rahmat-Samii, "Evaluation of dielectric physical optics in electromagnetic scattering," *AP-S Int. Symp. Dig.,* Ann Arbor, MI, vol. 3, pp. 1742-1745, June 1993.

[10] R. K. Gordon and R. Mittra, "Finite element analysis of axisymmetric radomes," *IEEE Trans. Antennas Propagat.*, vol. 41, pp. 975-981, July 1993.

[11] A. Y. Svezhentsev, A. I. Nosich, A. Altintas, and T. Oguzer, "Simulation of reflector antenna covered by a circular radome," *Proc. 9th Int. Conf. Antennas Propagat.,* Eindhoven, The Netherlands, pp. 532-535, April 1995.

[12] M. A. A. Moneum, Z. Shen, J. L. Volakis, and O. Graham, "Hybrid PO-MoM analysis of large axi-symmetric radomes," *IEEE Trans. Antennas Propagat.*, vol. 49, no. 12, pp. 1657-1666, Dec. 2001.

[13] R. Shavit, "Dielectric cover effect on rectangular microstrip antenna array," *IEEE Trans. Antennas Propagat.*, vol. 42, pp. 1180-1184, Aug. 1994.

[14] W. J. Zhao, L. W. Li, and Y. B. Gan, "Efficient analysis of antenna radiation in the presence of airborne dielectric radomes of arbitrary shape," *IEEE Trans. Antennas Propagat.*, vol. 53, no. 1, pp. 442-449, Jan. 2005.

[15] L. W. Li, M. S. Leong, P. S. Kooi, T. S. Yeo, and Y. L. Qiu, "Radiation of an aperture antenna covered by a spherical-shell chiral radome and fed by a circular waveguide," *IEEE Trans. Antennas Propagat.*, vol. 46, no. 5, pp. 664-671, May 1998.

[16] L. W. Li and M. S. Leong, "A 3-D discrete analysis of cylindrical radomes using dyadic Green's functions," *IEEE Antennas and Propagat. Soc. Int. Symp.*, vol. 2, pp. 846-849, 1999.

[17] Y. Zou, Q. Liu, and J. Guo, "Fast analysis of body-of-revolution radomes with method of moments," *J. of Electromag. Waves and Appl.*, vol. 21, no. 13, pp. 1803-1817, 2007.

[18] X. C. Nie, N. Yuan, L. W. Li, T. S. Yeo, and Y. B. Gan, "Fast analysis of electromagnetic transmission through arbitrarily shaped airborne radomes using precorrected-FFT method," *Progress In Electromagnetics Research, PIER,* vol. 54, pp. 37-59, 2005.

[19] S. Govind, D. R. Wilton, and A. W. Glisson, "Scattering from inhomogeneous penetrable bodies of revolution," *IEEE Trans. Antennas Propagat.*, vol. 32, no. 11, pp. 1163-1173, Nov. 1984.

[20] J. R. Mautz and R. F. Harrington, "Radiation and scattering from bodies of revolution," *Appl. Sci. Res.*, vol. 20, no. 6, pp. 405-435, June 1969.

[21] M. G. Andreasen, "Scattering from bodies of revolution," *IEEE Trans. Antennas Propagat.,* vol. 13, no. 2, pp. 303-310, March 1965.

[22] A. A. Kucharski, "A method of moments solution for electromagnetic scattering by inhomogeneous dielectric bodies of revolution," *IEEE Trans. Antennas Propagat.*, vol. 48, no. 8, pp. 1202-1210, Aug. 2000.

[23] J. R. Mautz and R. F. Harrington, "Electromagnetic scattering from a homogeneous material body of revolution," *AEŰ*, vol. 33, pp. 71-80, 1979.

[24] A. W. Glisson and D. R. Wilton, "A simple approach to the problem of coupling through azimuthally symmetric apertures in bodies of revolution," *IEEE Antennas and Propagat. Soc. Int. Symp.*, pp. 215–218, May 1978.

[25] J. R. Mautz and R. F. Harrington, "H–Field, E–Field and combined field solutions for bodies of revolution," *Technical Report TR-77-2, Department of Electrical and Computer Engineering*, Syracuse University, Syracuse, NY, pp. 13244-1240, Feb. 1977. See also J. R. Mautz and R. F. Harrington, "H–Field, E–Field and combined field solutions for conducting bodies of revolution," AEŰ, vol. 32, no. 4, pp. 157–164, Apr. 1978.

[26] J. R. Mautz and R. F. Harrington, "Electromagnetic scattering from a homogeneous body of revolution", *Technical Report TR-77-10*, Department of Electrical and Computer Engineering, Syracuse University, Syracuse, NY, 13244, Nov. 1977.

[27] B. Lin, S. Du, H. Zhang, and X. Ye, "Design and simulation of frequency-selective radome together with a monopole antenna," *Appl. Comp. Electromagnetics Society (ACES) Journal*, vol. 25, no. 7, pp. 620-625, July 2010.

[28] A. E. Fathy, "Design of a near field protective dielectric radome "window" for a curved phased array antenna-axial polarization case," *Appl. Comp. Electromagnetics Society (ACES) Journal*, vol. 23, no. 4, pp. 326-335, Dec. 2008.

[29] R. F. Wallenberg and R. F. Harrington, "Radiation from apertures in conducting cylinders of arbitrary cross section," *IEEE Trans. Antennas Propagat.*, vol. 17, no. 1, pp. 56-62, Jan. 1969.

[30] C. N. Chiu and C. I. G. Hsu, "Scattering and shielding properties of a chiral-coated fiber-reinforced plastic composite cylinder," *IEEE Trans. Electromag. Compat.*, vol. 47, no. 1, pp. 123-130, Feb. 2005.

[31] W. B. Wang and J. P. Xu, "An efficient method for analysis of EM performance of thin dielectric radomes together with wire antennas," *ICMMT2008 Proceedings*, pp. 778-780, April 2008.

[32] J. R. Mautz and R. F. Harrington, "A combined-source solution for radiation and scattering from a perfectly conducting body," *IEEE Trans. Antennas Propagat.*, vol. 27, no. 4, pp. 445-454, July 1979.

[33] E. Arvas and S. Ponnapalli, "Scattering cross section of a small radome of arbitrary shape," *IEEE Trans. Antennas Propagat.*, vol. 37, no. 5, pp. 655-658, May 1989.

[34] E. Arvas, A. Rahhalarabi, U. Pekel, and E. Gundogan, "Electromagnetic transmission through a small radome of arbitrary shape," *IEE Proceedings*, vol. 137, no. 6, pp. 401-405, Dec. 1990.

[35] E. Arvas and E. Gundogan, "Electromagnetic transmission through a small radome of arbitrary shape," *Technical Report TR-90-3*, Department of Electrical and Computer Engineering and The New York State Center for Advanced Technology in Computer Applications and Software Engineering (CASE), Syracuse University, Syracuse, NY, 13244, April 1990.

[36] H. Mustacoglu, J. R. Mautz, and E. Arvas, "Method of moments analysis of an axisymmetric chiral radome," *General Assembly and Scientific Symposium*, 2011 XXXth URSI, Oct. 2011.

[37] H. Mustacoglu, *MoM analysis of an axisymmetric chiral radome*, PhD. Dissertation, Syracuse University, Dec. 2010.

[38] R. F. Harrington, *Time-Harmonic Electromagnetic Fields*. New York: McGraw-Hill, 1961.

Halid Mustacoglu was born in Kocaeli, Turkey, in 1980. He received the B.Sc. degree in Electronics and Communication Engineering from Yildiz Technical University, Istanbul, Turkey, in 2002 and the M.Sc. and Ph.D. degrees in Electrical Engineering from Syracuse University, Syracuse, NY, in 2005 and 2011, respectively.

From 2002 to 2003, he was a Research Assistant at Syracuse University and between 2003 and 2004 he was an intern at Herley Microwave, working on microwave filter designs. From 2004 to 2011, he was a co-op at Anaren Microwave, Inc., where he worked on passive component designs. Since 2011, he has been an RF/Microwave Engineer at Anaren Microwave, Inc., where he designs RF/Microwave components. His research interests include RF/Microwave design, scattering problems, and computational electromagnetics.

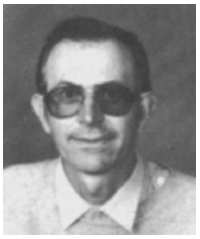

Joseph R. Mautz was born in Syracuse, NY, in 1939. He received the B.Sc., M.Sc., and Ph.D. degrees in Electrical Engineering from Syracuse University in 1961, 1965, and 1969, respectively.

Until July 1993, he was a Research Associate with the Electrical Engineering and Computer Science Department, Syracuse University, where he worked on radiation and scattering problems. Currently, he is affiliated with the Electrical Engineering and Computer Science Department at the same university. His primary fields of interest are electromagnetic theory and applied mathematics.

Ercument Arvas received the B.Sc. and M.Sc. degrees from the Middle East Technical University, Ankara, Turkey, in 1976 and 1979, respectively, and the Ph.D. degree from Syracuse University, Syracuse, NY, in 1983, all in Electrical Engineering.

From 1984 to 1987, he was with the Electrical Engineering Department, Rochester Institute of Technology, Rochester, NY. In 1987, he joined the Electrical Engineering and Computer Science Department, Syracuse University, where he is currently a Professor in the Electrical Engineering and Computer Science Department. His research and teaching interests are in electromagnetic scattering and microwave devices.

Broadband Miniaturized Efficient Array Antennas

Amir Jafargholi [1] and Ali Jafargholi [2]

[1]Institute of Space Science and Technology
Amirkabir University of Technology, 424 Hafez Ave., P. O. Box: 15875-4413, Tehran, Iran
jafargholi@ieee.org

[2]Department of Electrical Engineering
Sharif University of Technology, Azadi Ave., P. O. Box: 11365-11155. Tehran, Iran
jafargholi@sharif.edu

Abstract ― This paper introduces a new array architecture, in which antenna elements are arranged in a spiral curve. The spiral array enhances ultra-wideband (UWB) pattern characteristics compared to alternative array geometries of similar elements, without requiring a complex feed network for frequency change compensation. A number of examples are illustrated to demonstrate the array capability in broadband array designs. It is revealed that for the same number of elements and curvature lengths, a spiral array has a wider radiation bandwidth than the corresponding circular and linear array antennas. In addition, it is also demonstrated that the spiral architecture discussed here can be best suited for small antenna array applications. Simulations show that different spiral parameters lead to different size reduction, which vary from 30% to 90% with regards to a conventional circular array antenna.

Index Terms - Miniaturized array antenna, spiral array antenna, and ultra-wide band.

I. INTRODUCTION

Array elements, feed networks, and array architecture are three main factors determining the array size and its performance [1]. There is renewed interest in non-foster circuitry for antennas lately [2-6]. The antenna size implies limitations in bandwidth and gain characteristics. However, if non-foster/negative circuits are employed such restrictions can be partially overcome. As an important parameter in the array design, the feed network generally depends on the array elements and architecture. The selection of the array architecture for the realization of a desired array antenna is determined by requirements on the array bandwidth, pattern, size, and scan range [1]. In addition, broad radiation and input impedance bandwidths are two major characteristics of the antenna arrays for broadband applications. Since the input impedance bandwidth depends on the characteristics of the element used in the array, the radiation bandwidth is the limiting factor. In other words, the radiation bandwidth of the array limits its practical bandwidth. Since antenna arrays play a significant role, both in direction finding and in increasing the capacity of the systems, the use of suitable array architecture is becoming increasingly important. From an architecture point of view, there are still many theoretical as well as practical open issues despite the basic configurations found in the literature [1].

The broadband frequency characteristics can be obtained based on the fundamental theory introduced by Rumsey in the fall of 1954 [7]. As a result, we speculate that the spiral array architecture, in which antenna elements are arranged in a spiral curve, may be frequency independent. The simulation results confirmed this claim [8-9]. The proposed spiral architecture exhibits a great potential for applications such as radio direction finding and UWB systems. In UWB systems, one is interested in having an antenna or antenna array, which maintains a substantially stable radiation pattern over the entire frequency range of interest to keep UWB pulse distortion as small as possible.

Submitted On: May 26, 2012
Accepted On: Dec. 30, 2012

However, the bandwidth of conventional arrays (linear and circular arrays) is limited because the radiation pattern scans with frequency and thus moves off the target. In order to avoid this beam squint problem, wide band arrays are required.

In this paper, the miniaturization capability of the proposed spiral architecture as compared to conventional linear and circular arrays has been considered. Simulation shows that the spiral architecture can be best suited for small antenna array applications. They show that different spiral parameters lead to different size reduction, which vary from 30% to 90% with regards to a conventional circular array antenna.

II. ARRAY ANTENNA FORMULATION

Considering an m-element simple spiral-array antenna, the position vector may be written as,

$$\vec{r}_m = \vec{r}e^{a\phi_m} = r_0 e^{a\phi_m}\cos(\phi_m)\hat{x} + r_0 e^{a\phi_m}\sin(\phi_m)\hat{y} \quad (1)$$

here, a is the spiral constant and specifies the increasing rate of the spiral radius proportionate with angle ϕ_m , x_m, and y_m are the cartesian location of the array elements, and $\vec{r}$ is the vector of the spiral constellation. In Fig. 1, r_0 is the distance of the first element of the array from the origin, and $\phi_m = \frac{(m-1)\pi}{b}$ represents the angle of the m^{th} element in polar coordinate, where parameter b may be chosen arbitrarily in order to make a smoother change in spiral contour and to increase the degrees of freedom in the design.

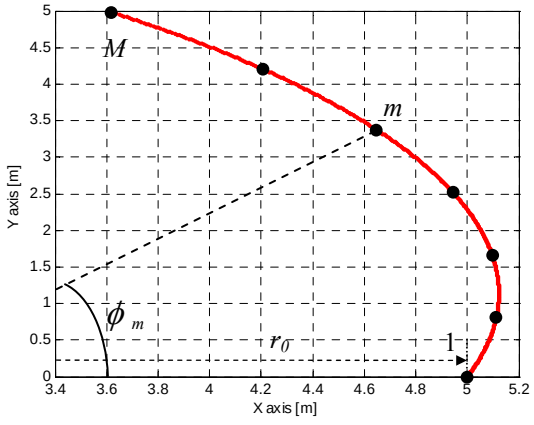

Fig. 1. Two possible array architectures, where the element locations are specified by equation (2): a = 0.221, M = 7, b = 20, f_0 = 30 MHz, and r_0 = 5 m.

It should be noted that b has a positive value. The array factor of the spiral array is [8],

$$AF(\theta,\phi) = \sum_{m=1}^{M} I_m e^{j\left(\frac{2\pi}{\lambda} r_0 e^{a\phi_m}\sin\theta\cos(\phi-\phi_m)+\delta_m\right)} . \quad (2)$$

The spiral array bandwidth has been calculated in before, [8-Appendix]. In order to gain further insight into the spiral array bandwdith, equation (3) introduces a spiral to linear bandwidth ratio (SLBWR)

$$SLBWR = \frac{\frac{1}{2}M(M+1)\left(e^{\frac{a\pi}{b}}-1\right)}{\left[e^{\frac{a\pi}{b}M}-1\right]} \quad \text{For } r_0 = d_{\text{Linear}} . \quad (3)$$

where, d_{Linear} is the element separation for the linear array.

III. ARRAY SYNTHESIS AND SIMULATION RESULTS

To verify the array performance, a 7 element spiral array antenna, with parameters $r_0 = \lambda_C/2$, a = 0.221, and b = 20, where the desired frequency f_c = 30MHz and λ_C = 10m, has been first analytically studied (Fig. 1). A comparison has been done using the simulation results obtained by SuperNEC software. Using equation (1), the element locations are specified in Table 1. According to the progressive-phase excitation method and uniform amplitude, for the main lobe located at (θ_0, ϕ_0) the phase δ_m for each element can be expressed as [7],

$$\delta_m = -\frac{2\pi}{\lambda} r_0 e^{a\phi_m}\sin\theta_0\cos(\phi_0-\phi_m) . \quad (4)$$

For the main lobe, which is directed to (θ_0, ϕ_0) = (90°, 90°), the array feed values are specified in Table 1. The analytic results for f = 10, 20, 30, 40, and 50 MHz are shown in Fig. 2. To simulate the structure with the aid of SuperNEC, the array elements are located on infinite perfect ground, and the length of monopole antennas is chosen to be L = 2 m. We have chosen monopole antennas (with omni-directional radiation patterns over the entire frequency band) as array elements instead of conventional broadband elements. In addition, we assumed in simulations that the impedance of elements is matched over the entire frequency band. Small changes in radiation patterns over the entire frequency band, 10–50 MHz, make the proposed array applicable as an ultra-wideband

array antenna. In Fig. 3, a comparison between the analytic and numeric (SuperNEC simulation results) simulations is presented. As can be seen clearly, the simulated results obtained by SuperNEC software show good agreement with the analytic calculations.

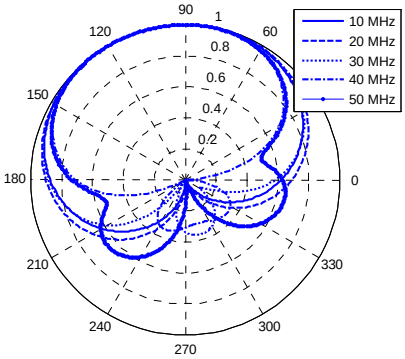

Fig. 2. A seven element spiral array architecture; a = 0.221, M = 7, b = 20, and $\theta = 90^0$ plane.

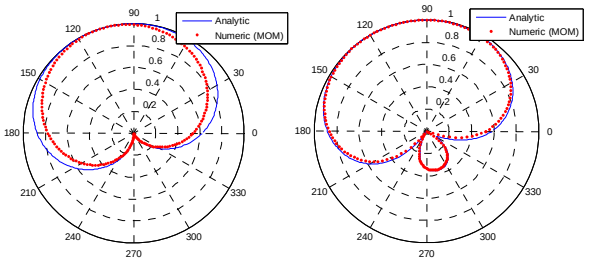

(a) (b)

Fig. 3. Analytic and numeric (SuperNEC) simulation results comparison, L = 2m, for (a) 10MHz and (b) 30 MHz.

Table 1: Spiral array elements properties for 10 – 50 MHz.

Element No.	Location, (x) (m)	Location, (y) (m)	Current
1	5.0	0	1.0
2	5.11	0.81	0.873-0.487i
3	5.09	1.65	0.506-0.863i
4	4.94	2.52	-0.012–1.0i
5	4.65	3.37	-0.523-0.852i
6	4.20	4.21	-0.878-0.478i
7	3.62	4.98	-1.0-0.01i

IV. COMPARISON OF SPIRAL, CIRCULAR, AND LINEAR ARRAY ARCHITECTURES

Various array architectures have been proposed and investigated in the literature [1, 8]. Besides the spiral array architecture proposed in this paper, the linear and circular array architectures are popularly used in antenna engineering.

In this section, two different high (1–10 GHz) and low (10–50 MHz) frequency architecture have been studied. Moreover, to compare them with linear and circular array antennas two different scenarios have been choose: equivalent and different array lengths conditions.

A. Equivalent array length

In [7–Fig. 8], the geometries of the spiral, linear, and circular arrays have been compared. To make a fair comparison, the number of elements and curvature lengths are the same in all cases. The total length of an M element linear array with an element separation of d_{Linear} is $L = (M\text{-}1)d_{Linear}$ while the circumference of an M element circular array with a radius of r_0 is $C_S = 2\pi r_{0,Circular}$. In addition, for an M element spiral array, the array circumference can be expressed by equation (5),

$$C_S = \frac{r_0\sqrt{1+a^2}}{a}\left(e^{a\phi_M} - 1\right). \quad (5)$$

To have a fair comparison, the element separation for linear array and the radius of the circular array are selected to satisfy equation (6)

$$r_{0,Circular} = C_S \cdot \frac{1}{2\pi}, \qquad d_{Linear} = C_S \cdot \frac{1}{(M-1)}. \quad (6)$$

The parameters of the spiral array are: M = 5, r_0 = 0.04 m, a = -0.125, and b = 1.75, where the desired frequency is f_c = 5 GHz. The configuration of the spiral, circular and linear arrays are labeled in [7–Fig. 8]. For all array geometries, simple monopole antennas are used as array elements. The directivity of these arrays for the main beam direction is plotted in [7–Fig. 9 (a)]. As revealed in the figure, the spiral array architecture provides a wider radiation bandwidth.

The 3 dB radiation bandwidth of the spiral array architecture is approximately 4.1 and 1.9 times wider than that of the linear and circular

arrays, respectively. Finally, it should be noted that the spiral arrangement allows the beam to be steered in any direction in the azimuth plane, similar to the linear and circular arrangements [1].

B. Different array lengths

Now, we compare the gain of a seven element spiral array antenna, $r_0 = \lambda_C/2$, $a = 0.221$, and $b = 20$, for the frequency $f_c = 30$ MHz and $\lambda_C = 10$ m, with that of linear and circular array (see Fig. 4). The distance between the elements of the linear array is $r_0 = \lambda_C/2 = 5$ m, whereas elements of the circular array are located on a circle with a radius of $r = \lambda_C$, with all of the elements having a 2 m length. As it seems in Fig. 5, the gain of the spiral array antenna changes smoothly over the entire frequency range, and consequently its 3 dB bandwidth is considerably greater than that of linear and circular arrays. It should be also considered that the gain of linear and circular arrays is not constant and fluctuate rapidly over the frequency range. The present result shows that the array bandwidth is defined over 10 MHz-35 MHz range and confirms SLBWR (equation (3), which is approximately 3.5:1). The arrays have been designed for the main lobe location in $(\theta_0, \phi_0) = (90^o, 90^o)$ and the feeding values for these elements are also specified in Table 1.

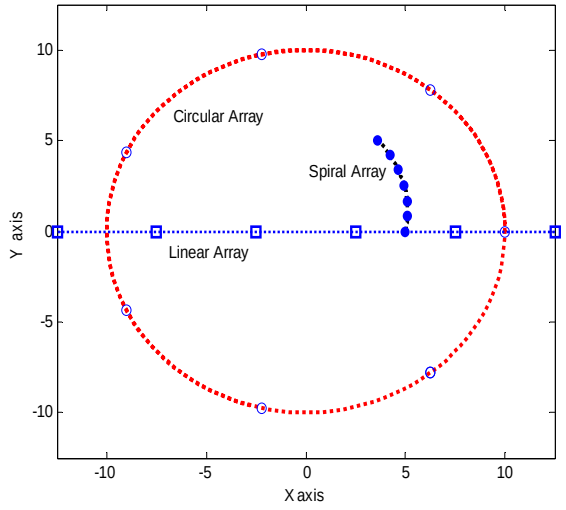

Fig. 4. The geometries of the spiral, circular, and linear arrays.

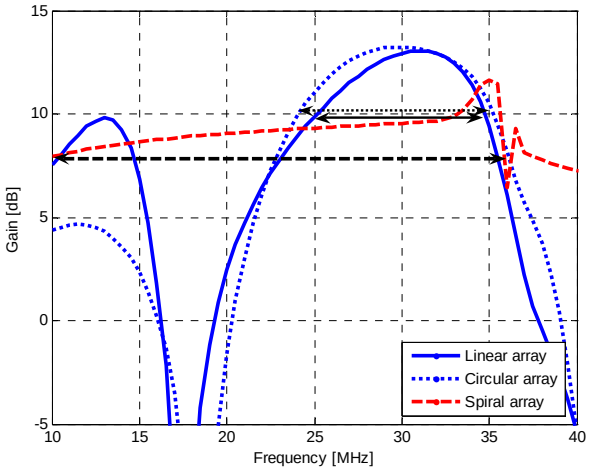

Fig. 5. Comparison between the directivity of different array geometries in the main lobe ($\theta = 90°$, $\phi = 0^o$) direction.

V. MINIATURIZATION CHARACTERISTIC

A comparison between circular and spiral array antennas has been presented before. It is shown that for the array with same number of elements and uniform feeding, the suggested spiral array is much more miniaturized than the simple linear and circular array architectures. Due to this fact that the linear array has worst condition in array miniaturization capability, here, we just studied the circular and spiral array antenna.

To have a better insight, again we investigated an equivalent, smaller and much smaller spiral array length with regards to a conventional circular array antenna. In each case, the radiation pattern, the array size, and its frequency bandwidth have been considered.

In Figs. 6, 7, and 8, we assumed that the desired main lobe is located in (a) $(\theta_0, \phi_0) = (90^o, 90^o)$, (b) $(\theta_0, \phi_0) = (45^o, 45^o)$, and (c) $(\theta_0, \phi_0) = (60^o, 30^o)$. The elements of the circular array are located on a circle with radius of $r = \lambda_C$, where the desired frequency is $f_c = 300$ MHz ($\lambda_C = 1$ m). In these figures, a simple spiral array antenna that has (a) 7 elements, with $r_0 = \lambda_C/4$, $a = -0.0221$, and $b = 3$; (b) 15 elements, with $r_0 = \lambda_C$, $a = -0.1221$, and $b = 4$; and (c) 15 elements, with $r_0 = \lambda_C/3$, $a = -0.221$, and $b = 7$, has been compared with the same element number circular array antennas.

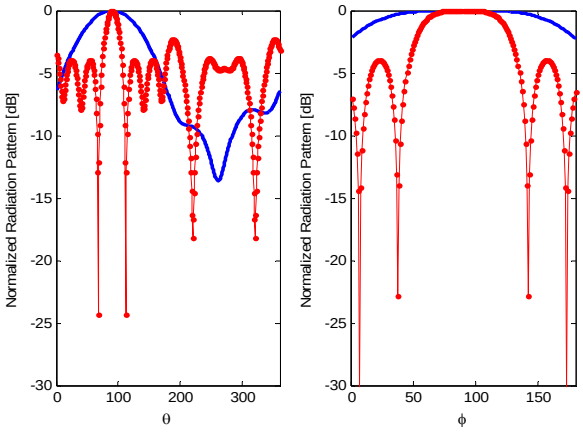

(a)

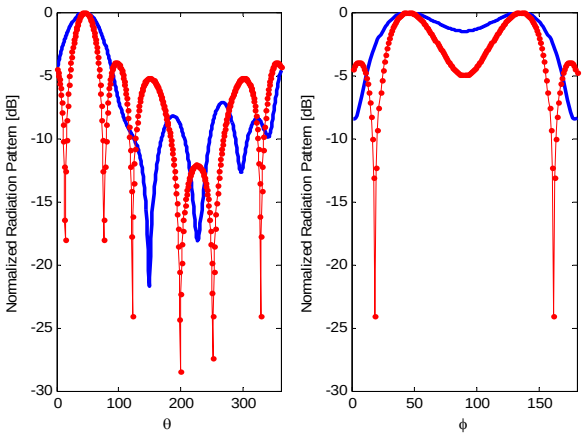

(b)

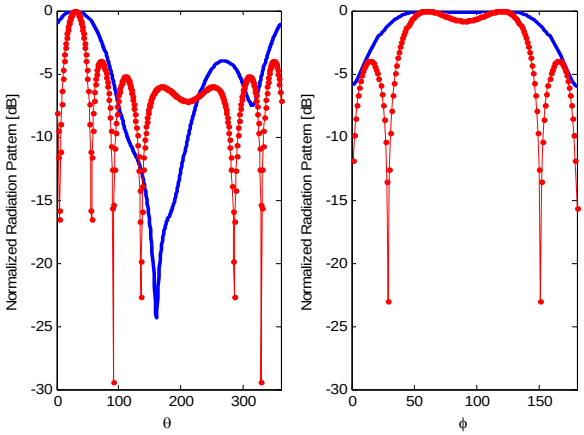

(c)

Fig. 6. Normalized radiation pattern comparison with uniform feeding in both the E- and H-planes, (solid) spiral and (dotted solid) circular array antennas for (a) (θ_0, ϕ_0) = (90°, 90°), (b) (θ_0, ϕ_0) = (45°, 45°), and (c) (θ_0, ϕ_0) = (60°, 30°).

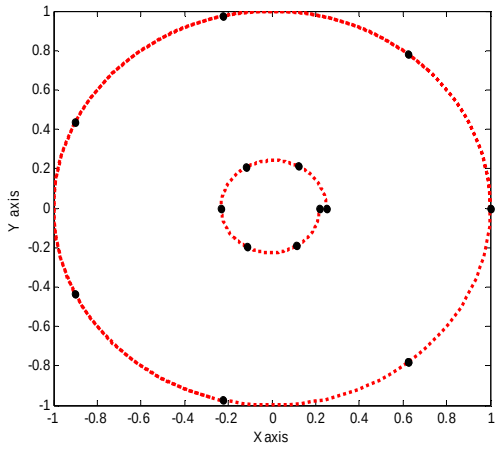

(a)

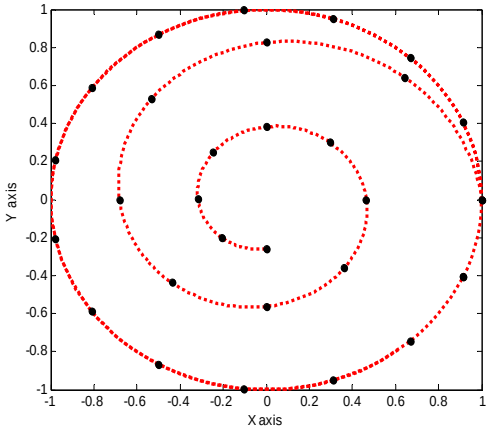

(b)

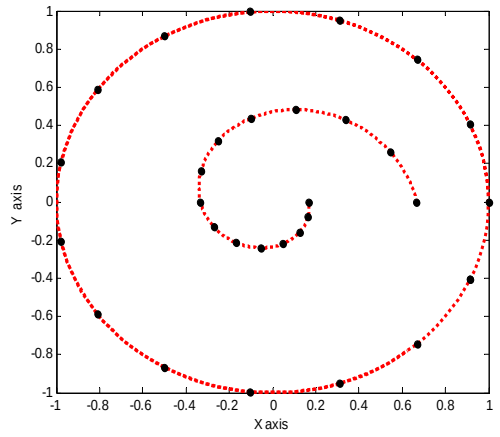

(c)

Fig. 7. (a) 7 and 15 elements spiral and circular array, (b) type I, and (c) type II.

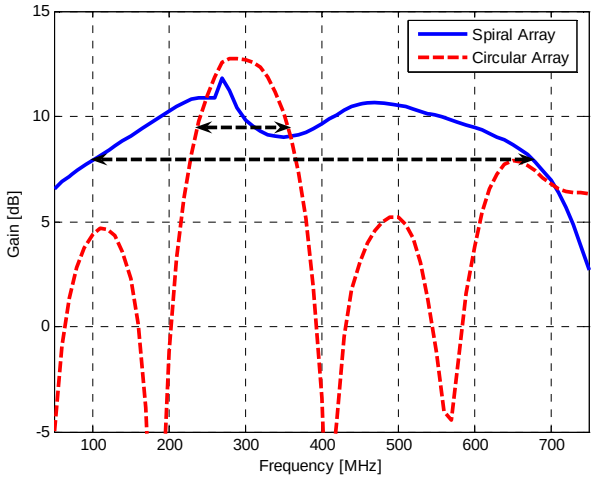

(a)

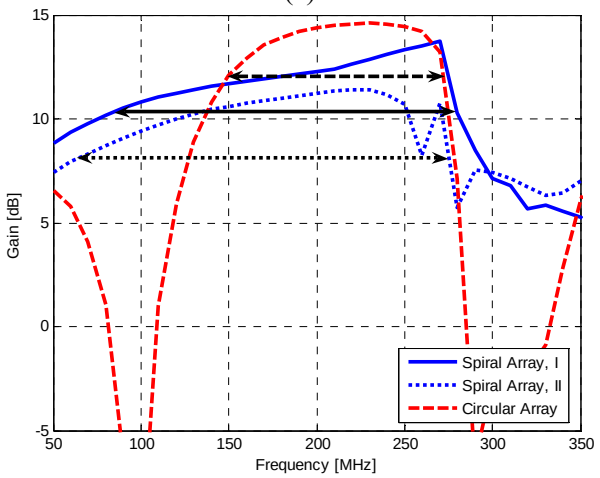

(b)

Fig. 8. Gain comparison for the desired main beam direction, f_{high}/f_{low} = (a) 1.49 for circular and 6.75 for spiral, (b) 1 for circular, 3.1 for type I and 4.46 for type II.

In these figures, the array radiation, architecture and size have been compared. It seems clearly that the spiral array antenna has been miniaturized with regards to simple circular array; whereas it approximately achieves the same radiation characteristics and even though broader bandwidth as shown in Fig. 6. From Fig. 7, over 90 %, 30 %, and 70 % size reductions have been achieved for the respective designed spiral array architectures. In Fig. 8, the gain of the arrays in the desired main beam direction has been compared. It seems that the array bandwidth (f_{high}/f_{low}) for circular and spiral cases are: (a) 1.49 and 6.75, (b) 1 for circular, 3.1 for type I and 4.46 for type II, respectively.

VI. CONCLUSION

In this paper, a novel planar array for broadband applications has been introduced and thoroughly investigated. A fair comparison between the spiral array architecture and its conventional counterparts, exhibits the ability of the proposed architecture to enhance the radiation bandwidth of an array. Several spiral array antennas have been designed and simulated to confirm the theoretical calculations. We also investigated the array miniaturization capability. Simulations show that choosing optimum parameters leads to array size reduction, which is vary from 30 % to 90 %.

REFERENCES

[1] B. Allen, M. Dohler, E. E. Okon, W. Q. Malik, A. K. Brown, and D. J. Edwards, *Ultra-Wideband Antennas and Propagation for Communications, Radar and Imaging*, *John Wiley*, 2007.

[2] J. T. Aberle, "Two-port representation of an antenna with application to non-foster matching networks," *IEEE Trans. Antennas Propag.*, vol. 56, no. 5, pp. 1218-1222, 2008.

[3] R. Ziolkowski, P. Jin, and C. Lin, "Metamaterial-inspired engineering of antennas," *Proc. IEEE*, vol. 99, pp. 1720-1731, 2011.

[4] P. Jin and R. Ziolkowski, "Broadband, efficient, electrically small metamaterial-inspired antennas facilitated by active near-field resonant parasitic elements," *IEEE Trans. Antennas Propag.*, vol. 58, pp. 318-327, 2010.

[5] N. Zhu and R. W. Ziolkowski, "Active metamaterial-inspired broad bandwidth, efficient, electrically small antennas," *IEEE Antennas Wireless Propag. Lett.*, vol. 10, pp. 1582-1585, 2011.

[6] S. E. Sussman-Fort and R. M. Rudish, "Non-foster impedance matching of electrically-small antennas," *IEEE Trans. Antennas Propag.*, vol. 57, no. 8, pp. 2230–2241, 2009.

[7] J. D. Dyson, "The equiangular spiral antenna," *IEEE Trans. Antennas Propag.*, vol. 7, no. 2, pp. 181–187, 1959.

[8] A. Jafargholi, M. Kamyab, and M. Veysi, "Spiral array architecture, design, synthesis and application," *IET Microwave Antenna Propag.*, vol. 5, pp. 503-511, April 2011.

[9] A. Jafargholi and M. Kamyab, "Pattern optimization in an UWB spiral array antenna," *Progress In Electromagnetics Research M*, vol. 11, pp. 137-151, 2010.

Amir Jafargholi received the Ph.D. degree in Electrical Engineering from K. N. Toosi University of Technology, Tehran, Iran, in 2011. He is the coauthor of about 50 scientific contributions published in international books, journals and peer-reviewed conference proceedings. His research interest includes the applications of metamaterials in the analysis and synthesis of antennas.

Dr. Jafargholi was a recipient of a Student's Best Thesis National Festival award for his B.Sc thesis, on May 2006. He was a recipient of the 22th Khawarizmi International and 13th Khawarizmi Youth Award on Jan. 2009 and Oct. 2011, respectively. He was also the recipient of Research Grant Awarded in Metamaterial 2010.

Ali Jafargholi was born in Tehran, Iran, on November 3, 1989. He received the B.Sc. degree in Electrical Engineering from Sharif University of Technology, Tehran, Iran, in 2012, and is currently working toward the M.Sc. degree in Communication Engineering. His research interests include metamaterial applications to antenna designs.

Unsplit-Field Implementation of the Higher-Order PML using *Z*-Transform Method and D-B Formulation for Arbitrary Media

Naixing Feng[1], Jianxiong Li[1], and Xiaoming Zhao[2]

[1] School of Electronics and Information Engineering
Tianjin Polytechnic University, Tianjin, 300387, China
fengnaixing@gmail.com, lijianxiong@tjpu.edu.cn

[2] School of Textiles
Tianjin Polytechnic University, Tianjin, 300387, China
zhaoxiaoming@tjpu.edu.cn

Abstract ─ On the basis of the stretched coordinate perfectly matched layer (SC-PML) formulations, the *Z*-transform method, and D-B formulation, an efficient and unsplit-field implementation of the higher-order PML scheme with more than one pole is proposed to truncate the finite-difference time-domain (FDTD) lattices. This method is completely independent of the material properties of the FDTD computational domain and hence can be applied to the modeling of arbitrary media without any modification. The higher-order PML has the advantages of both the conventional PML and the complex frequency shifted PML (CFS-PML) in terms of absorbing performances. The proposed algorithm is validated through two numerical tests carried out in three dimensional and two dimensional domains. It is shown in the numerical tests that the proposed PML formulations with the higher-order scheme are efficient in terms of attenuating both the low-frequency propagating waves and evanescent waves and reducing late-time reflections, and also hold much better absorbing performances than the conventional SC-PML and the convolutional PML (CPML) with the CFS scheme.

Index Terms ─ finite-difference time-domain (FDTD), perfectly matched layer (PML), and *Z*-transform method.

I. INTRODUCTION

Since the introduction of the perfectly matched layer (PML) absorbing boundary condition (ABC) by Berenger [1], various modified PMLs have been presented to terminate the finite-difference time-domain (FDTD) lattices. With the advantage of simple implementation in the corners and the edges of the PML regions, the stretched coordinate PML (SC-PML) [2] was proposed through mapping Maxwell's equations into a complex stretched coordinate space. As original Berenger's PML, the SC-PML formulations in [2] were ineffective at absorbing the evanescent waves. Besides, the complex frequency shifted PML (CFS-PML) [3], implemented by simply shifting the frequency dependent pole off the real axis and into the negative-imaginary half of the complex plane, has drawn considerable attention due to the fact that this PML is efficient in attenuating the low-frequency evanescent waves and reducing late-time reflections [4]. In [4], the convolutional PML (CPML), based on the SC-PML formulations and the convolution theorem, was presented in detail to efficiently implement the CFS-PML. However, the CFS-PML would have a poor absorption of low-frequency propagating waves as shown in [5-7]. To overcome the limitations of both the conventional PML and the CFS-PML, the higher-order PML was proposed by Correia, which retains the advantages of both the CFS-PML and conventional PML in [7]. It has shown that the second-order PML is highly effective in absorbing

Submitted On: May 29, 2012
Accepted On: Dec. 26, 2012

both evanescent and low-frequency propagating waves in both open-region and periodic problems in [8]. In [8], the 2nd-order PML based on the SC-PML was implemented by using the split-field PML formulations and the auxiliary differential equation (ADE) method. However, besides the drawback of more requirements of the memory and the computational time, the higher-order PML implementation proposed in [8] was difficult to be extended to the case with more than two poles because the polynomial expansion was employed.

In this paper, an efficient and unsplit-field implementation of the higher-order PML based on SC-PML formulations and the *Z*-transform method is proposed. For convenience, this PML is referred to here as the MZT PML. The proposed MZT PML algorithm is different from the proposed PML algorithm in [9] and [10-15], the proposed MZT PML algorithm is based on D-B formulations, and this method is fully independent of the material properties of the FDTD computational domain and hence can be applied to the modeling of arbitrary media without any modification. In addition, the proposed higher-order PML scheme requires less memory and computational time as compared with that in [8]. Only the 2nd-order case is described in this paper, but this approach is easy to be applied to any number of poles.

II. FORMULATION

In three-dimensional (3-D) SC-PML regions, the normalized frequency-domain modified Maxwell's curl equations can be written as,

$$j\omega\varepsilon_r(\omega)\mathrm{E}(\omega)=c_0\nabla_s\times\mathrm{H}(\omega) \tag{1}$$

$$j\omega\mu_r(\omega)\mathrm{H}(\omega)=-c_0\nabla_s\times\mathrm{E}(\omega), \tag{2}$$

where c_0 is the speed of light in free space, $\varepsilon_r(\omega)$ and $\mu_r(\omega)$ are, respectively, the relative permittivity and permeability of the FDTD computational domain and the operator ∇_s is expressed as,

$$\nabla_s=\hat{x}S_x^{-1}\partial_x+\hat{y}S_y^{-1}\partial_y+\hat{z}S_z^{-1}\partial_z \tag{3}$$

where ∂_x, ∂_y, and ∂_z are the partial derivatives with respect to x, y, and z and S_η, ($\eta = x, y, z$) are the complex stretched coordinate metrics, which was originally proposed [1] to be,

$$S_\eta=1+\sigma_\eta/j\omega\varepsilon_0 \tag{4}$$

with the CFS scheme and S_η ($\eta = x, y, z$) were defined as,

$$S_\eta=\kappa_\eta+\sigma_\eta/(\alpha_\eta+j\omega\varepsilon_0) \tag{5}$$

where σ_η and α_η are assumed to be positive real and K_η is real and ≥ 1. In order to make the PML completely independent of the material properties of the FDTD computational domain, both equations (1) and (2) can be written in terms of the electric flux density D and the magnetic flux density B as,

$$j\omega\mathrm{D}(\omega)=c_0\nabla_s\times\mathrm{H}(\omega) \tag{6}$$

$$j\omega\mathrm{B}(\omega)=-c_0\nabla_s\times\mathrm{E}(\omega), \tag{7}$$

where D and B are given by,

$$\mathrm{D}(\omega)=\varepsilon_r(\omega)\mathrm{E}(\omega) \tag{8}$$

$$\mathrm{B}(\omega)=\mu_r(\omega)\mathrm{H}(\omega)\ . \tag{9}$$

Consequently, this PML can be applied to truncate arbitrary media, such as lossy, dispersive, anisotropic, inhomogeneous or nonlinear without any modification and all that is needed is to modify equations (8) and (9) under consideration. The method is available in [16] to obtain E from D using equation (8) [and H from B using equation (9)]. It must be noted that if $\varepsilon_r(\omega)$ or $\mu_r(\omega)$ is not frequency-dependent, E or H formulation should be adopted to reduce memory requirement and save computational time.

The idea of the higher-order PML was proposed in [8] by generalizing this metric for the case where more than one pole was present. For the 2nd-order PML, S_η is defined as,

$$S_\eta=S_{1\eta}\cdot S_{2\eta}=\left(\kappa_{1\eta}+\frac{\sigma_{1\eta}}{\alpha_{1\eta}+j\omega\varepsilon_0}\right)\left(\kappa_{2\eta}+\frac{\sigma_{2\eta}}{\alpha_{2\eta}+j\omega\varepsilon_0}\right). \tag{10}$$

Owing to the frequency dependence of S_η, the transformation of equation (6) to the time domain will lead to convolutions on the right hand side [4]. However, because the convolution in the time domain is just a multiplication in the *Z*-domain [17], it is more efficient as shown below that equation (6) is first transformed to the *Z*-domain and then to the FDTD form.

$$\frac{1-z^{-1}}{\Delta t}\varepsilon_0 D_x=S_y(z)\cdot\frac{\partial H_z}{\partial y}-S_z(z)\cdot\frac{\partial H_y}{\partial z} \tag{11}$$

where Δt is the time step and $S_\eta(z)$, ($\eta = y, z$), is the *z*-transform of $1/S_\eta$, which can be obtained by first transforming $1/S_\eta$ to the *s*-domain using the relation $j\omega\rightarrow s$, and then applying the matched *z*-transform

method [17] using the relation $(s–p) \rightarrow (1–e^{p\Delta t}z^{-1})$,

$$S_\eta(z) = w_{1\eta}\left(\frac{1-h_{1\eta}\cdot z^{-1}}{1-g_{1\eta}\cdot z^{-1}}\right)\cdot w_{2\eta}\left(\frac{1-h_{2\eta}\cdot z^{-1}}{1-g_{2\eta}\cdot z^{-1}}\right) \tag{12}$$

where
$w_{m\eta} = 1/K_{m\eta}$, $g_{m\eta} = \exp[-(\Delta t/\varepsilon_0)(\alpha_{m\eta} + \sigma_{m\eta}/K_{m\eta})]$ and $h_{m\eta} = \exp(-\alpha_{m\eta}\Delta t/\varepsilon_0)$, $(m = 1, 2)$. Substituting equation (12) into equation (11), we obtain

$$\begin{aligned}\frac{1-z^{-1}}{\Delta t}\varepsilon_0 D_x = {} & w_{1y}w_{2y}\left(\frac{1-h_{1y}\cdot z^{-1}}{1-g_{1y}\cdot z^{-1}}\right)\left(\frac{1-h_{2y}\cdot z^{-1}}{1-g_{2y}\cdot z^{-1}}\right)\frac{\partial H_z}{\partial y} \\ & -w_{1z}w_{2z}\left(\frac{1-h_{1z}\cdot z^{-1}}{1-g_{1z}\cdot z^{-1}}\right)\left(\frac{1-h_{2z}\cdot z^{-1}}{1-g_{2z}\cdot z^{-1}}\right)\frac{\partial H_y}{\partial z}.\end{aligned} \tag{13}$$

Introducing four auxiliary variables Q_{xn} and P_{xn} ($\eta = y, z$).

$$\begin{aligned}Q_{xy} &= \frac{w_{1y}w_{2y}\Delta t}{\varepsilon_0}\cdot\left(\frac{1}{1-g_{1y}\cdot z^{-1}}\right)\cdot\frac{\partial H_z}{\partial y} \\ &= g_{1y}\cdot z^{-1}Q_{xy} + \frac{w_{1y}w_{2y}\Delta t}{\varepsilon_0}\cdot\frac{\partial H_z}{\partial y}\end{aligned} \tag{14}$$

$$\begin{aligned}P_{xy} &= \left(\frac{1-h_{2y}\cdot z^{-1}}{1-g_{2y}\cdot z^{-1}}\right)Q_{xy} \\ &= g_{2y}\cdot z^{-1}P_{xy} + Q_{xy} - h_{2y}\cdot z^{-1}Q_{xy}\ ,\end{aligned} \tag{15}$$

$$\begin{aligned}Q_{xz} &= \frac{w_{1z}w_{2z}\Delta t}{\varepsilon_0}\cdot\left(\frac{1}{1-g_{1z}\cdot z^{-1}}\right)\cdot\frac{\partial H_y}{\partial z} \\ &= g_{1z}\cdot z^{-1}Q_{xz} + \frac{w_{1z}w_{2z}\Delta t}{\varepsilon_0}\cdot\frac{\partial H_y}{\partial z}\ ,\end{aligned} \tag{16}$$

$$\begin{aligned}P_{xz} &= \left(\frac{1-h_{2z}\cdot z^{-1}}{1-g_{2z}\cdot z^{-1}}\right)Q_{xz} \\ &= g_{2z}\cdot z^{-1}P_{xz} + Q_{xz} - h_{2z}\cdot z^{-1}Q_{xz}\ .\end{aligned} \tag{17}$$

Considering that the z^{-1} operator corresponds to a single-step delay in the discrete time domain, equations (14) – (17) can be written in the FDTD form, respectively, as in equations (18) – (21), where

$$\begin{aligned}Q_{xy}\Big|^{n+1}_{i+1/2,j,k} &= g_{1y(j)}\cdot Q_{xy}\Big|^{n}_{i+1/2,j,k} \\ &+ u_{y(j)}\cdot\left(H_z\Big|^{n+1/2}_{i+1/2,j+1/2,k} - H_z\Big|^{n+1/2}_{i+1/2,j-1/2,k}\right)\end{aligned} \tag{18}$$

$$\begin{aligned}P_{xy}\Big|^{n+1}_{i+1/2,j,k} &= g_{2y(j)}\cdot P_{xy}\Big|^{n}_{i+1/2,j,k} \\ &+ Q_{xy}\Big|^{n+1}_{i+1/2,j,k} - h_{2y(j)}\cdot Q_{xy}\Big|^{n}_{i+1/2,j,k}\ ,\end{aligned} \tag{19}$$

$$\begin{aligned}Q_{xz}\Big|^{n+1}_{i+1/2,j,k} &= g_{1z(k)}\cdot Q_{xz}\Big|^{n}_{i+1/2,j,k} \\ &+ u_{z(k)}\cdot\left(H_y\Big|^{n+1/2}_{i+1/2,j,k+1/2} - H_y\Big|^{n+1/2}_{i+1/2,j,k-1/2}\right),\end{aligned} \tag{20}$$

$$\begin{aligned}P_{xz}\Big|^{n+1}_{i+1/2,j,k} &= g_{2z(k)}\cdot P_{xz}\Big|^{n}_{i+1/2,j,k} \\ &+ Q_{xz}\Big|^{n+1}_{i+1/2,j,k} - h_{2z(k)}\cdot Q_{xz}\Big|^{n}_{i+1/2,j,k}\ .\end{aligned} \tag{21}$$

Equation (11) can be written as,

$$\begin{aligned}D_x\Big|^{n+1}_{i+1/2,j,k} &= D_x\Big|^{n}_{i+1/2,j,k} + P_{xy}\Big|^{n+1}_{i+1/2,j,k} - h_{1y(j)} \\ &\cdot P_{xy}\Big|^{n}_{i+1/2,j,k} - \left(P_{xz}\Big|^{n+1}_{i+1/2,j,k} - h_{1z(k)}\cdot P_{xz}\Big|^{n}_{i+1/2,j,k}\right)\end{aligned} \tag{22}$$

where $u_y = w_{1y}w_{2y}\Delta t/(\varepsilon_0\Delta y)$, $u_z = w_{1z}w_{2z}\Delta t/(\varepsilon_0\Delta z)$. Both Δy and Δz are the space steps. All coefficients, which are calculated once prior to the field computation and stored in one-dimensional vector arrays, auxiliary variables and field components, are evaluated at the corresponding Yee grid position. Noting that storage of $P_{xy}|^n_{i+1/2,j,k}$, $P_{xz}|^n_{i+1/2,j,k}$, $Q_{xy}|^n_{i+1/2,j,k}$ and $Q_{xz}|^n_{i+1/2,j,k}$ can be avoided by means of temporary storage variables [18]. Consequently, the FDTD implementation of equation (1) by using equations (18) – (22) requires only the storage of four auxiliary variables (i.e., $P_{xy}{}^{n+1}$, $P_{xz}{}^{n+1}$, $Q_{xy}{}^{n+1}$, and $Q_{xz}{}^{n+1}$) per field component per cell in the SC-PML region.

The above formulations are applied to the corner PML regions and the edge PML regions, which run parallel with x direction (i.e., both $S_y \neq 1$ and $S_z \neq 1$ are chosen as in equation (12)). In the faces of the PML regions, which are normal to the y direction and the edge PML regions that run parallel with the z direction (i.e., $S_y \neq 1$ as in equation (12) and $S_z = 1$ are chosen), E_x can be obtained by using only two auxiliary variables, P_{xy} and Q_{xy}. Likewise, in the faces of the PML regions, which are normal to the z direction and the edge PML regions that run parallel with the y direction (i.e., $S_y = 1$ and $S_z \neq 1$ as in equation (12) are chosen), E_x can be obtained by using only two auxiliary variables, P_{xz} and Q_{xz}. For the face PML regions, which are perpendicular to x direction (i.e., both $S_y = 1$and $S_z = 1$ are chosen), no auxiliary variable is required. Similar formulations can be obtained for other field components of E and H.

In order to perform a comparison of the proposed formulations and the formulations in [8] in terms of memory, we assume a vacuum 3D FDTD computational domain with $L \times M \times N$ cells. A W-cell thick PML is used to truncate the FDTD computational domain on all directions. To obtain E_x, the proposed formulations require $4 \times (L+2W) \times W \times W \times 4 = 32W^3 + 16LW^2$ auxiliary variables in the corner PML regions and the edge PML regions, which run parallel with x direction (i.e., both $S_y \neq 1$ and $S_z \neq 1$ are chosen, and P_{xy}, P_{xz}, Q_{xy}, and Q_{xz} are required), $2 \times (L+2W) \times W \times N \times 2 = 8NW^2 + 4LNW$ auxiliary variables in the faces of the PML regions which are normal to y direction and the edge PML regions which run parallel with the z direction (i.e., $S_y \neq 1$ and $S_z = 1$ are chosen, and P_{xy} and Q_{xy} are required), $2 \times (L+2W) \times M \times W \times 2 = 8MW^2 + 4LMW$ auxiliary variables in the faces of the PML regions which are normal to the z direction and the edge PML regions that run parallel with the y direction (i.e., $S_y = 1$ and $S_z \neq 1$ are chosen, and P_{xz} and Q_{xz} are required), and 0 auxiliary variables in the face PML regions, which are perpendicular to the x direction (i.e., both $S_y = 1$ and $S_z = 1$ are chosen). By using the same means, auxiliary variables to obtain E_y, E_z, H_x, H_y, and H_z can be computed. In consequence, the proposed formulations require $192W^3 + 64\ (LW^2 + MW^2 + NW^2) + 16\ (LMW + LNW + MNW)$ auxiliary variables in total to obtain 6 field components. However, the formulations in [8] require $288W^3 + 112\ (LW^2 + MW^2 + NW^2) + 32\ (LMW + LNW + MNW)$ auxiliary variables. Therefore, the proposed formulations require $96W^3 + 48\ (LW^2 + MW^2 + NW^2) + 16\ (LMW + LNW + MNW)$ auxiliary variables less than the formulations in [8] in the PML regions.

As compared with [8], savings in the computation time can be achieved by the proposed algorithm due to the fact that the decrease of the auxiliary variables leads to the reduction of the calculation steps. The more the cells are required in the PML regions, the more the savings in memory and computation time. It is obvious that because of no polynomial expansion, the proposed implementation of the higher-order PML is easier than that in [8] to be extended to the case with more than two poles.

III. NUMERICAL RESULT

Two numerical tests are provided to validate the proposed method. In the first test, we implement the FDTD simulation for an inhomogeneous, dispersive, and conductive soil half-space problem in a highly elongated FDTD grid. It is shown in Fig. 1 that the dielectric constant of soil is specified as the second-order Debye model with an added term $\varepsilon_r(\omega) = \varepsilon_\infty + \sigma/j\omega\varepsilon_0 + \Sigma^2_{p=1} A_p/(1+j\omega\tau_p)$, where $\varepsilon_\infty = 4.15$ is the infinite frequency permittivity, $A_1 = 1.8$ and $A_2 = 0.6$ are the pole amplitudes, $\tau_1 = 3.79$ nsec and $\tau_2 = 0.151$ nsec are the relaxation time and $\sigma = 1.11$ ms/m is the conductivity [19]. The half-space occupies 50 % of the vertical height of the horizontally elongated simulation region. The simulation is done with a $126 \times 46 \times 26$ grid including 10-cell-thick PML layers on all sides with the space steps $\Delta x = \Delta y = \Delta z = 0.05$ m and the time step $\Delta t = 77$ psec. Assuming that the origin is at a corner of FDTD grid, a vertically polarized point source located at (13, 13, 13) (just above the soil) is excited by a differentiated Gaussian pulse with a half pulse bandwidth = 1155 psec. Within the PML, σ_η and K_η are scaled using a fourth-order polynomial scaling [20] and α_η is a constant. The relative reflection error (in decibel) versus time is computed at an observation point located at (113, 33, 12) (at the opposing corner of FDTD grid from the source and just below the interface of free space and soil) by using,

$$R_{dB}(t) = 20\log_{10}\left(\frac{\left|E_z(t) - E_{\text{zref}}(t)\right|}{\left|E_{\text{zrefmax}}\right|}\right) \qquad (23)$$

where $E_z(t)$ represents the time-dependent discrete electric field of the observation point, $E_{zref}(t)$ is a reference solution based on a larger computational domain, and $E_{zrefmax}$ represents the maximum value of the reference solution over the full-time simulation. The relative reflection error is first computed over 1500 time iterations. This same example is repeated with SC-PML ($\alpha_\eta = 0$, $K_{max} = 11$, and $\sigma_{max} = 0.18$ S/m) and the convolutional PML (CPML) [4] ($\alpha_\eta = 0.0015$, $K_{max} = 7$, and $\sigma_{max} = 0.24$ S/m). For the 2nd-order PML including the formulations in [8] and the proposed formulations, the following parameters is chosen as follow, $K_{1\eta} = 1$, $\alpha_{1\eta} = 0$, $K_{2\eta\text{opt}} = 8$, $\sigma_{1\eta} = \sigma_{1\eta\text{opt}}\,\rho^4$, $K_{2\eta} = 1 + K_{2\eta\text{opt}}\rho^2$, $\sigma_{1\eta\text{opt}} = 0.175/150\pi\Delta x$, $\alpha_{2\eta} = 0.0015 + \sigma_{1\eta}$, $\sigma_{2\eta\text{opt}} = 4/150\pi\Delta x$ and $\sigma_{2\eta\text{opt}} = \sigma_{2\eta\text{opt}}\rho^2$ where ρ is

zero at the interface of the PML and the FDTD computational domains and 1 at the end. In all computations of this paper, σ and K are evaluated as the average value in the cell around the index location [1]. These optimum parameters are chosen empirically to obtain the lowest reflection. The difference of the optimum parameters of MZT PML and CPML results from different scheme (i.e., the coefficients of equations (18) – (22) are different from the counterpart of CPML).

These results are illustrated in Fig. 2. The maximum relative reflection errors of the conventional SC-PML, the CPML, the 2nd-order PML in [8] and the proposed 2nd-order PML are -43 dB, -52 dB, -68 dB, and -66 dB, respectively. It can be concluded from Fig. 2 that the absorbing performance of the proposed 2nd-order PML formulations have 14 dB and 23 dB improvement in terms of the maximum relative error as compared with the CPML and the SC-PML, respectively, and holds much lower reflection error for the late-time region than the CPML and the SC-PML.

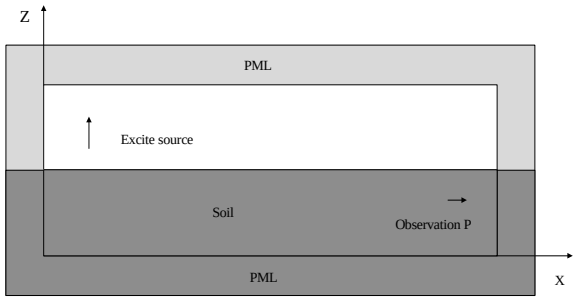

Fig. 1. 3D FDTD grid for an inhomogeneous, dispersive, and conductive soil half-space problem.

Tables 1 and 2 are using different perfectly matched layer algorithm procedures, which occupy memory and with different time steps occupy computational time, respectively. Obviously, when FDTD computational domain is invariant, saving memory will increase with the increase of PML layers and saving time will increase with the increase of time steps.

In the second test, to simplify the problem, but without loss of generality, we model a 2D TE-polarized electromagnetic wave interaction with an infinitely long perfectly electric conductor (PEC) sheet with the finite width to validate the proposed formulations. Figure 3 shows the FDTD grid geometry used in this simulation. The space is discretized with the FDTD lattice with $\Delta x = \Delta y = 1$ mm and time step Δt = 1.1785 psec. The FDTD computational domains consist of a 100-cell wide PEC sheet surrounded by free space. 10-cell thick PML layers terminate the grid and are placed only 3-cells away from the PEC sheet in all directions.

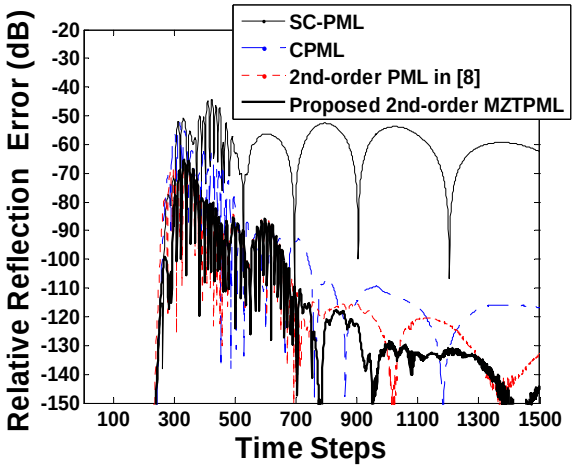

Fig. 2. Relative reflection error versus time, for the conventional SC-PML, CPML, 2nd-order PML in [8], and 2nd-order MZT PML.

Table 1: Using different perfectly matched layer algorithm procedures which occupy memory (bytes).

	PML layers=10	PML layers=16
2nd-order PML in [8]	49,506K	105,509K
2nd-order MZT PML	29,848K	65,224K
CPML	24,084K	49,664K
SC-PML	24,084K	49,672K

Table 2: Different time steps occupy computational time (s) (PML layers = 10).

	Time steps =2000	Time steps =4000
2nd-order PML in [8]	667.60	1344.58
2nd-order MZT PML	382.33	770.39
CPML	285.84	579.85
SC-PML	303.62	604.23

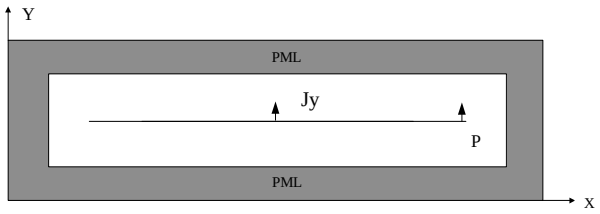

Fig. 3. The FDTD grid geometry in this simulation.

A *y*-polarized line electric current source, infinitely long in the *z* direction, is placed at the center and excited with a differentiated Gaussian pulse given by,

$$J_y(t) = -2\frac{t-t_0}{t_w}\exp\left[-\left(\frac{t-t_0}{t_w}\right)^2\right] \qquad (24)$$

where t_w = 26.53 psec. and $t_0 = 4t_w$. The *y*-component of the electric field is measured at the point *P*, where we expect very strong evanescent waves to appear. The relative reflection error (in dB) versus time is computed at the observation point *P* by using,

$$R_{dB}(t) = 20\log_{10}\left(\frac{|E_y^R(t) - E_y^T(t)|}{|E_{y\_\max}^R|}\right) \qquad (25)$$

where $E_y^T(t)$ represents the time-dependent discrete electric field of the observation point, $E_y^R(t)$ is a reference solution based on a larger computational domain, and $E_{y\_max}^R$ represents the maximum value of the reference solution over the full time simulation. The reference grid is sufficiently large such that there are no reflections from its outer boundaries during 1500 time steps, which are well past the steady-state response. The same example is repeated with the conventional SC-PML (equivalent to the CPML with $\alpha_\eta = 0$), the CPML and the 2nd-order PML in [8]. Within the conventional SC-PML and the CPML, K_η and σ_η are scaled by using a fourth-order polynomial scaling ($m = 4$) and α_η is a constant, as in [4]. The σ_{opt} is chosen as,

$$\sigma_{\text{opt}} = \frac{m+1}{150\pi\Delta x}.$$

For the conventional SC-PML, $K_{max} = 9$ and $\sigma_{max} = 0.5\,\sigma_{opt}$ are chosen. In the CPML simulation, $K_{max} = 9$, $\sigma_{max} = 0.9\,\sigma_{\text{opt}}$ and $\alpha_\eta = 0.06$ are chosen. For the 2nd-order PML including the formulations in [8] and the proposed formulations, the following parameters are chosen, $K_{1\eta} = 1$, $\alpha_{1\eta} = 0$, $K_{2\eta\text{opt}} = 8$, $\sigma_{1\eta} = \sigma_{1\eta\text{opt}}\,\rho^4$, $K_{2\eta} = 1 + K_{2\eta\text{opt}}\rho^2$, $\sigma_{1\eta\text{opt}} = 0.075/150\pi\Delta x$, $\alpha_{2\eta} = 0.09 + \sigma_{1\eta}$, $\sigma_{2\eta\text{opt}} = 4/150\pi\Delta x$ and $\sigma_{2\eta\text{opt}} = \sigma_{2\eta\text{opt}}\rho^2$. These optimum parameters are chosen empirically to obtain the lowest reflection.

The results are illustrated in Fig. 4. The maximum relative errors of the conventional SC-PML, CPML, 2nd-order PML in [8] and MZT PML are -49 dB, -75 dB, -90 dB and -90 dB, respectively. It can be concluded from figure that the absorbing performance of the proposed 2nd-order PML formulations is similar to that in [8] and has 15 dB and 41 dB improvement in terms of the maximum relative error as compared with the CPML and the SC-PML, respectively.

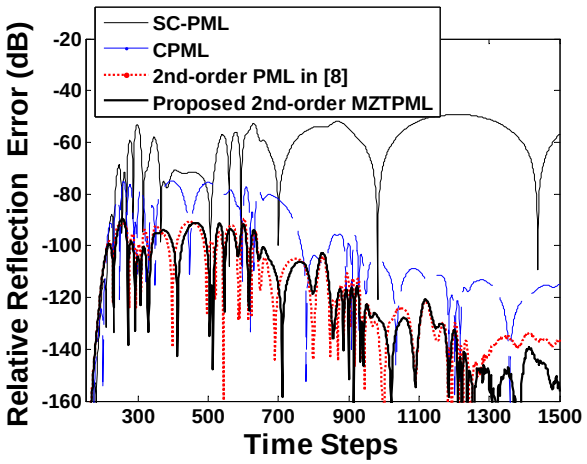

Fig. 4. Relative reflection error versus time for the conventional SC-PML, CPML, 2nd-order PML in [8], and 2nd-order MZT PML.

Tables 3 and 4 are similar to the first test by using different perfectly matched layer algorithm procedures which occupy of memory and different time steps that occupy computational time, respectively. Obviously, when FDTD computational domain is invariant, saving memory will increase with the increase of PML layers and saving time will increase with the increase of time steps.

IV. CONCLUSION

An efficient and unsplit-field implementation of the higher-order PML based on the SC-PML and

the *z*-transform method has been presented. It can be shown in the numerical tests that the proposed 2nd-order PML formulations hold better absorbing performance in terms of attenuating both the low-frequency propagating waves and evanescent waves and require less memory and computational time compared with the 2nd-order PML formulations implemented by using the split-field PML formulations and the auxiliary differential equation (ADE) method.

Table 3: Using different perfectly matched layer algorithm procedures, which occupy memory (bytes).

	PML layers=10	PML layers=16
2nd-order PML in [8]	1,256K	1,500K
2nd-order MZT PML	1,204K	1,412K
CPML	1,196K	1,220K
SC-PML	1,332K	1,428K

Table 4: Different time steps occupy computational time (s) (PML layers =10).

	Time steps =60000	Time steps =90000
2nd-order PML in [8]	61.60	92.46
2nd-order MZT PML	57.47	86.70
CPML	54.49	81.89
SC-PML	66.75	100.57

ACKNOWLEDGMENT

This work is supported by the Research Project of Applied Basic and Front Technologies of Tianjin (Grant No. 10JCZDJC15400) and the Natural Science Foundation of Tianjin (Grant No. 11JCYBJC26400).

REFERENCES

[1] J. P. Bérenger, "A perfectly matched layer for the absorption of electromagnetic waves," *J. Computat. Phys.*, vol. 114, no. 2, pp. 185-200, Oct. 1994.

[2] W. C. Chew and W. H. Weedon, "A 3-D perfectly matched medium from modified Maxwell's equations with stretched coordinates," *Microw. Opt. Technol. Lett.*, vol. 7, no. 13, pp. 599-603, Sep. 1994.

[3] M. Kuzuoglu and R. Mittra, "Frequency dependence of the constitutive parameters of causal perfectly matched anisotropic absorbers," *IEEE Microw. Guided Wave Lett.*, vol. 6, no. 12, pp. 447-449, Dec. 1996.

[4] J. A. Roden and S. D. Gedney, "Convolution PML (CPML): An efficient FDTD implementation of the CFS-PML for arbitrary media," *Microw. Opt. Technol. Lett.*, vol. 27, no. 5, pp. 334-339, Dec. 2000.

[5] E. Bécache, P. G. Petropoulus, and S. D. Gedney, "On the long-time behavior of unsplit perfectly matched layers," *IEEE Trans. Antennas Propag.*, vol. 52, no. 5, pp. 1335-1342, May 2004.

[6] J. P. Bérenger, "Numerical reflection from FDTD-PMLs: a comparison of the split PML with the unsplit CFS PML," *IEEE Trans. Antennas Propag.*, vol. 50, no. 3, pp. 258-265, Mar. 2002.

[7] D. Correia and J. M. Jin, "Performance of regular PML, CFS-PML, and second-order PML for waveguide problems," *Microw. Opt. Technol. Lett.*, vol. 48, no. 10, pp. 2121-2126, Oct. 2006.

[8] D. Correia and J. M. Jin, "On the development of a higher-order PML," *IEEE Trans. Antennas Propag.*, vol. 53, no. 12, pp. 4157-4163, Dec. 2005.

[9] N. Feng and J. Li "A *Z*-transform implementation of the Higher-Order perfectly matched layer," *Chinese Journal of Computational Physics* ,vol. 29, no. 2, pp. 271-276, Mar. 2012.

[10] N. Okada and J. B. Cole, "Nonstandard finite difference time domain algorithm for Berenger's perfectly matched layer," *Appl. Comp. Electrom. Society (ACES) Journal*, vol. 26, no. 2, pp. 153-159, Feb. 2011.

[11] J. B. Cole and D. Zhu, "Improved version of the second-order Mur absorbing boundary condition based on a nonstandard finite difference model," *Appl. Comp. Electrom. Society (ACES) Journal*, vol. 24, no. 4, pp. 375-381, August 2009.

[12] M. Wong and A. R. Sebak, "The floating PML applied to practical FDTD applications," *Appl. Comp. Electrom. Society (ACES) Journal*, vol. 23, no. 2, pp. 110-119, June 2008.

[13] M. J. Inman, A. Z. Elsherbeni, J. G. Maloney, and B. N. Baker, "Practical implementation of a CPML absorbing boundary for GPU accelerated FDTD technique," *Appl. Comp. Electrom. Society (ACES) Journal*, vol. 23, no. 1, pp. 16-22, March 2008.

[14] T. Kaufmann, K. Sankaran, C. Fumeaux, and R. Vahldieck, "A review of perfectly matched

absorbers for the finite-volume time-domain method," *Appl. Comp. Electrom. Society (ACES) Journal*, vol. 23, no. 3, pp. 184-192, Sep. 2008.

[15] D. M. Sullivan, "Frequency-dependent FDTD methods using Z transforms," *IEEE Trans. Antennas Propag.*, vol. 40, no. 10, pp. 1223-1230, 1992.

[16] J. G. Proakis and D. G. Manolakis, *Digital Signal Processing: Principles, Algorithms and Applications*, Prentice Hall International Editions, 3rd Edn., 1996.

[17] D. F. Kelley and R. J. Luebbers, "Piecewise linear recursive convolution for dispersive media using FDTD," *IEEE Trans. Antennas Propag.*, vol. 44, no. 6, pp. 792-797, June 1996.

[18] F. L. Teixeira, W. C. Chew, M. Straka, M. L. Oristaglio, and T. Wang, "Finite-difference time-domain simulation of ground penetrating radar on dispersive, inhomogeneous, and conductive soils," *IEEE Trans. Geosci. Remote Sens.*, vol. 36, no. 6, pp. 1928-1937, Nov. 1998.

[19] S. D. Gedney, A. Taflove, and Ed., "The perfectly matched layer absorbing medium," *Advance in Computational Electrodynamics: The Finite Difference Time Domain*, Boston, MA: Artech House, pp.263-340, 1998.

[20] O. Montazeri, M. H. Bakr, and Y. M. Haddara, "A PML for electroacoustic waves in piezoelectric materials using FDTD," *Appl. Comp. Electrom. Society (ACES) Journal*, vol. 26, no. 6, pp. 464-472, June 2011.

Naixing Feng was born in 1987, in Hainan, China. He received the B.Sc. degree in Electronic Science and Technology in 2010, from Tianjin Polytechnic University, Tianjin, China. He is currently pursuing the M.Sc. degree in the School of Electronics and Information Engineering, Tianjin Polytechnic University, Tianjin. His current research interests are in computational electromagnetics and metamaterials.

Jianxiong Li was born in 1969, in Tianjin, China. He received the B.Sc. and M.Sc. degrees in Physics in 1991 and 1994, respectively, and obtained the PhD degree in Communication and Information System in 2007, from Tianjin University, Tianjin, China. His main research interests are in computational electromagnetics, metamaterials, and RFID antenna.

Xiaoming Zhao obtained a PhD degree in textile science from the School of Textiles of Heriot-Watt University (UK) in 2004, and then he continued to his research work in Heriot-Watt University between 2004 and 2010. His work was focused on protective textiles. He joined Tianjin Polytechnic University (China) in2010, as Professor in Textile Science and Engineering, where he established the Flexible Materials for Protection Research Group.

Radiation from a Dielectric Coated Conducting Circular Cylinder Buried in a Conducting Corner (TM Case)

Hassan A. Ragheb

Department of Electrical Engineering
King Fahd University of Petroleum and Minerals, Dhahran, Saudi Arabia
hragheb@kfupm.edu.sa

Abstract –The paper presented a new design of a corner reflector antenna, fed through a dielectric coated slotted cylinder. An exact solution to a two dimensional problem is developed using the modal expansion solution for TM case. Computer program was developed to evaluate the radiation pattern, aperture conductance, and antenna gain. This antenna structure finds many applications on ships and airplanes in which the antenna is buried at corners of horizontal and vertical conducting planes. The radiation from this antenna showed many new features, which could not be achieved by the conventional corner reflector antenna.

Index Terms – Corner reflector antenna and dielectric coated slot antenna.

I. INTRODUCTION

Corner reflector antenna has been extensively investigated by many authors. The feed is usually considered as line source or dipole antenna. Various methods were employed to obtain the radiation characteristics of this antenna. For instance, analytical analysis [1], numerical analysis [2], and analysis using the geometrical theory of diffraction [3] were presented. Meanwhile, axial and circumferential slots of circular conducting cylinders were also examined by many investigators and different methods. The geometrical optics along with the residual series was represented in [4]. Green's function developed formulation was also introduced in [5]. In addition, an analytical development based on Fourier integral representation was presented in [6] and [7]. The combined slotted cylinder with reflecting corner was introduced in [8], to study the radiation from a transverse slot on a cylindrically tipped wedge. The wedge walls were considered infinite and analytical solution was obtained using Green's function method. Also radiation from an axial slot on a conducting circular cylinder with reflector wings was investigated in [9]. Integral equation for both TE and TM cases were developed using Green's functions. The resulting integral equation was numerically solved using moment method. A new geometry for cylindrically dielectric coated slotted antenna imbedded in a ground plane was the subject of the investigation in [10]. The radiation characteristic of this geometry was studied and showed that the ground plane can improve the antenna characteristics. Recently Romo et. al. [11], introduced an optimum design for cylindrical corner reflector antenna. Their results showed enhanced directive gain in the UHF bandwidth.

In this paper the dielectric coated slotted cylinder is assumed to be buried in a perfectly conducting corner of angle θ. The electric and magnetic fields for the TM case are assumed in terms of modal expansion of Fourier Bessel functions of unknown coefficients. The unknown coefficients were calculated by enforcing the boundary conditions. The formulation results in matrix equation of infinite dimensions, which can be truncated to a limited number of terms that satisfies the series convergence. A computer program was developed to calculate the antenna radiation pattern, aperture conductance, and antenna gain.

II. ANALYTICAL DEVELOPMENT (TM CASE)

A cross-sectional area of a conducting slotted circular cylinder of radius a coated with a

Submitted On: June 10, 2012
Accepted On: Nov. 23, 2012

concentric dielectric of outer radius *b*, permittivity ε, and permeability μ is illustrated in Fig. 1. The coated slotted cylinder is buried in a perfectly conducting corner as shown. The conducting corner planes are assumed to be infinitely long at $\phi = \theta^0/2$ and $\phi = -\theta^0/2$. The axial slot is centered at $\phi = \phi_0$ and has an angular angle equals to 2α. The space surrounding the conducting slotted cylinder is divided into two regions, region I ($a < \rho < b$) inside the dielectric coating, while region II ($\rho > b$, $-\theta^0/2 \geq \phi \geq \theta^0/2$) is outside the dielectric coated slotted cylinder in the space suspended by the corner conductors.

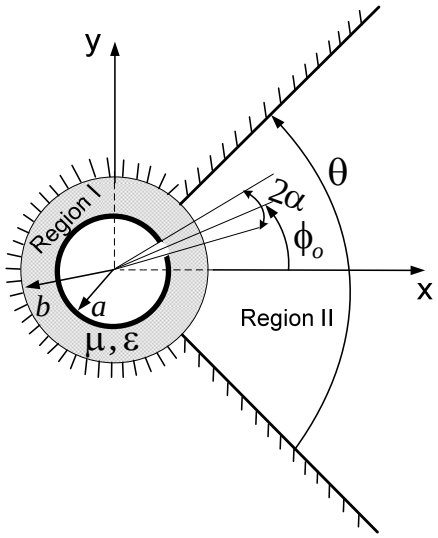

Fig. 1. Geometry of the problem.

The *z*-component of the electric field in region I can be written as,

$$E_z^{(I)} = E_o \sum_{n=-\infty}^{\infty} \left\{ A_n^{TM} J_n(k\rho) + B_n^{TM} N_n(k\rho) \right\} e^{jn\phi}. \quad (1)$$

The time dependence is assumed as $e^{j\omega t}$ and omitted throughout. The wave number $k_0 = 2\pi/\lambda$ where λ is the wavelength. Also, $J_n(x)$ and $N_n(x)$ are Bessel functions of the first and second kind, respectively of order *n* and argument *x*. Equation (1) is a solution of Helmholtz wave equation in cylindrical coordinates in region I, where A_n^{TM} and B_n^{TM} are unknown coefficients, which can be calculated from the boundary conditions. In a similar way one can write the *z*-component in region II as,

$$E_z^{(II)} = E_o \sum_{n=0}^{\infty} C_n^{TM} H_\nu^{(2)}(k_o\rho) \cos\nu\phi \qquad \nu = \frac{(2n+1)\pi}{\theta}. \quad (2)$$

Here $H_n^{(2)}(x)$ is the Hankel function of second kind with order *n* and argument *x*. C_n^{TM} are unknown coefficients that can be calculated from the boundary conditions. Furthermore, the boundary condition of vanishing $E_z^{(II)}$ at $\phi = \theta^0/2$ and $\phi = -\theta^0/2$ are satisfied in equation (2). The application of the boundary condition of vanishing $E_z^{(I)}$ on the surface of the conducting axially slotted cylinder results in,

$$E_o \sum_{n=-\infty}^{\infty} \left\{ A_n^{TM} J_n(ka) + B_n^{TM} N_n(ka) \right\} e^{jn\phi} = \begin{cases} E_z(\phi) & \phi_o - \alpha \leq \phi \leq \phi_o + \alpha \\ 0 & otherwise \end{cases}. \quad (3)$$

The *z*-component of the electric field on the axial slot aperture can be assumed as,

$$E_z(\phi) = E_o \cos\left(\frac{\pi(\phi - \phi_o)}{2\alpha} \right). \quad (4)$$

If one multiply both sides of equation (3) by $e^{-jm\phi}$ and integrates over ϕ from 0 to 2π, with some mathematical manipulations obtains,

$$B_m^{TM} = \frac{1}{N_m(ka)} \left\{ X_m^{TM} e^{-jm\phi_o} - A_m^{TM} J_m(ka) \right\} \quad (5)$$

where

$$X_m^{TM} = \frac{2\alpha \cos m\alpha}{\pi^2 - 4\alpha^2 m^2}.$$

The boundary condition at $\rho = b$ is given as,

$$E_z^{(I)} = \begin{cases} E_z^{(II)} & -\frac{\theta^o}{2} \leq \phi \leq \frac{\theta^o}{2} \\ 0 \quad otherwise \end{cases}. \quad (6)$$

Applying the above boundary condition, one can get,

$$\sum_{n=-\infty}^{\infty} \frac{X_n^{TM} N_n(kb) e^{-jn\phi_o}}{N_n(ka)} e^{jn\phi} + \sum_{n=-\infty}^{\infty} \frac{A_n^{TM} Y_n^{TM}}{N_n(ka)} e^{jn\phi} = \begin{cases} \sum_{n=0}^{\infty} C_n^{TM} H_\nu^{(2)}(k_o b) \cos\nu\phi & -\frac{\theta^o}{2} \leq \phi \leq \frac{\theta^o}{2} \\ 0 & otherwise \end{cases} \quad (7)$$

where

$$Y_n^{TM} = J_n(kb) N_n(ka) - J_n(ka) N_n(kb). \quad (8)$$

Multiplying both sides of equation (7) by $e^{-jm\phi}$ where (m = …, -3, -2, -1, 0, 1, 2, 3, …), and integrating over ϕ from 0 to 2π, we obtain,

$$2\pi\frac{X_m^{TM}N_m(kb)e^{-jm\phi_o}}{N_m(ka)}+2\pi\frac{A_m^{TM}Y_m^{TM}}{N_m(ka)}$$
$$=\sum_{n=0}^{\infty}C_n^{TM}H_\nu^{(2)}(k_ob)\;\;I_{mn}\;. \tag{9}$$

It can be re-arranged as,

$$A_m^{TM}=-\frac{X_m^{TM}N_m(kb)e^{-jm\phi_o}}{Y_m^{TM}}$$
$$+\frac{N_m(ka)}{2\pi Y_m^{TM}}\sum_{n=0}^{\infty}C_n^{TM}H_\nu^{(2)}(k_ob)\;\;I_{mn}\,. \tag{10}$$

where

$$I_{mn}=\begin{cases}\nu\left[\dfrac{2(-1)^{n+1}\cos\left(\frac{m\theta}{2}\right)}{m^2-\nu^2}\right] & \nu\neq m\\ \dfrac{\sin m\theta}{2m}+\dfrac{\theta}{2} & \nu=m\end{cases} \tag{11}$$

where n = 0, 1, 2, 3, … and m = …,-3, -2, -1, 0, 1, 2, 3, …. The magnetic fields in regions I and II can then be obtained from $H_\phi=(1/j\omega\mu)(dE_z/dr)$ as,

$$H_\phi^{(I)}=\frac{E_ok}{j\omega\mu}\sum_{n=-\infty}^{\infty}\frac{X_n^{TM}N_n'(k\rho)e^{-jn\phi_o}}{N_n(ka)}\;\;e^{jn\phi}$$
$$+\frac{E_ok}{j\omega\mu}\sum_{n=-\infty}^{\infty}\frac{A_n^{TM}}{N_n(ka)}\times$$
$$\left\{J_n'(k\rho)N_n(ka)-J_n(ka)N_n'(k\rho)\right\}e^{jn\phi} \tag{12}$$

and

$$H_\phi^{(II)}=\frac{E_ok_o}{j\omega\mu}\sum_{n=0}^{\infty}C_n^{TM}H_\nu^{(2)'}(k_o\rho)\cos\nu\phi\;. \tag{13}$$

The boundary condition of the continuous magnetic field H_ϕ at $\rho=b$ and $-\theta^0/2<\phi<\theta^0/2$ results in,

$$\sum_{n=-\infty}^{\infty}\frac{X_n^{TM}N_n'(kb)e^{-jn\phi_o}}{N_n(ka)}e^{jn\phi}+\sum_{n=-\infty}^{\infty}\frac{A_n^{TM}Y_n'^{TM}}{N_n(ka)}e^{jn\phi}$$
$$=\frac{1}{\sqrt{\varepsilon_r}}\sum_{n=0}^{\infty}C_n^{TM}H_\nu^{(2)'}(k_ob)\cos\nu\phi \tag{14}$$

where

$$Y_n'^{TM}=J_n'(kb)N_n(ka)-J_n(ka)N_n'(kb)\;. \tag{15}$$

Expanding equation (14) as,

$$\sum_{n=0}^{\infty}\frac{X_n^{TM}N_n'(kb)e^{-jn\phi_o}}{N_n(ka)}\;\;e^{jn\phi}$$
$$+\sum_{n=1}^{\infty}\frac{X_n^{TM}N_n'(kb)e^{jn\phi_o}}{N_n(ka)}\;\;e^{-jn\phi}$$
$$+\sum_{n=0}^{\infty}\frac{A_n^{TM}Y_n'^{TM}}{N_n(ka)}e^{jn\phi}$$
$$+\sum_{n=1}^{\infty}(-1)^n\frac{A_{-n}^{TM}Y_n'^{TM}}{N_n(ka)}e^{-jn\phi} \tag{16}$$
$$=\frac{1}{\sqrt{\varepsilon_r}}\sum_{n=0}^{\infty}C_n^{TM}H_\nu^{(2)'}(k_ob)\;\cos\nu\phi\,.$$

Since

$$I_{np}=I_{-np}\quad\text{and}\quad\nu=\frac{(2p+1)\pi}{\theta}\,. \tag{17}$$

Then, one can obtain,

$$(-1)^nA_{-n}^{TM}=-\frac{X_n^{TM}N_n(kb)e^{jn\phi_o}}{Y_n^{TM}}$$
$$+\frac{N_n(ka)}{2\pi Y_n^{TM}}\sum_{p=0}^{\infty}C_p^{TM}H_\nu^{(2)}(k_ob)\;\;I_{np} \tag{18}$$

Substituting from equations (10) and (18) into equation (16), one obtains,

$$\sum_{n=0}^{\infty}\left(\frac{X_n^{TM}N_n'(kb)e^{-jn\phi_o}}{N_n(ka)}\right.$$
$$\left.-\frac{X_n^{TM}N_n(kb)e^{-jn\phi_o}}{Y_n^{TM}}\frac{Y_n'^{TM}}{N_n(ka)}\right)e^{jn\phi}$$
$$+\sum_{n=1}^{\infty}\left(\frac{X_n^{TM}N_n'(kb)e^{jn\phi_o}}{N_n(ka)}\right.$$
$$\left.-\frac{X_n^{TM}N_n(kb)e^{jn\phi_o}}{Y_n^{TM}}\frac{Y_n'^{TM}}{N_n(ka)}\right)e^{-jn\phi} \tag{19}$$
$$+\sum_{n=0}^{\infty}\left(\frac{Y_n'^{TM}}{2\pi Y_n^{TM}}\sum_{p=0}^{\infty}C_p^{TM}H_\nu^{(2)}(k_ob)\;\;I_{np}\right)$$
$$(e^{jn\phi}+e^{-jn\phi})$$
$$=\frac{1}{\sqrt{\varepsilon_r}}\sum_{p=0}^{\infty}C_p^{TM}H_\nu^{(2)'}(k_ob)\;\;\cos\nu\phi\;.$$

Equation (19) can be simplified as,

$$\sum_{n=0}^{\infty}\frac{2\varepsilon_n X_n^{TM}}{\pi kbY_n^{TM}}\cos n(\phi-\phi_o) + \sum_{n=0}^{\infty}\varepsilon_n\left(\frac{Y_n'^{TM}}{2\pi Y_n^{TM}} \sum_{p=1}^{\infty}C_p^{TM}H_\nu^{(2)}(k_o b)\;\; I_{np}\right)\cos n\phi = \frac{1}{\sqrt{\varepsilon_r}}\sum_{p=0}^{\infty}C_p^{TM}H_\nu^{(2)'}(k_o b)\;\cos\nu\phi\,. \tag{20}$$

Multiplying both sides of equation (20) by cos $m\phi$ (m = 0, 1, 2, 3, …), and integrating over ϕ from $-\theta^0/2$ to $\theta^0/2$ to obtain,

$$\sum_{n=0}^{\infty}\frac{2\varepsilon_n X_n^{TM}}{\pi kbY_n^{TM}}\cos n\phi_o\;\; K_{mn} + \sum_{n=0}^{\infty}\varepsilon_n\left(\frac{Y_n'^{TM}}{2\pi Y_n^{TM}} \sum_{p=1}^{\infty}C_p^{TM}H_\nu^{(2)}(k_o b)\;\; I_{np}\right)K_{mn} = \frac{1}{\sqrt{\varepsilon_r}}\sum_{p=0}^{\infty}C_p^{TM}H_\nu^{(2)'}(k_o b)\;\; K_{m\nu} \tag{21}$$

$$K_{mn}=\begin{cases}\dfrac{\sin(m+n)\frac{\theta}{2}}{(m+n)}+\dfrac{\sin(m-n)\frac{\theta}{2}}{(m-n)} & n\neq m\\ \dfrac{\sin m\theta}{2m}+\dfrac{\theta}{2} & n=m,\end{cases} \tag{22}$$

where n= 0, 1, 2,… and m = 0, 1, 2,… Rearranging equation (21) takes the form,

$$\sum_{p=0}^{\infty}C_p^{TM}\left\{\frac{1}{\sqrt{\varepsilon_r}}H_\nu^{(2)'}(k_o b)\;\; K_{m\nu} - H_\nu^{(2)}(k_o b)\sum_{n=0}^{\infty}\frac{\varepsilon_n Y_n'^{TM}}{2\pi Y_n^{TM}}I_{np}K_{mn}\right\} = \sum_{n=0}^{\infty}\frac{2\varepsilon_n X_n^{TM}}{\pi kbY_n^{TM}}\cos n\phi_o K_{mn} \tag{23}$$

where ε_n is 1 for n = 0 and 2 otherwise. Equations (23) can be written in a matrix form,

$$[Z][C^{TM}]=[M] \tag{24}$$

where

$$Z_{mp}=\frac{1}{\sqrt{\varepsilon_r}}H_\nu^{(2)'}(k_o b)\;\; K_{m\nu} - H_\nu^{(2)}(k_o b)\sum_{n=0}^{\infty}\frac{\varepsilon_n Y_n'^{TM}}{2\pi Y_n^{TM}}I_{np}K_{mn}\,,$$

$$M_m=\sum_{n=0}^{\infty}\frac{2\varepsilon_n X_n^{TM}}{\pi kbY_n^{TM}}\cos n\phi_o K_{mn}\,.$$

III. RADIATION PATTERN AND SLOT CONDUCTANCE

The far zone radiation pattern for the electric field of the TM case can be calculated using the asymptotic expression of the Hankel function, i.e.,

$$E_z^{(II)}=E_o\sum_{n=1}^{\infty}C_n^{TM}H_\nu^{(2)}(k_o\rho)\sin\nu\phi\quad,\nu=\frac{n\pi}{\theta}$$

$$E_z^{(I)}=\sqrt{\frac{2}{\pi kr}}\quad e^{-jkr}\;\; e^{j\pi/4}\quad P_{TM}(\phi)$$

where

$$P_{TM}(\phi)=\sum_{n=0}^{\infty}j^{\frac{(2n+1)\pi}{\theta}}C_n^{TM}\cos\frac{(2n+1)\pi}{\theta}\phi. \tag{25}$$

The antenna gain and the aperture conductance are quantities of interest. Following the definition of Richmond [10], one can obtain the antenna gain as,

$$G(\phi)=\frac{2\,|\,P_{TM}(\phi)\,|^2}{\sum_{n=0}^{\infty}|\,C_n^{TM}\;|^2} \tag{26}$$

and the aperture conductance is

$$G_a/\lambda=\frac{1}{120\pi^2}\frac{\sum_{n=1}^{\infty}|\,C_n^{TM}\;|^2}{|\,E_o\,|^2}\,. \tag{27}$$

IV. RESULTS AND DISCUSSION

The accuracy of our computations will be verified first through two different methods. In the first, the integral equation formulation along with the moment method is employed to solve the problem when ε_r = 1. Figure 2, illustrates the far field pattern due to IEF and the present method. An excellent agreement is found in the range of -39^o to 39^o while the discrepancy in the rest is due to the finite size of the corner reflector considered in IEF (MoM). The second verification is through

some special cases published in [12]. The example shown in Fig. 3, illustrates the far field radiation pattern of a dielectric coated slotted cylinder embedded in a conducting ground plane. In this case the corner angle is considered as $\theta = 180^{o}$. The far field pattern obtained using the current formulation is compared with the corresponding published pattern [12] obtained for the same example. An excellent agreement is found. The parameters of both examples are given in the figure caption.

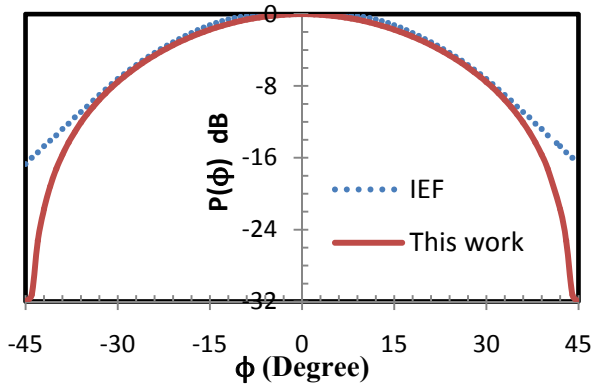

Fig. 2. Far field pattern of an axial slot on a dielectric coated conducting circular cylinder embedded in ground plane ($\theta = 90^{0}$, $a = 0.4\ \lambda$, $b = 0.69\ \lambda$, $2\alpha = 10^{0}$, $\phi_0 = 0^{0}$, $\varepsilon_r = 1$, and $\mu_r = 1$).

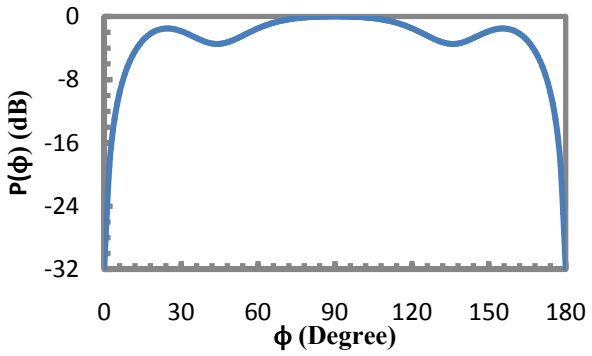

Fig. 3. Far field pattern of an axial slot on a dielectric coated conducting circular cylinder embedded in ground plane (($\theta = 180^{0}$, $a = 0.51\ \lambda$, $b = 0.63\ \lambda$, $2\alpha = 10^{0}$, $\phi_0 = 90^{0}$, $\varepsilon_r = 3.1$, and $\mu_r = 1$)

Figure 4, shows the antenna gain versus the dielectric thickness. The results obtained from the present formulation are compared with the corresponding results in [12], where an excellent agreement is noticed. Aperture conductance is also compared with same example presented in [12]. Our results showed in Fig. 5 are in typical agreement with the corresponding ones in [12].

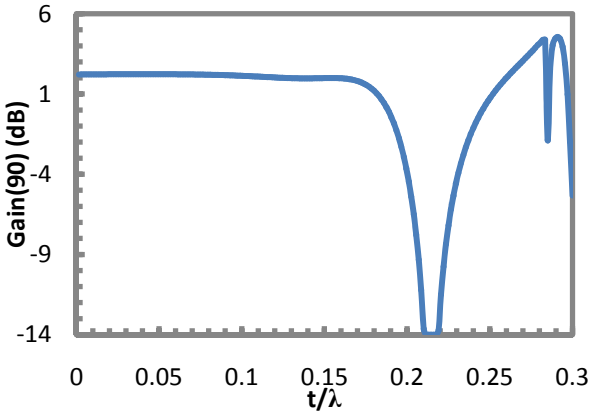

Fig. 4. Gain at 90^{0} of an axial slot on a dielectric coated conducting circular cylinder embedded in ground plane ($\theta = 180^{0}$, $a = 0.51\ \lambda$, $b = 0.63\ \lambda$, $2\alpha = 10^{0}$, $\phi_0 = 90^{0}$, $\varepsilon_r = 3.1$, and $\mu_r = 1$).

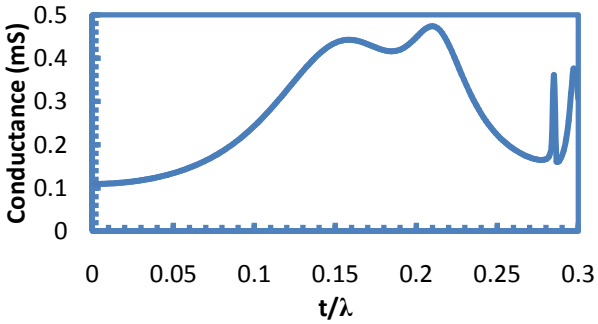

Fig. 5. Aperture conductance of an axial slot on a dielectric coated conducting circular cylinder embedded in ground plane ($\theta = 180^{0}$, $a = 0.51\ \lambda$, $b = 0.63\ \lambda$, $2\alpha = 10^{0}$, $\phi_0 = 90^{0}$, $\varepsilon_r = 3.1$, and $\mu_r = 1$).

In the following examples the corner reflector angle is considered as $\theta = 90^{0}$. In Fig. 6, the far field pattern corresponding to different values of dielectric coating are presented. As can be seen from Fig. 6, as the coating radius increases, the main beam gets narrower and side lobes starts to appear.

Another case is also presented in Fig. 7 for the far field patterns due to different dielectric thicknesses. A similar behavior is noticed in which the main beam gets narrower as the dielectric thickness increases. Increasing the dielectric thickness more creates side lobes.

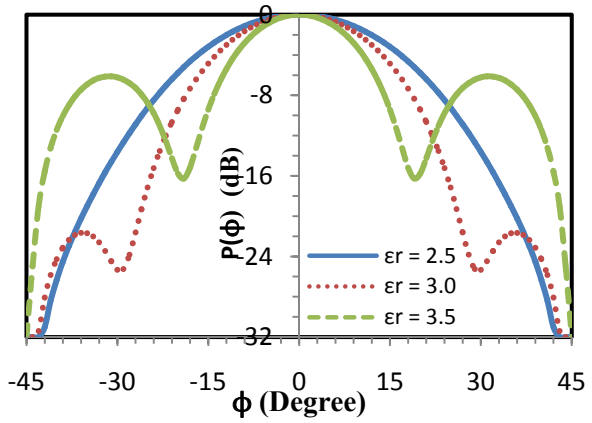

Fig. 6. Far field pattern of an axial slot on a dielectric coated conducting circular cylinder embedded in conducting corner ($\theta = 90^0$, a = 0.51 λ, b = 0.72 λ, $2\alpha = 10^0$, $\phi_0 = 0^0$, and $\mu_r = 1$).

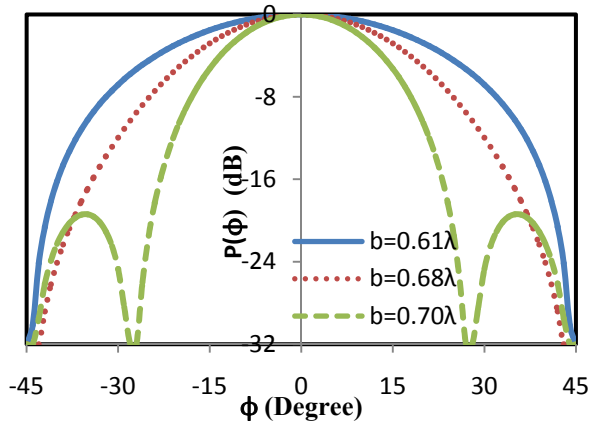

Fig. 7. Far field pattern of an axial slot on a dielectric coated conducting circular cylinder embedded in conducting corner ($\theta = 90^0$, a = 0.51 λ, $2\alpha = 10^0$, $\varepsilon_r = 3.6$, $\phi_0 = 0^0$, and $\mu_r = 1$).

The antenna gain at $\phi = 45^0$ versus the dielectric coating thickness for different dielectric permittivity is illustrated in Fig. 8. As one can see from Fig. 8, the gain at 45^0 angle, decreases as the dielectric permittivity increases. In addition, the higher the dielectric permittivity, the lower is the dielectric thickness before the gain drops.

Finally the aperture conductance at different dielectric permittivity versus dielectric thickness is shown in Fig. 9. It is noticed that the peak of the conductance occurs at lower thickness as the dielectric permittivity increases.

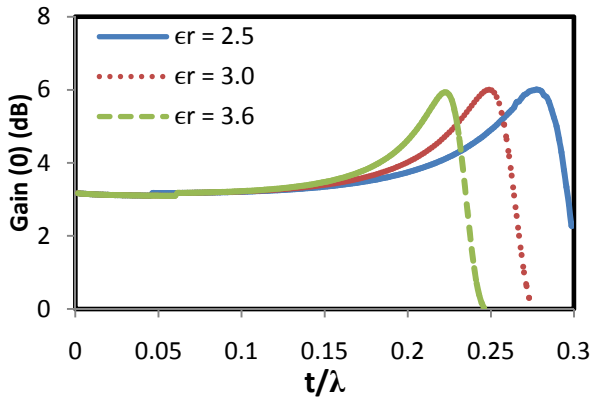

Fig. 8. Gain at 0^0 of an axial slot on a dielectric coated conducting circular cylinder embedded in conducting corner ($\theta = 90^0$, a = 0.45 λ, $2\alpha = 10^0$, $\phi_0 = 0^0$, and $\mu_r = 1$).

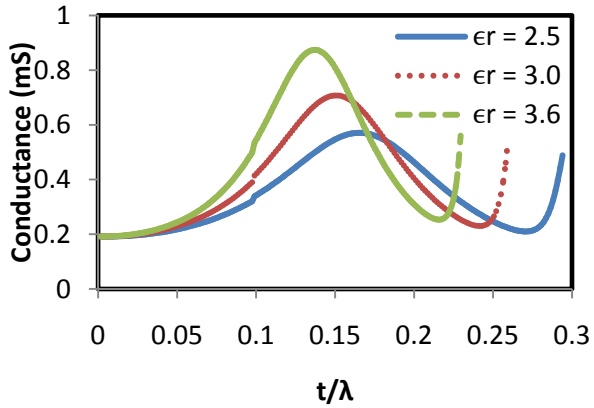

Fig. 9. Aperture conductance of an axial slot on a dielectric coated conducting circular cylinder embedded in conducting corner ($\theta = 90^0$, a = 0.45 λ, $2\alpha = 10^0$, $\phi_0 = 0^0$, and $\mu_r = 1$).

V. CONCLUSUON

New design of a corner reflector antenna, fed through a dielectric coated slotted cylinder was analyzed. The radiation pattern, aperture conductance and antenna gain was calculated. The study showed that for a constant gain at the bi-sector angle, the dielectric thickness decreases as the dielectric permittivity increases. Also the maximum conductance occurs at lower dielectric thickness as permittivity increases.

REFERENCES

[1] J. R. Wait, "On the theory of an antenna with an infinite corner reflector," *Canadian Journal of Physics*, vol. 32, pp. 365, 1954.

[2] A. C. Willson and H. V. Cottony, "Radiation pattern of finite size corner reflector antenna," *IRE Trans. Antennas and Propag.*, vol. 8, pp. 144-148, 1960.

[3] H. A. Ragheb, A. Z. Elsherbeni, and M. Hamid, "Radiation characteristics of the corner array," *Int. Journal of Electronics*, vol. 60, pp. 229-238, 1986.

[4] S. Sensiper, "Cylindrical radio waves," *IRE Trans. Antennas and Propag.*, vol. 5, pp. 56-70, 1957.

[5] C. H. Papas, "Radiation from a transverse slot in an infinite cylinder," *J. of Mathematics and Phys.*, vol. XXVII, pp. 227-236, 1949.

[6] S. Silver and W. K. Saunders, "The radiation from transverse rectangular slot in a circular cylinder," *J. of Appl. Phys.*, vol. 21, pp. 153-158, Feb. 1950.

[7] L. L. Bailin, "Radiation field produced by a slot in a large circular cylinder," *IRE Trans. Antennas and Propag.*, vol. 3, pp. 128-137, 1955.

[8] J. Wait and S. Kahana, "Radiation from a slot in a cylindrically tipped wedge," *Canadian Journal of Phys.*, vol. 32, pp. 714-721, 1954.

[9] H. Ragheb, A. Sebak, and L. Shafai, "Radiation from an axial slot on a conducting circular cylinder with reflector wings," *J. of Electromagnetic Waves and Appl.*, vol. 11, pp. 65-76, 1997.

[10] J. Richmond, "Axial slot antenna on dielectric-coated elliptic cylinder," *IEEE Trans. Antennas and Propag.*, vol. 37, pp. 1235-1241, Oct. 1989.

[11] J. A. Romo, I. F. Anitzine, and J. Garate, "Optimized design of cylindrical corner reflectors for applications on TV broadband antennas," *Applied Computational Electromagnetics Society (ACES) Journal*, vol. 26, no. 11, pp. 937-944, Nov. 2011.

[12] H. A. Ragheb and U. M. Johar, "Radiation characteristics of an infinite dielectric-coated axially slotted cylindrical antenna partly embedded in a ground plane," *IEEE Trans. Antennas and Propag.*, vol. 46, no. 10, pp. 1542-1547, Oct. 1998.

Hassan Ragheb was born in Port-Said, Egypt, in 1953. He received the B.Sc. degree in Electrical Engineering from Cairo University, Egypt in 1977 and the M.Sc. and Ph.D. degrees in Electrical Engineering from the University of Manitoba, Winnipeg, Canada in 1984 and 1987, respectively. From 1987 to 1989, he was a research assistant in the Department of Electrical Engineering, University of Manitoba. In 1989, he joined the Department of Electrical Engineering at the King Fahd University of Petroleum and Minerals, where he is now a Professor of Electrical Engineering. His research interests include electromagnetic scattering by multiple and coated objects, micro strip antennas, phased arrays, slot and open ended waveguide antennas.

A Novel Compact High-Gain Printed Quasi-Yagi Antenna and its Harmonic-Suppression Array

Lei Zhong, Jing-Song Hong, and Hong-Cheng Zhou

School of Physical Electronics
University of Electronic Science and Technology of China, Chengdu, China, 610054
albertzhonglei@163.com

Abstract ─ In this paper, a novel compact printed quasi-Yagi antenna with a high gain of 8.39 dB is presented, and its binary antenna array with harmonic suppression is explored. The proposed antenna fed by a 100 Ohm coplanar stripline (CPS) achieves a 14.32 % relative bandwidth for a -10 dB reflection coefficient. The stepped impedance resonator (SIR) structure is adopted to suppress the harmonic radiations in the binary array, which is fed by a 50 Ohm coplanar waveguide (CPW). Due to its single-sided structure, this high gain antenna element and the binary array have many advantages, such as easy fabrication, compactness, low profile, and low cost. The antenna and array can be widely applied in wireless communication systems, especially in wireless power transmission (WPT) system.

Index Terms - Binary array, compact high-gain antenna, harmonic suppression, and Quasi-Yagi antenna.

I. INTRODUCTION

Wireless power transmission via microwave has attracted significant attention in the past [1]. The rectenna is a key component in WPT and has been used to provide direct current (DC) power for radio frequency identification (RFID) tags, wireless sensor servers, and clock batteries [2]. Generally, a typical rectenna consists of an antenna to collect incoming RF power, a matching circuit, an input low-pass filter (LPF) to suppress unwanted higher harmonics generated by the rectifying diode, one or more rectifying diodes, an output DC pass filter, and a resistive load. However, the input LPF could be saved by the antenna with harmonic suppression, which also decreases the rectenna size and cost. Thus a high gain antenna with harmonic suppression is essential to improve the performance of rectenna and the total conversion efficiency of WPT.

Yagi-Uda antenna is a widely used high gain antenna with end fire radiation, which consists of a reflector, a driven element, and one or more directors. In recent years, printed quasi-Yagi antenna has been exhaustively analyzed and experimentally researched. According to the driven element form, the existing quasi-Yagi antenna can be divided into microstrip patch form [3, 4], double-sided dipole form [5, 6] and single-sided dipole form [7, 8]. The microstrip patch form is usually fed by a coaxial probe [9], while the double-sided dipole form often adopts a truncated ground plane as a reflector whose length could not be well optimized. The single-sided form is mostly fed by a CPS [8] or coplanar waveguide (CPW) [10], which is easy-fabricated and does not need a large ground plane on the other side of substrate.

In this paper, we present not only the design and measurements of a high gain and compact printed quasi-Yagi antenna element, but also the design and simulation of its binary antenna array. Since a 50 Ohm CPW line can be achieved directly by paralleling two 100 Ohm CPS lines together, the proposed antenna is fed by a 100 Ohm CPS, which aims to build a CPW-fed two-element antenna array in the next step. The antenna achieves a high gain of 7.96 dB, a 9.6 dB front-to-back ratio, efficiency of 85.1 % at 5.8 GHz, and a 14.32 % relative bandwidth for a -10 dB reflection coefficient. The binary array has maximum gain of 12.1 dB at 5.8 GHz and

Submitted On: July 16, 2012
Accepted On: Dec. 26, 2012

suppresses the harmonics very well. This compact antenna and its array are simply fabricated and easily integrated with other solid-state components in WPT system.

II. ANTENNA ELEMENT DESIGN

Figure 1 shows the schematic diagram of the high gain and compact printed quasi-Yagi antenna. The antenna utilizes five director elements and one reflector in order to maximize beam directivity, and is printed on a 0.5 mm thick Rogers RO4003C substrate (permittivity ε_r = 3.38, loss tangent tanδ = 0.0027). Both the convenience of constructing a feed network for antenna array and the high characteristic impedance of the CPS prompt us to use a 100 Ohm CPS as feed line. The gap of the CPS is 0.2 mm considering the resolution of the etching process. The driven element is a wide printed half wavelength dipole antenna.

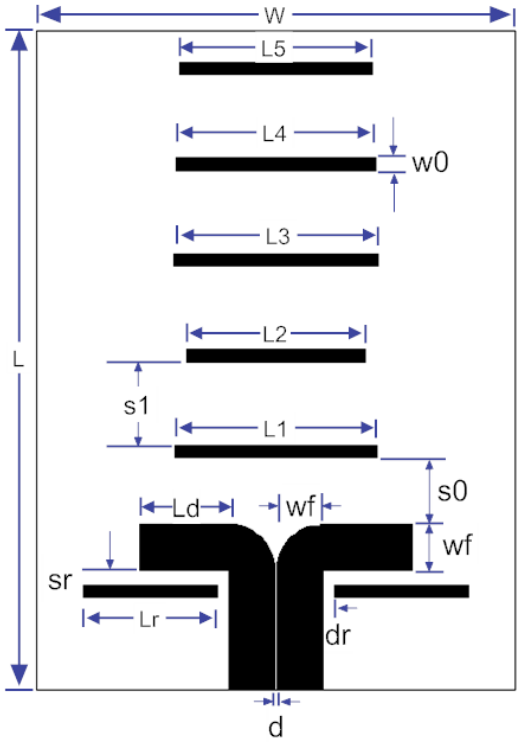

Fig. 1. Schematic diagram of the proposed quasi-Yagi antenna.

A pair of symmetrical reflector is placed under the dipole. Five directors are placed above the dipole. And the spacing between every two adjacent directors is the same. Additionally, the width of the reflector and directors is identical.

It is important to note that the reflectors are placed very close to the driven element in the proposed antenna. The traditional distance between the reflector and the driven element is 0.15λ~0.25λ, where λ is the wavelength of operating frequency. The wavelength can be calculated by,

$$\lambda_g = \frac{\lambda_0}{\sqrt{\varepsilon_{reff}}} \tag{1}$$

where λ_0 is the wavelength in vacuum and ε_{reff} is the effective dielectric constant, which can be calculated by

$$\varepsilon_{reff} = 1 + \frac{\varepsilon_r - 1}{2} \cdot \frac{K(k')}{K(k)} \cdot \frac{K(k_1)}{K(k_1')} . \tag{2}$$

The detailed derivation is introduced in [8], thus we can obtain the values of ε_{reff} and λ_g at 5.8 GHz, which are 1.43 and 43.29 mm, respectively. The optimized distance between the reflector and the driven element in our proposed antenna is only 0.03 λ (1.3 mm), which is much smaller than the traditional one. Furthermore, when compared with the reflector of the truncated ground plane, the utilization of a pair of independent reflectors behind the driven dipole not only enhances the pattern performance but also provides more design flexibility. The proposed antenna is simulated by the transient solver in CST Microwave Studio. The optimized parameters are given in Table 1.

Table 1: Design parameters of the optimized antenna.

Parameter	Value (mm)	Parameter	Value (mm)
L	55	s0	5.6
W	40	s1	7
wf	3.8	L1	16.9
d	0.2	L2	15
Ld	7.5	L3	17
Lr	11.2	L4	16.7
dr	1	L5	16.2
sr	1.3	w0	1

III. SIMULATED AND MEASURED RESULTS OF ANTENNA ELEMENT

The simulated and measured S_{11} (dB) results of the proposed antenna are shown in Fig. 2. The antenna was measured by using the Agilent E8363C network analyzer.

As shown in Fig. 2, the measured -10 dB impedance bandwidth is 5.25 GHz - 6.06 GHz (relative bandwidth 14.32%). The simulated bandwidth is 5.08 GHz - 6.02 GHz (relative bandwidth 16.94 %). The measured results agree well with the simulated results generally.

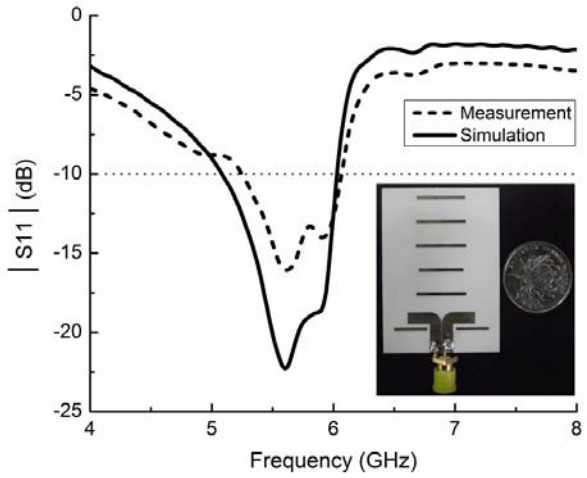

Fig. 2. Simulated and measured reflection coefficient magnitude of the proposed antenna.

The radiation patterns at 5.8 GHz for the E-plane and H-plane are shown in Figs. 3 and 4, respectively. A good agreement is observed between the simulated and measured results, for both the E- and H-plane patterns. The measured half power beam width (HPBW) is 46.7 degree along the E-plane and 57.4 degree along the H-plane.

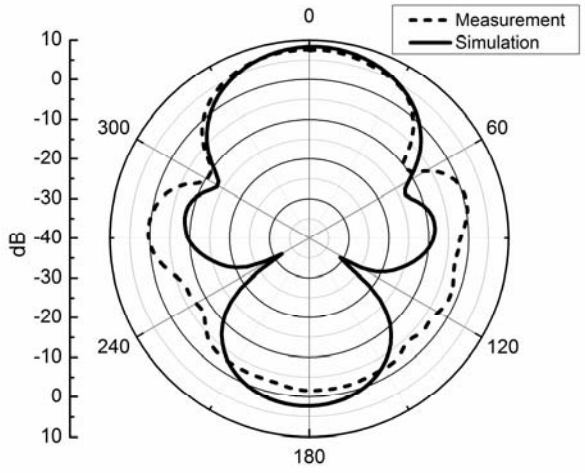

Fig. 3. Simulated and measured E-plane of the proposed antenna at 5.8 GHz.

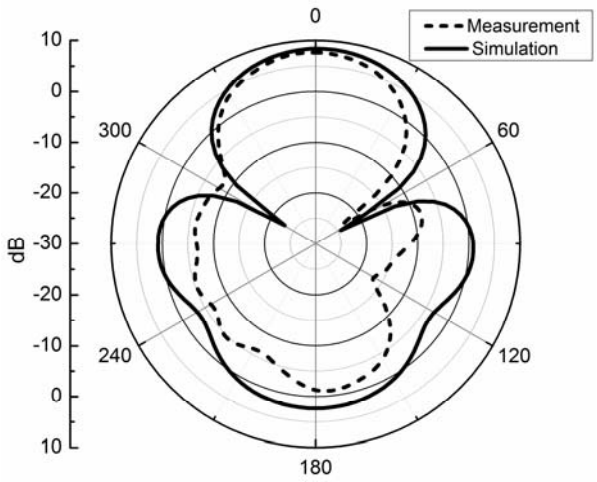

Fig. 4. Simulated and measured H-plane of the proposed antenna at 5.8 GHz.

Figure 5 illustrates the simulated and measured peak gain of the proposed antenna. The measured maximal absolute peak gain value in the main beam is 8.39 dB at 6 GHz, while the simulated value is 9.38 dB. At 5.8 GHz, the measured gain is 7.96 dB, which is approximately 2 dB higher than the results in [8]. Additionally, the gain varies much against frequency.

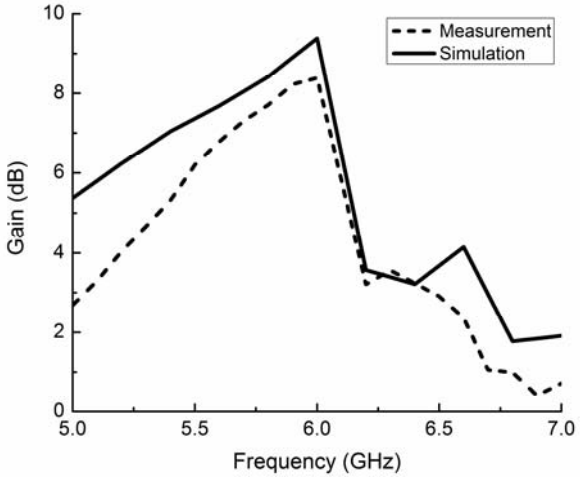

Fig. 5. Simulated and measured peak gain variation against frequency for the proposed antenna.

IV. DESIGN AND SIMULATION OF THE BINARY ARRAY

From the sections above, the compact quasi-Yagi antenna element can achieve a high gain of

7.96 dB at 5.8 GHz. To improve the gain, we can build a 50 Ohm CPW-fed two-element antenna array. A branch structure is adopted as the power divider for antenna feeding, in which a 50 Ohm CPW line is divided into two 100 Ohm CPS lines. However, due to the symmetry of the branch structure, the output signals are equal in magnitude but have a phase difference of 180 degrees. Therefore, a half wavelength CPS line is added to the right arm of the branch structure to ensure the same phase of the output signals.

We used the SIR structure on the ground of CPW line to suppress the harmonics. The analysis of the SIR can be found in [12]. Figure 6 shows the schematic diagram of the binary quasi-Yagi antenna array, which is simulated by the transient solver in CST Microwave Studio. The optimized parameters of the binary array are given in Table 2.

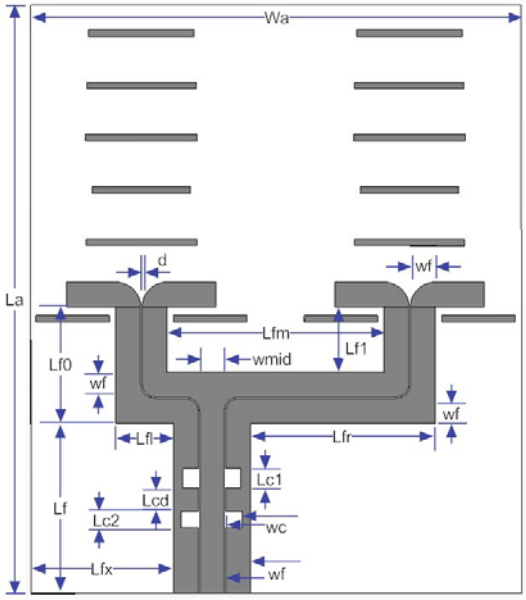

Fig. 6. Schematic diagram of the binary quasi-Yagi antenna array.

Table 2: Design parameters of the optimized array.

Parameter	Value (mm)	Parameter	Value (mm)
La	90	Lfm	33.2
Wa	75	Lfl	8.8
wf	3.8	Lfr	28.3
d	0.2	Lc1	3
Lf0	17.8	Lc2	2.6
Lf1	10	Lcd	3.5
Lf	26	wc	2.6
Lfx	21.8	wmid	33.2

As shown in Fig. 7, the simulated -10 dB impedance bandwidth is 5.12 GHz - 6.05 GHz (relative bandwidth 16.65%). The reflection coefficient on the second harmonic (11.6 GHz) is -0.45 dB and the reflection coefficient on the third harmonic (17.4 GHz) is -0.97 dB, which means that the radiations at the harmonic frequencies are well suppressed.

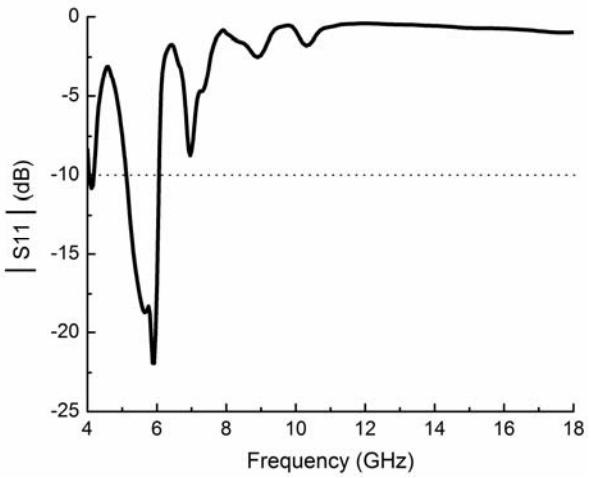

Fig. 7. Simulated reflection coefficient magnitude of the antenna array.

Figure 8 illustrates the simulated E-plane and H-plane at 5.8 GHz. The HPBW was 30.2 degree along the E-plane and 55.9 degree along the H-plane. Compared with the quasi-Yagi antenna element, the HPBW of the binary array in the E-plane is reduced by 16.5 degrees, while the HPBW in H-plane decreases only 1.5 degrees. The simulated peak gain at 5.8 GHz is 12.1 dB, which is 4.14 dB higher than the measured gain of single antenna element. The side lobe level is -10.5 dB in the E-plane and -7.2 dB in the H-plane.

V. CONCLUSION

This paper presents a novel compact printed quasi-Yagi antenna with a high gain of 8.39 dB. The proposed antenna also offers flexibility in designing reflector, instead of employing a truncated ground plane. Furthermore, the very small distance between the reflector and the driven element guarantees a compact structure. The binary array based on the proposed antenna is designed and simulated, which has high gain of 12.1 dB at 5.8 GHz. To have suppression at both the second and third harmonic frequencies, the

SIR structure is adopted. This high gain antenna and its array have advantages of easy fabrication, compactness, low profile and low cost, owing to its single-sided structure. Therefore, they can be widely applied in wireless communication systems, especially in WPT system.

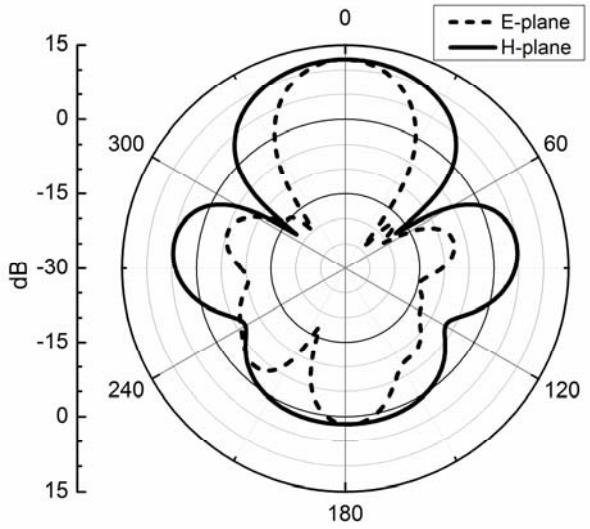

Fig. 8. Simulated E- and H-planes of the antenna array at 5.8 GHz.

ACKNOWLEDGMENT

This work was supported partially by the National Science Foundation of China (No. 60872029 and No. 60872034), partially by the High-Tech Research and Development Program of China (No. 2008AA01Z206), partially by the Aeronautics Foundation of China (No. 2010018003), and partially by the Fundamental Research Founds for the Central Universities (No. ZYGX 2009J037).

REFERENCES

[1] J. O. McSpadden and J. C. Mankins, "Space solar power programs and microwave wireless power transmission technology," *IEEE Micro*., vol. 3, no. 4, pp. 46-57, Dec. 2002.

[2] M. Ali, G. Yang, and R. Dougal, "A new circularly polarized rectenna for wireless power transmission and data communication," *IEEE Antennas Wireless Propag. Lett.*, vol. 4, pp. 205-208, 2005.

[3] H. -D. Lu, L. -M. Si, and Y. Liu, "Compact planar microstrip-fed quasi-Yagi antenna," *Electron. Lett.*, vol. 48, no. 3, pp. 140-141, Feb. 2012.

[4] G. R. DeJean, "Quasi-endfire antenna array for beam steering applications," *24th Annual Review of Progress in Applied Computational Electromagnetics (ACES)*, pp. 656-659, Niagara Falls, Canada , March 30 - April 4, 2008.

[5] R. A. Alhalabi, Y. -C. Chiou, and G. M. Rebeiz, "Self-shielded high-efficiency Yagi-Uda antennas for 60 GHz communications," *IEEE Trans. Antennas Propag.*, vol. 59, no. 3, pp. 742-750, Mar. 2011.

[6] P. Hsu and S. Chen, "Broadband microstrip-fed modified quasi-Yagi antenna", *2005 IEEE/ACES International Conference on Wireless Communications and Applied Computational Electromagnetics*, April 2005.

[7] H. Min, S. Arvas, W. Penn, and E. Arvas, "An X-band array of quasi-Yagi microstrip antennas", *24th Annual Review of Progress in Applied Computational Electromagnetics (ACES)*, pp. 738-743, Niagara Falls, Canada, March 30-April 4, 2008.

[8] Y. Park, H. Choo, and I. Park, "Broadband CPS-fed Yagi-Uda antenna," *Electron. Lett.*, vol. 45, no. 24, pp. 1207-1209, Nov. 2009.

[9] D. Yihan and Z. Xiaoying, "A novel microstrip Yagi antenna with tunable radiation pattern and central frequency," *IMWS-IRFPT,* pp. 1-2, Aug. 2011.

[10] Y. Ding, Y. C. Jiao, P. Fei, B. Li, and Q. T. Zhang, "Design of a multiband Quasi-Yagi-type antenna with CPW-to-CPS transition," *IEEE Antennas Wireless Propag. Lett.*, vol. 10, pp. 1120-1123, 2011.

[11] K. C. Gupta, R. Garg, and I. Bahl, *Microstrip Lines and Slotlines*, 2nd Ed., Massachusetts: Artech House, ch.7, 1996.

[12] Y. Zhao, L. Zhong, J. S. Hong, and G. M. Zhang, "A monopole antenna with SIR ground for harmonic suppression and bandwidth enhancement", *ACES Journal*, vol. 26, no. 8, pp. 705-708, Aug. 2011.

Harmonics Amplitude Measurement in UHF Band by Multi Harmonic Multiplication

A. Naserialiabadi, Gh. Moradi, A. Kheirdoost, and R. Sarraf Shirazi

Department of Electrical Engineering,
Amirkabir University of Technology, Tehran, 15914, Iran
naserialiabadi@aut.ac.ir, ghmoradi@aut.ac.ir, kheirdoost@aut.ac.ir, and sarraf@ aut.ac.ir

Abstract ─ Analysis of a system to measure the amplitude of harmonics of a signal in UHF band is presented. First, analytical considerations are proposed, in which multi harmonic signal is used as local oscillator signal. The results are used to obtain optimal implementation by which conversion loss of mixer becomes minimal. The proposed method is implemented by single diode mixer. In mixer, harmonics of the desired signal to be measured are fed into RF port and a comb signal is synthesized to be fed into LO port to down convert the desired signal. Bottle neck is the amplitude of each harmonic in comb signal fed in LO port of mixer. The proposed design is validated and optimized by ADS (a full wave electromagnetic simulator). Optimization of conversion loss of the mixer boots the system bandwidth.

Index Terms - Conversion loss, harmonics amplitude, and single diode mixer.

I. INTRODUCTION

Nowadays, spectrum analyzers are widely used to determine frequency contents of signals. These instruments are available in wide range of frequency and dynamic range. The overall method is to down convert the signal and determine its frequency content by digital signal processing. The signal which we intend to determine its frequency content is fed into a mixer and frequency of local oscillators is swept to ensure that all signal frequency content is down converted to frequency range that digital processing block works [1]. The behavioral modeling of RF and microwave amplifiers has attracted a great deal of attention [2, 3]. One method for accurate characterization of nonlinear RF and microwave devices involves use of time domain measurements [4, 5]. Various methods differ in DUT stimulating, methods of analyzing transmitted and reflected waves and also in models they provide. Behavioral modeling includes measurement of voltage and current waveforms in nonlinear regime, which are full of harmonics. LSNAs and NVNAs are two powerful devices for these measurements [6-8]. In recent years, X-parameters are defined for nonlinear modeling and design; these parameters could be measured by NVNAs [9, 10]. Time domain method proposed in [5] includes multi harmonic signal for driving the mixer. Like all other methods, the system in [5] utilizes a down convertor. We analyze mixer operation to obtain minimum conversion loss of mixer for multi harmonic signals. The problem we consider is that we have a single tone signal with its harmonics and we want to measure the amplitude of harmonics. It is assumed that frequency of fundamental tone is known. The following method, which is described in part II, is faster than measurement by spectrum analyzer, since it down converts harmonics simultaneously, not one by one, as the method used in spectrum analyzer (it sweeps frequency of local oscillator to down converts RF signal). It is also supposed that an attenuator is used to make small signal in RF port of the mixer. First we describe the method and then mixer consideration will be proposed.

II. METHODOLOGY

The signal whose frequency contents are to be determined is expressed as,

Submitted On: July 2, 2012
Accepted On: Nov. 23, 2012

$$RF(t) \triangleq \sum_{n=1}^{k} A_n \cos(n\omega_{RF}t + \alpha_n). \quad (1)$$

The LO signal used to down convert the RF signal expressed in equation (1) is given by,

$$LO(t) \triangleq \sum_{m=1}^{k} B_m \cos(m\omega_{Lo}t + \beta_m) \quad (2)$$

in which,

$$\omega_{LO} - \omega_{RF} \triangleq \omega_{IF}. \quad (3)$$

As mentioned before, ω_{RF} is known and ω_{LO} is chosen such that,

$$\frac{\omega_{IF}}{\omega_{LO}} \ll 1 \quad , \quad \frac{\omega_{IF}}{\omega_{RF}} \ll 1 \quad (4)$$

in which f_{RF} is in UHF band. We choose f_{IF} = 10 MHz, so in UHF band we have

$$\frac{\omega_{IF}}{\omega_{RF}} \le \frac{10}{300} \ll 1. \quad (5)$$

Multiplying equations (1) and (2) gives

$$RF(t) \times LO(t) = \left(\sum_{n=1}^{k} A_n \cos(n\omega_{RF}t + \alpha_n) \right) \times \left(\sum_{m=1}^{k} B_m \cos(m\omega_{Lo}t + \beta_m) \right)$$

$$= \sum_{n=1}^{k}\sum_{m=1}^{k} A_n B_m \cos(n\omega_{RF}t + \alpha_n)\cos(m\omega_{Lo}t + \beta_m)$$

$$= \sum_{n=1}^{k}\sum_{m=1}^{k} \frac{A_n B_m}{2} \begin{pmatrix} \cos(n\omega_{RF}t + \alpha_n + m\omega_{Lo}t + \beta_m) + \\ \cos(n\omega_{RF}t + \alpha_n - m\omega_{Lo}t - \beta_m) \end{pmatrix}. \quad (6)$$

Considering equation (4), the low frequency content of equation (6) is,

$$IF(t) = \sum_{m=1}^{k} \frac{A_m B_m}{2} \cos(m\omega_{IF}t + \alpha_m - \beta_m). \quad (7)$$

The maximum frequency content of equation (7) is kf_{IF}. Since we synthesize LO signal, B_m is known. If we detect equation (7), A_m, the amplitude to be measured, could be determined since B_m is known.

III. MIXER CONSIDERATION

As observed in Fig.1, in order to multiply equation (1) by equation (2), these signals should be fed to RF and LO ports of a mixer.

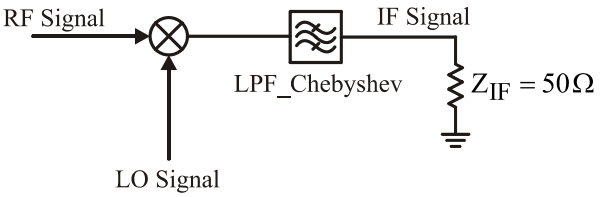

Fig. 1. Diagram of RF, LO, and IF ports.

In usual applications, a single tone LO signal is used in down converter mixers. But we want to multiply two multi harmonic signals. If single tone LO signal is fed to an LO port, the nonlinear element (i.e., here diode) produces harmonics of this tone and frequencies, which are linear combinations of f_{LO} and f_{RF}. These frequencies include desired IF frequencies, but conversion losses of harmonics of RF signal will be so large that result in the decrease of the level of IF signal to noise level. Since it is supposed that RF signal is small signal made by an attenuator, large conversion loss can decrease the level of IF signal to noise level. Let us consider on-off model for diode. So its conductance waveform is

$$g(t) = \begin{cases} g_{on} & \text{LO signal} > 0 \\ 0 & \text{LO signal} \le 0 \end{cases}. \quad (8)$$

The diode current is $i(t) = g(t)\ RF(t)$. If LO signal includes only f_{LO}, the fundamental tone of LO signal, then $g(t)$ does not include even harmonics of f_{LO} [11]. Therefore, even harmonics of RF signal will not be down converted and conversion losses for even harmonics of RF signal will be infinite. Then it should be investigated whether or not LO signal includes harmonics of f_{LO}. We choose LO signal to have first and second harmonics and the calculate conversion losses of RF harmonics. In this case, LO signal is given by

$$LO(t) = a\cos(\omega_{LO}t) + b\cos(2\omega_{LO}t), \quad (9)$$

in which a and b are amplitudes with positive values. According to equation (8), $g(t)$ is

$$g(t) = \begin{cases} g_{on} & a\cos(\omega_{LO}t) + b\cos(2\omega_{LO}t) > 0 \\ 0 & a\cos(\omega_{LO}t) + b\cos(2\omega_{LO}t) \le 0. \end{cases} \quad (10)$$

The Fourier series representation of $g(t)$ derived by finding the roots of LO(t) is given in equation (11). Conversion losses variations for the first to sixth harmonics of RF signal, as a function of c, are depicted in Fig. 2.

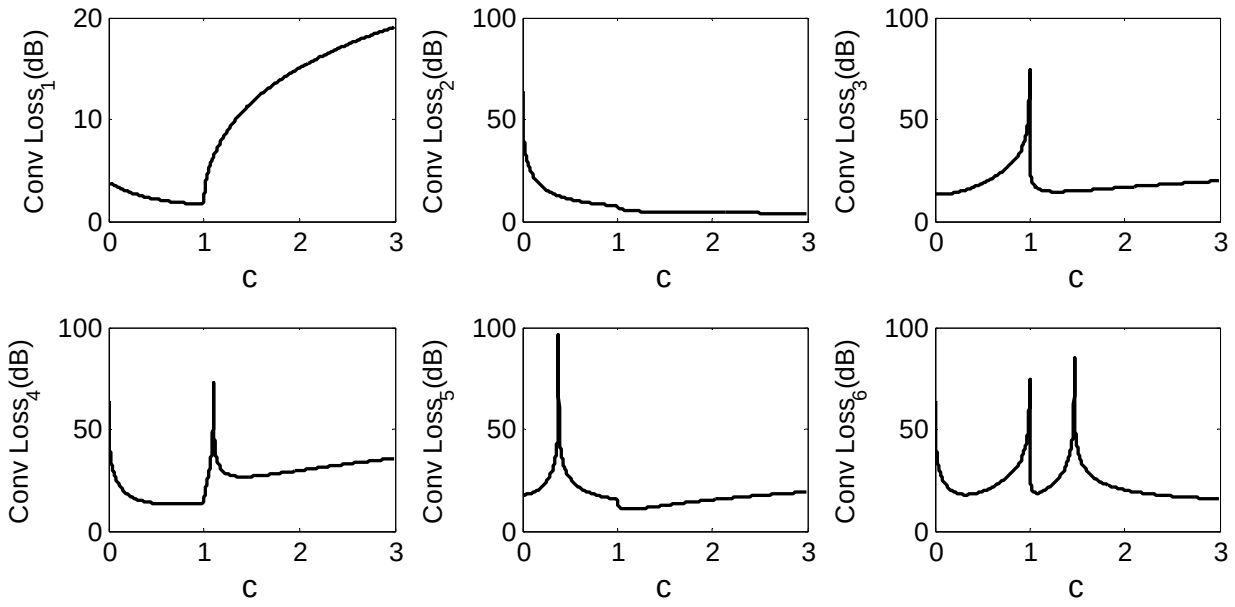

Fig. 2. Conversion losses of the first to sixth harmonics of the RF signal. *Conv Loss*$_m$ is the conversion loss of the mth harmonic.

$$\frac{b}{a}\le 1 \;\rightarrow\; \mathrm{g(t)}=\mathrm{g}_{on}\frac{\cos^{-1}(B)}{\pi}+$$
$$\mathrm{g}_{on}\sum_{n=1}^{\infty}\frac{2}{n\pi}\sin(n\cos^{-1}(B))\cos(n\omega_{LO}t)$$
$$\frac{b}{a}>1 \;\rightarrow\; \mathrm{g(t)}=\mathrm{g}_{on}\frac{\cos^{-1}(B)+\cos^{-1}(-A)}{\pi}+$$
$$\mathrm{g}_{on}\sum_{n=1}^{\infty}\frac{2}{n\pi}\left(\sin(n\cos^{-1}(B))-\sin(n\cos^{-1}(A))\right)\cos(n\omega_{LO}t)$$
$$\text{where } A=\frac{-1-\sqrt{1+8c^2}}{4c}\quad B=\frac{-1+\sqrt{1+8c^2}}{4c}\quad ,\ c=\frac{b}{a}\ . \tag{11}$$

As shown in Fig. 2, the conversion losses of the third and higher harmonics are very large. Conversion losses of the first and second harmonics are depicted in Fig. 3. For $c \ge 1$, these conversion losses vary in opposite directions.

In [11] for the single tone LO signal and on-off model for diode, it is shown that the conversion loss is 3.92 dB. Now for the two harmonics, we see that the conversion losses change rapidly by varying c, which is relative amplitude of harmonics of LO signal. For c = 1.071 conversion losses of first and second harmonics are 5.72 dB, which is 1.8 dB more than the single tone case.

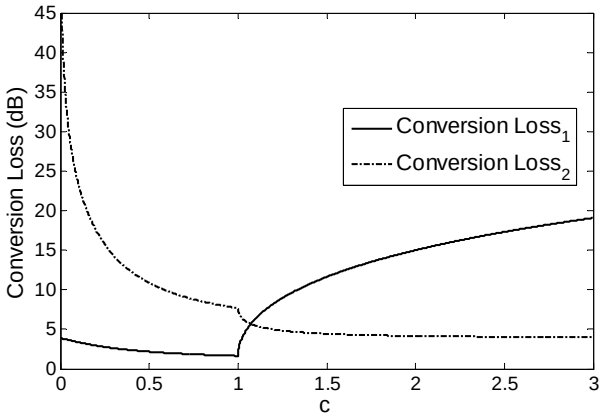

Fig. 3. The conversion losses of the first and second harmonics of the RF signal.

The LO signal includes first and third harmonics as shown,

$$LO(t)=a\cos(\omega_{LO}t)+b\cos(3\omega_{LO}t)\ . \tag{12}$$

The function $g(t)$ does not include even harmonics of f_{LO}, so even harmonics of RF signal will not be down converted. Therefore, conversion losses for even harmonics of RF signal will be infinite. Minimum conversion

losses for odd harmonics are 8.42 dB when b/a = 0.663. So conversion losses of the first and third harmonics that constitute LO signal are too smaller than other harmonics.

The LO signal which includes first and fourth harmonics is stated as,

$$LO(t) = a\cos(\omega_{LO}t) + b\cos(4\omega_{LO}t). \quad (13)$$

The minimum conversion losses of first to sixth harmonics of RF signal (by numerical calculation) are 6.72, 15.41, 21.15, 7.88, 18.69, and 15.17 dB, respectively, when b/a is 0.98. Conversion losses of first and fourth harmonics, that constitute LO signal, are too smaller than those of the other harmonics.

The LO signal which contains first three harmonics is given by,

$$LO(t) = a\cos(\omega_{LO}t) + b\cos(2\omega_{LO}t) + c\cos(3\omega_{LO}t) \quad (14)$$

in which a, b, and c are amplitudes (positive numbers). For this LO signal, the minimum conversion losses of first three harmonics are 6.83, 7, and 7.18 dB, respectively, when b/a is 1.4 and c/a is 1.1. The Fourier series of $g(t)$ is a complicated function of a, b, and c. So numerical calculation is carried out and it is concluded that conversion losses of fourth and higher harmonics are large. Conversion losses of fourth to sixth harmonics will be minimized subject to $b/a = 1.95$ and $c/a = 1.15$. By these values, conversion losses of first to sixth harmonics are 12.9, 5.88, 10.33, 11.78, 14.11, and 9.38 dB, respectively.

The LO signal which contains first to fourth harmonics can be described as,

$$LO(t) = a\cos(\omega_{LO}t) + b\cos(2\omega_{LO}t) + c\cos(3\omega_{LO}t) + d\cos(4\omega_{LO}t). \quad (15)$$

For this LO signal, minimum conversion losses of first to sixth harmonics are 11.09, 7.05, 8.49, 11.8, 9.54, and 12.43 dB, respectively when $b/a = 1.12$, $c/a = 1.14$ and $d/a = 0.1$.

Considering these results for conversion losses, it is concluded that to keep conversion losses of harmonics in RF signal minimum, LO signal should contain those harmonics too, and by more harmonics consideration, the minimum conversion losses will be larger.

IV. MIXER IMPLEMENTATION

In this section, a single diode mixer is used, which has the least complication to consider a multi harmonic signal as an LO signal. In single diode mixer, a multi section Wilkinson coupler in UHF band to mix RF and LO signal is used. HSMS 8101, which is a surface mount microwave Schottky mixer diode is used as Schottky diode to mix LO and RF signals. Resistor in IF section is set to 50 ohm (Z_IF = 50 ohm), which is the resistance of the digital processing block.

A common way to produce multi harmonic signal to make desired LO signal is to use comb generator, typically including step recovery diode (SRD). But amplitudes of harmonics in output signal of comb generators generally decrease or remain approximately constant by the increase of harmonic index; we have no control on the amplitude of the output harmonics. The power of different harmonics of an LO signal should be tuned to make the conversion losses of different harmonics of the RF signal minimum. Frequency multipliers with attenuators could be used to produce comb signal and control the power of harmonics.

A conversion Loss of the designed single diode mixer with a single tone RF signal and a single tone LO signal is 8.4 dB when the power of the LO signal is 8 dBm, it should be noted that 3 dB of this conversion loss is due to the coupler that dissipates half power of RF signal. If we fed the first two harmonics of LO signal in LO port and the first two harmonics of RF signal in RF port, then conversion loss_1 and conversion loss_2 will be so larger than 8.4 dB. Varying the power of LO harmonics changes the conversion losses of different harmonics. If conversion loss_1 decreases, conversion loss_2 increases and vice versa. For two harmonics of RF signal, the conversion $\text{loss}_{1,2} \approx 12$ dB can be reached and for the three harmonics of the RF signal we can reach conversion loss $_{1,2,3} \approx 14.75$ dB. The variations of conversion losses by an RF frequency for two and three harmonics are shown in Figs. 4 and 5. Simulations have been carried out by multi tone harmonic balance method in Advanced Design System (ADS) and genetic algorithm was used to optimize conversion losses. It should be noted that the 3dB conversion loss is due to the coupler (balanced mixer does not have this loss), and a 1 dB of conversion loss is due to the ohmic resistance of the diode, here we

have Rs = 6Ω. In IF port, amplitudes of IF harmonics are detected. Since we have the conversion loss of the mixer for different harmonics, we can determine the amplitude of RF harmonics. The results of part III and IV for the conversion losses are compared in Table 1.

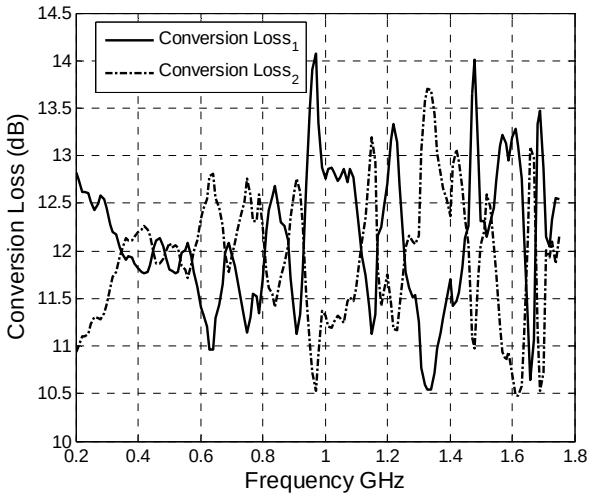

Fig. 4. Conversion losses of two harmonics of an RF signal. The power of the LO signal harmonics are 8 and 10.5 dBm, respectively.

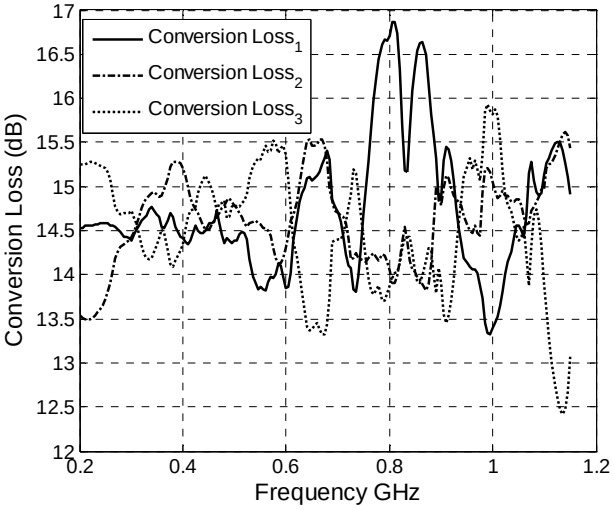

Fig. 5. Conversion losses of three harmonics of an RF signal. The power of the LO signal harmonics are -2.15, 4.6, and 4.6 dBm, respectively.

Table 1: Comparison of conversion losses.

Number of harmonics considered	2	3
Minimum conversion loss by ideal diode (dB)	5.72	~ 7
Minimum conversion loss by single diode mixer (dB)	~ 12	~ 14.75

V. CONCLUSION

A new approach to measure the harmonic's amplitude was introduced. Mixer considerations and limitations have been examined for ideal and real diode. Conversion losses of different harmonics were made minimum.

It was concluded that by more harmonics consideration, conversion loss will be larger. Additionally, using common comb generator causes large conversion losses since we have no control on amplitude and phase of different harmonics in comb signal. We optimized the power of the LO harmonics to obtain minimum conversion losses and as a result the dynamic range increased.

REFERENCES

[1] Application Note 150, *Agilent Spectrum Analysis Basics*, Agilent Technologies, Inc., Aug. 2006.

[2] J. Wood and D. E. Root, *Fundamentals of Nonlinear Behavioral Modeling for RF and Microwave Design*, Norwood, MA: Artech House, 2005.

[3] J. Wood, M. LeFevre, D. Runton, J. C. Nanan, B. H. Noori, and P. H. Aaen, "Envelope-domain time series (ET) behavioral model of a doherty RF power amplifier for system design," *IEEE Trans. Microwave Theory and Techniques*, vol. 54, no. 8, Aug. 2006.

[4] F. Macraigne, T. Reveyrand, G. Neveux, D. Barataud, J. M. Nebus, A. Soury, and E. N. Goya, "Time-domain envelope measurements for characterization and behavioral modeling of nonlinear devices with memory," *IEEE Trans. Microwave Theory and Techniques*, vol. 54, no. 8, Aug. 2006.

[5] D. Barataud, A. Mallet, M. Campovecchio, J. M. Nebus, J. P. Villotte, and J. Verspecht, "Measurements of time domain voltage/current waveforms at R.F. and microwave frequencies for the characterization of nonlinear devices," *Proc. IEEE Instrum. Meas. Technol. Conf.*, vol. 2, pp. 1006–1010, May 1998.

[6] W. V. Moer and Y. Rolain, "A large-signal network analyzer: Why is it needed?," *IEEE Microwave Mag.*, vol. 76, pp. 46-62, Dec. 2006.

[7] W. V. Moer and L. Gomme, "NVNA Versus LSNA: Enemies or Friends?," *IEEE Microwave Mag.*, vol. 11, no. 1, pp. 97–103, Feb. 2010.

[8] Application Note 1408-19, *High Power Amplifier Measurements Using Agilent's Nonlinear Vector Network Analyzer*, Agilent Technologies Inc., 26 Jan. 2010.

[9] J. Verspecht and D. E. Root "Poly harmonic distortion modeling," *IEEE Microwave Mag.*, vol. 7, no. 3, pp. 44-57, June 2006.

[10] Application Note 1408-22, *An Evaluation of X-parameter, P2D and S2D Models for Characterizing Nonlinear Behavior in Active Devices*, Agilent Technologies Inc., 29 Aug. 2011.

[11] R. Gilmore and L. Besser, *Practical RF Circuit Design for Modern Wireless Systems, Volume II , Active Circuits and Systems*, chapter 7, Artech House, 2003.

Miniaturized Wilkinson Power Divider with nth Harmonic Suppression using Front Coupled Tapered CMRC

Mohsen Hayati [1,2], Saeed Roshani [1,3], and Sobhan Roshani [1,3]

[1]Electrical Engineering Department, Faculty of Engineering
Razi University, Kermanshah, 67149, Iran
mohsen_hayati@yahoo.com

[2] Computational Intelligence Research Centre
Razi University, Kermanshah, 67149, Iran

[3] Department of Electrical Engineering
Islamic Azad University of Kermanshah, Kermanshah Branch, Kermanshah, Iran
roshany@ieee.org and sobhan_roshany@yahoo.ca

Abstract ─ In this paper, a novel microstrip power divider with a new technique for nth harmonic suppression is presented. This technique is based on using front coupled tapered compact microstrip resonant cell (FCTCMRC) that inserted into a quarter-wavelength transmission line of the conventional Wilkinson power divider. This cell is used to obtain high harmonic suppression. The proposed power divider not only impressively improves harmonic suppression, but also reduces the length of a quarter-wave line over 29.3 % as compared with the conventional power divider. From the measured results, the proposed structure achieved ultra wide stop-band bandwidth (6 GHz – 12 GHz) with a minimum attenuation level of 24 dB, while maintaining the characteristics of the conventional Wilkinson power divider. The input and output return losses at 2 GHz are 48 and 44 dB, respectively. The insertion loss is about 3.1 dB and better than 45 dB isolation is obtained.

Index Terms - Front coupled tapered compact microstrip resonant cell, harmonic suppression, miniaturization, and Wilkinson power divider.

I. INTRODUCTION

The power divider was first presented by J. Wilkinson in 1960 [1]. Power dividers are widely used in different microwave applications such as frequency multipliers, mixers, and power amplifiers [2]. The unwanted harmonics caused by nonlinear property of the active circuit should be removed. It will be cost-effective if the unwanted harmonics suppressed in the power divider or the combiner structure [3]. The conventional power divider consists of two quarter-wavelength transmission lines at the designed frequency that results in a large occupied area, especially at low frequencies. Thus, several methods have been proposed so far to design miniaturized harmonic suppressed power dividers with improved performance [3-7]. In [3] and [4] microstrip electromagnetic band-gap (EBG) structures have been applied to design power dividers. Thus, compact Wilkinson power dividers with harmonic suppression are realized due to the slow wave characteristics and band-stop of EBG. Power dividers with EBG cells have also reduced the occupied area. Furthermore, as defected ground structure (DGS) can provide the same properties as EBG, it has also been used to design compact power dividers with harmonic suppression. In [5] a miniaturized microstrip Wilkinson power divider based on standard PCB etching processes has been designed. It is composed of four microstrip high-low impedance resonator cells uniformly placed inside the Wilkinson power divider resulting in the high slow-wave effect. This power divider reduces the occupied area to 36.5 % of the conventional

Submitted On: Aug. 27, 2012
Accepted On: Nov. 25, 2012

one at 2.65 GHz. In [5] the third and fifth harmonic suppression levels are about 29 and 34 dB, respectively. Another power divider for the nth harmonic suppression has been presented that consists of two quarter-wavelength open stubs, which are located at the center of the quarter-wavelength branch-lines [6]. However, the physical dimensions of a power divider are proportional to the wavelength of the center frequency. A Wilkinson power divider with an asymmetric spiral defected ground structure (DGS) in a quarter-wave line for harmonic suppression has been demonstrated in [7]. Unfortunately, the major drawback of all works that have been referred above is that all of them need etching or back side processing or lumped reactive components.

In [8] and [9] the non-uniform transmission lines (NTLs) method has been used to reduce the circuit area and to suppress the harmonics of the fundamental frequency. However, in these works, obtaining harmonic suppression with high level of attenuation is still subject of discussion and challenge.

In this paper, the proposed power divider has very simple topology that only uses microstrip line and reduces the length of a quarter-wave line over 29.3 % as compared to the conventional divider at 2 GHz. Furthermore, it has an ultra wide stop-band bandwidth (6 GHz – 12 GHz) with a minimum attenuation level of 24 dB. This power divider suppresses the unwanted harmonics better than previous works without the need of backside etching or lumped reactive components.

II. CIRCUIT DESIGN

Figure 1 (a) shows the conventional Wilkinson power divider that consists of two quarter-wavelength transmission lines ($\sqrt{2}$ Z_0) and an isolation resistor (100 ohms). Figure 1(b) shows the schematic diagram of the proposed power divider, which consists of two FCTCMRC [10] that are placed within a quarter-wavelength transmission line of the conventional Wilkinson power divider. The aim of the inserted cells is to improve the performance of the power divider. The FCTCMRC acts as a low pass resonator that suppresses the unwanted harmonics.

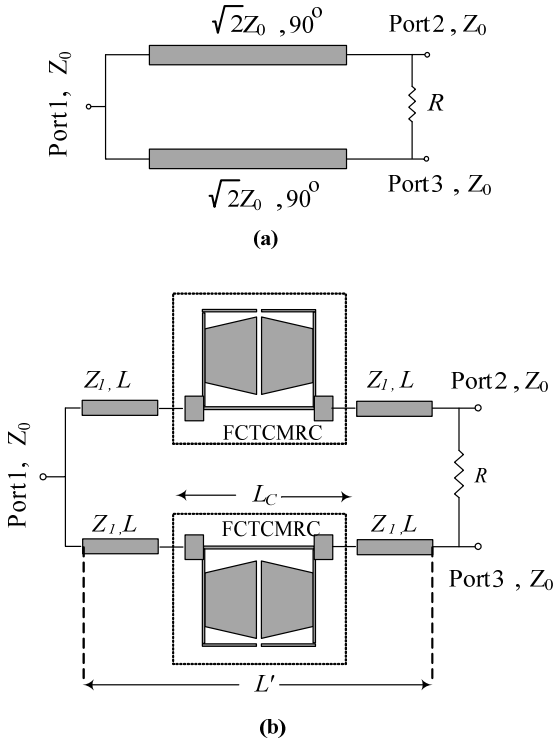

Fig. 1. Schematic diagram of the (a) conventional Wilkinson power divider and (b) proposed power divider using FCTCMRC.

Figure 2 demonstrates the FCTCMRC, which consists of two tapered cells, connected to the high impedance segment. They are essential blocks for harmonic suppression and stop-band improvement, because of their high capacitance and inductance properties.

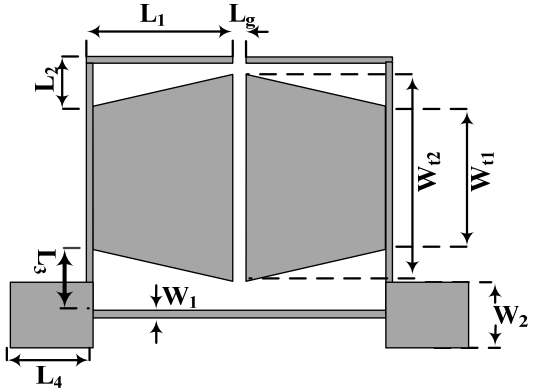

Fig. 2. Structure of the front coupled tapered CMRC.

The dimensions of FCTCMRC are obtained as follows: L_1 = 2.2 mm, L_2 = 0.75 mm, L_3 = 1.1 mm, L_4 = 1.1 mm, Lg = 0.2 mm, W_1 = 0.1 mm, W_2 = 1 mm, W_{t1} = 2.1 mm, and W_{t2} = 3.1 mm. The LC equivalent circuit of the FCTCMRC is introduced to understand the effect of variations in the dimensions of the proposed cell on inductances and capacitances and thereby to know their effect on the transmission zeros, and finally on the frequency response of the cell. In [11], the LC equivalent circuits for microstrip steps, open-ends, bends, gaps, and junctions are presented. Based on it, the LC equivalent circuit of the FCTCMRC is achieved. The relation between the reactive elements and geometrical parts of the microstrip cell such as transmission lines and gaps is shown in Fig. 3(a); where, l_4 is the inductance of feeding lines, C_3 is the capacitance between feeding and matching lines with respect to the ground, and the inductance of the high impedance lines is l_1, where the tapered cells are attached. In addition l_2 and C_2 are the inductance and the capacitance with respect to the ground of the tapered cell, respectively. The l_3 represents the inductance of the high impedance lines with length of L_1. Also C_{c2} is the coupling capacitance between two high impedance lines with length of L_1, and C_{C1} is the coupling capacitance between the tapered cells.

Figure 3 (b) depicts the simplified LC equivalent circuit of Fig. 3 (a). In this figure, l_2 is neglected due to the low impedance of tapered cell. Therefore, by eliminating l_2, the capacitor of C_g and C_C will be equal to $4C_2$ and $2C_{C1}$ respectively; furthermore, l_s will be $l_3 + l_1$ and finally, the equivalent circuit of the lower high impedance transmission line, is simplified to l_h. The component values of the simplified LC equivalent circuit is obtained, where l_h = 4 nH, l_1 = 2nH, l_s=2 nH, l_4=0.2nH, C_{c2} = 1pF, C_c = 19 pF and C_g=175pF. Figure 4 shows the electromagnetic (EM) and simplified LC equivalent circuit simulation results of the optimized FCTCMRC for harmonic suppression. As seen in this figure, the FCTCMRC has two transmission notches near 6 GHz and 10 GHz (3rd and 5th harmonics) with the rejection level of 51 dB and 49 dB, respectively, and it has better than 18 dB rejection level in the whole 6 GHz-12 GHz band. These results show the implementation feasibility of the power divider with high suppression of harmonics using FCTCMRC.

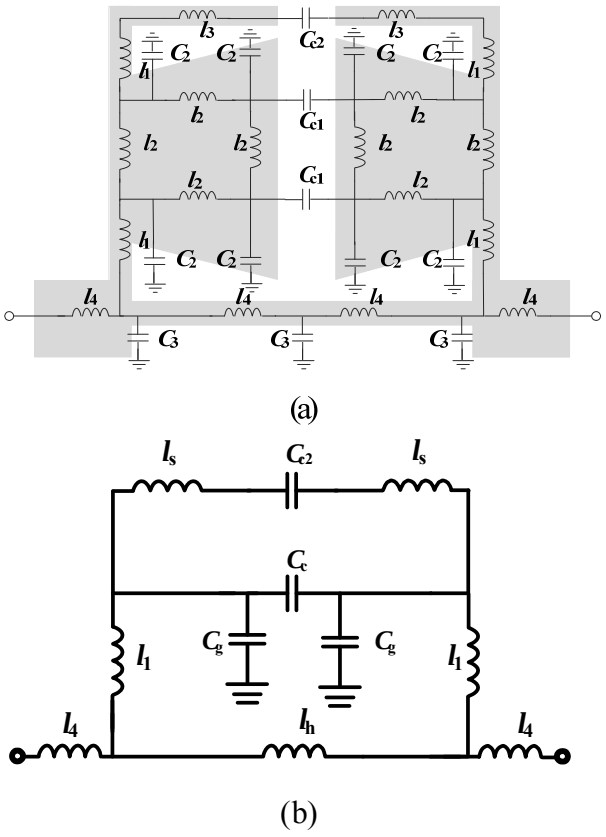

Fig. 3. (a) The derivation of LC equivalent circuit from FCTCMRC and (b) the simplified LC equivalent circuit of the FCTCMRC.

As seen in Fig. 4, there is a good agreement between the simplified LC equivalent circuit response and the EM simulation results. The EM simulated magnitude and phase responses of S_{12} of the FCTCMRC as the functions of L_1 are shown in Figs. 5 and 6. By adjusting the length of L_1, the desired performance can be achieved. It is also possible for the proposed structure to move the transmission notches close enough to the 2nd and 3rd harmonics by adjusting the length of L_1. With L_1= 5.5 mm the second and third harmonics are suppressed, as shown in Fig. 5.

Figure 7 shows the simulated responses of S_{12} for the simplified LC equivalent circuit as the function of C_g. The location of the transmission notches changes, by adjusting the value of C_g. The configuration of the proposed power divider for nth harmonic suppression as shown in Fig. 1 (b) consists of two microstrip FCTCMRC and four microstrip branch lines. Furthermore, the output ports are shunted through 100 ohms resistor. The

impedance of the microstrip branch lines connected to the input and output ports is represented by Z_1, and its length is represented by L. In the proposed power divider, the overall length of the quarter-wavelength transmission line is calculated as,

$$L' = (2 \times L) + L_C \quad (1)$$

where L_C is the length of the FCTCMRC that is equal to 2 × (L_1 + L_4) + Lg = 6.8 mm. Due to the slow-wave effect of the FCTCMRC, the dimension of L' = 17.86 mm, which is 29.3 % smaller than the conventional quarter-wavelength (25.28 mm).

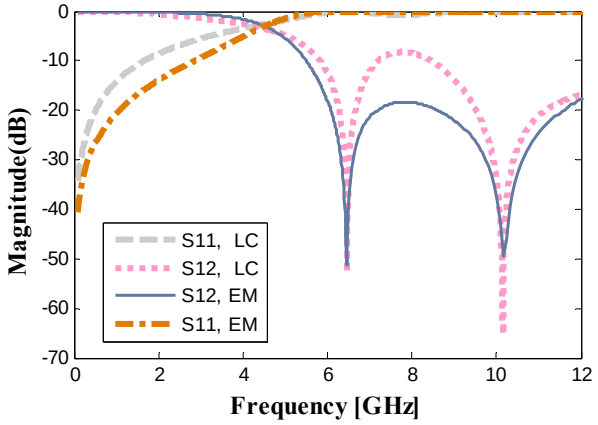

Fig. 4. EM and simplified LC equivalent circuit simulation results for the FCTCMRC.

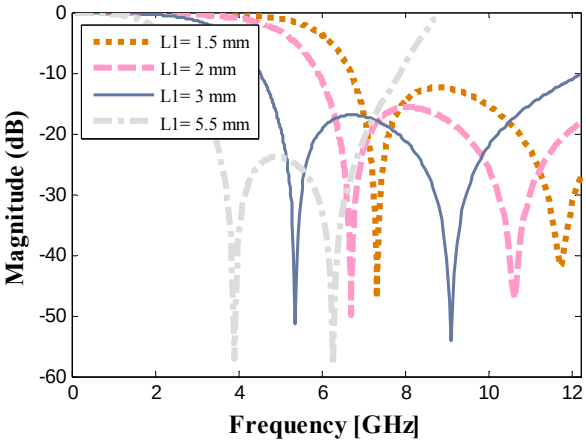

Fig. 5. EM simulated magnitude response of S_{12} as the function of L_1 for the FCTCMRC.

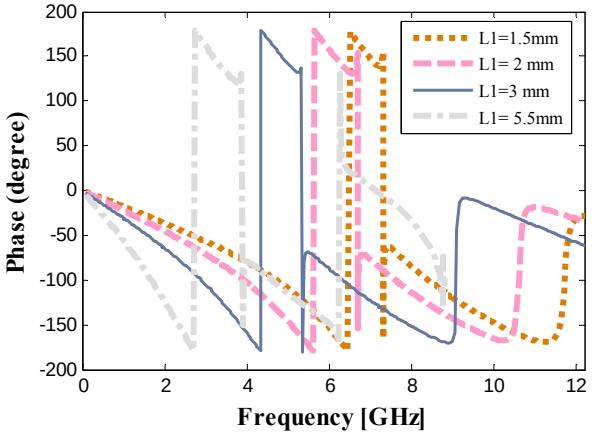

Fig. 6. EM simulated phase response of S_{12} as the function of L_1 for the FCTCMRC.

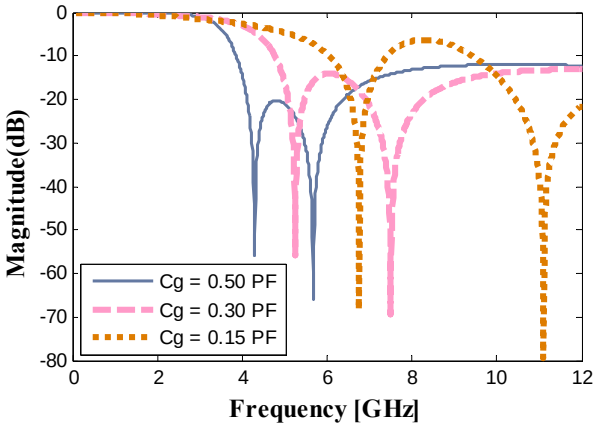

Fig. 7. Simulated response of S_{12} as the function of C_g for the simplified LC equivalent circuit.

III. SIMULATION AND MEASURMENT RESULTS

The proposed power divider is fabricated on RT/Duroid 5880, a substrate with dielectric constant of 2.2, thickness of 0.381 mm, and loss tangent of 0.0009. A photograph of the fabricated power divider with a center frequency fixed at 2 GHz for nth harmonic suppression is shown in Fig. 8. The overall dimension of the circuit is about 2.8 cm × 2.4 cm. The S-parameters are measured using an Agilent 8722ES network analyzer. Figures 9 to 12 illustrate the simulated and measured S-parameters of the proposed power divider. As seen, the simulated and measured results are in good agreement.

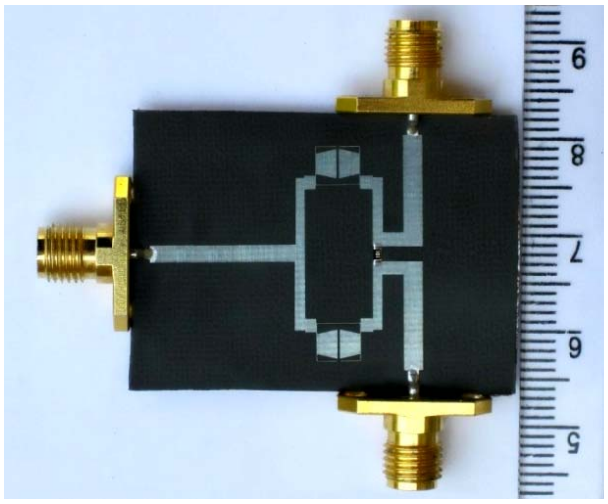

Fig. 8. Photograph of the proposed power divider.

The central frequency of the power divider is located at 2 GHz. At the central frequency, the measured input and output return losses are 48 dB and 44 dB, respectively. It can be seen in Fig. 11 that, the proposed power divider impressively suppresses harmonics, which has an ultra wide stop-band bandwidth (6 GHz – 12 GHz) with a minimum attenuation level of 24 dB. The S_{12} response of the conventional Wilkinson power divider is also shown in Fig. 11.

Figure 12 depicts the simulated and measured isolation of the two output ports. The measured isolation between port two and three is about 45 dB.

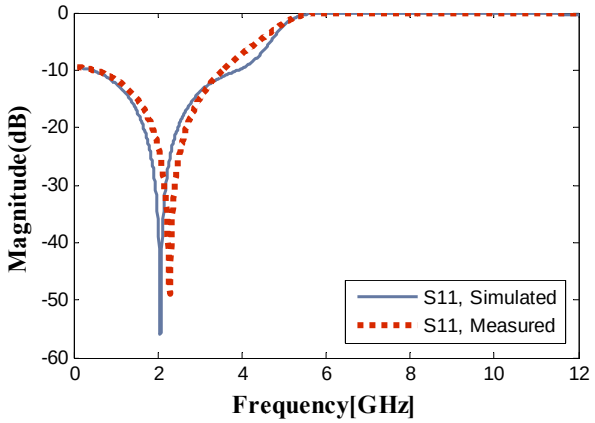

Fig. 9. Measured and simulated response of S_{11} for the fabricated power divider.

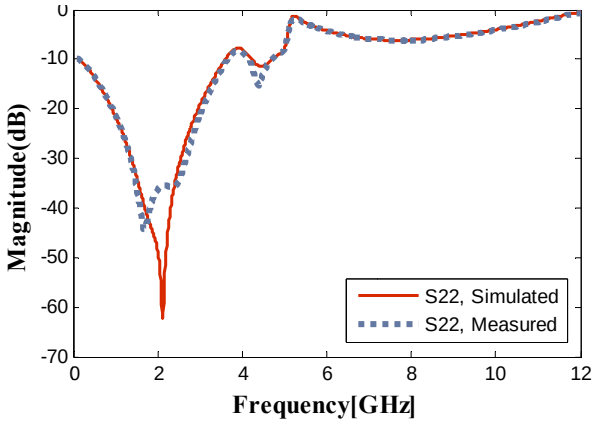

Fig. 10. Measured and simulated response of S_{22} for the fabricated power divider.

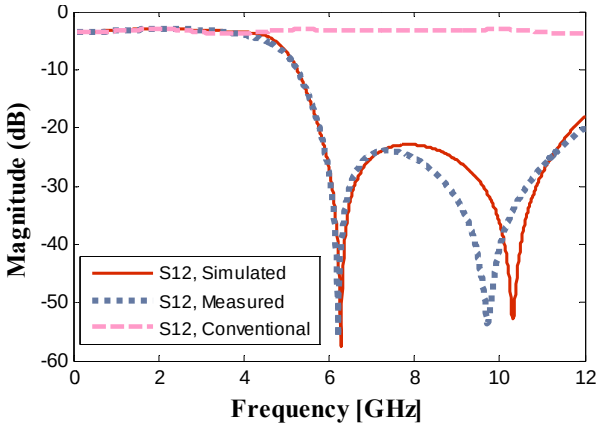

Fig. 11. Measured and simulated response of S_{12} for the fabricated power divider.

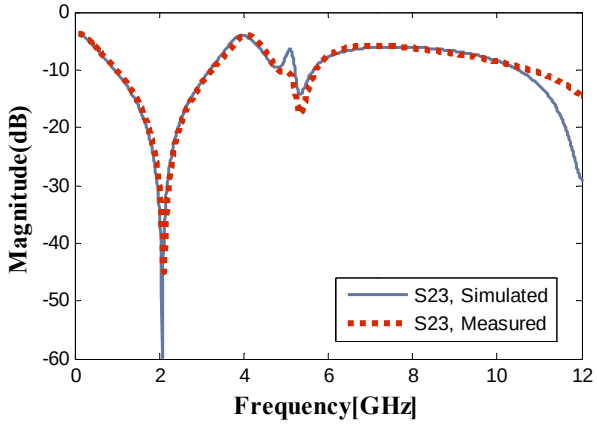

Fig. 12. Measured and simulated response of S_{23} for the fabricated power divider.

A comparison of the power dividers for nth harmonic suppression and λ/4 reduction is summarized in Table 1. The results show that this work presents a fair dimension decrement with superior harmonic suppressions as compared to the reported works.

Table 1: Performance comparison of the proposed power divider with other works.

Ref.	Freq.	λ/4 Line Reduction	Nth Harmonic Suppression
[3]	2.4 GHz	34.5 %	3rd 32.5 dB 5th 12 dB
[5]	2.65 GHz	-	3rd 29 dB 5th 34 dB
[6]	2.05 GHz	-	3rd 44 dB
[7]	1.5 GHz	9.1 %	2nd 18 dB 3rd 15 dB
This work	2 GHz	29.3%	3rd 53 dB 4th 25 dB 5th 56 dB 6th 20 dB

IV. CONCLUSION

In this paper, a novel power divider for nth harmonic suppression is proposed and implemented. By employing the microstrip FCTCMRC, a novel circuit configuration is presented with a smaller size and better harmonic suppression. With the presented method unwanted harmonics can be easily suppressed with high level of attenuations. As the measured results show, the magnitude values of S_{11}, S_{22}, S_{12}, and S_{23} at 2 GHz are 48 dB, 45 dB, 3.1 dB, and 45 dB, respectively. Furthermore, this power divider has an ultra wide stop-band bandwidth (6 GHz – 12 GHz) with a minimum attenuation level of 24 dB, which suppresses 3^{rd} to 6^{th} harmonics simultaneously. The proposed technique can be widely used to reject harmonics and miniaturize circuit dimensions in various microwave circuits such as power amplifiers, oscillators, mixers, and frequency multipliers.

REFERENCES

[1] E. J. Wilkinson, "An N-way power divider," *IEEE Trans. Microwave Theory Tech*., vol. 8, pp. 116-118, 1960.

[2] D. M. Pozar, *Microwave Engineering*, Wiley, New York, 2005.

[3] C. M. Lin, H. H. Su, J. C. Chiu, and Y. H. Wang, "Wilkinson power divider using microstrip EBG cells for the suppression of harmonics," *IEEE Microwave Wireless Components Letters*, vol. 17, pp. 700-702, 2007.

[4] J. Wang, J. Ni, Y. X. Guo, and D. Fang, "Miniaturized microstrip Wilkinson power divider with harmonic suppression," *IEEE Microwave Wireless Components Letters*, vol. 19, pp. 440-442, 2009.

[5] F. Zhang and C. F. Li, "Power divider with microstrip electromagnetic band gap element for miniaturization and harmonic rejection," *Electronic Letters*, vol. 44, pp. 422-423, 2008.

[6] K. H. Yi and B. Kang, "Modified Wilkinson power divider for nth harmonic suppression," *IEEE Microwave Wireless Components Letters*, vol. 13, pp. 178-180, 2003.

[7] D. J. Woo and T. K. Lee "Suppression of harmonics in Wilkinson power divider using dual-band rejection by asymmetric DGS," *IEEE Trans. Microwave Theory Tech*., vol. 53, pp. 2139-2144, 2005.

[8] D. Hawatmeh, K. A. Shamaileh, and N. Dib, "Design and analysis of multi-frequency unequal-split Wilkinson power divider using non-uniform transmission lines," *Applied Computational Electromagnetics Society (ACES) Journal*, vol. 27, pp. 248-255, 2012.

[9] K. A. Shamaileh, A. Qaroot, N. Dib, and A. Sheta, "Design of miniaturized unequal split Wilkinson power divider with harmonics suppression using non-uniform transmission lines," *Applied Computational Electromagnetics Society (ACES) Journal*, vol. 26, pp. 530-538, 2011.

[10] M. Hayati and A. Lotfi, "Compact low pass filter with high and wide rejection in stop band using front coupled tapered CMRC," *Electronic Letters*, vol. 46, pp. 846-848, 2010.

[11] J. S. Hong, *Microstrip Filters for RF/Microwave Applications*, Wiley, New York, 2001.

Mohsen Hayati received the B.Eng. in Electronics and Communication Engineering from Nagarjuna University, India, in 1985, and the M.Eng. and PhD in Electronics Engineering from Delhi University, Delhi, India, in 1987 and 1992, respectively. He joined the Electrical Engineering Department, Razi University, Kermanshah, Iran, as an Assistant Professor in 1993. At present, he is an associate professor with the Electrical Engineering Department, Razi University. He has published more than 110 papers in international and domestic journals and conferences. His current research interests include a Microwave and millimeter wave devices and circuits, application of computational intelligence, artificial neural networks, fuzzy systems, neuro-fuzzy systems, electronic circuit synthesis, modeling and simulations.

Saeed Roshani received the B.Eng. in Razi University, Kermanshah, Iran, in 2008, M.Eng. in Electrical Engineering in 2011, Shahed University, Tehran, Iran. He is currently working towards the Ph.D. degree in Electrical Engineering at the Razi University; His research interest includes the low-power and low-size integrated circuit design, microwave and millimeter wave devices and circuits.

Sobhan Roshani received the B.Eng. in Razi University, Kermanshah, Iran, in 2009, M.Eng. in Electrical Engineering in 2012, Iran Science and Technology University, Tehran, Iran, He is currently working towards the Ph.D. degree in Electrical Engineering at the Razi University, His research interest includes image processing, star trackers, optimization of solar energy and microwave circuits.

Design of Compact SITLs Low Pass Filter by Using Invasive Weed Optimization (IWO) Technique

Hamid Reza Khakzad, Seyed Hassan Sedighy, and Mohammad Khalaj Amirhosseini

School of Electrical and Electronic Engineering,
Iran University of Science and Technology, Tehran, Iran
H.khakzad@gmail.com, sedighy@iust.ac.ir, and khalaja@iust.ac.ir

Abstract ─ Step impedance transmission line (SITL) is optimized by Invasive Weed Optimization (IWO) technique to compact a low pass microstrip filter (LPF). In the proposed method, the uniform microstrip lines in the LPF structure are replaced by optimized SITLs. The equality of SITL and uniform transmission line gives two additional design parameters, which are optimized by IWO method to achieve the most compact SITLs. Finally, a compact high degree LPF is designed and fabricated with the area reduction of more than 70%. The measurement results of the fabricated LPF are in good agreement with the simulation ones.

Index Terms ─ Invasive weed optimization, low pass filter, and step impedance transmission line.

I. INTRODUCTION

Microstrip transmission lines are widely used in microwave circuits and play important roles in the microwave applications. In modern wireless communication systems, compact size and high performance devices are commonly required to reduce the cost and enhance system performances [1, 2]. Therefore, the miniaturization of microstrip transmission line devices has become a key issue for researchers, especially in low frequencies. Meandering of the transmission lines could be the most ordinary way for size reduction [3]. Moreover, the photonic bandgap (PBG) structure provides an alternative way for miniaturization [4-11]. Utilizing a slotted ground structure was reported in [12] as another way for size reduction and suppressing the spurious harmonics. Artificial transmission lines composed of microstrip quasi-lumped elements and their discontinuities are another approach for size reduction [13, 14].

Also, step impedance transmission lines (SITLs) and step impedance resonators (SIRs) are other ways to reduce the size of microstrip devices [15, 16]. In [17], the authors proposed a new idea based on SITLs in order to compact a quarter wave length transmission lines in the microstrip devices such as Wilkinson power divider. In this paper, we extend the idea to compact a microstrip transmission line with arbitrary specifications, electrical length, and characteristic impedance. In more details, the equality of the uniform and step impedance transmission lines ABCD matrices gives two equations with four unknown variables. It means that there are two degrees of freedom for solving the equations. Therefore, we used the Invasive Weed Optimization (IWO) algorithm to find the optimum answers of these equations to achieve the most equivalent compact SITL. This very simple algorithm inspired from the phenomena of colonization of invasive weeds in nature, achieves a reasonable performance compared with other numerical stochastic optimization algorithms such as GA and PSO [18-19]. Finally, the achieved SITLs with optimum values are used instead of the corresponding uniform transmission lines in a low pass filter structure. The simulation and fabrication results of the designed low pass filter show more than 70 % compactness in the proposed low pass filter.

II. STEP IMPEDANCE TRANSMISSION LINES (SITL)

Generally, step impedance transmission line (SITL) is a non-uniform transmission line that can be used in the microstrip circuits to reduce its size,

Submitted On: Sept. 30, 2012
Accepted On: Dec. 30, 2012

shift the spurious pass band to the higher frequency, and even to suppress the multiple spurious pass bands.

Figure 1 shows a step impedance transmission line composed of a transmission line with the length of θ_2 and characteristic impedance Z_2 between two lines with the length of $\theta_1/2$ and characteristic impedance Z_1, which should be equivalent to a transmission line with the length of θ_0 and characteristic impedance of Z_0, at frequency f_0. For this purpose, two independent entries of the two equivalent structures ABCD matrices have to be equal with each other at frequency f_0. After some algebraic manipulations, we have the following independent relations,

$$\cos\theta_1\cos\theta_2-\frac{1}{2}(k_z+\frac{1}{k_z})\sin\theta_1\sin\theta_2=\cos\theta_0 \quad (1)$$

$$z_1\sin\theta_1\cos\theta_2+\frac{z_1}{k_z}\sin\theta_2\times \left[\cos^2\theta_1/2-k_z^2\sin^2\theta_1/2\right]=z_0\sin\theta_0, \quad (2)$$

where Z_1, $k_z = Z_1/Z_2$, θ_1, and θ_2 are unknown variables. Therefore, we have two equations and four unknown variables. In other words, there are two degrees of freedom to design a step impedance transmission line instead of the uniform lines. To solve these equations, invasive weed optimization (IWO) technique can be used to reach the desired values of the most compact SITLs case.

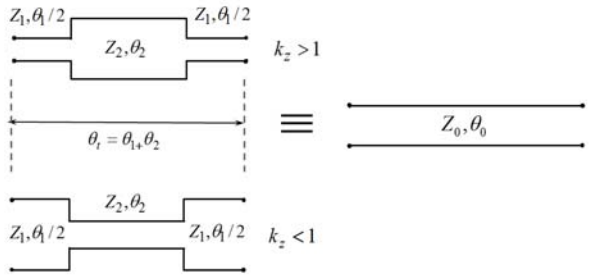

Fig. 1. The step impedance transmission line configuration.

III. OPTIMIZATION ALGORITHM DESIGN

IWO is a simple numerical stochastic search algorithm that mimics natural behavior of weed colonizing in the opportunity spaces for optimizing the function. Also, it has been shown to be effective in converging to an optimal solution by employing basic and simple properties such as seeding, growth, and competition in a weed colony. Some basic steps of the process are as follows [18-21]:

1) First, same as other stochastic algorithm, the parameters that need to be optimized, should be selected to determine the problem dimension, D. Then, for each of these variables, maximum and minimum values should be assigned.

2) Finite number of seeds, N, are spread out over the search area of the problem space with random positions.

3) Every seed grows to a flowering plant based on its fitness, which represents the goodness as a solution. Then each plant produces seeds depending on its own and the colonies lowest and highest fitnesses. In other words, the seeds number of each plant increases linearly from the minimum possible seed production level, S_{min}, to its maximum level, S_{max}, based on its fitness.

4) The produced seeds are being dispersed over the search area and grow to new plants by normally distributed random numbers with mean equal to the location of the producing plants and varying standard deviations. This ensures that the seeds will be randomly distributed near the parent plant. Also, the standard deviation (SD), σ, will be reduced from a previously defined initial value, $\sigma_{initial}$, to a final value, σ_{final}, in each iteration by,

$$\sigma_{iter}=\frac{(iter_{\max}-iter)^n}{iter_{\max}^n}(\sigma_{initial}-\sigma_{final})+\sigma_{final} \quad (3)$$

where $iter_{max}$ is the maximum number of iterations, σ_{iter} is the SD at the present step and n is the nonlinear modulation index.

5) This process continues until the maximum number of the plants, P_{max}, is reached. Then, only the plants with high fitness can survive and produce seeds, and others are eliminated. The process will be stopped after the maximum number of iterations is reached and, hopefully, the plant with the best fitness will be the closest one to the optimal solution.

In our system equations, i.e., equations 1 and 2, we introduce the error function to achieve the most compact SITL as,

$$e=\sqrt{e_1^{\,2}+e_2^{\,2}} \quad (4)$$

where e_1 and e_2 are the difference between the sides of equations (1) and (2), respectively for any

given values (trial SITL). The fitness function of each trial SITL is introduced as below,

$$f = \begin{cases} w_1\theta_t + w_2 e & e < error \\ w_3\theta_t + w_4 e & e > error \end{cases} \quad (5)$$

where w_1, w_2, w_3, and w_4 are the assigned weights, θ_t is the total electrical length of trial SITL and *error* is a threshold for accepting a trail structure as a good enough answer for the equations. The optimization goal is to minimize the fitness function. The high w_3/w_1 and w_4/w_2 values separate two parts of the fitness function very well. To be more specific, with these conditions, the trial SITLs with $e < error$ compete with each other just according to their electrical length, θ_t, while ones with $e > error$ compete with each other to enter the $e < error$ region. Moreover, w_1/w_2 and w_3/w_4 determine the importance of *error* against the electrical length.

IV. LOW PASS FILTER EXAMPLE DESIGN

Here, a low pass filter is designed and implemented to validate the proposed approach. The filter is a seven element Chebychev with four shunt capacitors and three series inductors, 0.01 dB ripple and 460 MHz cut-off frequency. In the traditional implementation of the LPF, the shunt capacitors and series inductors can be modeled with open-stubs and high-z lines, respectively. We consider the TLX Taconic substrate with thickness h = 0.8 mm and relative dielectric constant ε_r = 2.55 for simulations and fabrication. The designed values of the traditional LPF are tabulated in Table 1. In this step, each capacitors and inductors are replaced with a SITL configuration. The optimized values of the equivalent SITLs for these four different lines (two open stubs and two high impedance lines) have been computed by the IWO method. The IWO parameters are tabulated in Table. 2. Based on the defined fitness function in equation (5), the optimization method tries to find the equivalent SITL instead of the uniform transmission line (answers of equations (1) and (2)) with the lowest θ_t in the search area. As shown in Table. 2, 10 Ω and 180 Ω are chosen as the lower and higher limitation of the impedance research area. Furthermore, θ_1 and $\theta_2 < \theta_0/4$ guarantee that the optimized SITL electrical length is less than half of the conventional transmission line electrical length. Based on the different examples, it was concluded that selecting maximum and minimum number of seeds and non linear modulation index as 2, 10, and 3 leads to a good performance of the optimizer. Also, since the run time of the algorithm is very low, the number of initial population and maximum number of plant population are selected as high as 80 to achieve more accuracy in the method. Moreover, by choosing $\sigma_{initial}$ = 0.01, the error level can be decreased and more precise results may be achieved. The fitness values of one SITL used in the LPF are demonstrated in Fig. 2 versus iterations. It is clear that the IWO converges to the optimum values found by IWO method under the used conditions in the last iteration, $iter_{max}$.

Table 1: The traditional low pass filter design parameters.

Element	Z_c (Ω)	θ_0 (rad)
C_1=C_4	20	0.31
C_2= C_3	20	0.61
L_1= L_3	120	0.62
L_2	120	0.75

Figure 3 shows the layout of the proposed LPF with step impedance transmission lines instead of the inductor and capacitor parts of the conventional LPF filter. The specifications of the step impedance parts of the filter are obtained from the IWO method. The calculated values have to be tuned because the discontinuities are not considered in the ABCD equations. We used Agilent Advance Design System (ADS) for tuning the final results shown in Table. 3. In this table, Z_1 and Z_2 are corresponding to the SITLs impedances and θ_1 and θ_2 demonstrate the electrical length of the SITL segments as shown in Fig. 1. It can be seen that the vertical lines are more compact than the horizontal lines. Figure 4 shows the fabricated low pass filter. We used one level folded transmission lines in the high impedance segment of the horizontal transmission lines. Also, the end segment position of the middle stubs (C_2 and C_3) is rotated to achieve more compactness. Notice that the effect of these changing is considered in the full wave simulation, which is done by using the method of moment (MoM) in ADS. The required space for the optimized designed filter (99.04 mm × 22.32 mm) is 30% of the traditional LPF required space (177.68 mm × 42.21 mm) that

shows more than 70% compactness in the proposed structure.

Table 2: IWO parameter values for SITL optimization.

Symbols	Quantity	Value
N	Number of initial population	80
$iter_{max}$	Maximum number of iterations	72
D	Problem dimension	4
P_{max}	Maximum number of plant population	80
S_{max}	Maximum number of Seeds	10
S_{min}	Minimum number of Seeds	2
n	Nonlinear modulation index	3
$\sigma_{initial}$	Initial value of standard deviation	1
σ_{final}	final value of standard deviation	0.01
Z_1	Impedance of the sides	$10 < Z_1 < 180$
Z_2	Middle impedance	$10 < Z_2 < 180$
θ_1	Electrical length of the sides	$0 < \theta_1 < \theta_0/4$
θ_2	Electrical length of the middle lines	$0 < \theta_2 < \theta_0/4$

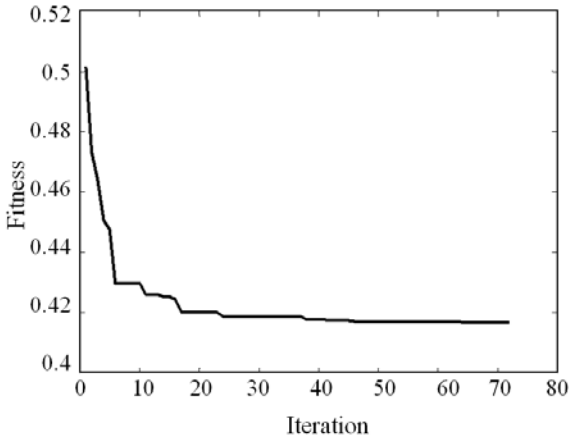

Fig. 2. The fitness function of a SITL versus iterations.

Table 3: Equivalent values for the proposed SITL LPF.

Elements	Z_1 (Ω)	Z_2 (Ω)	θ_1 (rad)	θ_2 (rad)
C_1=C_4	71	10	0.06	0.113
C_2= C_3	109.6	10	0.13	0.265
L_1= L_3	138.11	179.8	0.076	0.33
L_2	63.04	179.89	0.104	0.436

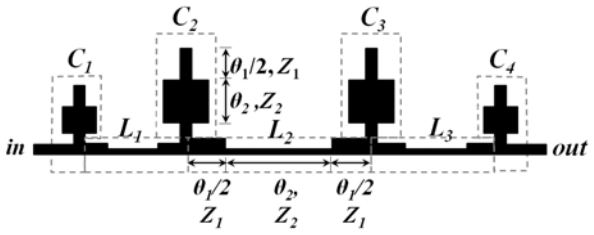

Fig. 3. Schematic of the compact filter.

Figure 5 shows the simulation and measurement results for the designed LPF. The measurements were taken by an Agilent network analyzer E5071C. There is a good agreement between the simulation and measurements results. Moreover, the results show that the first spurious response of the LPF is suppressed, which is achieved by using high Z- low Z lines in the filter configuration.

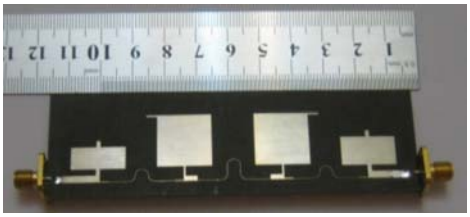

Fig. 4. Fabricated compact designed low pass filter.

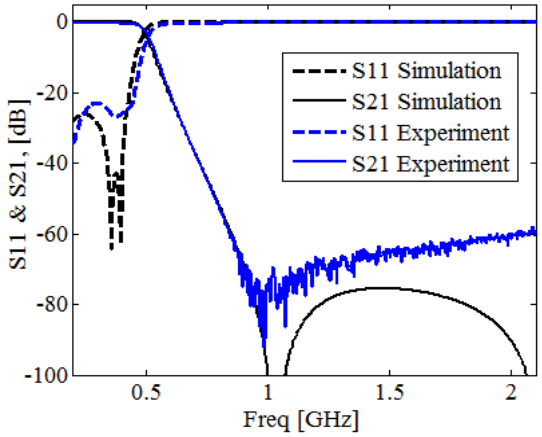

Fig. 5. The simulation and experiment results of the LPF.

V. CONCLUSION

The invasive weed optimization (IWO) approach has been applied to miniaturize the step impedance transmission lines (SITL). In the proposed method, the IWO technique attempts to

replace the uniform microstrip lines of low pass filter by the most compact SITLs. The designed and fabricated LPF with optimized SITLs segments has more than 70% area reduction compare with the traditional one. The proposed method can be extended to compact the other microwave devices as well.

REFERENCES

[1] D. M. Pozar, *Microwave Engineering*, Second Edition, *Wiley*, 1998.

[2] J. Lin Li , J. Xin Chen, Q. Xue, J. P. Wang, W. Shao, and L. J. Xue, "Compact microstrip low pass filter based on defected ground structure and compensated microstrip line," *IEEE MTT-S International Microwave Symposium Digest*, pp. 1483-1486, 2005.

[3] C. C. Chen, C. Kuang, and C. Tzuang, "Synthetic quasi-TEM meandered transmission lines for compacted microwave integrated circuits," *IEEE Transaction on Microwave Theory and Techniques*, vol. 52, no. 6, pp. 1637-1647, 2004.

[4] Q. Xue, K. M. Shum, and C. H. Chan, "Novel 1-D microstrip PBG cells," *IEEE Microwave and Wireless Component Letters*, vol. 10, no. 10, pp. 403-405, 2000.

[5] F. R. Yang, Y. Qian, and T. Itoh, "A novel uniplanar compact PBG structure for filter and mixer applications," *IEEE MTT International Microwave Symposium Digest*, vol. 3, pp. 919-922, 1999.

[6] S. K. Gupta and K. J. Vinoy, "A compact defected ground microstrip device with photonic bandgap effects," *J. of Electromagn. Waves and Appl*., vol. 23, pp. 255-266, 2009.

[7] M. Challal, A. Boutejdar, M. Dehmas, A. Azrar, and A. Omar, "Compact microstrip low-pass filter design with ultra-wide reject band using a novel quarter-circle DGS shape," *Applied Computational Electromagnetics Society (ACES) Journal*, vol. 27, no. 10, pp. 808-815, Oct. 2012.

[8] G. E. Al-Omair, S. F. Mahmoud, and A. S. Al-Zayed, "Lowpass and bandpass filter designs based on DGS with complementary split ring resonators," *Applied Computational Electromagnetics Society (ACES) Journal*, vol. 26, no. 11, pp. 907-914, Nov. 2011.

[9] M. Al Sharkawy, A. Boutejdar, F. Alhefnawi, and O. Luxor, "Improvement of compactness of lowpass/bandpass filter using a new electromagnetic coupled crescent defected ground structure resonators," *Applied Computational Electromagnetics Society (ACES) Journal*, vol. 25, no. 7, pp. 570-577, July 2010.

[10] N. M. Garmjani and N. Komjani, "Improved microstrip folded tri-section stepped impedance resonator bandpass filter using defected ground structure," *Applied Computational Electromagnetics Society (ACES) Journal*, vol. 25, no. 11, pp. 975-983, Nov. 2010.

[11] Y. J. Sung, C. S. Ahn, and Y. -S. Kim, "Size reduction and harmonic suppression of rat race coupler hybrid coupler using defected ground structure," *IEEE Microwave and Wireless Component Letters*, vol. 14, no.1, pp. 7-9, 2004.

[12] X. H. Wang and B. Z. Wang, "Compact broadband dual-band bandpass filters using slotted ground structures," *Progress In Electromagnetics Research, PIER,* vol. 82, pp. 151-166, 2008.

[13] T. Yang, C. Liu, L. Yan, and K. Huang, "A compact dual-band power divider using planar artificial transmission lines for GSM/DCS applications," *Progress In Electromagnetics Research Letters,* vol. 10, pp. 185-191, 2009.

[14] P. Hajizade, H. R. Hassani, and S. H. Sedighy, "Compact quasi-Yagi antenna loaded with artificial transmission lines for RFID applications," *IEEE International Symposium on APS*, pp. 1-2, 2012.

[15] H. W. Liu, L. Y. Li, X. H. Li, and S. X. Wang, "Compact microstrip lowpass filter using asymmetric stepped-impedance hairpin resonator and slotted grounded plane," *J. of Electromagn. Waves and Appl*., vol. 22, pp. 1615-1622, 2008.

[16] M. H. Yang, J. Xu, Q. Zhao, L. Peng, and G. P. Li, "Compact broad stopband low pass filters using SIRS-loaded circular hairpin resonators," *Progress In Electromagnetics Research, PIER*, vol. 102, pp. 95-106, 2010.

[17] S. H. Sedighy and M. Khalaj-Amirhosseini, "Compact Wilkinson power divider using stepped impedance transmission lines," *J. of Electromagnetics Waves and Appl*., vol. 25, pp.1773-1782, 2011.

[18] S. H. Sedighy, A. R. Mallahzadeh, M. Soleimani, and J. Rashed-Mohassel, "Optimization of printed Yagi antenna using invasive weed optimization (IWO)," *IEEE Antennas and Wireless Propagation Letters*, vol. 9, pp. 1275-1278, 2010.

[19] A. R. Mehrabian and C. Lucas, "A novel numerical optimization algorithm inspired from weed colonization," *Ecol. Inform*., vol. 1, pp. 355-366, 2006.

[20] S. Karimkashi and A. Kishk, "Invasive weed optimization and its features in electromagnetics," *IEEE Transaction on Antennas and Propagation*, vol. 58, no. 4, pp. 1269-1278, 2010.

[21] A. R. Mallahzadeh, S. Es'haghi, and H. R. Hassani, "Compact U-array MIMO antenna designs using IWO algorithm," *Int. J. RF Microw. Comput*., vol. 15, no. 5, pp. 568-576, 2009.

Hamidreza Khakzad was born in Tehran, Iran in 1987. He received his B.Sc. degree from Iran University of Science and Technology (IUST) in 2011. He is currently studying for M.Sc degree at Imam Khomeini International University (IKIU).

Seyed Hassan Seddighi was born in Qaen, South Khorasan, Iran in 1983. He received B.Sc. and M.Sc. degrees in Electrical Engineering from Iran University of Science and Technology (IUST) in 2006 and 2008, respectively. He is currently working toward the Ph.D. degree at IUST. His current research interests include microstrips antenna, optical transformation, design and application of metamaterials.

Mohammad Khalaj Amirhosseini was born in Tehran, Iran in 1969. He received his B.Sc., M.Sc., and Ph.D. degrees from Iran University of Science and Technology (IUST) in 1992, 1994, and 1998 respectively, all in Electrical Engineering. He is currently an Associate Professor at College of Electrical Engineering of IUST. His scientific fields of interest are electromagnetic direct and inverse problems including microwaves, antennas and electromagnetic compatibility.

Study and Applications of an Unconditionally Stable Multi-Resolution Time-Domain Scheme

Qunsheng Cao

College of Electronic Information Engineering
Nanjing University of Aeronautics and Astronautics, Nanjing, 210016, China
qunsheng@nuaa.edu.cn

Abstract ─ An unconditionally stable locally one-dimensional multi-resolution time-domain (LOD-MRTD) algorithm is studied, which is free of the Courant-Friedrich-Levy (CFL) stability condition. The LOD-MRTD method is reformulated to get more efficient and simple formulations. The unconditional stability and dispersion equations of the LOD-MRTD in two dimension (2D) case are analyzed, and a 2D example is calculated to demonstrate these characteristics.

Index Terms - Locally one-dimensional (LOD), multi-resolution time-domain (MRTD), and unconditional stability.

I. INTRODUCTION

The finite-difference time-domain (FDTD) method has been displayed in an effective way to provide accurate predictions to the field behaviors for varieties of electromagnetic interaction problems [1-2]. The FDTD method is very computationally intensive due to its two inherent physical constraints, one being the numerical dispersion, and another being the numerical stability. Because of the Courant – Friedrich – Levy (CFL) stability condition and the numerical dispersion errors, heavy meshing work and simulation cost time may be required to solve the electrically large structures. To reduce the value of the numerical dispersion, the spatial step of the FDTD method must be chosen fine, and normally it is less than one twentieth of wavelength. To make time-recursion stable, the time step must satisfy the CFL stability condition. Many efforts have been made in relaxing or removing the above two constraints to reduce the computational expenditures. To improve the numerical dispersion problems, some methods such as the MRTD method [3-5], the pseudo-spectral time domain (PSTD) method [6-7], and the higher order FDTD scheme [8], have been devoted to the way.

Among them, the space distribution functions of the MRTD scheme are expanded by the scaling and wavelet functions as basis functions [9-11]. The multi-resolution analysis (MRA) is applied to significantly reduce the dispersion errors. In order to further improve the computational efficiency of the MRTD methods and save the computational time, there are two approaches at least to be considered. One is the high-order method, in which the convergence of the time discretization is the same with the convergence of the spatial discretization, is called the RK-MRTD scheme [12]. Another approach is to use the ADI technology, which is applied into the MRTD scheme to form the ADI-MRTD method [13-14]. The ADI-MRTD method is free of the CFL stability condition and reduces significantly the computational time.

The locally one-dimensional (LOD) method is first introduced to the FDTD method by J. Shibayama [15]. The LOD-MRTD approach is proposed in [16], which shows the LOD-MRTD method more efficient compared with the ADI-MRTD method. In this paper, an improved LOD-MRTD method is studied. The scheme developed in [17] is applied in the conventional LOD-MRTD. The reformulated LOD-MRTD can get better efficiency than the conventional LOD-MRTD.

The remainder of the paper is organized as follows. In section II, the conventional and

Submitted On: Aug. 2, 2010
Accepted On: Oct. 10, 2012

reformulated LOD-MRTD method is introduced. In section III, the numerical properties of the method in 2D case are analyzed, which includes the stability condition and the numerical dispersive characteristics. In section IV, a validation of an example and discussion of numerical results is presented. Finally, conclusions are summarized in section V.

II. LOD-MRTD FORMULATION

For simplicity, let us consider a two-dimensional (2D) TM_z wave propagation in a lossless isotropic medium with permittivity ε and permeability μ. Maxwell's equations are expressed as follows,

$$\mu\frac{\partial H_x}{\partial t} = -\frac{\partial E_z}{\partial y} \tag{1a}$$

$$\mu\frac{\partial H_y}{\partial t} = +\frac{\partial E_z}{\partial x}, \tag{1b}$$

$$\varepsilon\frac{\partial E_z}{\partial t} = \frac{\partial H_y}{\partial x} - \frac{\partial H_x}{\partial y}. \tag{1c}$$

According to [15], applying the LOD method to the time discretization of equation (1), Maxwell's equations can be solved using two steps, the first step is

$$H_x^{n+\frac{1}{2}} = H_x^n - \frac{\Delta t}{2\mu}\left(\frac{\partial E_z^{n+\frac{1}{2}}}{\partial y} + \frac{\partial E_z^n}{\partial y}\right), \tag{2a}$$

$$H_y^{n+\frac{1}{2}} = H_y^n, \tag{2b}$$

$$E_z^{n+\frac{1}{2}} = E_z^n - \frac{\Delta t}{2\varepsilon}\left(\frac{\partial H_x^{n+\frac{1}{2}}}{\partial y} + \frac{\partial H_x^n}{\partial y}\right), \tag{2c}$$

and the second step is

$$H_x^{n+1} = H_x^{n+\frac{1}{2}}, \tag{2d}$$

$$H_y^{n+1} = H_y^{n+\frac{1}{2}} + \frac{\Delta t}{2\mu}\left(\frac{\partial E_z^{n+1}}{\partial x} + \frac{\partial E_z^{n+\frac{1}{2}}}{\partial x}\right), \tag{2e}$$

$$E_z^{n+1} = E_z^{n+\frac{1}{2}} + \frac{\Delta t}{2\varepsilon}\left(\frac{\partial H_y^{n+1}}{\partial x} + \frac{\partial H_y^{n+\frac{1}{2}}}{\partial x}\right). \tag{2f}$$

In the MRTD scheme, the Daubechies compactly supported scaling functions are adopted as basis functions in the expansion of the fields. Using the orthogonal relations for the scaling functions [4], the derivative of the update equations (2) are represented as follows, for step n to step n+1/2,

$$\begin{aligned} &{}_{\phi x}H_{i,j+\frac{1}{2}}^{n+\frac{1}{2}} \\ &= {}_{\phi x}H_{i,j+\frac{1}{2}}^{n} - \frac{\Delta t}{2\mu\Delta y}\sum_{v=-N_v}^{N_v-1} a(v)\left({}_{\phi z}E_{i,j+v+1}^{n+\frac{1}{2}} + {}_{\phi z}E_{i,j+v+1}^{n}\right) \end{aligned} \tag{3a}$$

$${}_{\phi y}H_{i+\frac{1}{2},j}^{n+\frac{1}{2}} = {}_{\phi y}H_{i+\frac{1}{2},j}^{n}, \tag{3b}$$

$$\begin{aligned} &{}_{\phi z}E_{i,j}^{n+\frac{1}{2}} \\ &= {}_{\phi z}E_{i,j}^{n} - \frac{\Delta t}{2\varepsilon\Delta y}\sum_{v=-N_v}^{N_v-1} a(v)\left({}_{\phi x}H_{i,j+v+\frac{1}{2}}^{n+\frac{1}{2}} + {}_{\phi x}H_{i,j+v+\frac{1}{2}}^{n}\right). \end{aligned} \tag{3c}$$

For step n+1/2 to step n+1

$${}_{\phi x}H_{i,j+\frac{1}{2}}^{n+1} = {}_{\phi x}H_{i,j+\frac{1}{2}}^{n+\frac{1}{2}}, \tag{3d}$$

$$\begin{aligned} &{}_{\phi y}H_{i+\frac{1}{2},j}^{n+1} \\ &= {}_{\phi y}H_{i+\frac{1}{2},j}^{n+\frac{1}{2}} + \frac{\Delta t}{2\mu\Delta x}\sum_{v=-N_v}^{N_v-1} a(v)\left({}_{\phi z}E_{i+v+1,j}^{n+1} + {}_{\phi z}E_{i+v+1,j}^{n+\frac{1}{2}}\right), \end{aligned} \tag{3e}$$

$$\begin{aligned} &{}_{\phi z}E_{i,j}^{n+1} \\ &= {}_{\phi z}E_{i,j}^{n+\frac{1}{2}} + \frac{\Delta t}{2\varepsilon\Delta x}\sum_{v=-N_v}^{N_v-1} a(v)\left({}_{\phi y}H_{i+v+\frac{1}{2},j}^{n+1} + {}_{\phi y}H_{i+v+\frac{1}{2},j}^{n+\frac{1}{2}}\right), \end{aligned} \tag{3f}$$

where the coefficients $a(v)$ are resulted from the scaling functions and satisfy the relation of $a(v) = -a(-v-1)$, $N_v = 2N-1$ and N is the order of vanishing moments of the Daubechies scaling functions used in the LOD-MRTD.

The 2D LOD-MRTD formulations can be further simplified, after some tedious derivations, we finally obtain the 2D LOD-MRTD iterative equations, and there are only four equations to be calculated.

$$\begin{aligned} &{}_{\phi z}E_{i,j}^{n+\frac{1}{2}} - \frac{\Delta t^2}{4\varepsilon\mu\Delta y^2}\sum_{v_1,v_2=-N_v}^{N_v-1} a(v_1)a(v_2)\,{}_{\phi z}E_{i,j+v_1+v_2+1}^{n+\frac{1}{2}} \\ &= {}_{\phi z}E_{i,j}^{n} + \frac{\Delta t^2}{4\varepsilon\mu\Delta y^2}\sum_{v_1,v_2=-N_v}^{N_v-1} a(v_1)a(v_2)\,{}_{\phi z}E_{i,j+v_1+v_2+1}^{n} \\ &\quad - \frac{\Delta t}{\varepsilon\Delta y}\sum_{v_1=-N_v}^{N_v-1} a(v_1)\,{}_{\phi x}H_{i,j+v_1+\frac{1}{2}}^{n}, \end{aligned} \tag{4a}$$

$$
\begin{aligned}
&{}_{\phi x}H_{i,j+\frac{1}{2}}^{n+1} \\
&= {}_{\phi x}H_{i,j+\frac{1}{2}}^{n} - \frac{\Delta t}{2\mu\Delta y}\sum_{v_2=-N_v}^{N_v-1} a(v_2)\left({}_{\phi z}E_{i,j+v_2+1}^{n+\frac{1}{2}} + {}_{\phi z}E_{i,j+v_2+1}^{n}\right),
\end{aligned}
\tag{4b}
$$

$$
\begin{aligned}
&{}_{\phi z}E_{i,j}^{n+1} - \frac{\Delta t^2}{4\varepsilon\mu\Delta x^2}\sum_{v_1,v_2=-N_v}^{N_v-1} a(v_1)a(v_2)\,{}_{\phi z}E_{i+v_1+v_2+1,j}^{n+1} \\
&= {}_{\phi z}E_{i,j}^{n+\frac{1}{2}} + \frac{\Delta t^2}{4\varepsilon\mu\Delta y^2}\sum_{v_1,v_2=-N_v}^{N_v-1} a(v_1)a(v_2)\,{}_{\phi z}E_{i+v_1+v_2+1,j}^{n+\frac{1}{2}} \\
&\quad + \frac{\Delta t}{\varepsilon\Delta x}\sum_{v_1=-N_v}^{N_v-1} a(v_1)\,{}_{\phi y}H_{i+v_1+\frac{1}{2},j}^{n},
\end{aligned}
\tag{4c}
$$

$$
\begin{aligned}
&{}_{\phi y}H_{i+\frac{1}{2},j}^{n+1} \\
&= {}_{\phi y}H_{i+\frac{1}{2},j}^{n} + \frac{\Delta t}{2\mu\Delta x}\sum_{v_2=-N_v}^{N_v-1} a(v_2)\left({}_{\phi z}E_{i+v_2+1,j}^{n+1} + {}_{\phi z}E_{i+v_2+1,j}^{n+\frac{1}{2}}\right).
\end{aligned}
\tag{4d}
$$

It needs to solve a banded matrix from the updated equations, and the width of the banded coefficient matrix is determined by the order of vanishing moments of the Daubechies scaling functions. In the 3D LOD-MRTD all the six components of the E and H should be solved. The iterative equations of the LOD-MRTD method [16] in the three-dimensional formula are expressed as follows, such as E_x and H_z components for step n to step n+1/2,

$$
\begin{aligned}
&{}_{\phi x}E_{i+\frac{1}{2},j,k}^{n+\frac{1}{2}} - \frac{\Delta t^2}{4\varepsilon\mu\Delta y^2}\sum_{v_1,v_2=-N_v}^{N_v-1} a(v_1)a(v_2)\,{}_{\phi x}E_{i+\frac{1}{2},j+v_1+v_2+1,k}^{n+\frac{1}{2}} \\
&= {}_{\phi x}E_{i+\frac{1}{2},j,k}^{n} + \frac{\Delta t^2}{4\varepsilon\mu\Delta y^2}\sum_{v_1,v_2=-N_v}^{N_v-1} a(v_1)a(v_2)\,{}_{\phi x}E_{i+\frac{1}{2},j+v_1+v_2+1,k}^{n} \\
&\quad + \frac{\Delta t}{\varepsilon\Delta y}\sum_{v_1=-N_v}^{N_v-1} a(v_1)\,{}_{\phi y}H_{i+\frac{1}{2},j+v_1+\frac{1}{2},k}^{n},
\end{aligned}
\tag{5a}
$$

$$
\begin{aligned}
&{}_{\phi z}H_{i+\frac{1}{2},j+\frac{1}{2},k}^{n+\frac{1}{2}} \\
&= {}_{\phi z}H_{i+\frac{1}{2},j+\frac{1}{2},k}^{n} \\
&\quad + \frac{\Delta t}{2\mu\Delta y}\sum_{v_2=-N_v}^{N_v-1} a(v_2)\left({}_{\phi x}E_{i+\frac{1}{2},j+v_2+1,k}^{n+\frac{1}{2}} + {}_{\phi x}E_{i+\frac{1}{2},j+v_2+1,k}^{n}\right).
\end{aligned}
\tag{5b}
$$

It is clear that all the electric field equations are implicit iteration equations related with coefficients $a(v)$, but the magnetic field equations are the explicit iterative.

For the 2D problem, because the number of the update electric and updated magnetic fields are different, the required memory used in the LOD-MRTD algorithm is more than one third that of the original MRTD method; but in the three-dimensional case, the electric and the magnetic fields requires all six components, the total cost memory is 1.5 times to the classical MRTD method.

According to [17], the LOD-FDTD method can be reformulated, which makes the right-hand sides much simpler and more concise. We use this method to reformulate the LOD-MRTD algorithm to improve its efficiency. First an auxiliary variable P is defined as,

$$
P^{n+\frac{1}{2}} = E^{n+\frac{1}{2}} + E^{n}. \tag{6}
$$

Then substitute equation (6) to equations (4) and (5), the formulations of the conventional LOD-MRTD method can be rewritten as,

$$
\begin{aligned}
&{}_{\phi z}P_{i,j}^{n+\frac{1}{2}} - \frac{\Delta t^2}{4\varepsilon\mu\Delta y^2}\sum_{v_1,v_2=-N_v}^{N_v-1} a(v_1)a(v_2)\,{}_{\phi z}P_{i,j+v_1+v_2+1}^{n+\frac{1}{2}} \\
&= 2\,{}_{\phi z}E_{i,j}^{n} - \frac{\Delta t}{\varepsilon\Delta y}\sum_{v_1=-N_v}^{N_v-1} a(v_1)\,{}_{\phi x}H_{i,j+v_1+\frac{1}{2}}^{n}
\end{aligned}
\tag{7a}
$$

$$
{}_{\phi x}H_{i,j+\frac{1}{2}}^{n+1} = {}_{\phi x}H_{i,j+\frac{1}{2}}^{n} - \frac{\Delta t}{2\mu\Delta y}\sum_{v_2=-N_v}^{N_v-1} a(v_2)\,{}_{\phi z}P_{i,j+v_2+1}^{n+\frac{1}{2}}, \tag{7b}
$$

$$
{}_{\phi z}E_{i,j}^{n+\frac{1}{2}} = {}_{\phi z}P_{i,j}^{n+\frac{1}{2}} - {}_{\phi z}E_{i,j}^{n}, \tag{7c}
$$

$$
\begin{aligned}
&{}_{\phi z}P_{i,j}^{n+1} - \frac{\Delta t^2}{4\varepsilon\mu\Delta x^2}\sum_{v_1,v_2=-N_v}^{N_v-1} a(v_1)a(v_2)\,{}_{\phi z}P_{i+v_1+v_2+1,j}^{n+1} \\
&= 2\,{}_{\phi z}E_{i,j}^{n+\frac{1}{2}} + \frac{\Delta t}{\varepsilon\Delta x}\sum_{v_1=-N_v}^{N_v-1} a(v_1)\,{}_{\phi y}H_{i+v_1+\frac{1}{2},j}^{n}
\end{aligned}
\tag{7d}
$$

$$
{}_{\phi y}H_{i+\frac{1}{2},j}^{n+1} = {}_{\phi y}H_{i+\frac{1}{2},j}^{n} + \frac{\Delta t}{2\mu\Delta x}\sum_{v_2=-N_v}^{N_v-1} a(v_2)\,{}_{\phi z}P_{i+v_2+1,j}^{n+1}, \tag{7e}
$$

$$
{}_{\phi z}E_{i,j}^{n+1} = {}_{\phi z}P_{i,j}^{n+1} - {}_{\phi z}E_{i,j}^{n+\frac{1}{2}}, \tag{7f}
$$

for 2D TM_z case, and

$$
\begin{aligned}
&{}_{\phi x}P_{i+\frac{1}{2},j,k}^{n+\frac{1}{2}} - \frac{\Delta t^2}{4\varepsilon\mu\Delta y^2}\sum_{v_1,v_2=-N_v}^{N_v-1} a(v_1)a(v_2)\,{}_{\phi x}P_{i+\frac{1}{2},j+v_1+v_2+1,k}^{n+\frac{1}{2}} \\
&= 2\,{}_{\phi x}E_{i+\frac{1}{2},j,k}^{n} + \frac{\Delta t}{\varepsilon\Delta y}\sum_{v_1=-N_v}^{N_v-1} a(v_1)\,{}_{\phi z}H_{i+\frac{1}{2},j+v_1+\frac{1}{2},k}^{n},
\end{aligned}
\tag{8a}
$$

$$ {}_{\phi z}H^{n+\frac{1}{2}}_{i+\frac{1}{2},j+\frac{1}{2},k} = {}_{\phi z}H^{n}_{i+\frac{1}{2},j+\frac{1}{2},k} + \frac{\Delta t}{2\mu\Delta y}\sum_{v_2=-N_v}^{N_v-1} a(v_2)\,{}_{\phi x}P^{n+\frac{1}{2}}_{i+\frac{1}{2},j+v_2+1,k} \quad ,(8b) $$

for the 3D case, respectively.

It can be found that the right-hand sides of equations (7) and (8) become much simpler. Table 1 is listed in the number of arithmetic operations for the two methods. Furthermore, it is easy to know that the reformulated equations do not change the accuracy of the LOD-MRTD method.

Table 1: Number of multiplication / division operations for the conventional LOD-MRTD and the reformulated LOD-MRTD algorithms.

3D MRTD method		Conventional LOD-MRTD	Reformulated LOD-MRTD
Implicit	multiplication/ division	$(2*(2N_v)^2+7)$ $+(2N_v+3)$	$2N_v+4$
	For D2 scaling function (N=2, Nv=3)	88	10
Explicit	multiplication/ division	$2N_v+4$	$2N_v+4$
	For D2 scaling function (N=2, Nv=3)	10	10
Total	multiplication/ division	$(2*(2N_v)^2+8)$ $+2*(2N_v+3)$	$4N_v+8$
	For D2 scaling function (N=2, Nv=3)	98	20

III. CHARACTERISTICS ANALYSIS

The unconditional stability and dispersion equations of the LOD-MRTD in 3D case have been discussed in [16]. Here, we talk about these characteristics in 2D case. For the unconditional stability of the LOD-MRTD method, we employ the Fourier method described in [18-19] to obtain. The field components in the spatial spectral domain for the TMz wave can be written as,

$$ \begin{aligned} {}_{z}E^{n}_{I,J} &= E^{n}_{z}e^{j(k_x I\Delta x + k_y J\Delta y)} \\ {}_{x}H^{n}_{I,J+\frac{1}{2}} &= H^{n}_{x}e^{j\left[k_x I\Delta x + k_y (J+\frac{1}{2})\Delta y\right]} \\ {}_{y}H^{n}_{I+\frac{1}{2},J} &= H^{n}_{y}e^{j\left[k_x (I+\frac{1}{2})\Delta x + k_y J\Delta y\right]} \end{aligned} \qquad (9) $$

where k_x and k_v are wave numbers along the x- and y-directions, respectively, and denote the field vector in the spatial spectral domain as,

$$ \mathrm{X}^n = \begin{bmatrix} E^n_z \\ H^n_x \\ H^n_y \end{bmatrix} . \qquad (10) $$

The Fourier analysis can be performed by substituting equations (9) and (10) into equation (3), then the following equation is obtained,

$$ \mathrm{X}^{n+\frac{1}{2}} = \Lambda_1 \mathrm{X}^n \quad \text{and} \quad \mathrm{X}^{n+1} = \Lambda_2 \mathrm{X}^{n+\frac{1}{2}} \qquad (11) $$

where,

$$ \Lambda_1 = \begin{bmatrix} \dfrac{1+\frac{W_y^2}{\varepsilon\mu}}{1-\frac{W_y^2}{\varepsilon\mu}} & \dfrac{-\frac{2W_y}{\varepsilon}}{1-\frac{W_y^2}{\varepsilon\mu}} & 0 \\ \dfrac{-\frac{2W_y}{\mu}}{1-\frac{W_y^2}{\varepsilon\mu}} & \dfrac{1+\frac{W_y^2}{\varepsilon\mu}}{1-\frac{W_y^2}{\varepsilon\mu}} & 0 \\ 0 & 0 & 1 \end{bmatrix} $$

$$ \Lambda_2 = \begin{bmatrix} \dfrac{1+\frac{W_x^2}{\varepsilon\mu}}{1-\frac{W_x^2}{\varepsilon\mu}} & 0 & \dfrac{\frac{2W_x}{\varepsilon}}{1-\frac{W_x^2}{\varepsilon\mu}} \\ 0 & 1 & 0 \\ \dfrac{\frac{2W_x}{\mu}}{1-\frac{W_x^2}{\varepsilon\mu}} & 0 & \dfrac{1+\frac{W_x^2}{\varepsilon\mu}}{1-\frac{W_x^2}{\varepsilon\mu}} \end{bmatrix}, $$

with $W_x = j\dfrac{\Delta t}{\Delta x}\sum_{v=0}^{N_v-1} a(v)\sin(k_x(v+\dfrac{1}{2})\Delta x)$ and

$$ W_y = j\frac{\Delta t}{\Delta y}\sum_{v=0}^{N_v-1} a(v)\sin(k_y(v+\frac{1}{2})\Delta y) . $$

Therefore,

$$\mathrm{X}^{n+1} = \Lambda \mathrm{X}^{n} = \Lambda_2 \Lambda_1 \mathrm{X}^{n} \tag{12}$$

$$\Lambda = \begin{bmatrix} \dfrac{1+\dfrac{W_x^2}{\varepsilon\mu}}{1-\dfrac{W_x^2}{\varepsilon\mu}} \cdot \dfrac{1+\dfrac{W_y^2}{\varepsilon\mu}}{1-\dfrac{W_y^2}{\varepsilon\mu}} & -\dfrac{1+\dfrac{W_x^2}{\varepsilon\mu}}{1-\dfrac{W_x^2}{\varepsilon\mu}} \cdot \dfrac{\dfrac{2W_y}{\varepsilon}}{1-\dfrac{W_y^2}{\varepsilon\mu}} & \dfrac{\dfrac{2W_x}{\varepsilon}}{1-\dfrac{W_x^2}{\varepsilon\mu}} \\ -\dfrac{\dfrac{2W_y}{\mu}}{1-\dfrac{W_y^2}{\varepsilon\mu}} & \dfrac{1+\dfrac{W_y^2}{\varepsilon\mu}}{1-\dfrac{W_y^2}{\varepsilon\mu}} & 0 \\ \dfrac{\dfrac{2W_x}{\mu}}{1-\dfrac{W_x^2}{\varepsilon\mu}} & -\dfrac{\dfrac{2W_x}{\mu}}{1-\dfrac{W_x^2}{\varepsilon\mu}} \cdot \dfrac{\dfrac{2W_y}{\varepsilon}}{1-\dfrac{W_y^2}{\varepsilon\mu}} & \dfrac{1+\dfrac{W_x^2}{\varepsilon\mu}}{1-\dfrac{W_x^2}{\varepsilon\mu}} \end{bmatrix}. \tag{13}$$

Here, Λ is called the amplification matrix. In order to value the eigen values of the matrix Λ, the following eigen equation of Λ can be used.

$$\begin{aligned} &\left|\mathrm{I}\lambda - \Lambda\right| \\ &= \left(\lambda - \frac{1-r_x^2}{1+r_x^2}\frac{1-r_y^2}{1+r_y^2}\right)\left(\lambda - \frac{1-r_x^2}{1+r_x^2}\right) \\ &\times \left(\lambda - \frac{1-r_y^2}{1+r_y^2}\right) - \left(\frac{2r_x}{1+r_x^2}\frac{2r_y}{1+r_y^2}\right)^2 \\ &+ \left(\lambda - \frac{1-r_x^2}{1+r_x^2}\right)\left(\frac{1-r_x^2}{1+r_x^2}\right)\left(\frac{2r_y}{1+r_y^2}\right)^2 \\ &+ \left(\lambda - \frac{1-r_y^2}{1+r_y^2}\right)\left(\frac{1-r_y^2}{1+r_y^2}\right)\left(\frac{2r_x}{1+r_x^2}\right)^2 = 0 . \end{aligned} \tag{14}$$

The eigen values of Λ can be found, with the help of Matlab, as

$$\lambda_1 = 1 \tag{15a}$$

$$\lambda_{2,3} = -\frac{r_x^2 + r_y^2 + r_x^2 r_y^2 - 1 \pm 2j\sqrt{r_x^2 + r_y^2 + r_x^2 r_y^2}}{r_x^2 + r_y^2 + r_x^2 r_y^2 + 1}, \tag{15b}$$

where $r_x = \dfrac{c\Delta t}{\Delta x}\sum_{v=0}^{N_v-1} a(v)\sin(k_x(v+\frac{1}{2})\Delta x)$, $c = \dfrac{1}{\sqrt{\varepsilon\mu}}$,

$$r_y = \frac{c\Delta t}{\Delta y}\sum_{v=0}^{N_v-1} a(v)\sin(k_y(v+\frac{1}{2})\Delta y) .$$

It can be found that all the three eigen values have magnitude of unity, so the LOD-MRTD is unconditionally stable. Further, we can derive the dispersion equation of the LOD-MRTD method [20],

$$\tan^2\left(\frac{\omega\Delta t}{2}\right) = r_x^2 + r_y^2 + r_x^2 r_y^2 \quad . \tag{16}$$

Equation (16) is the same as that of the ADI-MRTD method, which means that the LOD-MRTD and the ADI-MRTD methods have the same order dispersion errors.

IV. NUMERICAL RESULTS

To examine the performance of the LOD-MRTD, we consider a 2D parallel plate resonator. The total size is 1m × 1m and $\Delta x = \Delta y = \Delta s = 0.05$m for the TM_z polarization model. The CFL number α for the MRTD scheme is chosen as 0.3, and the parameters $\varepsilon = \varepsilon_0$ and $\mu = \mu_0$. It is noted that when one calculates the resonant frequency, we need to set the adequate time step, so that the frequency resolution of FFT meets the requirements to ensure the validity of the results data of the resonant frequency.

Figure 1 shows the relation of the computational errors increasing with the decrease of N_c and the CFLN. Figure 2 is the comparison of error of the proposed method with those of the ADI-MRTD method when CFLN takes different values. The calculation accuracy of the LOD-MRTD method is consistent with the ADI-MRTD method, and also agrees with the theoretical analysis described in the above section. From Fig. 2, we find that the simulation results of the LOD-MRTD method are reasonable and acceptable when the stability coefficient is taken some times as the classical MRTD method. Table 2 lists the parameters used in the LOD-MRTD and the MRTD methods, here CFLN = $\alpha_{LOD\text{-}MRTD} / \alpha_{MRTD}$, $N_c = \lambda/\Delta s$.

V. CONCLUSIONS

In this paper, an improved LOD-MRTD method is studied. The improved LOD-MRTD is more efficient than the conventional LOD -MRTD without loss of accuracy. A 2D case is calculated to demonstrate the characteristics of the LOD-MRTD.

Table 2: Analytic solutions and the results of the MRTD and the LOD-MRTD methods.

Mode (m, n)	1,1	1,3	3,3	1,5	3,5	5,5	3,7	5,7	1,9
N_c	28.28	12.65	9.43	7.84	6.86	5.66	5.25	4.65	4.42
Analytic (GHz)	0.2121	0.4743	0.6364	0.7649	0.8746	1.0607	1.1422	1.2904	1.3583
MRTD/ $\alpha_{MRTD} = 0.3$	0.2124	0.4749	0.6378	0.7678	0.8789	1.0675	1.1542	1.3049	1.3837
LOD-MRTD/ CFLN=1	0.2118	0.4736	0.6354	0.7629	0.8722	1.0565	1.1377	1.2842	1.3519
LOD-MRTD/ CFLN=2	0.2118	0.4712	0.6311	0.7526	0.8606	1.0388	1.1102	1.2506	1.2970
LOD-MRTD/ CFLN=4	0.2115	0.4630	0.6165	0.7166	0.8200	0.9427	0.9760	1.0193	1.1362
LOD-MRTD/ CFLN=5	0.2109	0.4565	0.6060	0.6934	0.7935	0.8921	0.9360	0.9658	1.0523
LOD-MRTD/ CFLN=10	0.2075	0.4150	-	-	-	-	-	-	-
LOD-MRTD/ CFLN=15	0.2018	0.3682	-	-	-	-	-	-	-
LOD-MRTD/ CFLN=20	0.1948	0.3252	-	-	-	-	-	-	-

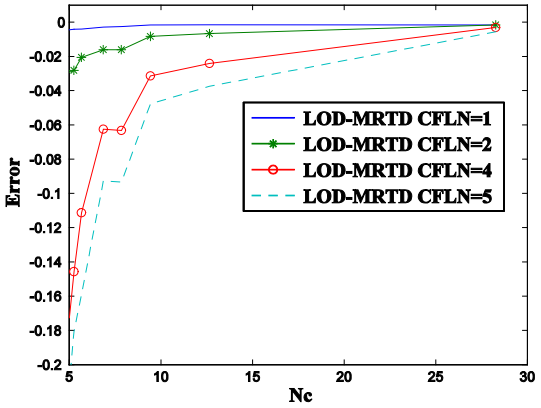

Fig. 1. The error varied of the LOD-MRTD method for different N_c and CFLN.

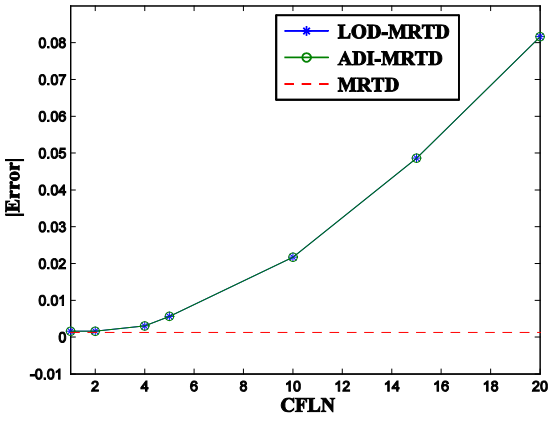

Fig. 2. The error comparisons of the LOD-MRTD and the ADI-MRTD methods.

ACKNOWLEDGEMENT

This work was supported by the National Nature Science Foundation of China under Contract 60771018.

REFERENCES

[1] K. S. Yee, "Numerical solution of initial boundary value problems involving Maxwell's equations in isotropic media," *IEEE Trans. Antennas Propagat.,* vol. 14, no. 3, pp. 302-307, Apr. 1996.

[2] A. Taflove, *Computational Electromagnetics: The Finite-Difference Time-Domain Method*, Artech House, Norwood, MA, 2005.

[3] M. Krumpholz and L. P. B. Katehi, "MRTD: new time-domain schemes based on mltiresolution aalysis," *IEEE Trans. Microw. Theory Tech.,* vol. 44, no. 4, pp. 555-571, Apr. 1996.

[4] Y. Chen, Q. Cao, and R. Mittra, *Multi-resolution Time Domain Scheme for Electromagnetic Engineering*, John Wiley & Sons Inc., 2005.

[5] C. Represa, C. Pereira, A. C. L. Cabeceira, I. Barba, and J. Represa, "An approach to multi-resolution in time domain based on the discrete wavelet transform," *ACES Journal*, vol. 18, no. 3, pp. 210-218, 2003.

[6] Q. H. Liu, "The PSTD algorithm: a time-domain method requiring only two cells per wavelength," *Microwave Opt. Technol. Lett*, vol. 15, no. 3, pp. 158-165, 1997.

[7] L. Li and Q. Cao, "Application of the unconditionally stable ADI-MPSTD for

scattering analysis," *ICMMT2008 Proceedings,* Nanjing, China, vol. 2, pp. 760-763, April 2008.

[8] T. Deveze and W. Tabbara, "A fourth-order scheme for the FDTD algorithm applied to Maxwell's equations," *IEEE Trans. Antennas Propagat. Soc. Int. Symp*., Chicago, IL, pp. 346-349, 1992.

[9] Q. Cao and K. K. Tamma, "Multi-resolution time domain based different wavelet basis studies of scattering of planar stratified medium and rectangular dielectric cylinder," *ACES Journal*, vol. 20, no. 1, pp. 86-95, 2005.

[10] S. Barmada, A. Musolino, and M. Raugi, "Wavelet based time domain solution of Multiconductor transmission lines with skin and proximity effect," *IEEE Trans. Electromagn. Compat.*, vol. 47, no. 4, pp. 774-780, Nov. 2005.

[11] S. Barmada and M. Raugi, "New wavelet based approach for time domain simulations," *IEEE Trans. Antennas. Propagat.,* vol. 51, no. 7, pp. 1590-1598, July 2003.

[12] Q. Cao, R. Kanapady, and F. Reitich, "High-order Runge-Kutta Multi-resolution time-domain methods for computational electromagnetics," *IEEE Trans. Microw. Theory Tech*., vol. 54, pp. 3316-3326, 2006.

[13] Z. Chen and J. Zhang, "An unconditionally stable 3-D ADI-MRTD method free of the CFL stability condition," *IEEE Microwave and Wireless Components Letters*, vol. 11, pp. 349-351, 2001.

[14] M. K. Sun and W. Y. Tam, "Stability and dispersion analysis of ADI-MRTD and ADI high-order schemes," *Microwave Opt. Technol. Lett.*, vol. 45, no. 1, pp. 43-46, 2005.

[15] J. Shibayama, M. Muraki, J. Yamauchi, and H. Nakano, "Efficient implicit FDTD algorithm based on locally one-dimensional scheme," *Electron. Lett.*, vol. 41, no. 19, pp. 1046-1047, 2005.

[16] J. Ryu, W. Lee, and H. Kim, "A three-dimensional locally one-dimensional multi-resolution time-domain method using Daubechies scaling function," *Journal of The Korea Electromagnetic Engineering Society*, vol. 9, no. 4, pp. 175-231, 2009.

[17] E. L. Tan, "Fundamental schemes for efficient unconditionally stable implicit finite-difference time-domain methods", *IEEE Trans. Antennas Propagat.*, vol. 56, no. 1, pp. 170-177, Jan. 2008.

[18] Y. Liu, "Fourier analysis of numerical algorithms for the Maxwell's equations," *J. Comput. Phys.*, vol. 124, pp. 396-416, 1996.

[19] F. Zheng, Z. Chen, and J. Zhang, "Toward the development of a three-dimensional unconditionally stable finite-difference time-domain method," *IEEE Trans. Microwave Theory Tech.*, vol. 48, no. 9, pp. 1550-1558, Sept. 2000.

[20] G. Sun and C. W. Trueman, "Analysis and numerical experiments on the numerical dispersion of two-dimensional ADI-FDTD," *IEEE Antennas and Wireless Propagation Letters*, vol. 2, pp. 78-81, 2003.

Electromagnetic Device Optimization Based on Electromagnetism-Like Mechanism

H. R. E. H. Bouchekara

Electrical Laboratory of Constantine, LEC, Department of Electrical Engineering,
University of Mentouri Constantine, 25000 Constantine, Algeria
bouchekara.houssem@gmail.com

Abstract ─ The algorithm based on the Electromagnetism-Like mechanism results from the Coulomb's law of electromagnetics. In this paper, a novel stochastic approach based on the Electromagnetism-Like mechanism is applied to the optimization of electromagnetic devices. In order to show the effectiveness of the proposed method, it has been demonstrated on a magnetizer by optimizing its pole face to obtain the desired sinusoidal magnetic flux density distribution.

Index Terms ─ Electromagnetic devices, Electromagnetism-Like mechanism, finite element method, and optimization.

I. INTRODUCTION

In all areas of engineering the efficient and effective design of products is crucial. Therefore, designers are faced with the challenge of optimizing ever more complex components, devices and systems this is more specifically so in the field of electromagnetic devices (EMD) where the optimization is of paramount importance [1-3]. In the area of EMD, building physical prototypes is a time consuming and prohibitively high cost approach and can represent a large percentage of the total costs involved in bringing a product to market [1, 4]. Reducing this time and cost burden has been, and still is, a key issue. Therefore, designing engineers have spent considerable time and effort on the creation of algebraic models to simulate the physical EMD and eventually to predict its performance [1]. Nowadays, real laboratories are replaced by computer environments for this purpose. In these virtual laboratories the physical EMD is replaced by a virtual prototype, which can be tested with the same level of accuracy as the physical EMD but with significant reductions in time and cost [4]. Moreover, with the development of more accurate and complex models in addition to the development of cheap and powerful computing systems, we are able now to simulate the physics involved in the operation of an EMD at a high level, which is as good as, or sometimes better than, what can be achieved from a physical prototype in a real laboratory [1].

Prototype evaluation is a critical component of the design process. In general, such a system explores the design space in order to find a set of parameters, which most nearly meet the specifications without violating a set of imposed constraints [5]. Such a search has two basic steps. In order to improve the performance of an existing prototype device, this last one is modified which represents the first step. The second step consists of measuring that performance to determine if any improvements have been done. This is generally described as an optimization process [1]. Thus, the purpose of optimization within a design activity is to find an improved solution for given requirements [1].

In general, searching techniques can be divided into two distinctive groups: deterministic and stochastic techniques [6]. The deterministic searching techniques are usually based on the calculation of the gradient of the objective function. On the other hand, for stochastic methods, computation of gradients is not necessary [6].

In the field of EMD design, optimization problems are very complex and involve many difficulties [7, 8]. Therefore, in many cases, deterministic methods are inappropriate for EMD

Submitted On: Sept. 23, 2012
Accepted On: Jan. 3, 2013

optimization and stochastic techniques become a necessity [2]. Therefore, recently stochastic methods have been widely applied for multivariable inverse shape optimization, mainly due to their ability to avoid being trapped in a local optimum of the objective function [6]. Consequently, many researchers have devoted themselves in finding some reliable stochastic optimization methods, such as Electromagnetism-Like mechanism (EM) method.

The EM algorithm, which is proposed by Birbil and Fang [9] is one of the newest meta-heuristic. It is based on the attraction-repulsion mechanism of electromagnetism theory to move the sample points towards the optimality [10]. This method is applicable on nonlinear problems with bounded variables. This method considers each point as a charged particle. Each particle is impressed by other particles and consequently transmitted to better solution space [10]. The ease implementation and flexibility of the EM gains more attention from a lot of researchers, and it has been extended and applied in different researches, most of which have reported its promising performance [10].

In this work our main objective is to apply the EM for the optimization of EMD. First, we present the EM method, its advantages and how it works. Next, we illustrate the performance of our proposed method on the optimization of the pole face shape of a magnetizer problem. Finally, we conclude our paper with some final remarks and points.

II. ELECTROMAGNETISM-LIKE MECHANISM

As mentioned earlier, the EM is a flexible, effective, and a population based heuristic method, which is used to search for the optimal solution of global optimization problems proposed by Bïrbïl and Fang in 2003 [9]. It originates from the attraction–repulsion mechanism of the electromagnetism theory of physics by considering potential solutions as electrically charged particles spread around the solution space.

This heuristic EM consists of four stages. These are initialization of the algorithm, calculation of the total force exerted on each particle, movement along the direction of the force, and application of neighbourhood search to exploit the local minima [9]. Each of these four stages is discussed in more detail below. The general EM algorithm proposed in Birbil and Fang's paper is described in Algorithm 1.

Algorithm 1: EM (m, MAXITER, LSIT ER, δ)
m: number of sample points,
MAXITER: maximum number of iterations,
LSITER: maximum number of local search iterations,
δ: local search parameter, δ ∈ [0, 1].

```
1: Initialize()
2: iteration ←1
3: while iteration <MAXITERdo
4:       Local(LSITER, δ)
5:       F ←CalcF()
6:       Move(F)
7:       iteration ←iteration + 1
8: end while
```

As mentioned earlier, the first stage is the initialization of the algorithm. In this procedure, *m* particles are randomly generated inside the feasible domain, which is an *n* dimensional hyper-solid. Each coordinate of a point is assumed to be uniformly distributed among the corresponding upper and lower bounds. After a point is sampled from the space, the objective function value for the point is calculated using the function pointer *f(x)*. At the end of the initialization procedure, *m* points are identified and the point that has the best function value is stored in x^{best} [9, 11].

After determination of the initial solutions, the second step is to conduct a local search for the local optimum. Local search can be divided into three kinds, i.e., no local search, local search only on current better particle and local search on all particles [12]. Any local method of optimization such as hill-climbing [13, 14] or gradient-based methods [15] could be introduced in this phase. Random selection near the original solution is proposed in the primary algorithm [11].

The third step is to calculate the total force exerted on each particle. Here the superposition principle of the electromagnetism theory is used. The proportion of the charges of the points and the inverse proportion of the distance between the points are utilized to calculate the force exerted on the particle through other points [11]. In each iteration we compute the charges of the particles according to their objective function values. The

virtual charge q^i of the i-th particle determines point i's power of attraction or repulsion. It is determined by the cost function value, and is calculated by,

$$q^i = \exp\left(-n\frac{f(x^i)-f(x^{best})}{\sum_{k=1}^{m}\left(f(x^k)-f(x^{best})\right)}\right) \quad \forall i \quad (1)$$

where $f(.)$ denotes the cost function and m denotes the population size. The $f(x^{best})$ denotes the best cost function value. The particle with largest charge (i.e., best cost function value) is called the "optimum particle". A particle will have stronger attraction, as it appears near the optimum particle. The particle attracts other particles with better cost function values, and repels other particles with worse cost function values [12].

In order to improve efficiency and solution accuracy by exploring the attraction-repulsion mechanism of the EM algorithm, [16] studied the effect of charges associated with each point in the population. The total force exerted on the i-th particle is determined from the Coulomb's law and superposition principle, and is given as,

$$F^i = \sum_{\substack{j=1 \\ j\neq i}}^{m} \begin{cases} (x^j - x^i)\dfrac{q^i q^j}{\|x^j - x^i\|^2} \\ if f(x^j) < f(x^i) \\ (x^i - x^j)\dfrac{q^i q^j}{\|x^j - x^i\|^2} \\ if f(x^j) \geq f(x^i) \end{cases} \forall i \quad (2)$$

where $f(x^j) < f(x^i)$ represents attraction and $f(x^j) \geq f(x^i)$ represents repulsion. From equation (2), we conclude that the resultant force between particles is proportional to the product of the charges and is in inverse proportion to the distance between the particles. Of course, a particle will not produce the force to affect itself. In general, the force in equation (2) is normalized as,

$$F^i = \frac{F^i}{\|F^i\|} \quad \forall i \,. \quad (3)$$

The final stage involves moving along the orientation of the force. After calculating the total force of one point, this point moves by a random step length in the path of the force to cause the particles to move into any unvisited zones along this path. The update of each particle depends on the resultant force, and is given by,

$$x^i = \begin{cases} x^i + \alpha F^i(b_{upper} - x^i) \\ if F^i > 0 \\ x^i + \alpha F^i(x^i - b_{lower}) \\ if F^i \leq 0 \end{cases}, \quad \forall i;\ \ i \neq best \,, \quad (4)$$

where b_{upper} is the upper bound, b_{lower} is the lower bound, and α is a random value uniformly distributed between zero and one. The particle moves toward the upper bound by a random step length α as the resultant force is positive, whereas it moves toward the lower bound as the resultant force is negative. In the mechanism, the optimum particle of the population does not move, because it has the best cost function value and then attracts all other particles [12].

The second through the fourth stages are repeated until a termination criterion is reached. The termination criterion could be the maximum number of iterations given by the user or the amount of iterations performed without replacing the current optimal solution. In other words, if the current best point is not changed for certain number of iterations, the algorithm may be stopped. However, this decision has to be studied carefully since algorithm may be stopped before converging to the global optimum. On the other hand, un-necessary function evaluations may be avoided by stopping earlier [9]. In the initial algorithm, the maximum number of iterations was used [11]. EM has been successfully applied to various cases [11]. As the EM algorithm has not yet been utilized for EMD optimization, this study attempts to apply EM for this purpose.

III. APPLICATION EXAMPLE

In shape optimization tasks, each set of particles or charges of the total number of sample points represents the geometry of a specific design. This design is translated into a model to be solved using the Finite Element Method (FEM). Then a fitness value is obtained after solving this model. Thus, it is a paramount task to identify the optimal set of parameters by comparing the obtained fitness. These parameters are used to form the outlines of different regions of the modeled EMD, in our case the magnetizer.

The initial version of the magnetizer problem was the pole face shape of a motor. Then, it has been developed and has become an independent

benchmark for the optimization of EMD called the magnetizer problem. The most important constraint of the design is to have a smooth pole face shape with no zigzags. This is achieved by not allowing individual nodes on the pole face to move independently but by determining their position from the 3rd order polynomial used to define the pole face geometry as it is detailed in the following section. The advantage of this problem is its ability to consider more design variables by adding more nodes to the pole face shape.

A. Magnetizer problem description

The application of EM for electromagnetic device optimization is illustrated on a magnetizer problem modeled as a 2D magneto static field analysis using FEM. The geometry of the modeled part of the magnetizer example is shown in Fig. 1. It has four main parts, which are the pole face, the coil or windings, the outer shell, and the material to be magnetized. In the FEM model, a low permeability (close to that of the air) is assigned to the object to be magnetized (non-magnetic material). However, the pole face and the outer shell are treated as magnetic materials and a permeability of 1000 is assigned to them. A high current is applied to the coil region. The non-linearity is not taken into account when solving the governing equations of the model. The goal is to optimize the magnetizer's pole shape in order to obtain a sinusoidal increasing magnetic flux density along chord AB positioned halfway through the width of the magnetized piece.

The pole shape is modeled using Uniform Non-rational Cubic B-splines (UNBS) with n control points. UNBS interpolation provides local control of the curve i.e., when a control point is moved, this affects only a small part of the curve. A B-spline is constructed from a string of curve segments whose geometry is determined by the control points. These curves are known as piecewise polynomials. A curve segment does not have to pass through a control point, unless this control point is repeated at least three times, which is desirable at the two end-points [17, 18].

Once the locations of the n control points are set, the shape of the pole face is constructed from a series of curve segments S_1, S_2, S_3,…,S_{n-3}. As the curve is cubic, curve segment S_i is influenced by the control points P_i, P_{i+1}, P_{i+2}, P_{i+3}, and curve segment S_{i+1} is influenced by P_{i+1}, P_{i+2}, P_{i+3}, P_{i+4}. There are n control points, so there are n-3 curve segments. A single segment $S_i(t)$ of a B-spline curve is defined by [19],

$$\begin{aligned} S_i(t) &= \frac{(1-t)^3}{6} P_i(t) \\ &+ \frac{3t^3 - 6t^2 + 4}{6} P_{i+1}(t) \\ &+ \frac{-3t^3 + 3t^2 + 3t + 1}{6} P_{i+2}(t) \\ &+ \frac{t^3}{6} P_{i+3}(t) . \end{aligned} \tag{5}$$

In equation (5), the coefficients are called the B-spline blending functions and $0 \le t \le 1$.

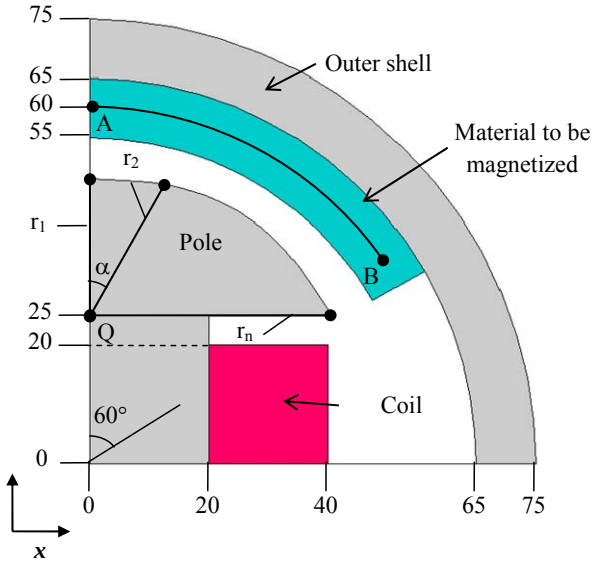

Fig. 1. Geometry of the magnetizer to be optimized.

In this work, we have chosen to apply the EM on two cases called CASE 1 and CASE 2. In CASE 1 the pole shape is modeled using eight control points, P_1, P_2, P_3, and P_4, where P_1 and P_2 are repeated three times each to force the curve to pass at these two ending points. For the eight control points of the pole face shape, five curve segments are generated. The nodes on the pole face are then placed on this B-spline approximation.

In CASE 2 we have added two more control points. Similarly to CASE 1, once the locations of the control points are set, the curve that shapes the

pole face is constructed with B-splines. In this case the pole face curve touches the control points P_1 and P_6, each of which is represented with three coinciding B-spline control points.

1. Design variables

There are n (n = 4 for CASE 1 and n = 6 for CASE 2) points that control the pole face's shape, which are noticed as P_1 through P_n. The control points are mapped onto a polar coordinate system with its origin at Q as shown in Fig. 1. The radial coordinates, r_1 through r_n (separated from each other by 30° and 18° for CASE 1 and CASE 2, respectively), constitute the n design variables with mapping ranges given in Table 1 for CASE 1 and in Table 2 for CASE 2. These ranges are calculated for each design parameter based on the geometry of the device and the number of control points. Once determined, the radial and angular coordinates of a control point are mapped back to the x and y coordinates and UNBS are used to approximate the shape of the pole face from the n control points.

Table 1: Design variables and their ranges used in the magnetizer problem for CASE 1.

Design variable	Lower bound [mm]	Upper bound[mm]
r_1	22.0	29.5
r_2	22.0	31.3
r_3	22.0	38.7
r_4	22.0	48.5

Table 2: Design variables and their ranges used in the magnetizer problem for CASE 2.

Design variable	Lower bound [mm]	Upper bound[mm]
r_1	22.0	29.5
r_2	22.0	30.2
r_3	22.0	32.3
r_4	22.0	36.0
r_5	22.0	41.4
r_6	22.0	48.5

2. Objective function

The difference which has to be minimized between the desired and calculated magnetic flux densities along the chord AB (as shown in Fig. 1) is,

$$F = \sum_{1}^{N} \frac{|B_{desired} - B_{calculated}|}{B_{desired}} \quad (6)$$

where N is the number of test points. $B_{desired}$ and $B_{calculated}$ represent the desired and calculated magnetic flux densities, respectively. The desired flux density distribution $B_{desired}$, is calculated using the following formula,

$$B_{desired} = B_0 \sin(\theta) \quad 35° \le \theta \le 89° \quad (7)$$

where B_0 is the maximum value (magnitude) of the desired magnetic flux density distribution to be specified by the designer. In this paper B_0 is chosen to be 0.27 T.

3. EM optimization parameters

The proposed EM based method has been implemented using Matlab Software. Initially, several runs have been done with different values of the EM key parameters (such us the number of sample points and the local search parameters) in order to identify the best combination. In our implementation the EM runs for each case with the key parameters given in Table 3.

B. Results

The results obtained when the EM described above runs for CASE 1 and CASE 2 are given in Table 4 and 5 and Fig. 2 through Fig. 7. In Table 4 and Table 5 the values of the optimized control points are given for CASE 1 and CASE 2, respectively. Figures 2 and 5 show the optimized magnetizer pole face and the isopotential lines for CASE 1 and CASE 2, respectively. In Fig. 3 the desired magnetic flux density distribution along chord AB is compared against the distribution of the optimal solution calculated using EM for CASE 1. Figure 6 gives the same comparison for CASE 2. We can notice that there is a clear improvement, which is due to the higher number of control points. Finally, Figs. 4 and 6 sketch the changes in the best fitness of each iteration over the 50 iterations for CASE 1 and CASE 2, respectively. We can notice here that the fitness for CASE 1converges quickly and to a best value than CASE 2. This is due to the same reason mentioned earlier.

Table 3: EM optimization parameters for CASE 1 and CASE 2.

Name	Description	Value
n	Dimension of the problem (number of design variables)	CASE 1: 4 CASE 2: 6
m	Number of sample points	10
MAXITER	Maximum number of iterations	50
LSITER	Maximum number of local search iterations	5
δ	Local search parameter, $\delta \in [0,1]$	1×10^{-4}

Table 4: Coordinates of the optimized control points for the magnetizer of CASE 1.

Design variable	Optimal solution [mm]
r_1	25.458
r_2	27.576
r_3	33.349
r_4	37.626

Table 5: Coordinates of the optimized control points for the magnetizer of CASE 2.

Design variable	Optimal solution [mm]
r_1	25.239
r_2	26.338
r_3	27.583
r_4	30.544
r_5	34.318
r_6	37.405

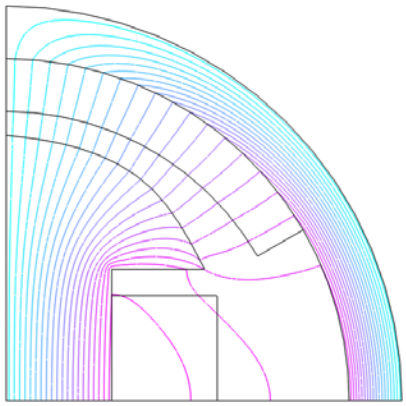

Fig. 2. Optimized magnetizer pole face and iso-potential lines for CASE 1.

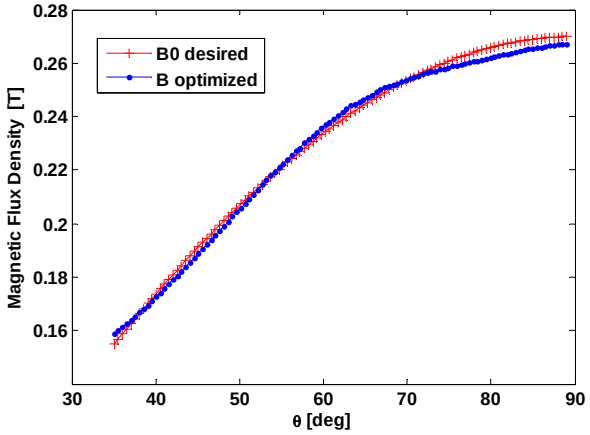

Fig. 3. Comparison between the desired and optimal magnetic flux density for CASE 1.

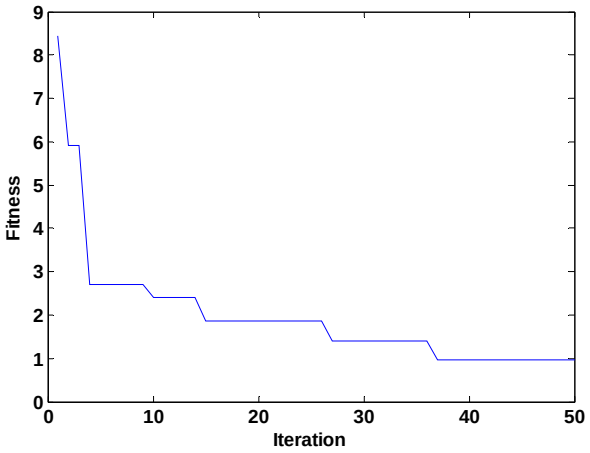

Fig. 4. Change of the best fitness over iterations for CASE 1.

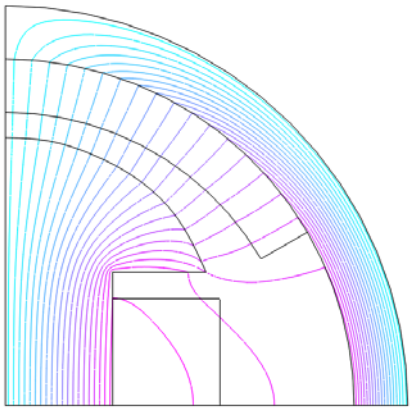

Fig. 5. Optimized magnetizer pole face and isopotential lines for CASE 2.

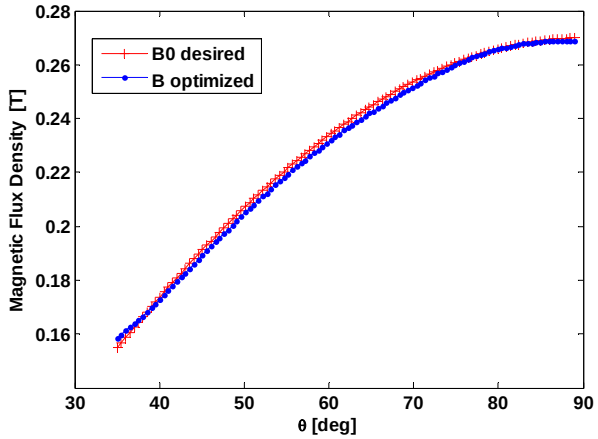

Fig. 6. Comparison between the desired and optimal magnetic flux density for CASE 2.

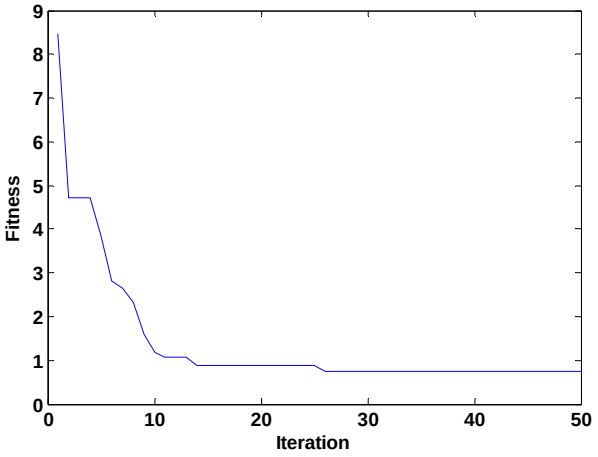

Fig. 7. Change of the best fitness over iterations for CASE 2.

IV. CONCLUSION

This paper describes an electromagnetism based algorithm, which is a powerful yet easy algorithm for EMD design and optimization. The results obtained in this paper show that the EM constitutes a potential and efficient tool for the design and optimization of EMD. The proposed method is successfully applied on a magnetizer shape optimization problem. Two cases with different number of control points are studied. In both cases the EM converges rapidly to optimum (in less than 50 iterations). However, the comparison of the results between these two cases indicates that the efficiency is increased in CASE 2. These improvements are primarily attributed to the higher number of control points used.

EM algorithm is a free derivative method it uses only the fitness value. These characteristics render it robust as it can adapt to the environment. EM can be used as a stand-alone approach or as an accompanying algorithm for other methods. The strength of the algorithm lies in the idea of directing the sample points toward local optimizers by utilizing an attraction-repulsion mechanism. Finally, EM is fully parallelizable. The evaluation of each set of points is independent from other sets. This trait makes the use of Connection Machine type computers or work stations farms where CPUs are shared very profitable for EM applications.

REFERENCES

[1] J. Ouyang and D. A. Lowther, "Comparison of evolutionary and rule-based strategies for electromagnetic device optimization," *IEEE Transactions on Magnetics*, vol. 48, no. 2, pp. 371-374, 2012.

[2] P. Alotto, "A hybrid multi objective differential evolution method for electromagnetic device optimization," *COMPEL: The International Journal for Computation and Mathematics in Electrical and Electronic Engineering*, vol. 30, no. 6, pp. 1815-1828, 2011.

[3] D. A. G. Vieira, A. C. Lisboa, and R. R. Saldanha, "An enhanced ellipsoid method for electromagnetic devices optimization and design," *IEEE Transactions on Magnetics*, vol. 46, no. 8, pp. 2843-2851, 2010.

[4] O. A. Mohammed, D. A. Lowther, M. H. Lean, and B. Alhalabi, "On the creation of a generalized design optimization environment for electromagnetic devices," *IEEE Transactions on Magnetics*, vol. 37, no. 5, pp. 3562-3565, 2001.

[5] J. Seguin, F. Dandurand, D. A. Lowther, and J. K. Sykulski, "The optimisation of electromagnetic devices using a combined finite element/neural network approach with on-line training," *COMPEL: The International Journal for Computation and Mathematics in Electrical and Electronic Engineering*, vol. 18, no. 3, pp. 266-274, 1999.

[6] Y. Yokose, V. Cingoski, K. Kaneda, and H. Yamashita, "Shape optimization of magnetic devices using genetic algorithms with dynamically adjustable parameters," *IEEE Transactions on Magnetics*, vol. 35, no. 3, pp. 1686-1689, 1999.

[7] M. Huang, S. Yang, J. Teng, Q. Zhu, and Z. -P. Nie, "Multi objective optimization and design of a luneberg lens antenna with multiband multi-polarized feed-system," *Progress In*

Electromagnetics Research, vol. 129, pp. 251-269, 2012.

[8] A. Qing, "Electromagnetic inverse scattering of multiple two-dimensional perfectly conducting objects by the differential evolution strategy," *IEEE Transactions on Antennas and Propagation*, vol. 51, no. 6, pp. 1251- 1262, 2003.

[9] S. I. Birbil and S. C. Fang, "An electromagnetism-like mechanism for global optimization," *Journal of Global Optimization*, vol. 25, 263-282, 2003.

[10] F. Jolai, R. Tavakkoli-Moghaddam, A. Golmohammadi, and B. Javadi, "An Electromagnetism-like algorithm for cell formation and layout problem," *Expert Systems with Applications*, vol. 39, no. 2, pp. 2172-2182, 2012.

[11] C. T. Su and H. C. Lin, "Applying electromagnetism-like mechanism for feature selection," *Information Sciences*, vol. 181, no. 5, pp. 972-986, 2011.

[12] K. -C. Lee and J. -Y. Jhang, "Application of electromagnetism-like algorithm to phase-only syntheses of antenna arrays," *Progress In Electromagnetics Research*, vol. 83, pp. 279-291, 2008.

[13] A. H. G. R. Kan and G. T. Timmer, "Stochastic global optimization methods, Part I: clustering methods," *Mathematical Programming*, vol. 39, pp. 27-56, 1987.

[14] S. Törn and Viitanen, "Topographical global optimization using pre-sampled points," *Journal of Global Optimization*, vol. 5, pp. 267-276, 1994.

[15] R. Fletcher and C. Reeves, "Function minimization by conjugate directions," *Computer Journal*, vol. 7, pp. 149-154, 1964.

[16] M. A. C. Rocha and E. Fernandes, "On charge effects to the electromagnetism-like algorithm," *Proceedings of Euro Mini Conference "Continuous Optimization and Knowledge-Based Technologies"*, Neringa, pp. 198-203, 2008.

[17] G. F. Uler, O. A. Mohammed, K. Chang-Seop, "Design optimization of electrical machines using genetic algorithms," *IEEE Transactions on Magnetics*, vol. 31, no. 3, pp. 2008-2011, 1995.

[18] O. A. Mohammed and G. F. Uler, "A hybrid technique for the optimal design of electromagnetic devices using direct search and genetic algorithms," *IEEE Transactions on Magnetics*, vol. 33, no. 2, pp. 1931-1934, 1997.

[19] J. A. Vince, *Mathematics for Computer Graphics*, Springer; 3rd ed. USA, 2010.

Houssem R. E. H. Bouchekara is an Assistant Professor in the Electrical Engineering Department of University Mentouri Constantine. He has received his B.Sc. in Electrical Engineering from the University of Mentouri Constantine, Algeria, in 2004. He received his Masters in Electronic Systems and Electrical Engineering from Polytechnic School of the University of Nantes, France, 2005. He received his Ph.D. in Electrical Engineering from Grenoble Electrical Engineering Laboratory, France, in 2008. Then he joined the Electrical Engineering Departement of Umm El Qura University in Saudi arabia for theree years. After that he moved to University Mentouri Constantine Algeria. His research interest includes Magnetic refrigeration, Electric machines, Electromagnetics and Power system.

Performance Improvement of the AOA Estimation Algorithm Using the Newton Iteration

Joon-Ho Lee and Sung-Woo Cho

Department of Information and Communication Engineering,
Sejong University, Seoul 143-747, Korea
joonhlee@sejong.ac.kr and cheage@nate.com

Abstract ― In this paper, a simple numerical method based on the Newton iteration for improving the accuracy of the Conventional beam forming algorithm, the Capon beam forming algorithm, and the MUSIC algorithm for AOA (Angle-of-Arrival) estimation is presented. Based on observation, the estimates of the AOA's for a specific AOA algorithm can be obtained from the extrema of a cost function associated with the specific AOA algorithm employed. We derive explicit expressions of the iterations used for the recursive update of the estimates of the AOA's for the conventional beam forming algorithm, the Capon beam forming algorithm, and the MUSIC algorithm. The formulation is only for the update of the azimuth angle, while the extension to the update of the elevation angle and the azimuth angle can be implemented by taking into account the dependence of the array manifold on the elevation angle as well as the azimuth angle. Note that, for estimation of the azimuth, both the UCA (uniform circular array) and the ULA (uniform linear array) can be employed, and that, for simultaneous estimation of the elevation and the azimuth angle, the UCA, not the ULA, should be adopted since ULA-based algorithm cannot uniquely estimate both the azimuth and the elevation due to the ambiguity pertinent to the ULA structure. We consider the array structure of the ULA and the UCA, but it is quite straightforward to extend the proposed scheme to an arbitrary array structure by simply modifying the array vector consistently with the specific array structure.

Index Terms - AOA, accuracy improvement, conventional beam forming algorithm, Capon beam forming algorithm, MUSIC algorithm, Newton method, UCA, and ULA.

I. INTRODUCTION

Determination of the AOA (angle-of-arrival) [1-8] of signal has been of interest to the signal processing community. The plication of the study ranges from military [9-13] to civilian [14-21] applications. The conventional beam forming algorithm [1], the Capon beam forming algorithm [22, 23], the MUSIC (multiple signal classification) algorithm [24], the ESPRIT (estimation of signal parameters via rotational invariance techniques) algorithm [25], and the ML (maximum likelihood) algorithm [26] have been the main algorithms for AOA estimation.

In [23], the authors showed how to apply the Newton iteration to TOA (time of arrival) estimation for performance improvement. In this paper, we propose how to improve the performance of the conventional beam forming algorithm, the Capon beam forming algorithm and the MUSIC algorithm by applying Newton iteration to the initial AOA estimates with the ULA structure and the UCA structure. Although, for ease of numerical manipulation, we adopt the ULA and the UCA structure, it is quite straight forward to apply the proposed scheme to an arbitrary array structure by simply modifying the array vector in accordance with the specific array structure employed.

The formulation for the Newton iteration is based on the cost function derived from the conventional beam forming algorithm, the Capon beam forming algorithm, and the MUSIC

Submitted On: Jan. 27, 2012
Accepted On: Oct. 13, 2012

algorithm, respectively. In numerical results, we demonstrate the validity of the proposed scheme in terms of the estimation accuracy and the computational complexity.

The accuracy of the AOA estimation is usually quantified via the RMS error of the estimates. Our interest in this paper is to reduce the RMS error of the estimates using numerical methods. The proposed numerical procedure does not require too much computation time, which will be quite clear in the numerical results. More specifically, we give an explicit numerical formulation for the improvement of the AOA estimation for the ULA structure and the UCA structure for three different AOA estimation algorithms. The numerical formulation is essentially Newton iteration for the recursive update of AOA angles corresponding to the local extrema of the cost function of each AOA algorithm.

In practical implementation of nonparametric spectral based AOA estimation, the output can only be evaluated at discrete angles. The estimate is determined from the angle at which the output achieves the maximum value. This estimate is called the initial estimate.

II. DATA MODEL

The signal received at each antenna element can be formulated as,

$$\begin{bmatrix} x_1(k) \\ \vdots \\ x_M(k) \end{bmatrix} = \begin{bmatrix} \mathbf{a}(\theta_1) & \cdots \mathbf{a}(\theta_N) \end{bmatrix} \begin{bmatrix} s_1(k) \\ \vdots \\ s_N(k) \end{bmatrix} + \begin{bmatrix} n_1(k) \\ \vdots \\ n_M(k) \end{bmatrix} = \mathbf{A} \cdot \mathbf{s}(k) + \mathbf{n}(k) \tag{1}$$

where $s(k)$, $\mathbf{n}(k)$, $\mathbf{a}(\theta_i)$, and $\mathbf{A}$ are defined as,

$s(k)$: vector of incident complex monochromatic signal at time k;

$\mathbf{n}(k)$: noise vector at each array element m, zero mean, variance σ_n^2;

$\mathbf{a}(\theta_i)$: M element array steering vector for the θ_i direction of arrival;

$\mathbf{A} = [\mathbf{a}(\theta_1) \quad \mathbf{a}(\theta_2) \quad \ldots \quad \mathbf{a}(\theta_N)]$ $M \times N$ matrix of steering vector $\mathbf{a}(\theta_1)$..

In a communication channel, noise is an undesired random signal, often modelled as additive white gaussian noise (AWGN), that may be caused by thermal noise or electromagnetic interference (EMI) from unknown sources. Noise should not be confused with crosstalk and other interference from other communication system transmitters. Another possible source of the communication channel noise is the reflection from the ground when the antenna elements are close to the ground surface. Similarly, the reflection from antenna tower supporting the array antenna can be another source of noise. The effect of the reflection from antenna tower may be more serious if the antenna tower is electrically conducting.

III. NEWTON METHOD

Newton method make a sequence $\theta^{(i)}$ from an initial guess $\theta^{(0)}$ that converges towards $\theta^{(\text{true})}$ such that $P'(\theta^{(\text{true})}) = 0$ [27]. This $\theta^{(\text{true})}$ corresponds to one of the estimates of true AOA's. The second order Taylor expansion $P_T(\theta)$ of function $P(\theta)$ around $\theta^{(i)}$ is

$$P_T\left(\theta^{(i)} + \Delta\theta\right) \simeq P\left(\theta^{(i)}\right) + P'\left(\theta^{(i)}\right)\Delta\theta + \frac{1}{2}P''\left(\theta^{(i)}\right)\left(\Delta\theta\right)^2, \tag{2}$$

which attains its extrema when its derivative with respect to $\Delta\theta$ is equal to zero,

$$P'\left(\theta^{(i)}\right) + P''\left(\theta^{(i)}\right)\left(\Delta\theta\right) = 0. \tag{3}$$

Thus, provided that $P(\theta)$ is a twice-differentiable function well approximated by its second order Taylor expansion and the initial guess $\theta^{(0)}$ is chosen close enough to $\theta^{(\text{true})}$, the sequence $\theta^{(i)}$ defined by the following sequence will converge to $\theta^{(\text{true})}$,

$$\theta^{(i+1)} = \theta^{(i)} - \frac{P'\left(\theta^{(i)}\right)}{P''\left(\theta^{(i)}\right)} \qquad i = 0,1,\cdots. \tag{4}$$

IV. CONVENTIONAL BEAM FORMING ALGORITHM

In the conventional beam forming algorithm for AOA estimation, the array output power is computed as the arrival angle varies, and the arrival angles corresponding to the local maxima value in the output power distribution are considered to be the estimates of the true directions of arrival. AOA's are selected from the angle at which the following output achieves the local maxima,

$$P_{\text{CBF}}(\theta) = \mathbf{a}^{\text{H}}(\theta)\hat{\mathbf{R}}\mathbf{a}(\theta) \tag{5}$$

where θ is the arrival angle of an interest, and $\hat{\mathbf{R}}$

is the ML (maximum likelihood) estimate of the array output covariance matrix **R**. That is, we evaluate equation (5) as a function of θ at discrete values, and find θ's at which $P_{\mathrm{CBF}}(\theta)$ achieve the local maxima.

We consider the case that there are N incident signals. We compute the beam forming spectrum at,

$$\left\{\begin{array}{l}\theta_{\mathrm{start}}, \theta_{\mathrm{start}}+\Delta\theta, \theta_{\mathrm{start}}+2\Delta\theta, \cdots \theta_{\mathrm{start}} \\ +\left\lfloor \dfrac{\theta_{\mathrm{stop}}-\theta_{\mathrm{start}}}{\Delta\theta} \right\rfloor \Delta\theta \end{array}\right\}. \quad (6)$$

The initial angle estimates, $\theta_1^{(0)}$, $\theta_2^{(0)}$,…, $\theta_N^{(0)}$, are found from the N local maxima of $\mathbf{a}^{\mathrm{H}}(\theta)\,\hat{\mathbf{R}}\,\mathbf{a}(\theta)$ out of all the $P_{CBF}(\theta)$ in equation (5) at the following discrete angles,

$$\theta = \theta_{\mathrm{start}}, \theta_{\mathrm{start}}+\Delta\theta, \theta_{\mathrm{start}}+2\Delta\theta, \cdots \theta_{\mathrm{start}} + \left\lfloor \frac{\theta_{\mathrm{stop}}-\theta_{\mathrm{start}}}{\Delta\theta} \right\rfloor \Delta\theta \quad (7)$$

where $\lfloor\ \rfloor$ rounds the argument toward zero. θ_{start} and θ_{stop} specify a search range of the angle, and $\Delta\theta$ is a search step.

Consider the case of the ULA and the UCA with M antenna elements. The array manifold is expressed as follows [1],

$$\mathbf{a}(\theta) = \left[\exp(j\psi_1)\ \exp(j\psi_2)\ \cdots \exp(j\psi_M)\right]^{\mathrm{T}}. \quad (8)$$

A. ULA

The symbol ψ_m for the ULA is given by,

$$\psi_m = (m-1)\frac{2\pi}{\lambda} d \sin\theta \quad m = 1, \cdots, M. \quad (9)$$

If the distance between the antenna elements in the ULA is $\lambda/2$, equation (9) can be written as,

$$\psi_m = (m-1)\pi \sin\theta \quad m = 1, \cdots, M. \quad (10)$$

Using equations (8) and (10) in equation (5), after some manipulation, for the ULA, we have,

$$\begin{aligned} P_{\mathrm{CBF}}(\theta) &= \mathbf{a}^{\mathrm{H}}(\theta)\hat{\mathbf{R}}\mathbf{a}(\theta) \\ &= \left[e^{-j\psi_1} \quad \cdots \quad e^{-j\psi_M}\right] \begin{bmatrix} \hat{R}_{11} & \cdots & \hat{R}_{1M} \\ \vdots & \ddots & \vdots \\ \hat{R}_{M1} & \cdots & \hat{R}_{MM} \end{bmatrix} \\ &= \left[\sum_{m=1}^{M} e^{-j\psi_m}\hat{R}_{m1} \quad \cdots \quad \sum_{m=1}^{M} e^{-j\psi_m}\hat{R}_{mm}\right] \begin{bmatrix} e^{j\psi_1} \\ \vdots \\ e^{j\psi_M} \end{bmatrix} \\ &= \left(\sum_{m=1}^{M} e^{-j\psi_m}\hat{R}_{m1}\right) e^{j\psi_1} + \cdots + \left(\sum_{m=1}^{M} e^{-j\psi_m}\hat{R}_{mM}\right) e^{j\psi_M} \\ &= \sum_{n=1}^{M}\sum_{m=1}^{M} e^{-j\psi_m}\hat{R}_{mn} e^{j\psi_n} = \sum_{n=1}^{M}\sum_{m=1}^{M} e^{j(\psi_n-\psi_m)}\hat{R}_{mn} \end{aligned}$$

$$P_{\mathrm{CBF,\ ULA}}(\theta) = \sum_{m=1}^{M}\sum_{n=1}^{M} \exp\left[j(n-m)\pi\sin\theta\right]\hat{R}_{mn} \quad (11)$$

where $\hat{R}_{mn}$ denotes the m-th row and n-th column of the matrix $\hat{\mathbf{R}}$. Using equations (A3) and (A5) in appendix A, the following iteration is repeated until the update of the estimate is less than the specified tolerance [9]. That is, when the updates of all the estimates, $\left|\hat{\theta}_n^{(i+1)} - \hat{\theta}_n^{(i)}\right|$, $n = 1, \cdots, N$, are less than the specified tolerance, the estimates are considered to be convergent,

$$\begin{aligned} \hat{\theta}_n^{(i+1)} &= \hat{\theta}_n^{(i)} - \left.\frac{\dfrac{dP_{\mathrm{CBF,\ ULA}}(\theta)}{d\theta}}{\dfrac{d}{d\theta}\left(\dfrac{dP_{\mathrm{CBF,\ ULA}}(\theta)}{d\theta}\right)}\right|_{\theta=\hat{\theta}_n^{(i)}} \\ &= \hat{\theta}_n^{(i)} - \frac{\sum_{m=1}^{M}\sum_{n=1}^{M}\left[j(n-m)\pi\cos\hat{\theta}_n^{(i)} \exp\left(j(n-m)\pi\sin\hat{\theta}_n^{(i)}\right)\right]\hat{R}_{mn}}{\sum_{m=1}^{M}\sum_{n=1}^{M}\left[j(n-m)\pi\exp\left(j(n-m)\pi\sin\hat{\theta}_n^{(i)}\right) \left(j(n-m)\pi\cos^2\hat{\theta}_n^{(i)} - \sin\hat{\theta}_n^{(i)}\right)\right]\hat{R}_{mn}} \\ & i = 0, 1, \cdots \quad n = 1, \cdots, N. \end{aligned} \quad (12)$$

B. UCA

The symbol ψ_m for the UCA is written as,

$$\psi_m = 2\pi\frac{r}{\lambda}\left[\cos\left(\theta - \frac{2\pi(m-1)}{M}\right)\right] \quad m = 1, \cdots, M. \quad (13)$$

Similarly, for the UCA, from equations (8), (13) and (5), we have,

$$P_{\mathrm{CBF,\ UCA}}(\theta) = \sum_{m=1}^{M}\sum_{n=1}^{M} \exp\left[-j4\pi\frac{r}{\lambda} \sin\left(\theta - \frac{\pi(n+m-2)}{M}\right)\sin\left(\frac{\pi(m-n)}{M}\right)\right]\hat{R}_{mn}. \quad (14)$$

For the UCA, using equations (A4) and (A6) in appendix A, we have,

$$\hat{\theta}_n^{(i+1)} = \hat{\theta}_n^{(i)} - \left.\frac{\dfrac{dP_{\text{CBF, UCA}}(\theta)}{d\theta}}{\dfrac{d}{d\theta}\left(\dfrac{dP_{\text{CBF, UCA}}(\theta)}{d\theta}\right)}\right|_{\theta=\hat{\theta}_n^{(i)}}$$

$$\hat{\theta}_n^{(i+1)} = \hat{\theta}_n^{(i)} - \frac{\displaystyle\sum_{m=1}^{M}\sum_{n=1}^{M}\left[-j4\pi\frac{r}{\lambda}\sin\left(\frac{\pi(m-n)}{M}\right)\times\cos\left(\hat{\theta}_n^{(i)}-\frac{\pi(n+m-2)}{M}\right)\times\exp\left[\begin{array}{l}-j4\pi\dfrac{r}{\lambda}\sin\left(\dfrac{\pi(m-n)}{M}\right)\times\\ \sin\left(\hat{\theta}_n^{(i)}-\dfrac{\pi(n+m-2)}{M}\right)\end{array}\right]\hat{R}_{mn}\right]}{\left[\begin{array}{l}\displaystyle\sum_{m=1}^{M}\sum_{n=1}^{M}\left[j4\pi\frac{r}{\lambda}\sin\left(\frac{\pi(m-n)}{M}\right)\times\exp\left[\begin{array}{l}-j4\pi\dfrac{r}{\lambda}\sin\left(\dfrac{\pi(m-n)}{M}\right)\times\\ \sin\left(\hat{\theta}_n^{(i)}-\dfrac{\pi(n+m-2)}{M}\right)\end{array}\right]\times\right.\\ \left.\left[\begin{array}{l}j4\pi\dfrac{r}{\lambda}\sin\left(\dfrac{\pi(m-n)}{M}\right)\times\\ \cos^2\left(\hat{\theta}_n^{(i)}-\dfrac{\pi(n+m-2)}{M}\right)+\\ \sin\left(\hat{\theta}_n^{(i)}-\dfrac{\pi(n+m-2)}{M}\right)\end{array}\right]\hat{R}_{mn}\right]\end{array}\right]} \quad (15)$$

$i = 0,1,\cdots \quad n = 1,\cdots,N$

where $\hat{\theta}_n^{(i)}$ represents the AOA estimate for the i-th iteration of the n-th incident signal. The estimates obtained from the last iteration are designated as the final estimates, $\hat{\theta}_1^{(\text{final})},\cdots,\hat{\theta}_N^{(\text{final})}$. The termination criterion can be explicitly expressed as,

$$\left|\hat{\theta}_n^{(i+1)} - \hat{\theta}_n^{(i)}\right| < \text{tolerance} \quad n = 1,\cdots,N. \quad (16)$$

The above iteration should be applied to each incident signals, respectively.

V. CAPON BEAM FORMING ALGORITHM

In the Capon beam forming algorithm for AOA estimation, AOA's are selected from the angles at which the following spectrum achieves the local maxima,

$$P_{\text{Capon}}(\theta) = \frac{1}{\mathbf{a}^{\text{H}}(\theta)\hat{\mathbf{R}}^{-1}\mathbf{a}(\theta)} \equiv \frac{1}{D_{\text{Capon}}(\theta)} \quad (17)$$

Where $D_{\text{Capon}}(\theta)$ is defined as follows,

$$D_{\text{Capon}}(\theta) = \mathbf{a}^{\text{H}}(\theta)\hat{\mathbf{R}}^{-1}\mathbf{a}(\theta). \quad (18)$$

The initial angle estimates, $\theta_1^{(0)}$, $\theta_2^{(0)}$,…, $\theta_N^{(0)}$, are found from the N local minima of $D_{\text{Capon}}(\theta) = \mathbf{a}^{\text{H}}(\theta)\,\hat{\mathbf{R}}^{-1}\,\mathbf{a}(\theta)$ at the discrete angles specified in equation (7). Note that, unlike the conventional beam forming algorithm, we have to find the angles, which are the local minima of $D_{\text{Capon}}(\theta) = \mathbf{a}^{\text{H}}(\theta)\,\hat{\mathbf{R}}^{-1}\,\mathbf{a}(\theta)$ because we have to maximize $P_{\text{Capon}}(\theta) = 1/D_{\text{Capon}}(\theta)$, which is equivalent to minimizing $D_{\text{Capon}}(\theta)$.

A. ULA

Using equations (10) and (8) in equation (18) results in,

$$D_{\text{Capon, ULA}}(\theta) = \sum_{m=1}^{M}\sum_{n=1}^{M}\exp\left[j(n-m)\pi\sin\theta\right]\hat{R}_{mn}^{-1}. \quad (19)$$

The iteration for the Capon beam forming can be explicitly written as,

$$\hat{\theta}_n^{(i+1)} = \hat{\theta}_n^{(i)} - \left.\frac{\dfrac{dD_{\text{Capon, ULA}}(\theta)}{d\theta}}{\dfrac{d}{d\theta}\left(\dfrac{dD_{\text{Capon, ULA}}(\theta)}{d\theta}\right)}\right|_{\theta=\hat{\theta}_n^{(i)}}$$

$$= \hat{\theta}_n^{(i)} - \frac{\displaystyle\sum_{m=1}^{M}\sum_{n=1}^{M}\left[j(n-m)\pi\cos\hat{\theta}_n^{(i)}\exp\left(j(n-m)\pi\sin\hat{\theta}_n^{(i)}\right)\right]\hat{R}_{mn}^{-1}}{\displaystyle\sum_{m=1}^{M}\sum_{n=1}^{M}\left[j(n-m)\pi\exp\left(j(n-m)\pi\sin\hat{\theta}_n^{(i)}\right)\left(j(n-m)\pi\cos^2\hat{\theta}_n^{(i)} - \sin\hat{\theta}^{(i)}\right)\right]\hat{R}_{mn}^{-1}}$$

$$i = 0,1,\cdots \quad n = 1,\cdots,N. \quad (20)$$

B. UCA

By substituting equations (8) and (13) in equation (18), we get, for the UCA,

$$D_{\text{Capon, UCA}}(\theta) = \sum_{m=1}^{M}\sum_{n=1}^{M}\exp\begin{bmatrix} -j4\pi\frac{r}{\lambda}\times \\ \sin\left(\theta-\frac{\pi(n+m-2)}{M}\right)\times \\ \sin\left(\frac{\pi(m-n)}{M}\right)\end{bmatrix}\hat{R}_{mn}^{-1} \tag{21}$$

$$\hat{\theta}_n^{(i+1)} = \hat{\theta}_n^{(i)} - \left.\frac{\frac{dD_{\text{Capon, UCA}}(\theta)}{d\theta}}{\frac{d}{d\theta}\left(\frac{dD_{\text{Capon, UCA}}(\theta)}{d\theta}\right)}\right|_{\theta=\hat{\theta}_n^{(i)}}$$

$$= \hat{\theta}_n^{(i)} - \frac{\begin{bmatrix} -j4\pi\frac{r}{\lambda}\sin\left(\frac{\pi(m-n)}{M}\right)\times \\ \cos\left(\hat{\theta}^{(i)}-\frac{\pi(n+m-2)}{M}\right)\end{bmatrix}\sum_{m=1}^{M}\sum_{n=1}^{M}\exp\begin{bmatrix} -j4\pi\frac{r}{\lambda}\sin\left(\frac{\pi(m-n)}{M}\right)\times \\ \sin\left(\hat{\theta}_n^{(i)}-\frac{\pi(n+m-2)}{M}\right)\end{bmatrix}\hat{R}_{mn}^{-1}}{j4\pi\frac{r}{\lambda}\sin\left(\frac{\pi(m-n)}{M}\right)\times \sum_{m=1}^{M}\sum_{n=1}^{M}\exp\begin{bmatrix} -j4\pi\frac{r}{\lambda}\sin\left(\frac{\pi(m-n)}{M}\right)\times \\ \sin\left(\hat{\theta}^{(i)}-\frac{\pi(n+m-2)}{M}\right)\end{bmatrix}\sum_{m=1}^{M}\sum_{n=1}^{M}\begin{bmatrix} j4\pi\frac{r}{\lambda}\sin\left(\frac{\pi(m-n)}{M}\right)\times \\ \cos^2\left(\hat{\theta}_n^{(i)}-\frac{\pi(n+m-2)}{M}\right)+ \\ \sin\left(\hat{\theta}_n^{(i)}-\frac{\pi(n+m-2)}{M}\right)\end{bmatrix}\hat{R}_{mn}^{-1}}$$

$$i=0,1,\cdots\ n=1,\cdots,N\ , \tag{22}$$

where the termination criterion for the Capon algorithms is the same as that for the conventional beam forming algorithm.

VI. MUSIC ALGORITHM

The beam forming algorithm is the basic AOA algorithm, whose merit is the low computational cost [1, 22, 23]. In the beam forming algorithm, signals from certain directions are added constructively by forming a weighted sum of the array outputs. The antenna is steered to different directions by varying the array weights. On the other hand, in the MUSIC algorithm, we make use of the orthogonality between the noise eigenvectors and the array vectors corresponding to the true directions of incident signals in the MUSIC algorithm. In the MUSIC algorithm, the AOA's are obtained from the local maxima of the following spectrum,

$$P_{\text{MUSIC}}(\theta) = \frac{1}{\mathbf{a}^H(\theta)\mathbf{U}_N\mathbf{U}_N^H\mathbf{a}(\theta)} \equiv \frac{1}{D_{\text{MUSIC}}(\theta)} \tag{23}$$

where the columns of the matrix $\mathbf{U}_N$ are the noise eigenvectors of the covariance matrix $\hat{\mathbf{R}}$, and $D_{\text{MUSIC}}(\theta)$ is defined as,

$$D_{\text{MUSIC}}(\theta) = \mathbf{a}^H(\theta)\mathbf{U}_N\mathbf{U}_N^H\mathbf{a}(\theta)\,. \tag{24}$$

The array vector is defined in equations (8) and (10) for the ULA and equations (8) and (13) for the UCA. The initial estimates, $\theta_1^{(0)}$, $\theta_2^{(0)}$,…, $\theta_N^{(0)}$, are obtained from the N local minima of $D_{\text{MUSIC}}(\theta)$ at the discrete angles specified in equation (7).

A. ULA

Substituting equations (10) and (8) in equation (24) yields,

$$D_{\text{MUSIC, ULA}}(\theta) = \sum_{m=1}^{M}\sum_{n=1}^{M}\exp\left[j(n-m)\pi\sin\theta\right]\left(\mathbf{U}_N\mathbf{U}_N^H\right)_{mn} \tag{25}$$

where ($\mathbf{U}_N\ \mathbf{U}_N{}^H$) denotes the m-th row and the n-th column of the matrix ($\mathbf{U}_N\ \mathbf{U}_N{}^H$). Using equations (C3) and (C5) in appendix C for the ULA, the following iterations are repeated until the convergence is achieved,

$$\hat{\theta}_n^{(i+1)} = \hat{\theta}_n^{(i)} - \left.\frac{\frac{dD_{\text{MUSIC, ULA}}(\theta)}{d\theta}}{\frac{d}{d\theta}\left(\frac{dD_{\text{MUSIC, ULA}}(\theta)}{d\theta}\right)}\right|_{\theta=\hat{\theta}_n^{(i)}}$$

$$\hat{\theta}_n^{(i+1)} = \hat{\theta}_n^{(i)} - \frac{\sum_{m=1}^{M}\sum_{n=1}^{M}\left[\begin{array}{l} j(n-m)\pi\cos\hat{\theta}_n^{(i)}\times \\ \exp\left(j(n-m)\pi\sin\hat{\theta}_n^{(i)}\right)\times\left(\mathbf{U}_N\mathbf{U}_N^H\right)_{mn}\end{array}\right]}{\begin{array}{r} j(n-m)\pi\exp\left(j(n-m)\pi\sin\hat{\theta}_n^{(i)}\right)\times \\ \sum_{m=1}^{M}\sum_{n=1}^{M}\left(j(n-m)\pi\cos^2\hat{\theta}_n^{(i)}-\sin\hat{\theta}_n^{(i)}\right)\times \\ \left(\mathbf{U}_N\mathbf{U}_N^H\right)_{mn}\end{array}}$$

$$i = 0,1,\cdots \quad n = 1,\cdots,N \quad . \tag{26}$$

B. UCA

Similarly, from equations (13), (8) and (24), we have,

$$D_{\text{MUSIC, UCA}}(\theta) = \sum_{m=1}^{M}\sum_{n=1}^{M}\exp\left[\begin{array}{l} -j4\pi\frac{r}{\lambda}\sin\left(\frac{\pi(m-n)}{M}\right)\times \\ \sin\left(\theta-\frac{\pi(n+m-2)}{M}\right)\end{array}\right]\left(\mathbf{U}_N\mathbf{U}_N^H\right)_{mn} . \tag{27}$$

Using equations (B3) and (B5) from appendix B for the UCA, the following iterations are repeated until the convergence is achieved,

$$\hat{\theta}^{(i+1)} = \hat{\theta}_n^{(i)} - \frac{\begin{array}{r} -j4\pi\frac{r}{\lambda}\sin\left(\frac{\pi(m-n)}{M}\right)\times\cos\left(\hat{\theta}_n^{(i)}-\frac{\pi(n+m-2)}{M}\right)\times \\ \sum_{m=1}^{M}\sum_{n=1}^{M}\exp\left[\begin{array}{l} -j4\pi\frac{r}{\lambda}\sin\left(\frac{\pi(m-n)}{M}\right)\times \\ \sin\left(\hat{\theta}_n^{(i)}-\frac{\pi(n+m-2)}{M}\right)\end{array}\right]\times\left(\mathbf{U}_N\mathbf{U}_N^H\right)_{mn}\end{array}}{\begin{array}{r} j4\pi\frac{r}{\lambda}\sin\left(\frac{\pi(m-n)}{M}\right)\times\exp\left[\begin{array}{l} -j4\pi\frac{r}{\lambda}\sin\left(\frac{\pi(m-n)}{M}\right)\times \\ \sin\left(\hat{\theta}_n^{(i)}-\frac{\pi(n+m-2)}{M}\right)\end{array}\right]\times \\ \sum_{m=1}^{M}\sum_{n=1}^{M}\left[\begin{array}{l} j4\pi\frac{r}{\lambda}\sin\left(\frac{\pi(m-n)}{M}\right)\cos^2\left(\hat{\theta}_n^{(i)}-\frac{\pi(n+m-2)}{M}\right)+ \\ \sin\left(\hat{\theta}_n^{(i)}-\frac{\pi(n+m-2)}{M}\right)\end{array}\right]\times \\ \left(\mathbf{U}_N\mathbf{U}_N^H\right)_{mn}\end{array}}$$

$$i=0,1,\cdots\ n=1,\cdots,N. \tag{28}$$

We adopt the stopping criterion in equation (16) for the MUSIC algorithm.

VII. COMMENTS ON HOW TO GET THE INITIAL ESTIMATES

Similarly, in section IV, we use the conventional beam forming algorithm for getting the initial estimates, which will be refined by applying the Newton method to the conventional beam forming algorithm. The same is true for the Capon beam forming algorithm in section V. In section VI, we arbitrarily assume that the initial estimates, which will be refined by using the cost function of the MUSIC algorithm, are obtained from the MUSIC algorithm. That is, the same AOA algorithm is used for the initialization and the refinement of the estimates, which does not have to be necessarily true.

It is not necessarily true that the initial estimates, which will be subsequently refined via the Newton method applied to the cost function of the MUSIC algorithm, should be estimated by using the MUSIC algorithm. That is, we can use any AOA estimation algorithm for getting the initial estimates to be further refined by applying the Newton method to the cost function of the MUSIC algorithm. In addition, the alternating projection algorithm [26] is very popular algorithm for getting the initial estimates due to the fact that it is computationally efficient at the cost of an accuracy degradation of the initial estimates. Similarly, we can use any AOA estimation algorithm including the AP algorithm for getting the initial estimates, which will be refined by applying the Newton method to the cost function of the conventional beam forming algorithm, and the Capon beam forming algorithm.

VIII. NUMERICAL RESULTS

At first, we designate the computer specification and the Matlab environment. The computer specification is as follows: Intel® Pentium CPU G620 @ 2.60GHz (2 CPU) 3018MB RAM. The Matlab environment is as follows: Matlab version 7.11.0.584 (R2010b). The operating system: Microsoft windows XP version 5.1 (build 2600: service pack 3). Java VM version: Java 1.6.0_17-b04 with Sun microsystems Inc. Java HotSpot (TM) Client VM mixed mode. The version of the signal processing toolbox is version 6.14.

In this section, the validity of the proposed scheme is illustrated via numerical results. The ULA and the UCA are used and the number of antenna elements, M, is chosen to be five. $\theta^{(start)}$ and $\theta^{(stop)}$ are selected to be $\theta^{(start)} = -80^0$ and $\theta^{(stop)} = 80^0$. The distance between the antenna elements in the ULA is $\lambda/2$, and the radius of the UCA is 0.679λ. The number of snapshots used for the calculation of $\hat{\mathbf{R}}$ is chosen to be 64. The tolerance, which is the termination criterion for the iteration in equation (16) is 10^{-3}. The maximum number of iteration in the Newton method is 100. The RMSE (root mean square error) and operation time in Figs. 1–12 are obtained from the 1000 repetitions. The search steps, $\Delta\theta$, in equation (7) are chosen to be 1.2^0, 4.7^0, and 8.8^0. The main beam width of the half-wavelength-spaced ULA consisting of M elements is $2\sin^{-1}(2/M)$. For $M = 5$, the beam width is BW= $2\sin^{-1}(2/5) = 0.823$ (rad) = 47 (degrees). The two incident signals are chosen so that their separation is larger than the BW. The following is how we get the search steps used in the simulation, $(BW/4)\times[0.1 \quad 0.4 \quad 0.75] = [1.2^0 \quad 4.7^0 \quad 8.8^0]$. Note that BW/4 is a search step to get four samples in the main beam width. To make sure that we have more than four samples in the main beam width, the search step should be smaller than the BW/4. Therefore, we arbitrarily let the search steps be equal to 0.1 times BW/4, 0.4 times BW/4 and 0.75 times BW/4.

For $\Delta\theta = 1.2$, there are 40 sampled points within the main beam width. Similarly, the sampled points within the main beam width are 10 and 5 for $\Delta\theta = 4.7^0$ and $\Delta\theta = 8.8^0$, respectively. We investigate the RMSE (root mean square error) and the execution time for various true incident angles, the search steps and SNR's. We consider the case that there are two incident signals, which implies that N is equal to two. The results with legend 'CBF', 'CAPON', and 'MUSIC' refer to the initial estimates for the conventional beam forming, the Capon beam forming, and the MUSIC algorithm, respectively. The results with legend 'CBF+NT' refer to the estimates obtained by applying the Newton iteration to the initial estimates from the conventional beam forming algorithm. The results for the ULA are from equation (12), and those for the UCA are from equation (15).

Similarly, the results with the legend 'CAPON+NT' refer to the final estimate obtained by applying the Newton iteration to the initial estimates of the Capon beam forming algorithm. The results for the ULA are obtained from equation (20) and those for the UCA are obtained from equation (22). The Newton-iteration based final estimates for the MUSIC algorithm are shown with legend 'MUSIC+NT'. The results are from equations (26) and (28) for the ULA and the UCA, respectively. The results for the conventional beam forming are shown in Figs. 1, 4, 7, and 10, and those for the Capon beam forming are shown in Figs. 2, 5, 8, and 11. Figures 3, 6, 9, and 12 show the performance for the MUSIC algorithm. Figures 1–6 are for the ULA and Figs. 7–12 are for the UCA. Figures 1–3 show the performance improvement by the Newton iteration for a specific search step used for the calculation of the initial estimate for the conventional beam forming, the Capon beam forming, and the MUSIC algorithm, respectively. Figures 4–6 illustrate the fact that by employing the Newton iteration, we can improve the performance of the initial estimate obtained from the sparser search step. The results for the ULA with $[\theta_1^{(true)} \; \theta_2^{(true)}] = [-60^0 \; -6.9^0]$ and $[\theta_1^{(true)} \; \theta_2^{(true)}] = [-60^0 \; 10.7^0]$ and with the search steps, $\Delta\theta = 1.2^0$, $\Delta\theta = 4.7^0$, and $\Delta\theta = 8.8^0$ for various SNR's are shown in Figs. 1–3. The RMSE of the initial estimates and those of the final estimates are shown. The execution time is also illustrated to quantitatively describe the computational complexity of each scheme. The execution time of the algorithm is measured using Matlab function 'etime'.

The final estimates are superior to the initial estimates in terms of the RMSE, but getting the final estimates take more time than getting the initial estimates, which can be seen in the second figure of each case because the final estimates are obtained by applying the Newton iteration to the initial estimates. The initial estimates in Figs. 1–3 for search step of 8.8^0 are inferior to those for search step of 4.7^0 because, in the case of $\Delta\theta = 8.8^0$, we use sparser grid points than in the case of $\Delta\theta = 4.7^0$ in estimating the initial estimates. Consequently, the execution time of the initial estimates for $\Delta\theta = 8.8^0$ is shorter than those for $\Delta\theta = 4.7^0$. From Figs. 1–3, we can see that the Newton iteration can improve the accuracy of the estimates at the expense of longer execution time. In Figs. 4–6, we show the results of the initial estimates

with the search step of $\Delta\theta = 1.2^0$ in equation (7) and those of the final estimates with $\Delta\theta = 4.7^0$. The performances of the initial estimates with $\Delta\theta = 1.2^0$ and those of the final estimates with $\Delta\theta = 4.7^0$ are approximately equal. But, it is clear from the figures that by applying the Newton iteration to the initial estimates obtained with $\Delta\theta = 4.7^0$, we can reduce the computational cost in comparison with the case that the initial estimates are obtained with $\Delta\theta = 1.2^0$ without applying the Newton iteration to the initial estimates.

The difference between the results in Figs. 7–9 and those in Figs. 1–3 is the array structure employed for the implementation of the AOA estimation algorithm. The results in Figs. 7–9 are for the UCA, while those in Figs. 1–3 are for the ULA. For the same search step, getting the final estimates takes longer time than getting the initial estimates since the final estimates are obtained by applying the Newton iteration to the initial estimates. Figures 10–12 are for the UCA. The simulation conditions for the Figs. 10–12 are the same as those for the Figs. 4–6 except that Figs. 10–12 are for the UCA and that Figs. 4–6 are for the ULA.

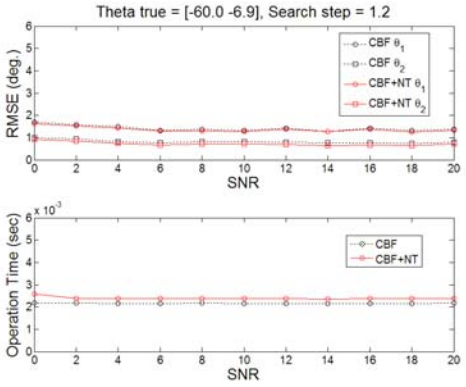

$[\theta_1^{(\text{true})} \;\; \theta_2^{(\text{true})}] = [-60^0 \;\; -6.9^0]$, $\Delta\theta = 1.2^0$

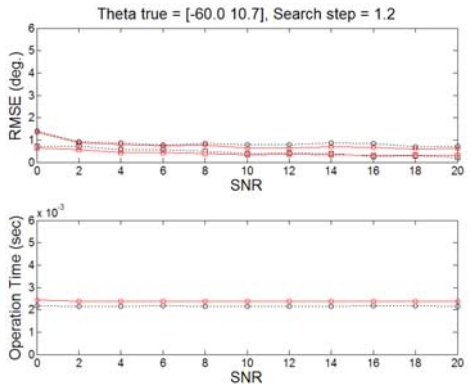

$[\theta_1^{(\text{true})} \;\; \theta_2^{(\text{true})}] = [-60^0 \;\; 10.70]$, $\Delta\theta = 1.2^0$

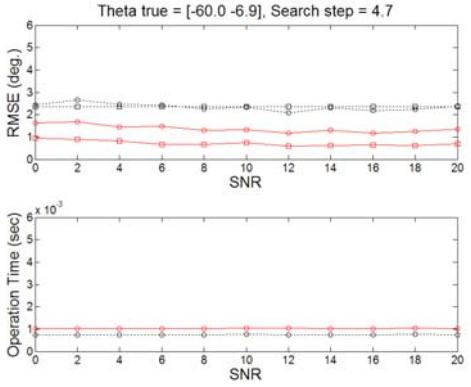

$[\theta_1^{(\text{true})} \;\; \theta_2^{(\text{true})}] = [-60^0 \;\; -6.9^0]$, $\Delta\theta = 4.7^0$

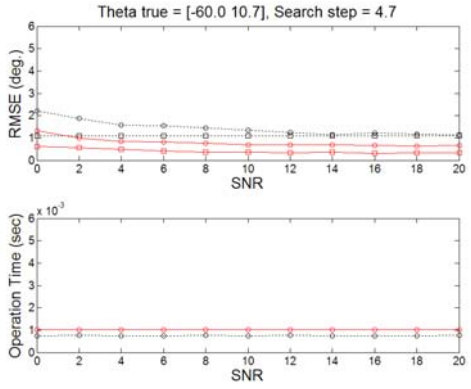

$[\theta_1^{(\text{true})} \;\; \theta_2^{(\text{true})}] = [-60^0 \;\; 10.7^0]$, $\Delta\theta = 4.7^0$

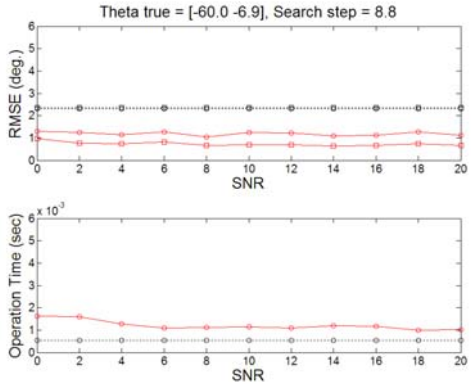

$[\theta_1^{(\text{true})} \;\; \theta_2^{(\text{true})}] = [-60^0 \;\; -6.9^0], \Delta\theta = 8.8^0$

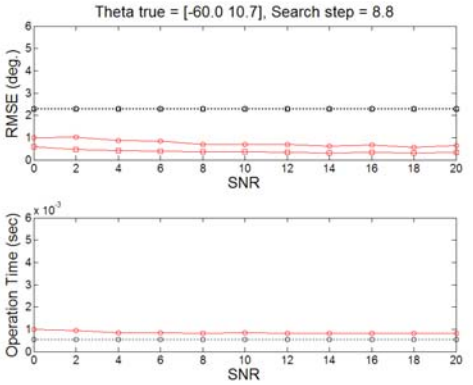

$[\theta_1^{(\text{true})} \;\; \theta_2^{(\text{true})}] = [-60^0 \;\; 10.7^0], \Delta\theta = 8.8^0$

Fig. 1. Initial estimates without the Newton iteration and the final estimates with the Newton iteration of the conventional beam forming algorithm for the ULA.

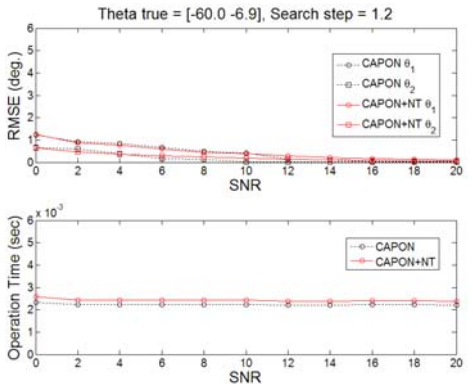

$[\theta_1^{(\text{true})} \;\; \theta_2^{(\text{true})}] = [-60^0 \;\; -6.9^0], \Delta\theta = 1.2^0$

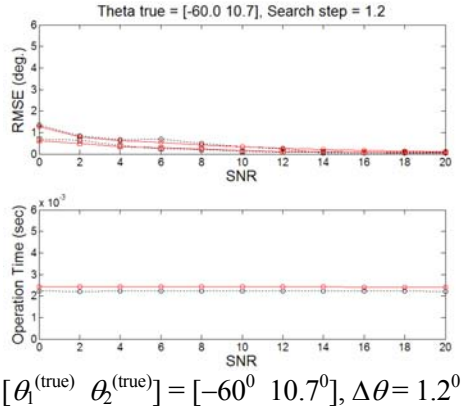

$[\theta_1^{(\text{true})} \;\; \theta_2^{(\text{true})}] = [-60^0 \;\; 10.7^0], \Delta\theta = 1.2^0$

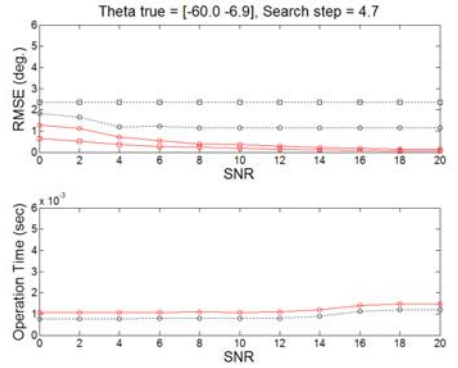

$[\theta_1^{(\text{true})} \;\; \theta_2^{(\text{true})}] = [-60^0 \;\; -6.9^0], \Delta\theta = 4.7^0$

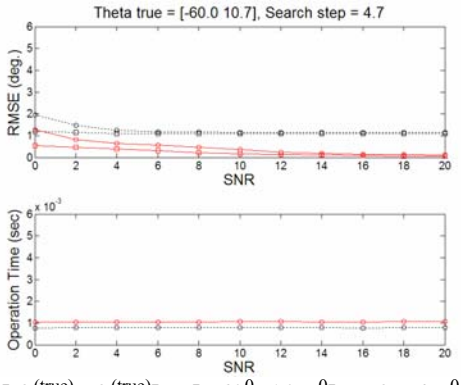

$[\theta_1^{(\text{true})} \;\; \theta_2^{(\text{true})}] = [-60^0 \;\; 10.7^0], \Delta\theta = 4.7^0$

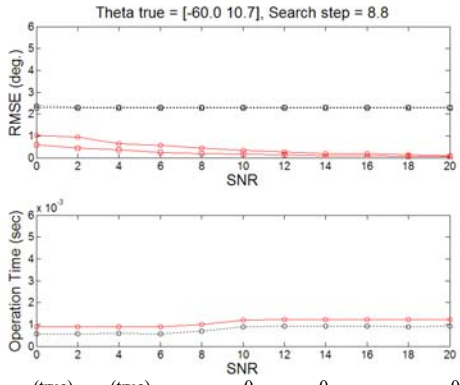

$[\theta_1^{(\text{true})} \;\; \theta_2^{(\text{true})}] = [-60^0 \;\; -6.9^0], \Delta\theta = 8.8^0$

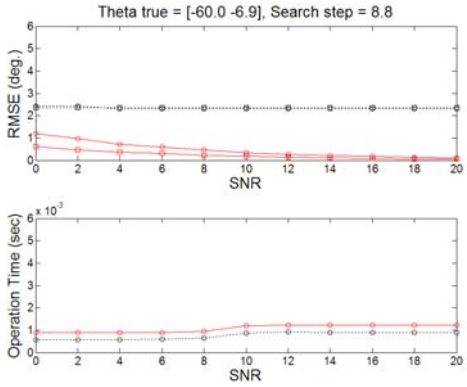

$[\theta_1^{(\text{true})} \;\; \theta_2^{(\text{true})}] = [-60^0 \;\; 10.7^0], \Delta\theta = 8.8^0$

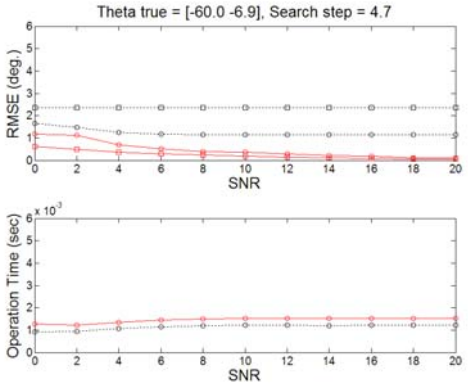

$[\theta_1^{(\text{true})} \;\; \theta_2^{(\text{true})}] = [-60^0 \;\; -6.9^0], \Delta\theta = 4.7^0$

Fig. 2. Initial estimates without the Newton iteration and the final estimates with the Newton iteration of the Capon beam forming algorithm for the ULA.

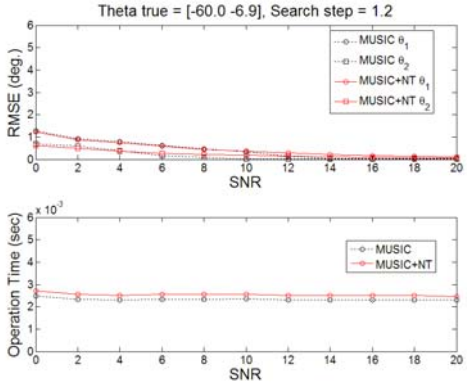

$[\theta_1^{(\text{true})} \;\; \theta_2^{(\text{true})}] = [-60^0 \;\; -6.9^0], \Delta\theta = 1.2^0$

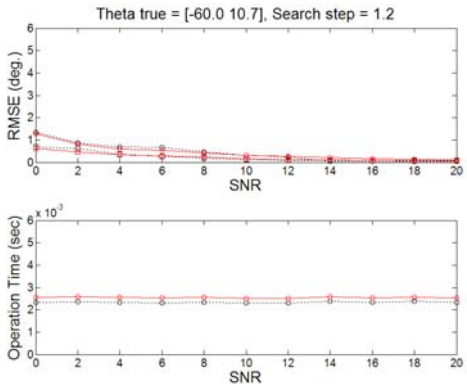

$[\theta_1^{(\text{true})} \;\; \theta_2^{(\text{true})}] = [-60^0 \;\; 10.7^0], \Delta\theta = 1.2^0$

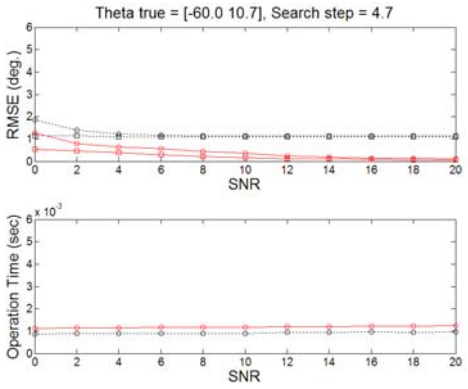

$[\theta_1^{(\text{true})} \;\; \theta_2^{(\text{true})}] = [-60^0 \;\; 10.7^0], \Delta\theta = 4.7^0$

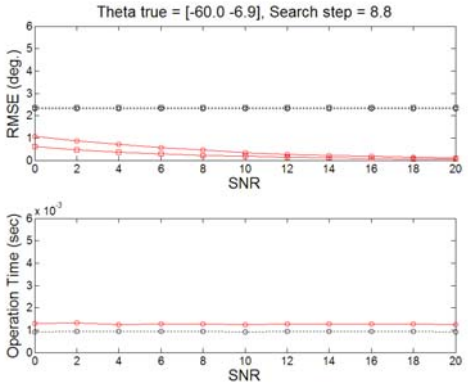

$[\theta_1^{(\text{true})} \;\; \theta_2^{(\text{true})}] = [-60^0 \;\; -6.9^0], \Delta\theta = 8.8^0$

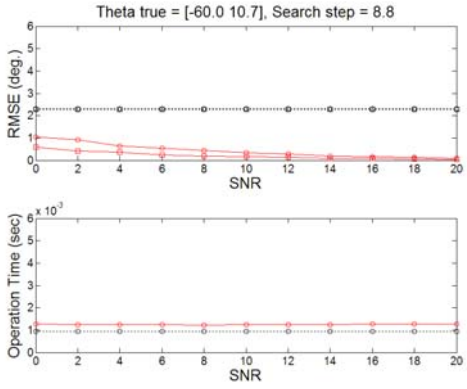

$[\theta_1^{(\text{true})} \;\; \theta_2^{(\text{true})}] = [-60^0 \;\; 10.7^0], \Delta\theta = 8.8^0$

Fig. 3. Initial estimates without the Newton iteration and the final estimates with the Newton iteration of the MUSIC algorithm for the ULA.

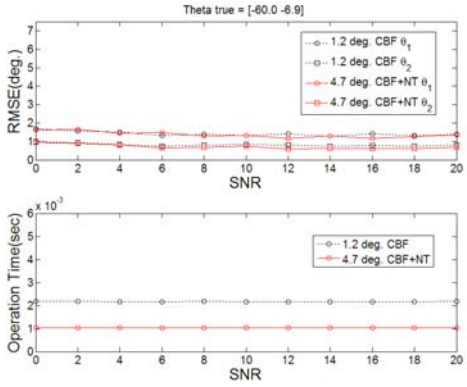

$[\theta_1^{(\text{true})} \;\; \theta_2^{(\text{true})}] = [-60^0 \;\; -6.9^0]$

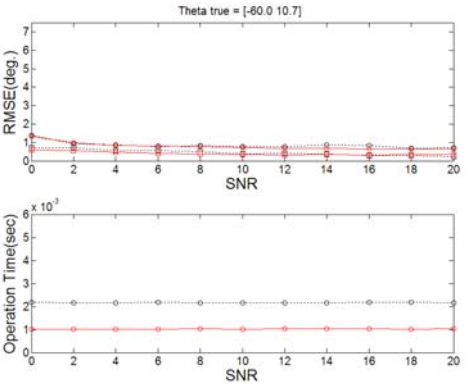

$[\theta_1^{(\text{true})} \;\; \theta_2^{(\text{true})}] = [-60^0 \;\; 10.7^0]$

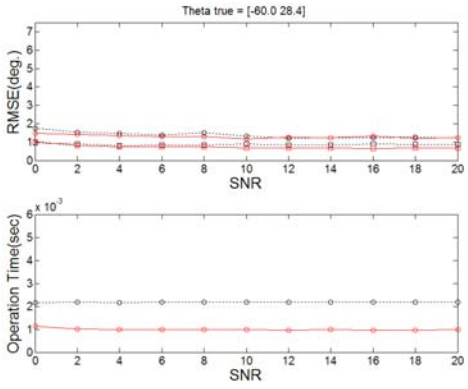

$[\theta_1^{(\text{true})} \;\; \theta_2^{(\text{true})}] = [-60^0 \;\; 28.4^0]$

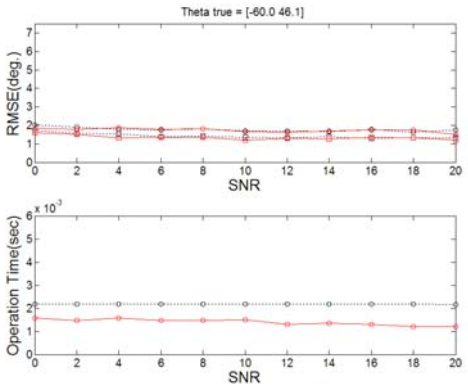

$[\theta_1^{(\text{true})} \;\; \theta_2^{(\text{true})}] = [-60^0 \;\; 46.1^0]$

Fig. 4. Initial estimates for $\Delta\theta = 1.2^0$ without the Newton iteration and the final estimates for $\Delta\theta = 4.7^0$ with the Newton iteration of the conventional beam forming algorithm for the ULA.

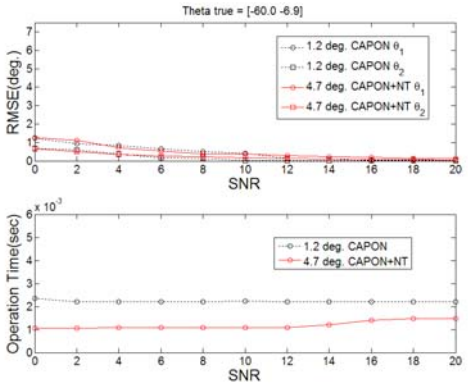

$[\theta_1^{(\text{true})} \;\; \theta_2^{(\text{true})}] = [-60^0 \;\; -6.9^0]$

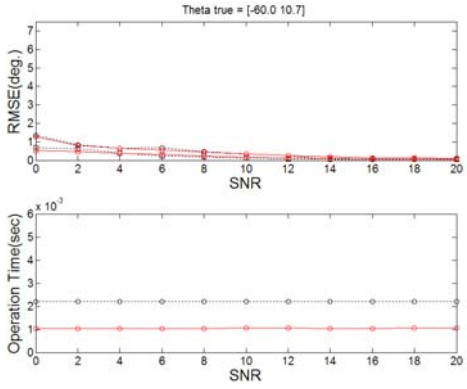

$[\theta_1^{(\text{true})} \;\; \theta_2^{(\text{true})}] = [-60^0 \;\; 10.7^0]$

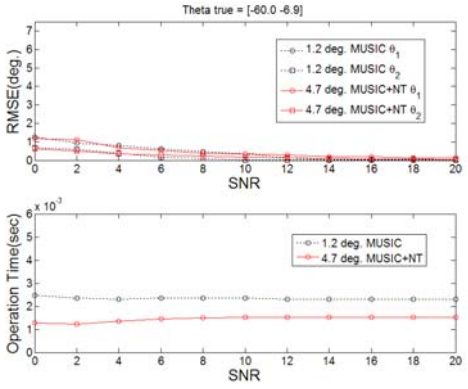

$[\theta_1^{(\text{true})} \;\; \theta_2^{(\text{true})}] = [-60^0 \;\; -6.9^0]$

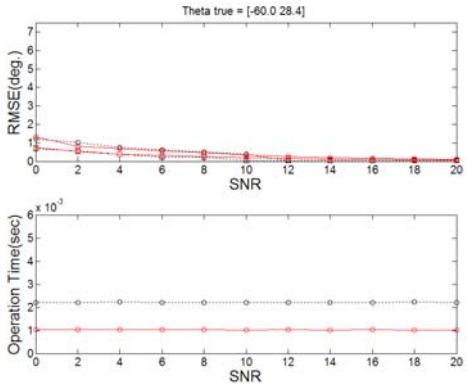

$[\theta_1^{(\text{true})} \;\; \theta_2^{(\text{true})}] = [-60^0 \;\; 28.4^0]$

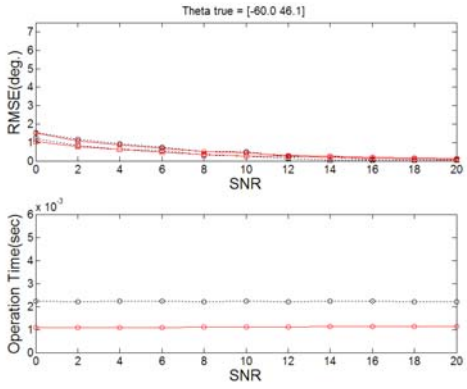

$[\theta_1^{(\text{true})} \;\; \theta_2^{(\text{true})}] = [-60^0 \;\; 46.1^0]$

Fig. 5. Initial estimates for $\Delta\theta = 1.2^0$ without the Newton iteration and the final estimates for $\Delta\theta = 4.7^0$ with the Newton iteration of the Capon beam forming algorithm for the ULA.

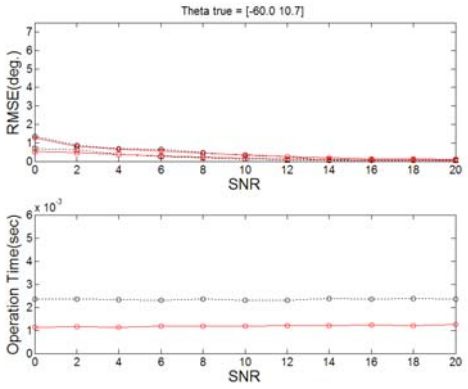

$[\theta_1^{(\text{true})} \;\; \theta_2^{(\text{true})}] = [-60^0 \;\; 10.7^0]$

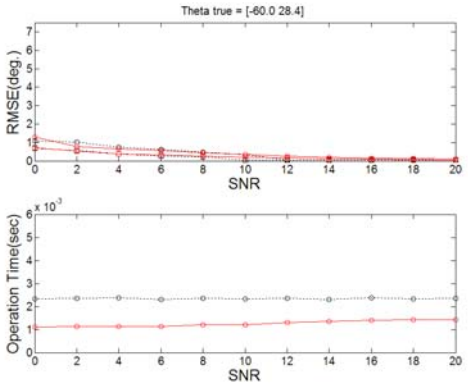

$[\theta_1^{(\text{true})} \;\; \theta_2^{(\text{true})}] = [-60^0 \;\; 28.4^0]$

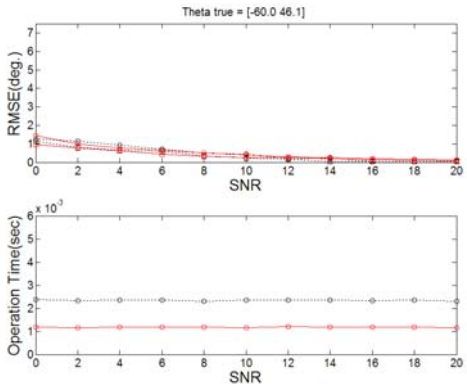

$$[\theta_1^{(\text{true})} \quad \theta_2^{(\text{true})}] = [-60^0 \quad 46.1^0]$$

Fig. 6. Initial estimates for $\Delta\theta = 1.2^0$ without the Newton iteration and the final estimates for $\Delta\theta = 4.7^0$ with the Newton iteration of the MUSIC algorithm for the ULA.

Table 1: Quantitative improvement of the RMSE and the execution time in Figs. 1–3.

Conventional Beam forming		$[\theta_1^{(\text{true})} \quad \theta_2^{(\text{true})}] = [-60^\circ \quad -6.9^\circ]$		$[\theta_1^{(\text{true})} \quad \theta_2^{(\text{true})}] = [-60^\circ \quad 10.7^\circ]$	
Search step	True angle	RMSE improvement	Time increment	RMSE improvement	Time increment
1.2°	θ_1	3.4 %	10.8 %	11.2 %	10.2 %
	θ_2	12.0 %		9.9 %	
4.7°	θ_1	41.3 %	37.5 %	44.6 %	35.3 %
	θ_2	69.6 %		62.7 %	
8.8°	θ_1	48.6 %	123.4 %	67.3 %	56.9 %
	θ_2	69.0 %		83.0 %	

Capon Beam forming		$[\theta_1^{(\text{true})} \quad \theta_2^{(\text{true})}] = [-60^\circ \quad -6.9^\circ]$		$[\theta_1^{(\text{true})} \quad \theta_2^{(\text{true})}] = [-60^\circ \quad 10.7^\circ]$	
Search step	True angle	RMSE improvement	Time increment	RMSE improvement	Time increment
1.2°	θ_1	-5.3 %	9.0 %	-1.1 %	9.1 %
	θ_2	-32.9 %		2.5 %	
4.7°	θ_1	61.3 %	32.5 %	64.2 %	32.8 %
	θ_2	89.7 %		79.2 %	
8.8°	θ_1	79.6 %	41.3 %	81.0 %	39.5 %
	θ_2	89.9 %		90.3 %	

MUSIC		$[\theta_1^{(\text{true})} \quad \theta_2^{(\text{true})}] = [-60^\circ \quad -6.9^\circ]$		$[\theta_1^{(\text{true})} \quad \theta_2^{(\text{true})}] = [-60^\circ \quad 10.7^\circ]$	
Search step	True angle	RMSE improvement	Time increment	RMSE improvement	Time increment
1.2°	θ_1	-8.4 %	8.5 %	-1.3 %	8.7 %
	θ_2	-33.3 %		2.5 %	
4.7°	θ_1	61.6 %	26.7 %	63.9 %	28.6 %
	θ_2	89.8 %		79.4 %	
8.8°	θ_1	80.7 %	35.8 %	81.1 %	33.8 %
	θ_2	90.0 %		90.4 %	

Table 2: Quantitative improvement of the RMSE and the execution time in Figs. 4–6.

Conventional Beam forming			
True angle	Search step	1.2°, 4.7° +NT	
		θ_1	θ_2
$[\theta_1^{(\text{true})} \quad \theta_2^{(\text{true})}] = [-60^\circ \quad -6.9^\circ]$	RMSE improvement	3.4 %	12.5 %
	Time decrement	52.1 %	
$[\theta_1^{(\text{true})} \quad \theta_2^{(\text{true})}] = [-60^\circ \quad 10.7^\circ]$	RMSE improvement	7.0 %	10.1 %
	Time decrement	52.7 %	
$[\theta_1^{(\text{true})} \quad \theta_2^{(\text{true})}] = [-60^\circ \quad 28.4^\circ]$	RMSE improvement	5.8 %	15.1 %
	Time decrement	54.1 %	
$[\theta_1^{(\text{true})} \quad \theta_2^{(\text{true})}] = [-60^\circ \quad 46.1^\circ]$	RMSE improvement	2.0 %	5.6 %
	Time decrement	35.5 %	

Capon Beam forming			
True angle	Search step	1.2°, 4.7° +NT	
		θ_1	θ_2
$[\theta_1^{(\text{true})} \quad \theta_2^{(\text{true})}] = [-60^\circ \quad -6.9^\circ]$	RMSE improvement	-8.3 %	-34.1 %
	Time decrement	46.5 %	
$[\theta_1^{(\text{true})} \quad \theta_2^{(\text{true})}] = [-60^\circ \quad 10.7^\circ]$	RMSE improvement	-3.0 %	4.1 %
	Time decrement	52.6 %	
$[\theta_1^{(\text{true})} \quad \theta_2^{(\text{true})}] = [-60^\circ \quad 28.4^\circ]$	RMSE improvement	-8.3 %	-21.7 %
	Time decrement	53.8 %	
$[\theta_1^{(\text{true})} \quad \theta_2^{(\text{true})}] = [-60^\circ \quad 46.1^\circ]$	RMSE improvement	-2.7 %	-5.4 %
	Time decrement	50.2 %	

MUSIC			
True angle	Search step	1.2°, 4.7° +NT	
		θ_1	θ_2
$[\theta_1^{(\text{true})} \quad \theta_2^{(\text{true})}]$	RMSE improvement	-9.1 %	-34.7 %
$= [-60^\circ \quad -6.9^\circ]$	Time decrement	37.9 %	
$[\theta_1^{(\text{true})} \quad \theta_2^{(\text{true})}]$	RMSE improvement	-3.0 %	4.2 %
$= [-60^\circ \quad 10.7^\circ]$	Time decrement	49.3 %	
$[\theta_1^{(\text{true})} \quad \theta_2^{(\text{true})}]$	RMSE improvement	-10.2 %	-16.1 %
$= [-60^\circ \quad 28.4^\circ]$	Time decrement	46.4 %	
$[\theta_1^{(\text{true})} \quad \theta_2^{(\text{true})}]$	RMSE improvement	-4.1 %	-1.0 %
$= [-60^\circ \quad 46.1^\circ]$	Time decrement	49.8 %	

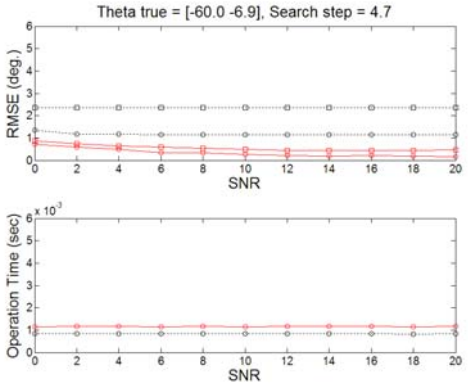

$[\theta_1^{(\text{true})} \quad \theta_2^{(\text{true})}] = [-60^0 \quad -6.9^0], \Delta\theta = 4.7^0$

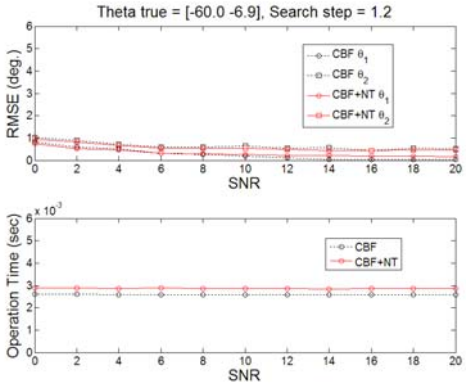

$[\theta_1^{(\text{true})} \quad \theta_2^{(\text{true})}] = [-60^0 \quad -6.9^0], \Delta\theta = 1.2^0$

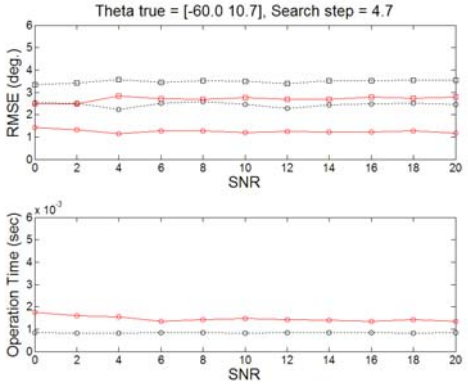

$[\theta_1^{(\text{true})} \quad \theta_2^{(\text{true})}] = [-60^0 \quad 10.7^0], \Delta\theta = 4.7^0$

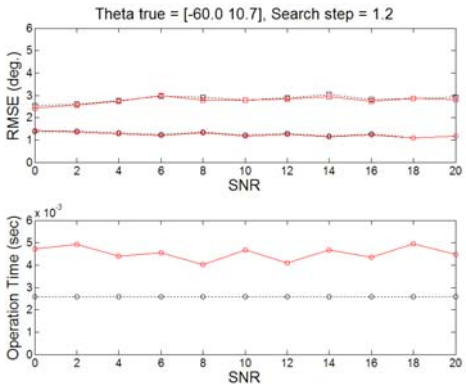

$[\theta_1^{(\text{true})} \quad \theta_2^{(\text{true})}] = [-60^0 \quad 10.7^0], \Delta\theta = 1.2^0$

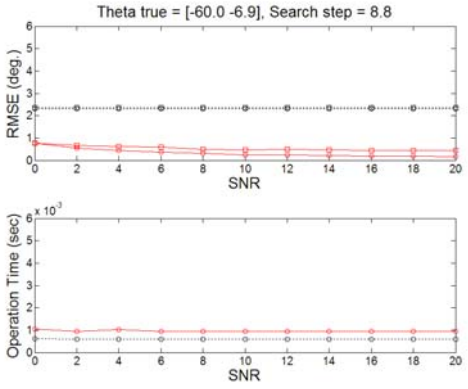

$[\theta_1^{(\text{true})} \quad \theta_2^{(\text{true})}] = [-60^0 \quad -6.9^0], \Delta\theta = 8.8^0$

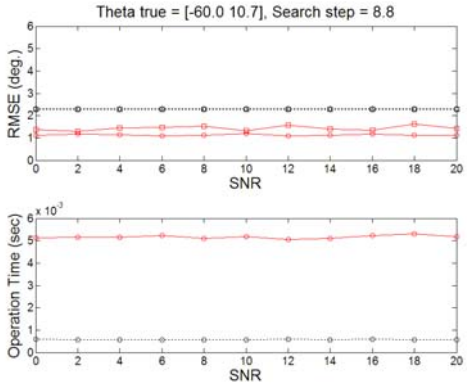

$[\theta_1^{(\text{true})} \;\; \theta_2^{(\text{true})}] = [-60^0 \;\; 10.7^0], \Delta\theta = 8.8^0$

Fig. 7. Initial estimates without the Newton iteration and the final estimates with the Newton iteration of the conventional beam forming algorithm for the UCA.

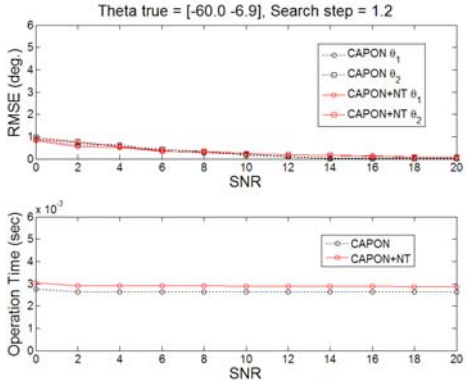

$[\theta_1^{(\text{true})} \;\; \theta_2^{(\text{true})}] = [-60^0 \;\; -6.9^0], \Delta\theta = 1.2^0$

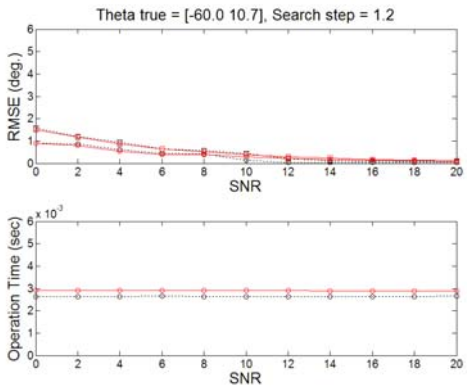

$[\theta_1^{(\text{true})} \;\; \theta_2^{(\text{true})}] = [-60^0 \;\; 10.7^0], \Delta\theta = 1.2^0$

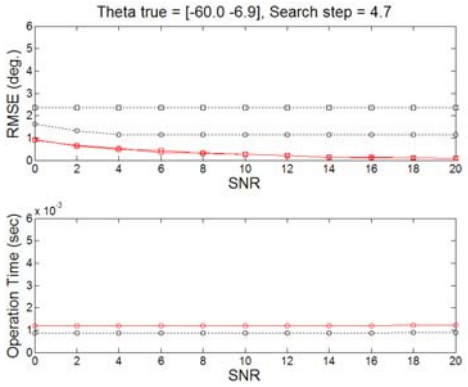

$[\theta_1^{(\text{true})} \;\; \theta_2^{(\text{true})}] = [-60^0 \;\; -6.9^0], \Delta\theta = 4.7^0$

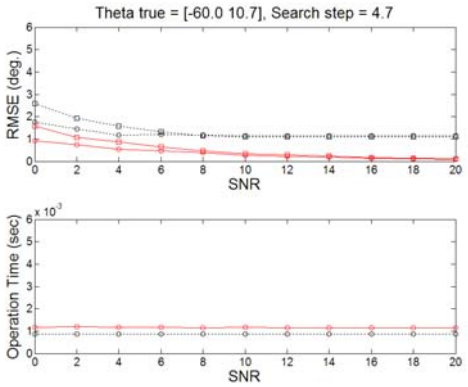

$[\theta_1^{(\text{true})} \;\; \theta_2^{(\text{true})}] = [-60^0 \;\; 10.7^0], \Delta\theta = 4.7^0$

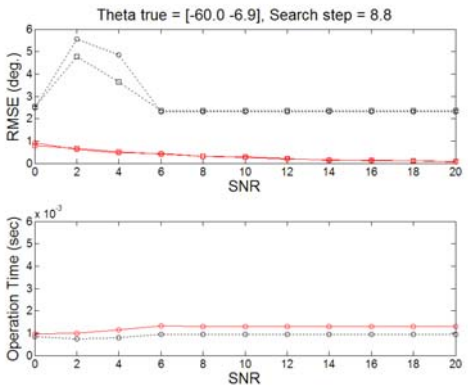

$[\theta_1^{(\text{true})} \;\; \theta_2^{(\text{true})}] = [-60^0 \;\; -6.9^0], \Delta\theta = 8.8^0$

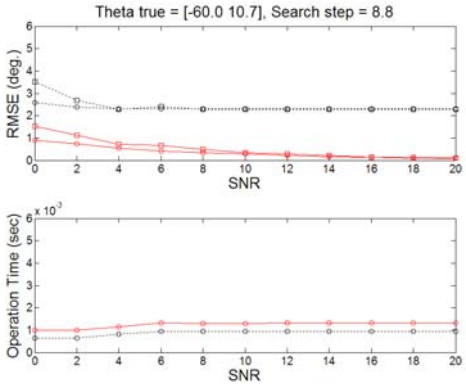

$[\theta_1^{(\text{true})} \;\; \theta_2^{(\text{true})}] = [-60^0 \;\; 10.7^0], \Delta\theta = 8.8^0$

Fig. 8. Initial estimates without the Newton iteration and the final estimates with the Newton iteration of the Capon beam forming algorithm for the UCA.

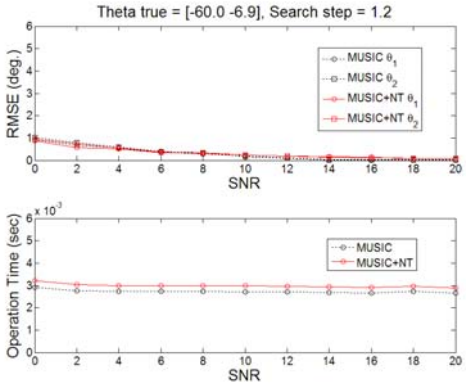

$[\theta_1^{(\text{true})} \;\; \theta_2^{(\text{true})}] = [-60^0 \;\; -6.9^0], \Delta\theta = 1.2^0$

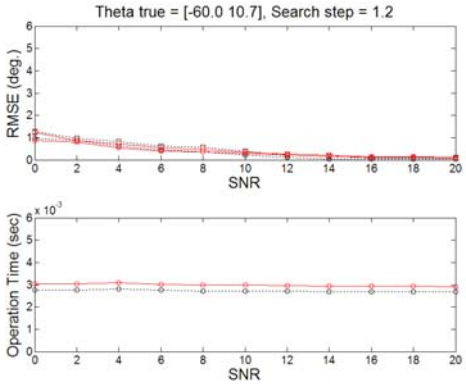

$[\theta_1^{(\text{true})} \;\; \theta_2^{(\text{true})}] = [-60^0 \;\; 10.7^0], \Delta\theta = 1.2^0$

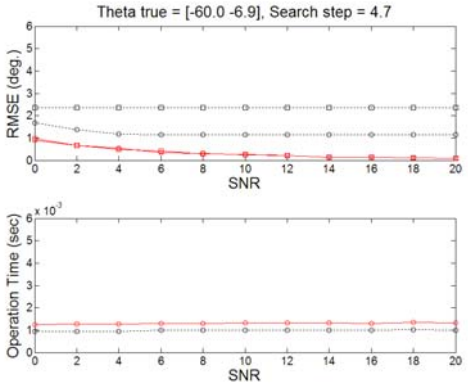

$[\theta_1^{(\text{true})} \;\; \theta_2^{(\text{true})}] = [-60^0 \;\; -6.9^0], \Delta\theta = 4.7^0$

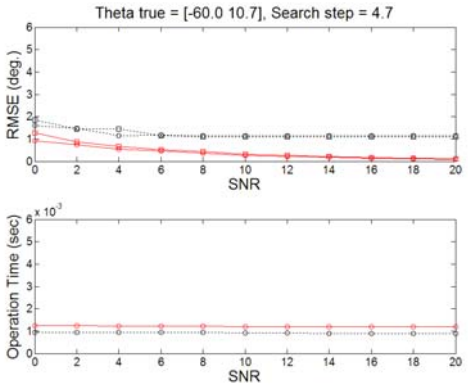

$[\theta_1^{(\text{true})} \;\; \theta_2^{(\text{true})}] = [-60^0 \;\; 10.7^0], \Delta\theta = 4.7^0$

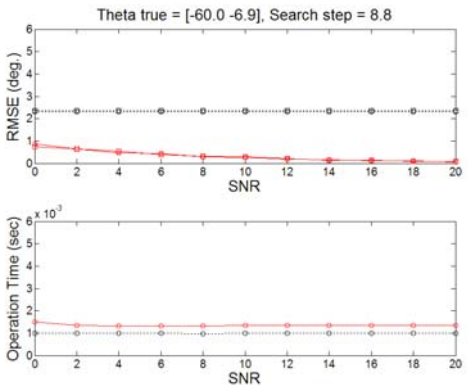

$[\theta_1^{(\text{true})} \;\; \theta_2^{(\text{true})}] = [-60^0 \;\; -6.9^0], \Delta\theta = 8.8^0$

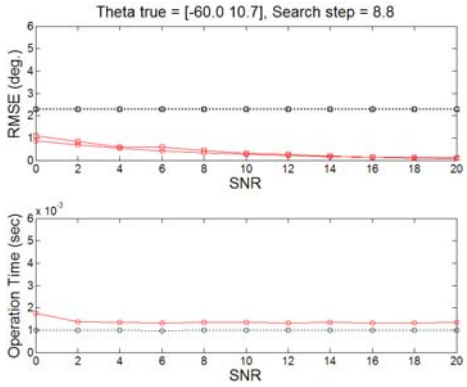

$[\theta_1^{(\text{true})} \;\; \theta_2^{(\text{true})}] = [-60^0 \;\; 10.7^0], \Delta\theta = 8.8^0$

Fig. 9. Initial estimates without the Newton iteration and the final estimates with the Newton iteration of the MUSIC algorithm for the UCA.

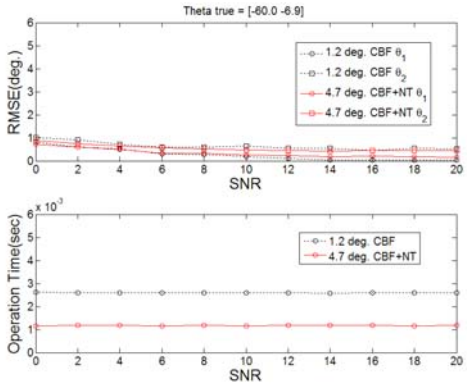

$[\theta_1^{(\text{true})} \;\; \theta_2^{(\text{true})}] = [-60^0 \;\; -6.9^0]$

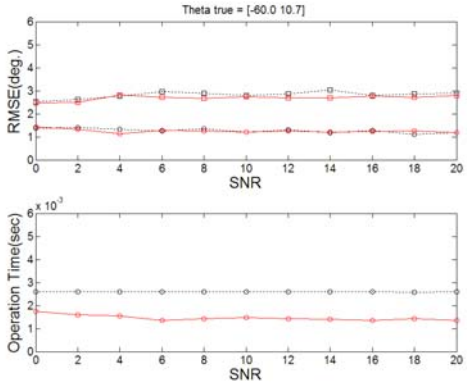

$[\theta_1^{(\text{true})} \;\; \theta_2^{(\text{true})}] = [-60^0 \;\; 10.7^0]$

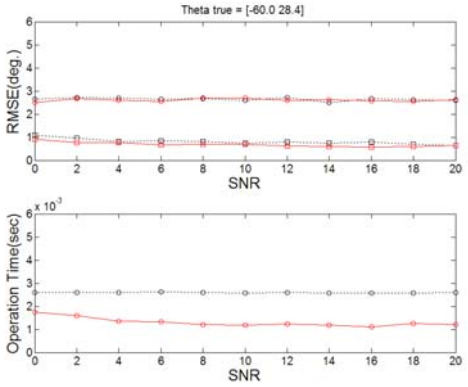

$[\theta_1^{(\text{true})} \;\; \theta_2^{(\text{true})}] = [-60^0 \;\; 28.4^0]$

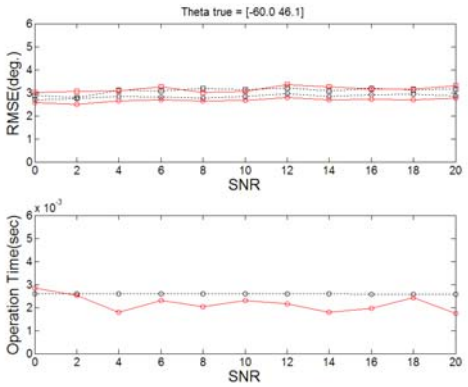

$[\theta_1^{(\text{true})} \;\; \theta_2^{(\text{true})}] = [-60^0 \;\; 46.1^0]$

Fig. 10. Initial estimates for $\Delta\theta = 1.2^0$ without the Newton iteration and the final estimates for $\Delta\theta = 4.7^0$ with the Newton iteration of the conventional beam forming algorithm for the UCA.

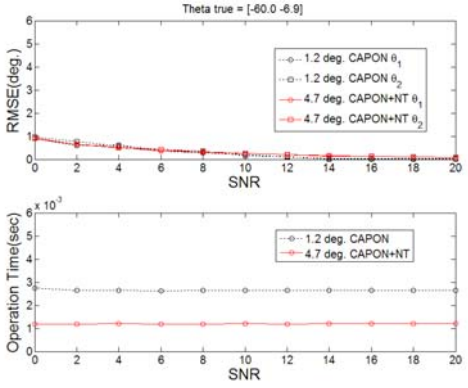

$[\theta_1^{(\text{true})} \;\; \theta_2^{(\text{true})}] = [-60^0 \;\; -6.9^0]$

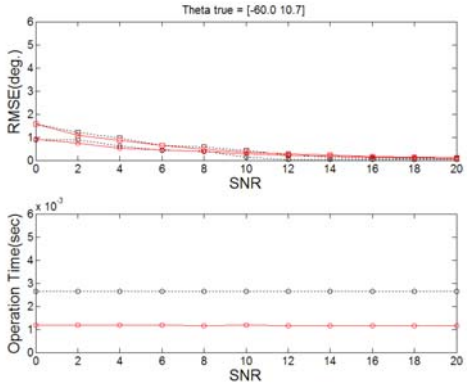

$[\theta_1^{(\text{true})} \;\; \theta_2^{(\text{true})}] = [-60^0 \;\; 10.7^0]$

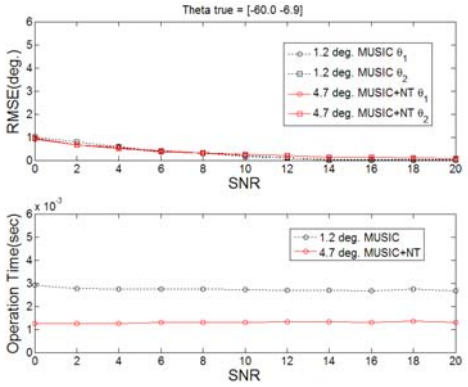

$[\theta_1^{(\text{true})} \;\; \theta_2^{(\text{true})}] = [-60^0 \;\; -6.9^0]$

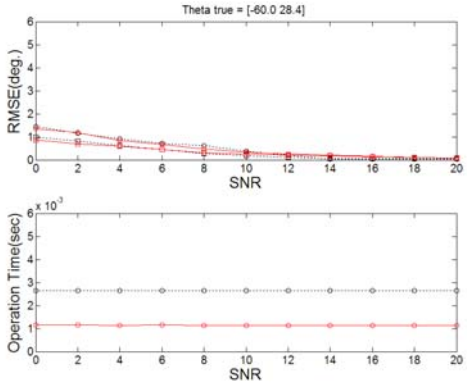

$[\theta_1^{(\text{true})} \;\; \theta_2^{(\text{true})}] = [-60^0 \;\; 28.4^0]$

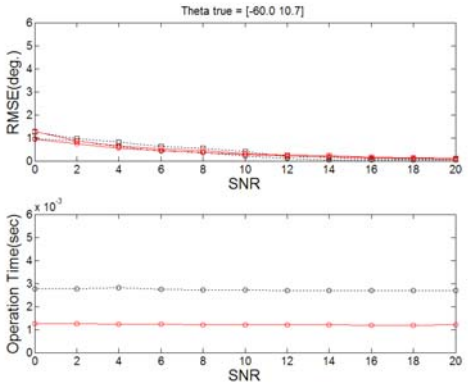

$[\theta_1^{(\text{true})} \;\; \theta_2^{(\text{true})}] = [-60^0 \;\; 10.7^0]$

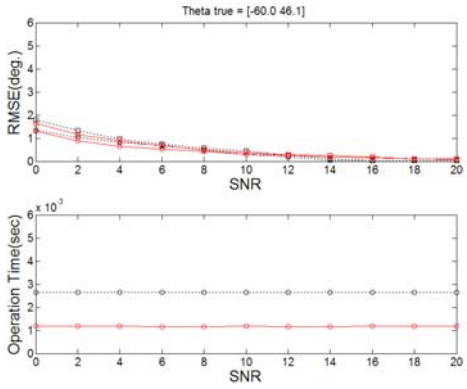

$[\theta_1^{(\text{true})} \;\; \theta_2^{(\text{true})}] = [-60^0 \;\; 46.1^0]$

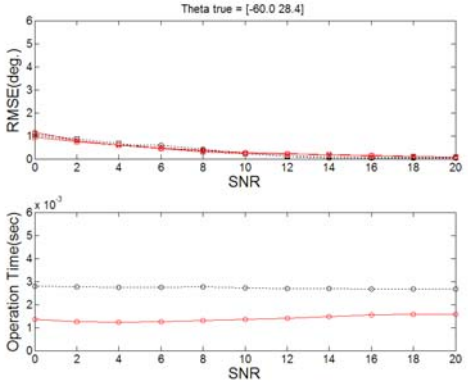

$[\theta_1^{(\text{true})} \;\; \theta_2^{(\text{true})}] = [-60^0 \;\; 28.4^0]$

Fig. 11. Initial estimates for $\Delta\theta = 1.2^0$ without the Newton iteration and the final estimates for $\Delta\theta = 4.7^0$ with the Newton iteration of the Capon beam forming algorithm for the UCA.

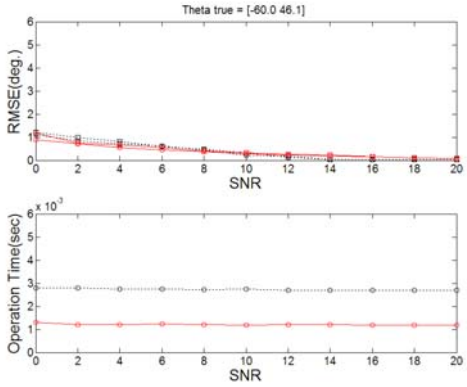

$[\theta_1^{(\text{true})} \;\; \theta_2^{(\text{true})}] = [-60^0 \;\; 46.1^0]$

Fig. 12. Initial estimates for $\Delta\theta = 1.2^0$ without the Newton iteration and the final estimates for $\Delta\theta = 4.7^0$ with the Newton iteration of the MUSIC algorithm for the UCA.

Table 3: Quantitative improvement of the RMSE and the execution time in Figs. 7–9.

Conventional Beam forming		$[\theta_1^{(\text{true})} \;\; \theta_2^{(\text{true})}] = [-60^\circ \;\; -6.9^\circ]$		$[\theta_1^{(\text{true})} \;\; \theta_2^{(\text{true})}] = [-60^\circ \;\; 10.7^\circ]$	
Search step	True angle	RMSE improvement	Time increment	RMSE improvement	Time increment
1.2°	θ_1	-20.6 %	10.3 %	2.5 %	74.7 %
	θ_2	11.0 %		1.9 %	
4.7°	θ_1	71.0 %	38.5 %	48.9 %	74.9 %
	θ_2	76.4 %		22.6 %	
8.8°	θ_1	85.5 %	60.4 %	51.0 %	78.7 %
	θ_2	77.5 %		36.9 %	

Capon Beam forming		$[\theta_1^{(\text{true})} \;\; \theta_2^{(\text{true})}] = [-60^\circ \;\; -6.9^\circ]$		$[\theta_1^{(\text{true})} \;\; \theta_2^{(\text{true})}] = [-60^\circ \;\; 10.7^\circ]$	
Search step	True angle	RMSE improvement	Time increment	RMSE improvement	Time increment
1.2°	θ_1	-8.2 %	9.5 %	-10.9 %	9.7 %
	θ_2	-10.5 %		-0.8 %	
4.7°	θ_1	72.1 %	36.6 %	70.1 %	33.1 %
	θ_2	85.5 %		61.0 %	
8.8°	θ_1	88.3 %	34.6 %	84.9 %	40.6 %
	θ_2	87.8 %		78.4 %	

MUSIC		$[\theta_1^{(\text{true})} \;\; \theta_2^{(\text{true})}] = [-60^\circ \;\; -6.9^\circ]$		$[\theta_1^{(\text{true})} \;\; \theta_2^{(\text{true})}] = [-60^\circ \;\; 10.7^\circ]$	
Search step	True angle	RMSE improvement	Time increment	RMSE improvement	Time increment
1.2°	θ_1	-6.0 %	9.2 %	-5.3 %	9.3 %
	θ_2	-11.2 %		2.7 %	
4.7°	θ_1	72.3 %	32.6 %	69.8 %	31.1 %
	θ_2	85.3 %		63.4 %	
8.8°	θ_1	85.7 %	37.7 %	85.0 %	40.1 %
	θ_2	86.3 %		81.1 %	

Table 4: Quantitative improvement of the RMSE and the execution time in Figs. 10–12.

Conventional Beam forming			
True angle	Search step	1.2°, 4.7° +NT	
		θ_1	θ_2
$[\theta_1^{(\text{true})} \;\; \theta_2^{(\text{true})}] = [-60^\circ \;\; -6.9^\circ]$	RMSE improvement	-25.4 %	14.1 %
	Time decrement	55.1 %	
$[\theta_1^{(\text{true})} \;\; \theta_2^{(\text{true})}] = [-60^\circ \;\; 10.7^\circ]$	RMSE improvement	1.2 %	4.6 %
	Time decrement	43.5 %	
$[\theta_1^{(\text{true})} \;\; \theta_2^{(\text{true})}] = [-60^\circ \;\; 28.4^\circ]$	RMSE improvement	1.5 %	15.3 %
	Time decrement	49.4 %	
$[\theta_1^{(\text{true})} \;\; \theta_2^{(\text{true})}] = [-60^\circ \;\; 46.1^\circ]$	RMSE improvement	6.0 %	-2.2 %
	Time decrement	16.3 %	

Capon Beam forming			
True angle	Search step	1.2°, 4.7° +NT	
		θ_1	θ_2
$[\theta_1^{(\text{true})} \;\; \theta_2^{(\text{true})}] = [-60^\circ \;\; -6.9^\circ]$	RMSE improvement	-14.1 %	-10.5 %
	Time decrement	54.7 %	
$[\theta_1^{(\text{true})} \;\; \theta_2^{(\text{true})}] = [-60^\circ \;\; 10.7^\circ]$	RMSE improvement	-12.8 %	0.8 %
	Time decrement	56.0 %	
$[\theta_1^{(\text{true})} \;\; \theta_2^{(\text{true})}] = [-60^\circ \;\; 28.4^\circ]$	RMSE improvement	0.1 %	-5.4 %
	Time decrement	56.7 %	
$[\theta_1^{(\text{true})} \;\; \theta_2^{(\text{true})}] = [-60^\circ \;\; 46.1^\circ]$	RMSE improvement	1.8 %	2.4 %
	Time decrement	55.9 %	

MUSIC			
True angle	Search step	1.2°, 4.7° +NT	
		θ_1	θ_2
$\left[\theta_1^{(\text{true})} \quad \theta_2^{(\text{true})}\right]$	RMSE improvement	-11.6 %	-11.7 %
$=\left[-60^\circ \quad -6.9^\circ\right]$	Time decrement	52.5 %	
$\left[\theta_1^{(\text{true})} \quad \theta_2^{(\text{true})}\right]$	RMSE improvement	-7.9 %	4.7 %
$=\left[-60^\circ \quad 10.7^\circ\right]$	Time decrement	55.4 %	
$\left[\theta_1^{(\text{true})} \quad \theta_2^{(\text{true})}\right]$	RMSE improvement	-12.7 %	1.5 %
$=\left[-60^\circ \quad 28.4^\circ\right]$	Time decrement	48.9 %	
$\left[\theta_1^{(\text{true})} \quad \theta_2^{(\text{true})}\right]$	RMSE improvement	5.9 %	-0.4 %
$=\left[-60^\circ \quad 46.1^\circ\right]$	Time decrement	55.4 %	

It is clearly shown that the performance of the final estimates for $\Delta\theta = 4.7^0$ with the Newton iteration is nearly as good as the that of the initial estimates for $\Delta\theta = 1.2^0$ without the Newton iteration for all the three algorithms and that the computational complexity of getting the final estimates for $\Delta\theta = 4.7^0$ is less than that of getting the initial estimates for $\Delta\theta = 1.2^0$. In Tables 1–4, we clearly indicate quantitative improvement of the proposed method over the conventional method, which does not employ the Newton iteration in Figs. 1–12. The improvement of the RMSE and the execution time is indicated.

IX. CONCLUSION

In this paper, we propose essentially different approach of applying the Newton iteration to the AOA estimate to improve the accuracy of the AOA estimate. We apply the Newton iteration to the initial estimate obtained from the beam forming algorithm and the MUSIC algorithm to obtain the final estimates, which are more accurate than the initial estimates. We have demonstrated the performance improvement using the numerical results.

It is quite straightforward to apply the proposed scheme to other AOA estimation algorithm. In this paper, we showed the results for the case that there are two incident signals. It is also possible to apply the proposed scheme when there are more than two incident signals because the Newton iteration is applied to each incident signal, respectively. The scheme can also be applied to any arbitrary array structure by modifying the array vector consistently. The improvement of the proposed method over the conventional method in terms of the RMSE and the execution time is shown in Tables 1–4, qualitatively.

APPENDIX A

To find the angles, which are the local maxima of equation (11), we find the angle at which the derivative of equation (11) is zero. If we differentiate equation (11) with respect to θ, we have,

$$\frac{dP_{\text{CBF, ULA}}(\theta)}{d\theta} = \sum_{m=1}^{M}\sum_{n=1}^{M} j(n-m)\pi\cos\theta\exp\left(j(n-m)\pi\sin\theta\right)\hat{R}_{mn}. \tag{A1}$$

For the UCA, differentiating equation (14) with respect to θ yields,

$$\frac{dP_{\text{CBF, UCA}}(\theta)}{d\theta} = \sum_{m=1}^{M}\sum_{n=1}^{M}\left[-j4\pi\frac{r}{\lambda}\sin\left(\frac{\pi(m-n)}{M}\right)\cos\left(\theta-\frac{\pi(n+m-2)}{M}\right)\right] \exp\left[-j4\pi\frac{r}{\lambda}\sin\left(\frac{\pi(m-n)}{M}\right)\sin\left(\theta-\frac{\pi(n+m-2)}{M}\right)\right]\hat{R}_{mn}. \tag{A2}$$

Since equation (A1) is the derivative of equation (11), to find the angles which are local maxima of equation (11), we have to find the solution of,

$$\frac{dP_{\text{CBF, ULA}}(\theta)}{d\theta} = \sum_{m=1}^{M}\sum_{n=1}^{M} j(n-m)\pi\cos\theta\exp\left(j(n-m)\pi\sin\theta\right)\hat{R}_{mn} = 0. \tag{A3}$$

Similarly, to find the local maxima of equation (14), we have to find the solution of the following,

$$\frac{dP_{\text{CBF, UCA}}(\theta)}{d\theta} = \sum_{m=1}^{M}\sum_{n=1}^{M}\left\{-j4\pi\frac{r}{\lambda}\sin\left(\frac{\pi(m-n)}{M}\right)\cos\left(\theta-\frac{\pi(n+m-2)}{M}\right) \exp\left[-j4\pi\frac{r}{\lambda}\sin\left(\frac{\pi(m-n)}{M}\right)\sin\left(\theta-\frac{\pi(n+m-2)}{M}\right)\right]\right\}\hat{R}_{mn} = 0. \tag{A4}$$

Since the local maxima of equation (11) are obtained from the solutions of equation (A3), the initial guess of the solution of equation (A3) are the initial AOA estimates of equation (11). As previously stated, the initial guesses of the solution of equation (A3) are also calculated from the N local maxima of $\mathbf{a}^{\text{H}}(\theta)\,\hat{\mathbf{R}}\,\mathbf{a}(\theta)$ at the discrete angles given by equation (7). $\mathbf{a}(\theta)$ are defined in equations (8) and (10). Similarly, the initial estimates of equation (A4), which is for the UCA, are calculated from the N local maxima of $\mathbf{a}^{\text{H}}(\theta)\,\hat{\mathbf{R}}\,\mathbf{a}(\theta)$ at the discrete angles given by equation (7) and $\mathbf{a}(\theta)$is defined in equations (8) and (13).

Our concern is, given the initial estimates, $\theta_1^{(0)}$, $\theta_2^{(0)}$,…, $\theta_N^{(0)}$, how to find the solutions of equations (A3) and (A4) numerically. The final estimates, $\theta_1^{(\text{final})}$, $\theta_2^{(\text{final})}$,…, $\theta_N^{(\text{final})}$, can be found using the iterative update. To find the solutions of equation (A3) using the Newton iteration, we have to find the derivative of $[dP_{\text{CBF,ULA}}(\theta)/\text{d}\theta]$ and $[dP_{\text{CBF,UCA}}(\theta)/\text{d}\theta]$ with respect to θ. The derivative of equation (A3) is easily obtained to be,

$$\begin{aligned}\frac{d}{d\theta}\left(\frac{dP_{\text{CBF, ULA}}(\theta)}{d\theta}\right) &= \sum_{m=1}^{M}\sum_{n=1}^{M}\left[\begin{matrix}-j(n-m)\pi\sin\theta\\ \exp\left(j(n-m)\pi\sin\theta\right)\end{matrix}\right. \\ &\qquad \left.\begin{matrix}+\left(j(n-m)\pi\right)^2\cos^2\theta\\ \exp\left(j(n-m)\pi\sin\theta\right)\end{matrix}\right]\hat{R}_{mn} \\ &= \sum_{m=1}^{M}\sum_{n=1}^{M} j(n-m)\pi\exp\left(j(n-m)\pi\sin\theta\right)\left(j(n-m)\pi\cos^2\theta-\sin\theta\right)\hat{R}_{mn}\end{aligned} \quad \text{(A5)}$$

Similarly, the derivative of (A4) is,

$$\begin{aligned}&\frac{d}{d\theta}\left(\frac{dP_{\text{CBF, UCA}}(\theta)}{d\theta}\right) \\ &= \sum_{m=1}^{M}\sum_{n=1}^{M}\left\{j4\pi\frac{r}{\lambda}\sin\left(\frac{\pi(m-n)}{M}\right)\sin\left(\theta-\frac{\pi(n+m-2)}{M}\right)\right. \\ &\quad \exp\left[-j4\pi\frac{r}{\lambda}\sin\left(\frac{\pi(m-n)}{M}\right)\sin\left(\theta-\frac{\pi(n+m-2)}{M}\right)\right] \\ &\quad +\left(-j4\pi\frac{r}{\lambda}\sin\left(\frac{\pi(m-n)}{M}\right)\right)^2\cos^2\left(\theta-\frac{\pi(n+m-2)}{M}\right) \\ &\quad \left.\exp\left[-j4\pi\frac{r}{\lambda}\sin\left(\frac{\pi(m-n)}{M}\right)\sin\left(\theta-\frac{\pi(n+m-2)}{M}\right)\right]\right\}\hat{R}_{mn} \\ &= \sum_{m=1}^{M}\sum_{n=1}^{M}\left\{-j4\pi\frac{r}{\lambda}\sin\left(\frac{\pi(m-n)}{M}\right)\exp\left[\begin{matrix}-j4\pi\frac{r}{\lambda}\sin\left(\frac{\pi(m-n)}{M}\right)\\ \sin\left(\theta-\frac{\pi(n+m-2)}{M}\right)\end{matrix}\right]\right. \\ &\quad \left.\left[\begin{matrix}-j4\pi\frac{r}{\lambda}\sin\left(\frac{\pi(m-n)}{M}\right)\cos^2\left(\theta-\frac{\pi(n+m-2)}{M}\right)\\ -\sin\left(\theta-\frac{\pi(n+m-2)}{M}\right)\end{matrix}\right]\hat{R}_{mn}\right\}.\end{aligned} \quad \text{(A6)}$$

APPENDIX B

Differentiation of equations (19) and (21) with respect to θ gives,

$$\begin{aligned}&\frac{dD_{\text{Capon, ULA}}(\theta)}{d\theta} \\ &= \sum_{m=1}^{M}\sum_{n=1}^{M} j(n-m)\pi\cos\theta\exp\left(j(n-m)\pi\sin\theta\right)\hat{R}_{mn}^{-1}\end{aligned} \quad \text{(B1)}$$

$$\begin{aligned}&\frac{dD_{\text{Capon, UCA}}(\theta)}{d\theta} \\ &= \left\{\sum_{m=1}^{M}\sum_{n=1}^{M} -j4\pi\frac{r}{\lambda}\sin\left(\frac{\pi(m-n)}{M}\right)\cos\left(\theta-\frac{\pi(n+m-2)}{M}\right)\right. \\ &\quad \left.\exp\left[-j4\pi\frac{r}{\lambda}\sin\left(\frac{\pi(m-n)}{M}\right)\sin\left(\theta-\frac{\pi(n+m-2)}{M}\right)\right]\right\}\hat{R}_{mn}^{-1}.\end{aligned} \quad \text{(B2)}$$

We have to find the solutions of,

$$\begin{aligned}&\frac{dD_{\text{Capon, ULA}}(\theta)}{d\theta} \\ &= \sum_{m=1}^{M}\sum_{n=1}^{M} j(n-m)\pi\cos\theta\exp\left(j(n-m)\pi\sin\theta\right)\hat{R}_{mn}^{-1} = 0\end{aligned} \quad \text{(B3)}$$

$$\begin{aligned}\frac{dD_{\text{Capon, UCA}}(\theta)}{d\theta} &= \left\{\sum_{m=1}^{M}\sum_{n=1}^{M}\begin{matrix}-j4\pi\frac{r}{\lambda}\sin\left(\frac{\pi(m-n)}{M}\right)\\ \cos\left(\theta-\frac{\pi(n+m-2)}{M}\right)\end{matrix}\right. \\ &\quad \left.\exp\left[\begin{matrix}-j4\pi\frac{r}{\lambda}\sin\left(\frac{\pi(m-n)}{M}\right)\\ \sin\left(\theta-\frac{\pi(n+m-2)}{M}\right)\end{matrix}\right]\right\}\hat{R}_{mn}^{-1} = 0.\end{aligned} \quad \text{(B4)}$$

The derivatives of equations (B3) and (B4) are easily obtained to be,

$$\begin{aligned}\frac{d}{d\theta}\left(\frac{dD_{\text{Capon, ULA}}(\theta)}{d\theta}\right) &= \sum_{m=1}^{M}\sum_{n=1}^{M}\left[\begin{matrix}-j(n-m)\pi\sin\theta\\ \exp\left(j(n-m)\pi\sin\theta\right)\end{matrix}\right. \\ &\qquad \left.\begin{matrix}+\left(j(n-m)\pi\right)^2\cos^2\theta\\ \exp\left(j(n-m)\pi\sin\theta\right)\end{matrix}\right]\hat{R}_{mn}^{-1} \\ &= \sum_{m=1}^{M}\sum_{n=1}^{M} j(n-m)\pi\exp\left(j(n-m)\pi\sin\theta\right)\left(j(n-m)\pi\cos^2\theta-\sin\theta\right)\hat{R}_{mn}^{-1}\end{aligned} \quad \text{(B5)}$$

$$\begin{aligned}&\frac{d}{d\theta}\left(\frac{dD_{\text{Capon, UCA}}(\theta)}{d\theta}\right) = \sum_{m=1}^{M}\sum_{n=1}^{M}\left\{j4\pi\frac{r}{\lambda}\sin\left(\frac{\pi(m-n)}{M}\right)\sin\left(\theta-\frac{\pi(n+m-2)}{M}\right)\right. \\ &\quad \exp\left[-j4\pi\frac{r}{\lambda}\sin\left(\frac{\pi(m-n)}{M}\right)\sin\left(\theta-\frac{\pi(n+m-2)}{M}\right)\right] \\ &\quad +\left(-j4\pi\frac{r}{\lambda}\sin\left(\frac{\pi(m-n)}{M}\right)\right)^2\cos^2\left(\theta-\frac{\pi(n+m-2)}{M}\right) \\ &\quad \left.\exp\left[-j4\pi\frac{r}{\lambda}\sin\left(\frac{\pi(m-n)}{M}\right)\sin\left(\theta-\frac{\pi(n+m-2)}{M}\right)\right]\right\}\hat{R}_{mn}^{-1} \\ &= \sum_{m=1}^{M}\sum_{n=1}^{M}\left\{-j4\pi\frac{r}{\lambda}\sin\left(\frac{\pi(m-n)}{M}\right)\exp\left[\begin{matrix}-j4\pi\frac{r}{\lambda}\sin\left(\frac{\pi(m-n)}{M}\right)\\ \sin\left(\theta-\frac{\pi(n+m-2)}{M}\right)\end{matrix}\right]\right. \\ &\quad \left.\left[\begin{matrix}-j4\pi\frac{r}{\lambda}\sin\left(\frac{\pi(m-n)}{M}\right)\cos^2\left(\theta-\frac{\pi(n+m-2)}{M}\right)\\ -\sin\left(\theta-\frac{\pi(n+m-2)}{M}\right)\end{matrix}\right]\hat{R}_{mn}^{-1}\right\}.\end{aligned} \quad \text{(B6)}$$

APPENDIX C

The differentiation of equations (25) and (27) with respect to θ results in,

$$\frac{dD_{\text{MUSIC, ULA}}(\theta)}{d\theta} = \sum_{m=1}^{M}\sum_{n=1}^{M} j(n-m)\pi\cos\theta\exp\left(j(n-m)\pi\sin\theta\right)\left(\mathbf{U}_N\mathbf{U}_N^H\right)_{mn} \tag{C1}$$

$$\frac{dD_{\text{MUSIC, UCA}}(\theta)}{d\theta} = \sum_{m=1}^{M}\sum_{n=1}^{M}\left\{\begin{bmatrix}-j4\pi\frac{r}{\lambda}\sin\left(\frac{\pi(m-n)}{M}\right)\\ \cos\left(\theta-\frac{\pi(n+m-2)}{M}\right)\end{bmatrix}\exp\left[\begin{matrix}-j4\pi\frac{r}{\lambda}\sin\left(\frac{\pi(m-n)}{M}\right)\\ \sin\left(\theta-\frac{\pi(n+m-2)}{M}\right)\end{matrix}\right]\right\}\left(\mathbf{U}_N\mathbf{U}_N^H\right)_{mn}. \tag{C2}$$

Accordingly, our objective is to find the solution of the followings,

$$\frac{dD_{\text{MUSIC, ULA}}(\theta)}{d\theta} = \sum_{m=1}^{M}\sum_{n=1}^{M} j(n-m)\pi\cos\theta\exp\left(j(n-m)\pi\sin\theta\right)\left(\mathbf{U}_N\mathbf{U}_N^H\right)_{mn} = 0 \tag{C3}$$

$$\frac{dD_{\text{MUSIC, UCA}}(\theta)}{d\theta} = \sum_{m=1}^{M}\sum_{n=1}^{M}\begin{bmatrix}-j4\pi\frac{r}{\lambda}\sin\left(\frac{\pi(m-n)}{M}\right)\\ \cos\left(\theta-\frac{\pi(n+m-2)}{M}\right)\end{bmatrix}\exp\left[\begin{matrix}-j4\pi\frac{r}{\lambda}\sin\left(\frac{\pi(m-n)}{M}\right)\\ \sin\left(\theta-\frac{\pi(n+m-2)}{M}\right)\end{matrix}\right]\left(\mathbf{U}_N\mathbf{U}_N^H\right)_{mn} = 0. \tag{C4}$$

Differentiation of equation (C3) and (C4) results in,

$$\frac{d}{d\theta}\left(\frac{dD_{\text{MUSIC, ULA}}(\theta)}{d\theta}\right) = \sum_{m=1}^{M}\sum_{n=1}^{M}\left[\begin{matrix}-j(n-m)\pi\sin\theta\\ \exp\left(j(n-m)\pi\sin\theta\right)\end{matrix}\right.$$
$$\left.\begin{matrix}+\left(j(n-m)\pi\right)^2\cos^2\theta\\ \exp\left(j(n-m)\pi\sin\theta\right)\end{matrix}\right]\left(\mathbf{U}_N\mathbf{U}_N^H\right)_{mn}$$
$$= \sum_{m=1}^{M}\sum_{n=1}^{M} j(n-m)\pi\exp\left(j(n-m)\pi\sin\theta\right)\left(j(n-m)\pi\cos^2\theta-\sin\theta\right)\left(\mathbf{U}_N\mathbf{U}_N^H\right)_{mn} \tag{C5}$$

$$\frac{d}{d\theta}\left(\frac{dD_{\text{MUSIC, UCA}}(\theta)}{d\theta}\right)$$
$$= \sum_{m=1}^{M}\sum_{n=1}^{M}\left\{j4\pi\frac{r}{\lambda}\sin\left(\frac{\pi(m-n)}{M}\right)\sin\left(\theta-\frac{\pi(n+m-2)}{M}\right)\right.$$
$$\exp\left[-j4\pi\frac{r}{\lambda}\sin\left(\frac{\pi(m-n)}{M}\right)\sin\left(\theta-\frac{\pi(n+m-2)}{M}\right)\right]$$
$$+\left(-j4\pi\frac{r}{\lambda}\sin\left(\frac{\pi(m-n)}{M}\right)\right)^2\cos^2\left(\theta-\frac{\pi(n+m-2)}{M}\right)$$
$$\left.\exp\left[-j4\pi\frac{r}{\lambda}\sin\left(\frac{\pi(m-n)}{M}\right)\sin\left(\theta-\frac{\pi(n+m-2)}{M}\right)\right]\right\}\left(\mathbf{U}_N\mathbf{U}_N^H\right)_{mn}$$
$$= \sum_{m=1}^{M}\sum_{n=1}^{M}\left\{-j4\pi\frac{r}{\lambda}\sin\left(\frac{\pi(m-n)}{M}\right)\exp\begin{bmatrix}-j4\pi\frac{r}{\lambda}\sin\left(\frac{\pi(m-n)}{M}\right)\\ \sin\left(\theta-\frac{\pi(n+m-2)}{M}\right)\end{bmatrix}\right.$$
$$\left.\begin{bmatrix}-j4\pi\frac{r}{\lambda}\sin\left(\frac{\pi(m-n)}{M}\right)\cos^2\left(\theta-\frac{\pi(n+m-2)}{M}\right)\\ -\sin\left(\theta-\frac{\pi(n+m-2)}{M}\right)\end{bmatrix}\right\}\left(\mathbf{U}_N\mathbf{U}_N^H\right)_{mn} \tag{C6}$$

ACKNOWLEDGMENT

This research was supported by Basic Science Research Program through the National Research Foundation of Korea (NRF) funded by the Ministry of Education, Science and Technology (2012-0002347).

REFERENCES

[1] H. Krim and M. Viberg, "Two decades of array signal processing research – The parametric approach," *IEEE Signal Processing Magazine*, vol. 13, pp. 67-94, July 1996.

[2] J. –H. Lee and S. –H. Cho, "On initialization of ML DOA cost function for UCA," *Progress in Electromagnetics Research M*, vol. 3, pp. 91-102, 2008.

[3] J. –H. Lee, H. -J. Kwon, and Y. -K. Jin, "Numerically efficient implementation of JADE ML algorithm," *Journal of Electromagnetic Waves and Applications*, vol. 22, pp. 1693-1704, 2008.

[4] J. –H. Lee and S. –H. Cho, "Initialization of cost function for ML-based DOA estimation," *The Journal of Korea Information and Communications Society*, vol. 33, no. 1, pp. 110-116, Jan. 2008.

[5] M. Rubsamen and A. Gershman, "Direction-of-arrival estimation for non uniform sensor arrays: From manifold separation to Fourier domain MUSIC methods," *IEEE Trans. on Signal Processing*, vol. 57, no. 2, pp. 588-599, 2009.

[6] S. A. Vorobyov, A. B. Gershman, and K. M. Wong, "Maximum likelihood direction-of-arrival

estimation in unknown noise fields using sparse sensor arrays," *IEEE Trans. Signal Processing*, vol. 53, pp. 34-43, Jan. 2005.

[7] H. Cao, L. Yang, X. Tan, and S. Yang, "Computationally efficient 2-D DOA estimation using two parallel uniform linear arrays," *ETRI Journal*, vol. 31, no. 6, pp. 806-808, Dec. 2009.

[8] J. A. Olague, D. C. Rosales, and J. L. Rivera, "Efficiency evaluation of the unconditional maximum likelihood estimator for near-field DOA estimation," *ETRI Journal*, vol. 28, no.6, pp. 761-769, Dec. 2006.

[9] N. Deblauwe and L. Van Biesen, "An angle of arrival location estimation technique for existing GSM networks," *IEEE International Conference on Signal Processing and Communications*, pp. 1527-1530, 2007.

[10] S. Lalchand, A. Ijaz, M. M. Manzoor, I. A. Awan, and A. A. Siddique, "Error estimation in angle of arrival in smart antenna," *International Conference on Information and Communication Technologies*, pp. 1-3, 2011.

[11] I. Jami and R. F. Ormondroyd, "Improved method for estimating angle of arrival in multipath conditions using the `MUSIC' algorithm," *IEEE-APS Conference on Antennas and Propagation for Wireless Communications*, pp. 99-102, 2000.

[12] I. Amundson, X. Koutsoukos, J. Sallai, and A. Ledeczi, "Mobile sensor navigation using rapid RF-based angle of arrival localization," *17th IEEE Real-Time and Embedded Technology and Applications Symposium*, 2011.

[13] Y. Luo and C. L. Law, "Angle-of-arrival estimation with array in a line-of-sight indoor UWB-IR," *7th International Conference on Information, Communications and Signal Processing*, pp. 1-5, 2009.

[14] J. Friedman, A. Davitian, D. Torres, D. Cabric, and M. Srivastava, "Angle-of-arrival-assisted relative interferometric localization using software defined radios," *IEEE Military Communications Conference*, pp. 1-8, 2009.

[15] V. Kezys, E. Vertatschitsch, T. Greenlay, and S. Haykin, "High-resolution techniques for angle-of-arrival estimation," *IEEE Military Communications Conference - Communications-Computers: Teamed for the 90's*, pp. 41.3.1-41.3.6, 1986.

[16] N. B. Buchanan and V. Fusco, "Angle of arrival detection using retrodirective radar," *Radar Conference*, pp. 133-136, 2010.

[17] T. Chan, Y. Kuga, and S. Roy, "Combined use of various passive radar techniques and angle of arrival using music for the detection of ground moving objects," *IEEE International Symposium on Antennas and Propagation*, pp. 2561-2564, 2011.

[18] J. Friedman, T. Schmid, Z. Charbiwala, M. B. Srivastava, and Y. H. Cho, "Multistatic pulse-wave angle-of-arrival-assisted relative interferometric radar," *IEEE Radar Conference*, pp. 458- 463, 2011.

[19] Y. Kalkan and B. Baykal, "Target localization and velocity estimation methods for frequency-only mimo radars," *IEEE Radar Conference*, pp. 458-463, 2011.

[20] Y. Norouzi and M. Derakhshani, "Joint time difference of arrival/angle of arrival position finding in passive radar," *Radar, Sonar & Navigation, IET*, vol. 3, no.2, pp. 167-176, 2009.

[21] C. Du, J. S. Thompson, and Y. R. Petillot, "Hybrid bistatic radar," *International Radar Conference - Surveillance for a Safer World, International*, pp. 1-6, 2009.

[22] J. Capon, "High resolution frequency-wavenumber spectrum analysis," *Proceedings of the IEEE*, vol. 57, pp. 1408-1418, Aug. 1969.

[23] J. -H. Lee, Y. S. Jeong, S. -W. Cho, W. Y. Yeo, and K. Pister, "Application of the Newton method to improve the accuracy of TOA estimation with the beam forming algorithm and the MUSIC algorithm," *Progress in Electromagnetics Research*, vol. 116, pp. 475-515, 2011.

[24] R. O. Schmidt, "Multiple emitter location and signal parameter estimation," *Proceedings of RADC Spectral Est. Work shop*, pp. 243-258, Oct. 1979.

[25] R. Roy, A. Paulraj, and T. Kailath, "ESPRIT – a subspace rotation approach to estimation of parameters of cisoids in noise," *IEEE Trans. Acoustics, Speech, Signal Processing*, vol. 34, pp. 1340-1342, Oct. 1986.

[26] I. Ziskind and M. Wax, "Maximum likelihood localization of multiple sources by alternating projection," *IEEE Trans. on Signal Processing*, vol. 36, no. 10, pp. 1553-1560, Oct. 1988.

[27] H. W. Press, P. B. Flannery, A. S. Teukolsky, and T. W. Vetterling, *Numerical Recipes in C*, Cambridge University Press, 1992.

[28] http://en.wikipedia.org/wiki/Newton_method_in_optimization, August, 2012.

Joon-Ho Lee received the B.Sc. degree (Magna Cum Laude) in 1994, the M.Sc. degree in 1996, and the Ph.D. in 1999 in Electronics Engineering, all from Pohang University of Science and Technology (POSTECH), Pohang, Korea. From July 1999 to Feb. 2004, he was with Electronics and Telecommunications Research Institute (ETRI), Daejeon, Korea. Since March 2004, he has been with Sejong University, Seoul, Korea, where he is an Associate Professor with the Department of Information and Communication Eng. His research interests are in radio signal processing, array signal processing, spectrum estimation and radar target recognition. He was on Sabbatical leave at UC. Berkeley from Jan. 2010 to Jan. 2011.

Sung-Woo Cho received the B.Sc. degree in Information and Communication Engineering from Sejong University, Seoul, Korea in 2011. He is currently working toward his M.Sc. degree in Information and Communication Engineering from Sejong University. His research interests include array signal processing and radio signal processing.

2013 INSTITUTIONAL MEMBERS

DTIC-OCP LIBRARY
8725 John J. Kingman Rd, Ste 0944
Fort Belvoir, VA 22060-6218

AUSTRALIAN DEFENCE LIBRARY
Northcott Drive
Canberra, A.C.T. 2600 Australia

BEIJING BOOK CO, INC
701 E Linden Avenue
Linden, NJ 07036-2495

DARTMOUTH COLLEGE
6025 Baker/Berry Library
Hanover, NH 03755-3560

DSTO EDINBURGH
AU/33851-AP, PO Box 830470
Birmingham, AL 35283

SIMEON J. EARL – BAE SYSTEMS
W432A, Warton Aerodome
Preston, Lancs., UK PR4 1AX

ENERGY KEN LIBRARY
PO Box 300613
Jamaica, NY, 11430

ENGINEERING INFORMATION, INC
PO Box 543
Amsterdam, Netherlands 1000 Am

ETSE TELECOMUNICACION
Biblioteca, Campus Lagoas
Vigo, 36200 Spain

GA INSTITUTE OF TECHNOLOGY
EBS-Lib Mail code 0900
74 Cherry Street
Atlanta, GA 30332

TIMOTHY HOLZHEIMER
Raytheon
PO Box 1044
Rockwall, TX 75087

HRL LABS, RESEARCH LIBRARY
3011 Malibu Canyon
Malibu, CA 90265

IEE INSPEC
Michael Faraday House
6 Hills Way
Stevenage, Herts UK SG1 2AY

INSTITUTE FOR SCIENTIFIC INFO.
Publication Processing Dept.
3501 Market St.Philadelphia, PA
19104-3302

LIBRARY – DRDC OTTAWA
3701 Carling Avenue
Ottawa, Ontario, Canada K1A OZ4

LIBRARY of CONGRESS
Reg. Of Copyrights
Washington DC, 20559

LINDA HALL LIBRARY
5109 Cherry Street
Kansas City, MO 64110-2498

MISSOURI S&T
400 W 14th Street
Rolla, MO 56409

MIT LINCOLN LABORATORY
244 Wood Street
Lexington, MA 02420

NATIONAL CHI NAN UNIVERSITY
Lily Journal & Book Co, Ltd
20920 Glenbrook Drive
Walnut, CA 91789-3809

JOHN NORGARD
UCCS
20340 Pine Shadow Drive
Colorado Springs, CO 80908

OSAMA MOHAMMED
Florida International University
10555 W Flagler Street
Miami, FL 33174

NAVAL POSTGRADUATE SCHOOL
Attn:J. Rozdal/411 Dyer Rd./ Rm 111
Monterey, CA 93943-5101

NDL KAGAKU
C/0 KWE-ACCESS
PO Box 300613 (JFK A/P)
Jamaica, NY 11430-0613

OVIEDO LIBRARY
PO BOX 830679
Birmingham, AL 35283

DAVID PAULSEN
E3Compliance
1523 North Joe Wilson Road
Cedr Hill, TX 75104-1437

PENN STATE UNIVERSITY
126 Paterno Library
University Park, PA 16802-1808

DAVID J. PINION
1122 E Pike Street #1217
SEATTLE, WA 98122

KATHERINE SIAKAVARA
Gymnasiou 8
Thessaloniki, Greece 55236

SWETS INFORMATION SERVICES
160 Ninth Avenue, Suite A
Runnemede, NJ 08078

YUTAKA TANGE
Maizuru Natl College of Technology
Maizuru, Kyoto, Japan 625-8511

TIB & UNIV. BIB. HANNOVER
Welfengarten 1B
Hannover, Germany 30167

UEKAE
PO Box 830470
Birmingham, AL 35283

UNIV OF CENTRAL FLORIDA
4000 Central Florida Boulevard
Orlando, FL 32816-8005

UNIVERSITY OF COLORADO
1720 Pleasant Street, 184 UCB
Boulder, CO 80309-0184

UNIVERSITY OF KANSAS – WATSON
1425 Jayhawk Blvd 210S
Lawrence, KS 66045-7594

UNIVERSITY OF MISSISSIPPI
JD Williams Library
University, MS 38677-1848

UNIVERSITY LIBRARY/HKUST
Clear Water Bay Road
Kowloon, Honk Kong

CHUAN CHENG WANG
8F, No. 31, Lane 546
MingCheng 2nd Road, Zuoying Dist
Kaoshiung City, Taiwan 813

THOMAS WEILAND
TU Darmstadt
Schlossgartenstrasse 8
Darmstadt, Hessen, Germany 64289

STEVEN WEISS
US Army Research Lab
2800 Powder Mill Road
Adelphi, MD 20783

YOSHIHIDE YAMADA
NATIONAL DEFENSE ACADEMY
1-10-20 Hashirimizu
Yokosuka, Kanagawa,
Japan 239-8686

APPLIED COMPUTATIONAL ELECTROMAGNETICS SOCIETY JOURNAL
http://aces.ee.olemiss.edu

INFORMATION FOR AUTHORS

PUBLICATION CRITERIA

Each paper is required to manifest some relation to applied computational electromagnetics. **Papers may address general issues in applied computational electromagnetics, or they may focus on specific applications, techniques, codes, or computational issues.** While the following list is not exhaustive, each paper will generally relate to at least one of these areas:

1. **Code validation.** This is done using internal checks or experimental, analytical or other computational data. Measured data of potential utility to code validation efforts will also be considered for publication.

2. **Code performance analysis.** This usually involves identification of numerical accuracy or other limitations, solution convergence, numerical and physical modeling error, and parameter tradeoffs. However, it is also permissible to address issues such as ease-of-use, set-up time, run time, special outputs, or other special features.

3. **Computational studies of basic physics.** This involves using a code, algorithm, or computational technique to simulate reality in such a way that better, or new physical insight or understanding, is achieved.

4. **New computational techniques** or new applications for existing computational techniques or codes.

5. **"Tricks of the trade"** in selecting and applying codes and techniques.

6. **New codes, algorithms, code enhancement, and code fixes.** This category is self-explanatory, but includes significant changes to existing codes, such as applicability extensions, algorithm optimization, problem correction, limitation removal, or other performance improvement. **Note: Code (or algorithm) capability descriptions are not acceptable, unless they contain sufficient technical material to justify consideration.**

7. **Code input/output issues.** This normally involves innovations in input (such as input geometry standardization, automatic mesh generation, or computer-aided design) or in output (whether it be tabular, graphical, statistical, Fourier-transformed, or otherwise signal-processed). Material dealing with input/output database management, output interpretation, or other input/output issues will also be considered for publication.

8. **Computer hardware issues.** This is the category for analysis of hardware capabilities and limitations of various types of electromagnetics computational requirements. Vector and parallel computational techniques and implementation are of particular interest.

Applications of interest include, but are not limited to, antennas (and their electromagnetic environments), networks, static fields, radar cross section, inverse scattering, shielding, radiation hazards, biological effects, biomedical applications, electromagnetic pulse (EMP), electromagnetic interference (EMI), electromagnetic compatibility (EMC), power transmission, charge transport, dielectric, magnetic and nonlinear materials, microwave components, MEMS, RFID, and MMIC technologies, remote sensing and geometrical and physical optics, radar and communications systems, sensors, fiber optics, plasmas, particle accelerators, generators and motors, electromagnetic wave propagation, non-destructive evaluation, eddy currents, and inverse scattering.

Techniques of interest include but not limited to frequency-domain and time-domain techniques, integral equation and differential equation techniques, diffraction theories, physical and geometrical optics, method of moments, finite differences and finite element techniques, transmission line method, modal expansions, perturbation methods, and hybrid methods.

Where possible and appropriate, authors are required to provide statements of quantitative accuracy for measured and/or computed data. This issue is discussed in "Accuracy & Publication: Requiring, quantitative accuracy statements to accompany data," by E. K. Miller, *ACES Newsletter*, Vol. 9, No. 3, pp. 23-29, 1994, ISBN 1056-9170.

SUBMITTAL PROCEDURE

All submissions should be uploaded to ACES server through ACES web site (http://aces.ee.olemiss.edu) by using the upload button, journal section. Only pdf files are accepted for submission. The file size should not be larger than 5MB, otherwise permission from the Editor-in-Chief should be obtained first. Automated acknowledgment of the electronic submission, after the upload process is successfully completed, will be sent to the corresponding author only. It is the responsibility of the corresponding author to keep the remaining authors, if applicable, informed. Email submission is not accepted and will not be processed.

EDITORIAL REVIEW

In order to ensure an appropriate level of quality control, papers are peer reviewed. They are reviewed both for technical correctness and for adherence to the listed guidelines regarding information content and format.

PAPER FORMAT

Only camera-ready electronic files are accepted for publication. The term **"camera-ready" means that the material is neat, legible, reproducible, and in accordance with the final version format listed below.**

The following requirements are in effect for the final version of an ACES Journal paper:

1. The paper title should not be placed on a separate page.

The title, author(s), abstract, and (space permitting) beginning of the paper itself should all be on the first page. The title, author(s), and author affiliations should be centered (center-justified) on the first page. The title should be of font size 16 and bolded, the author names should be of font size 12 and bolded, and the author affiliation should be of font size 12 (regular font, neither italic nor bolded).

2. An abstract is required. The abstract should be a brief summary of the work described in the paper. It should state the computer codes, computational techniques, and applications discussed in the paper (as applicable) and should otherwise be usable by technical abstracting and indexing services. The word "Abstract" has to be placed at the left margin of the paper, and should be bolded and italic. It also should be followed by a hyphen (—) with the main text of the abstract starting on the same line.

3. All section titles have to be centered and all the title letters should be written in caps. The section titles need to be numbered using roman numbering (I. II. ….)

4. Either British English or American English spellings may be used, provided that each word is spelled consistently throughout the paper.

5. Internal consistency of references format should be maintained. As a guideline for authors, we recommend that references be given using numerical numbering in the body of the paper (with numerical listing of all references at the end of the paper). The first letter of the authors' first name should be listed followed by a period, which in turn, followed by the authors' complete last name. Use a coma (,) to separate between the authors' names. Titles of papers or articles should be in quotation marks (" "), followed by the title of journal, which should be in italic font. The journal volume (vol.), issue number (no.), page numbering (pp.), month and year of publication should come after the journal title in the sequence listed here.

6. Internal consistency shall also be maintained for other elements of style, such as equation numbering. Equation numbers should be placed in parentheses at the right column margin. All symbols in any equation have to be defined before the equation appears or right immediately following the equation.

7. The use of SI units is strongly encouraged. English units may be used as secondary units (in parentheses).

8. Figures and tables should be formatted appropriately (centered within the column, side-by-side, etc.) on the page such that the presented data appears close to and after it is being referenced in the text. When including figures and tables, all care should be taken so that they will appear appropriately when printed in black and white. For better visibility of paper on computer screen, it is good to make color figures with different line styles for figures with multiple curves. Colors should also be tested to insure their ability to be distinguished after black and white printing. Avoid the use of large symbols with curves in a figure. It is always better to use different line styles such as solid, dotted, dashed, etc.

9. A figure caption should be located directly beneath the corresponding figure, and should be fully justified.

10. The intent and meaning of all text must be clear. For authors who are not masters of the English language, the ACES Editorial Staff will provide assistance with grammar (subject to clarity of intent and meaning). However, this may delay the scheduled publication date.

11. Unused space should be minimized. Sections and subsections should not normally begin on a new page.

ACES reserves the right to edit any uploaded material, however, this is not generally done. It is the author(s) responsibility to provide acceptable camera-ready files in pdf and MSWord formats. Incompatible or incomplete files will not be processed for publication, and authors will be requested to re-upload a revised acceptable version.

COPYRIGHTS AND RELEASES

Each primary author must execute the online copyright form and obtain a release from his/her organization vesting the copyright with ACES. Both the author(s) and affiliated organization(s) are allowed to use the copyrighted material freely for their own private purposes.

Permission is granted to quote short passages and reproduce figures and tables from and ACES Journal issue provided the source is cited. Copies of ACES Journal articles may be made in accordance with usage permitted by Sections 107 or 108 of the U.S. Copyright Law. This consent does not extend to other kinds of copying, such as for general distribution, for advertising or promotional purposes, for creating new collective works, or for resale. The reproduction of multiple copies and the use of articles or extracts for commercial purposes require the consent of the author and specific permission from ACES. Institutional members are allowed to copy any ACES Journal issue for their internal distribution only.

PUBLICATION CHARGES

All authors are allowed for 8 printed pages per paper without charge. Mandatory page charges of $75 a page apply to all pages in excess of 8 printed pages. Authors are entitled to one, free of charge, copy of the printed journal issue in which their paper was published. Additional reprints are available for $ 50. Requests for additional re-prints should be submitted to the managing editor or ACES Secretary.

Corresponding author is required to complete the online form for the over page charge payment right after the initial acceptance of the paper is conveyed to the corresponding author by email.

ACES Journal is abstracted in INSPEC, in Engineering Index, DTIC, Science Citation Index Expanded, the Research Alert, and to Current Contents/Engineering, Computing & Technology.